It's All in the Wrist:
A Quantitative Characterization of Human Wrist Control

by

Steven K. Charles

S.M., Mechanical Engineering
Massachusetts Institute of Technology, 2004

B.S., Mechanical Engineering
Brigham Young University, 2001

Submitted to the Harvard-MIT Division of Health Sciences and Technology
in Partial Fulfillment of the Requirements for the Degree of

Doctor of Philosophy in Mechanical and Medical Engineering

at the

Massachusetts Institute of Technology

September 2008

Signature of Author: ____
Harvard-MIT Division of Health Sciences and Technology
August 22, 2008

Certified by: ____
Neville Hogan, Ph.D.
Professor of Mechanical Engineering
Professor of Brain and Cognitive Sciences
Thesis Supervisor

Accepted by: ____
Martha L. Gray, Ph.D.
Edward Hood Taplin Professor of Medical and Electrical Engineering
Director, Harvard-MIT Division of Health Sciences and Technology

It's All in the Wrist:
A Quantitative Characterization of Human Wrist Control

by

Steven K. Charles

Submitted to the Harvard-MIT Division of Health Sciences and Technology
on August 22, 2008 in Partial Fulfillment of the Requirements for the Degree of
Doctor of Philosophy in Mechanical and Medical Engineering

Abstract

Over the past three decades, much research in motor neuroscience has focused on understanding how humans make coordinated reaching movements, yielding valuable insight into the planning and control of reaching movements, and establishing a foundation for robot-assisted rehabilitation. The goal of this doctoral research was to provide a quantitative characterization of humans' wrist rotations, paving the way for intelligent robot-assisted wrist rehabilitation. More specifically, we have characterized the kinematics, dynamics, and adaptation of wrist rotations, and discussed implications for planning and control.

Kinematics: It is well known that humans make relatively straight reaching movements, suggesting that reaching movements are primarily under kinematic control of hand position. We used a motion capture system to test if wrist rotations are also under kinematic control. We found that wrist rotations exhibit a pattern with significantly more path curvature and variability than reaching movements ($p \leq 0.001$). While the increased path curvature could indicate that wrist rotations are not under kinematic control, this work provides evidence that the curvature is instead due to imperfect peripheral execution.

Dynamics: In order to determine the exact cause of path curvature, an anatomically-accurate, mathematical model of the wrist was developed, including recent measurements of passive wrist stiffness. Combining experimentally-measured kinematics from human subjects with the wrist model revealed that moderately-sized wrist rotations can be approximated by a very simple model with virtually no loss in accuracy. Interaction torques, for which the nervous system compensates in reaching movements, are present but negligible in wrist rotations. Rather, wrist rotation dynamics are dominated by stiffness, which was shown to be the likely cause of path curvature.

Adaptation: When perturbed during reaching movements, humans adapt by straightening their paths, confirming that kinematics play a prominent role in planning reaching movements. We found that subjects consistently adapted to a conservative, velocity-dependent force field. Interestingly, this adaptation was more difficult to detect than in perturbation studies involving reaching movements. Taken together, these results suggest that wrist rotations are also primarily under kinematic control (albeit imperfect).

Thesis supervisor:	Neville Hogan
Title:	Professor, Mechanical Engineering Professor, Brain and Cognitive Sciences

Acknowledgements

The research in this thesis was performed in the Newman Laboratory for Biomechanics and Human Rehabilitation at the Massachusetts Institute of Technology in Cambridge, MA. I must admit that I thoroughly enjoyed my time in the Newman Laboratory. On more than one occasion, I found myself pulling yet another all-nighter trying to make a deadline and I suddenly (and amazingly) realized that I loved what I was doing. I cannot think of a more fascinating pastime than applying mechanical engineering tools to problems in human motor control.

Many people have contributed to this thesis and supported me in my quest for a Ph.D. I'd like to acknowledge my research advisor, Neville Hogan. He has been kind and fair, and given me room and time to explore, which is exactly what I needed. No matter what new idea or result I came up with, he always seemed intrigued and excited. I will continue to try to emulate his academic rigor and courage.

I'd like to thank Hermano Igo Krebs for hours of mentoring. When I first started in the Newman Lab, Igo spent many hours with me helping me learn the new lab software. That started me off on a good foot and gave me confidence, and I was later able to use that training to help other lab members.

I am indebted to Peter Strick, Rob Howe, and Emilio Bizzi, who generously agreed to serve on my thesis committee even though none of them knew me when I first approached them. I'm especially grateful to Peter for making room in his extremely busy schedule to travel to Boston on multiple occasions. Even more importantly, Peter has been a mentor through his encouragement, advice, and praise.

What made my lab experience most enjoyable were my fellow graduate students. Having grown up in a large family, I saw our lab as a family, and I enjoyed every opportunity to talk one-on-one or convene in group meetings. Countless humor-filled moments provided a healthy distraction from the pressures of research.

I'd also like to acknowledge the people that give life to my Ph.D. program, the administrators and fellow graduate students in the Harvard-MIT Division of Health Sciences and Technology (HST). HST is remarkable for camaraderie and social support. I'm especially indebted to H. Frederick Bowman, Cathy Modica, and Valerie Pronio-Stelluto.

I received constant and warm support and service from many friends at my local congregation of The Church of Jesus Christ of Latter-day Saints as well as in the MIT Eastgate community, especially from Cort and Corey Johnson, who were like family during our seven years in Boston. Likewise, my parents and parents-in-law have been ever-ready with praise and encouragement and support, for me and for my family, for which I will always be grateful.

I interviewed for the HST program two weeks after my oldest son, Samuel, was born. Two weeks after I took my qualifying exams, my second son, Benjamin, was born. My third son, William, was born in between my clinical rotations. These three boys have kept me sane, always reminding me what matters most in life. For years they prayed that Daddy would finish his paper, finish his thesis, and get a job. I feel uniquely blessed that throughout these years of graduate studies I could leave the work I loved each evening and go home to children I loved much more and who mattered infinitely more.

Most importantly, I want to thank and give credit to my wife Cristie. I have never had a friend as close or as deep or as meaningful as her. She has helped me through truly low and difficult times—times when I didn't know if I would graduate, times when she had to sacrifice her own goals and desires to help me. She has helped me write and re-write countless documents and presentations, listened to me talk about my research, and given me professional advice. She has spent numberless hours watching little children so that I could focus on coursework and research. She has been my constant support and personal cheerleader. In fact, I'm sure I wouldn't have started this program without her, let alone finished it. This degree belongs to her as much as it does to me. Thank you, Cristie, for giving meaning to my work and life.

Lastly, I'd like to acknowledge the numerous blessings, small and large, which I have received from God. Although these years of graduate study have been rewarding, they have also been extremely challenging for me and for my family, and we have petitioned God on a daily basis. I can attest that He has blessed us daily through countless tender mercies and even some overt miracles. I understand that it is now my obligation to go forth and serve others as I have been served.

Table of Contents

List of Figures

List of Tables

1 Introduction

1.1 Overview

Over the past three decades, much research in motor neuroscience has focused on understanding how humans make coordinated reaching movements. This research has yielded valuable insight into the planning and control of reaching movements. One successful application of this research has come in the form of robot-assisted rehabilitation of reaching movements for persons who are recovering from neurological or biomechanical injury.

The goal of this dissertation is to provide a quantitative characterization of humans' wrist rotations, paving the way for intelligent robot-assisted rehabilitation of wrist movements. More specifically, this dissertation characterizes the kinematics and dynamics of natural wrist rotations, and investigates adaptation in the face of force perturbations. Implications for the planning and control of wrist rotations are discussed. Throughout this dissertation, characteristics of wrist rotations are compared and contrasted to reaching movements.

1.1.1 Kinematics

The objective of a reaching movement is often to transport the hand from one position in three-dimensional space to another. While the hand does undergo rotation, reaching tasks focus on translating the hand. In contrast, wrist motion, which by nature is almost purely rotational, moves the hand from one *orientation* in space to another. Such finite rotations are fundamentally different from translations in that finite rotations do not commute in addition (Chapter 2). *Thus, the wrist presents to the nervous system a potential challenge which is completely absent in planar reaching movements.*

It has long been known that humans tend to make reaching movements in such a way that the hand traces a relatively straight path through space. The straightness of the path is significant insofar as it suggests that reaching movements are under kinematic control of hand position.

In apparent contrast, we have shown that wrist rotations exhibit significantly more path curvature and variability than reaching movements (Chapter 3). This path curvature forms a stereotypical pattern in different directions and increases significantly with movement speed. The increased path curvature could lead one to believe that wrist rotations may not be under kinematic control of hand position. However, we provide evidence that the observed pattern of curvature is not due to central planning or control, but rather to imperfect peripheral execution (more specifically, the stiffness of the wrist may be sufficient to account for the observed pattern of curvature—see below).

1.1.2 Dynamics

The dynamics of reaching movements are dominated by inertial effects, arising from the acceleration of each limb separately, as well as from inertial interaction between the arm and forearm. Controlling reaching movements in the face of non-linear inertial coupling presents a significant control challenge to the nervous system, and has been the focus of much research.

We have created an anatomically accurate model of wrist dynamics, in which the wrist is modeled as a universal joint with an offset between the axes. Combining experimental measurements with the inverse dynamic wrist model, we have shown that wrist rotation dynamics are dominated by stiffness, not inertia as in reaching movements (Chapter 4). Only at the upper limit of movement speed do inertial effects become important in wrist rotations. Even then, inertial interactions between the degrees of freedom of the wrist are negligible. In fact, we show that for wrist rotations limited to ±15° (which represents a significant portion of the wrist's range of motion in radial-ulnar deviation) the anatomically accurate wrist model can be simplified to the point where wrist dynamics are well approximated by a set of linear, uncoupled equations of motion.

Using the model of wrist dynamics, we have shown that the pattern of curvature observed in wrist rotations is most likely caused by wrist stiffness (Chapters 5 and 6). In fact, two features of wrist stiffness—wrist stiffness is anisotropic and slightly pronated—can account for five of six prominent features of the observed pattern of path curvature.

1.1.3 Adaptation

The strongest evidence for the kinematic control of reaching movements has been provided by studies in which the path is artificially curved, either mechanically or visually. Under such conditions, subjects adapt by straightening their paths, confirming that kinematics play a prominent role in planning reaching movements. Though dynamic considerations may play a role, the kinematic plan appears to be primary.

In order to determine whether wrist rotations are under kinematic or dynamic control, we have performed similar force perturbation experiments for the wrist (Chapter 7). Subjects consistently adapted to a conservative, velocity-dependent force field. Interestingly, this adaptation was more difficult to detect than in perturbation studies involving reaching movements, consistent with the hypothesis that wrist rotations are implemented by a less perfect controller. Taken together, the results in Chapter 7 suggest that wrist rotations are also primarily under kinematic control (albeit imperfect control).

1.2 Background

1.2.1 Wrist Joint

The wrist joint involves motion between the radius and the carpal bones, the carpal bones themselves, and the carpal and metacarpal bones. The combined effect is to allow the hand to move relative to the forearm in flexion and extension (flex-ext) and radial and ulnar deviation (rad-uln). Immediately proximal to the wrist is the distal radio-ulnar joint, where the radius rotates about the ulna, allowing the forearm to rotate in pronation and supination (pro-sup). Together, these joints allow the hand to assume any orientation relative to the arm (within joint limits). See Chapter 2 for more details about wrist anatomy and kinematics.

1.2.2 Wrist function

A defining feature of humans is the use of their hands for tasks which are highly complex in space and time. Any functional use of the hands demands orientation, stability, and/or mobility of the wrist. Therefore, the wrist undergoes rotations of significant amplitude, frequency, and loading throughout the day. For many professionals, wrist motion of some form or another is critical to performing their job. Some professionals, such as performing artists and athletes, spend years training their wrists—among other joints—to behave with desired characteristics, involving smoothness, overshoot, tremor, precision, and strength, etc.

1.2.3 Diseases affecting the wrist

Due to its active role in a large number of daily activities, and its prominent position near the end of the upper limb, the wrist is vulnerable to injury and dysfunction. The wrist provides a protected conduit for all nerves, vessels, and extrinsic muscles of the hand. Disorders affecting the wrist can involve biomechanics (e.g., arthritis, tears, fractures), peripheral nervous system (e.g. carpal tunnel syndrome), or central nervous system (e.g. stroke). Whatever the cause, wrist functionality is reduced or eliminated due to reduced mobility, strength, and/or coordination.

1.2.4 Robot-assisted rehabilitation

One particular application of this research is wrist rehabilitation after stroke. Traditional stroke rehabilitation consists of individual therapy sessions with a physical therapist. There is increasing cost-related pressure to decrease such individual attention. At the same time, the number of persons in need of therapy has increased as the size of the aging population grows. In the face of increasing demand for, but decreasing supply of therapy time, robot-aided therapy provides a potential solution [1]. Not only can robotic therapy increase individual therapy time, but it is capable of precisely identifying subtle kinematic characteristics of patient movement. Based on such characteristics, the robot can then adapt to the patient's progress in real time. Such performance-based progressive robotic therapy on a planar reaching robot (for movement of the upper and lower arm) has been shown to substantially increase the benefits of therapy, as assessed by traditional clinical scores [2]. These improvements were achieved well beyond the expected period for improvement after stroke.

Robot-assisted rehabilitation for reaching movements owes much of its success to decades of research investigating fundamental aspects of the kinematics, dynamics, and control of *unimpaired* reaching movements. This research laid a quantitative foundation on which to build and evaluate rehabilitation. In contrast, unimpaired wrist rotations have received much less attention (see Literature Review below). Thus, although a robot for rehabilitation of wrist and forearm rotations is available [3], we have lacked a quantitative foundation on which to design and evaluate intelligent robot-assisted rehabilitation of wrist rotations.

1.3 Literature Review

Prior studies involving kinematics of the human wrist can be split roughly into three domains based on scale: bones, ligaments and muscles of the wrist joint; the wrist joint as a whole; and the upper limb. Following is a brief summary of prior work in each of these three domains.

1.3.1 Bones, ligaments and muscles of the wrist

Studies characterize the anatomy and biomechanics of the wrist joint [4] or deal with the effects of bone fractures, ligament and tendon tears and the subsequent repair interventions (surgery, fixation, etc.) on the kinematics of individual carpal bones and the interactions between carpal bones. Many publications deal with the practical issues involved in sensing/imaging carpal bone motion. Emphasis is placed on movement of individual or groups of carpal bones rather than the entire joint.

1.3.2 Global Wrist Motion

These studies look at motion of the wrist joint as a whole and in isolation of movement at other joints. Some of these studies focus on techniques to measure [5, 6], represent (determining, e.g., reference frames [7, 8] and axes of rotation [9, 10]), and analyze [11, 12] wrist rotations. One study investigates mechanical coupling of the degrees of freedom of the wrist [13], and another the viscosity of global wrist motion[14]. Several studies explore how wrist joint motion changes under different conditions, such as elastic, viscous, and inertial loading [15-18] and fatigue [19]. Other studies use the wrist to study more general phenomena such as rhythmic movement [20], bimanual coordination [21], learning [22, 23], and perception [24]. Some focus on patterns of muscle activation [25-27] whereas others look at the neurophysiologic activity involved in wrist movements [28-31]. A few studies address wrist movements inherent in the work of performing artists [32, 33] and athletes [34, 35]. Of the psychophysical experiments investigating wrist kinematics, most limit themselves to one degree of freedom (almost always flexion or flexion-extension). Very few studies investigate wrist motion behavior in two DOF [13, 32], let alone in three DOF.

Unfortunately, these studies are generally isolated and short-lived excursions to the wrist; it is clear that there has been little attempt to make a thorough and systematic investigation of wrist motion behavior, with one exception: Donna Hoffman and Peter Strick (University of Pittsburgh School of Medicine) have performed what is by far the most thorough and systematic set of studies of wrist motion behavior. Their studies have investigated the kinematics and muscle activity of the wrist [36-40], responses to load perturbations [41], and muscle and movement representation in the motor cortex [42-44]. Their subjects, which include humans and monkeys, were asked to rotate the wrist in one DOF (flexion-extension [37] or abduction-adduction [38, 40, 41]) or two DOF (abduction-adduction, flexion-extension, and combinations) [36, 42-44]. Some studies compare rotation in 2-DOF when the wrist is constrained in pronation, supination, or neutral position [42-44].

1.3.3 Coordination of upper-limb movements

Studies generally investigate movement at the shoulder and elbow (reaching) or shoulder, elbow and hand (reaching and grasping). Although the wrist joint plays an important role in functional whole arm movements—insofar that it allows a person to orient the hand for proper engagement with an object and then stabilize and manipulate the object—its motion is usually overlooked in favor of movement at the shoulder, elbow, and/or hand. Emphasis is placed on understanding control, coordination, and adaptation at these joints in the face of kinematic redundancy—for examples, see [45-52]. Experimental settings are split between health (e.g. vision vs. no vision, force perturbations, rhythmic vs. discrete, unilateral vs. bilateral, etc.) and disease (hemiplegia, spinal cord injury, Parkinson’s Disease, stroke, etc.). While it is clear that motor control of other limbs profoundly influence the functional efficacy of the wrist, my research will focus on motion at the wrist joint.

1.3.4 Summary

Of the few studies that investigate wrist motion behavior, most only consider flexion-extension or abduction-adduction separately. Very few look at flexion-extension and abduction-adduction combined. I am not aware of any study that investigates the kinematics of flex-ext, rad-uln, and pro-sup, not to mention the coordination of finite wrist rotations in three DOF. Nevertheless, the research performed by Hoffman and Strick is by far the most substantial body of work on step-tracking movements of the wrist, and forms a significant part of the foundation on which this research is built.

2 Anatomy and Kinematics

2.1 Anatomy of the Wrist

2.1.1 Bone Structure

The bone structure of the wrist consists of its eight carpal[1] bones, roughly arranged in two rows, which connect proximally to the radius of the forearm (the ulna doesn't actually interface with the carpal bones) and distally to the five metacarpals of the hand. The wrist allows flexion-extension (flex-ext) and radial-ulnar deviation (rad-uln) of the hand through articulation at the radiocarpal joint (between the radius and the proximal carpal row), the midcarpal joint (between the proximal and distal rows of carpal bones), the carpo-metacarpal joint (between the distal row of carpal bones and the metacarpal bones), and between individual carpal bones. The distal radioulnar joint, which allows pronation-supination (pro-sup) of the forearm, is proximal to the wrist joint and is generally not considered part of the wrist. Global wrist motion is achieved as individual carpal bones translate and rotate relative to each other and to bones proximal and distal to the wrist in complex in-plane and out-of-plane motions. While it is unlikely that the motion of individual carpal bones can be reduced to a simplified model such as a two-row system [53], one can view global wrist motion simply as the motion of the hand relative to the forearm. Global wrist motion, which is the focus of this research, *can* be approximated by a simple model (see Wrist Kinematics).

2.1.2 Wrist Muscles

Wrist Joint

Two dozen muscles cross the wrist and are therefore capable of exerting a torque about the wrist joint. These muscles are grouped into flexors and extensors:

flexor carpi radialis (FCR)
flexor carpi ulnaris (FCU)
flexor pollicis longus

---

[1] carpal comes from the Greek *karpos*, meaning wrist

palmaris longus
flexor digitorum superficialis (a group of 4 muscles)
flexor digitorum profundus (a group of 4 muscles)

extensor carpi radialis longus (ECRL)
extensor carpi radialis brevis (ECRB)
extensor carpi ulnaris (ECU)
abductor pollicis longus
extensor pollicis brevis
extensor pollicis longus
extensor indicis
extensor digitorum (a group of 4 muscles)
extensor digiti minimi

While all of these muscles are, in theory, capable of rotating the wrist, “movement at the wrist is produced primarily by the “carpi” muscles of the forearm...

Flexion of the wrist is produced by the flexor carpi radialis and flexor carpi ulnaris, with assistance from the flexors of the fingers and thumb, the palmaris longus and the abductor pollicis longus.

Extension of the wrist is produced by the extensor carpi radialis longus, extensor carpi radialis brevis, and extensor carpi ulnaris, with assistance from the extensors of the fingers and thumb.

[Radial deviation] of the wrist is produced by the abductor pollicis longus, flexor carpi radialis, extensor carpi radialis longus, and extensor carpi radialis brevis; it is limited to approximately 15° because of the projecting radial styloid process.

[Ulnar deviation] of the wrist is produced by simultaneous contraction of the extensor carpi ulnaris and flexor carpi ulnaris.” [54].

More detailed studies of the muscle activity associated with movements in different directions have been performed by Hoffman and Strick. They have extensive experience recording from muscles of the wrist and arm, as summarized in [44]. In the fourth paper of their series on step-tracking movements of the wrist [36], they outline their EMG measuring methods and report the directional involvement of the five main wrist muscles (the "carpi" muscles).

Distal Radio-ulnar joint

An entirely different set of muscles are responsible for rotating the forearm in pronation and supination.

"*Supination* is produced by the supinator (when resistance is absent) and biceps brachii (when power is required because of resistance), with some assistance from the [extensor pollicis longus] and [extensor carpi radialis longus]. *Pronation* is produced by the pronator quadratus (primarily) and pronator teres (secondarily), with some assistance from the flexor carpi radialis, palmaris longus, and brachioradialis (when the forearm is in the midpronated position)." [54]

2.1.3 Nerves, Blood Vessels, Ligaments, and Tendons

Clearly, all transfer to and from the hand—be it mechanical, neural, or nutritional—must travel through the wrist. On the volar surface of the wrist, the carpal bones form a protective cavity, the carpal tunnel, through which pass the median nerve and the tendons of the superficial and deep finger flexors. Stretched over this tunnel is a thick transverse ligament called the flexor retinaculum. The ulnar artery and nerve and the radial artery also pass the wrist but are not protected in the carpal tunnel.

2.2 Wrist Kinematics

2.2.1 Wrist Orientation

In this section, we discuss challenges inherent in *representing* finite rotations such as the wrist, and solutions for dealing with these challenges.

Representations of wrist orientation vs. models of wrist kinematics

It is important to distinguish between representations of wrist orientation and models of wrist kinematics. Representations of orientation, such as Cartesian coordinates or Euler angles, define the orientation, or state, of the wrist. Humans' proprioceptive abilities indicate that the central nervous system uses some type (or many types) of representation to define and store the orientation of the wrist. Importantly, this representation may or may not reflect the kinematic behavior of the wrist. Likewise, we can represent *orientation* of the wrist by any number of possible representations which may or may not reflect wrist *kinematics*. In this section, we present various representations of wrist orientation. As we shall see, they are all equally correct, but some are more practical than others.

In contrast, kinematic models, such as the kinematic pairs listed above, are attempts to approximate the kinematic *behavior* of the wrist. The choice of kinematic model *is* important because some models approximate the system's behavior more accurately than others. For example, we show in the next section that a universal joint approximates the kinematic constraints of the wrist more accurately than a spherical joint.

Representations of wrist orientation

Global wrist orientation is generally defined as the orientation of the third metacarpal relative to the forearm [8]. It takes at least three variables to describe the orientation of a rigid body in space. The choice of these three variables is not unique. Assuming that the wrist joint is purely rotational, i.e. does not allow any translation (this is a good approximation—see Wrist as Kinematic Pair, below), these three variables could be the Cartesian[2] or polar coordinates of any point on the third metacarpal, the Euler angles of the third metacarpal, or an infinite number of other representations.

2.2.2 Finite rotations

The problem with finite rotations: they do not commute in addition

When a rigid body is sequentially translated in different directions, the sequence of translations does not affect the final position of the body. For example, whether I move an object forward and then to the right, or to the right and then forward, the final position of the object is the same. Not so for rotations: when a rigid body is rotated in sequence about multiple axes, the rotation sequence does affect the final orientation of the body. In

---

[2] Cartesian coordinates simply refer to coordinates whose axes are mutually orthogonal.

mathematical parlance, finite[3] rotations are not commutative in addition. This phenomenon is easily demonstrated, as shown in Figure 2.1. This dependence on rotation sequence, or non-commutativity, is a property of any rotation involving more than 1 axis. In other words, it doesn't take three axes—even rotations about two axes do not commute in addition. Furthermore, non-commutativity occurs for rotations about body-fixed axes as well as space-fixed axes.

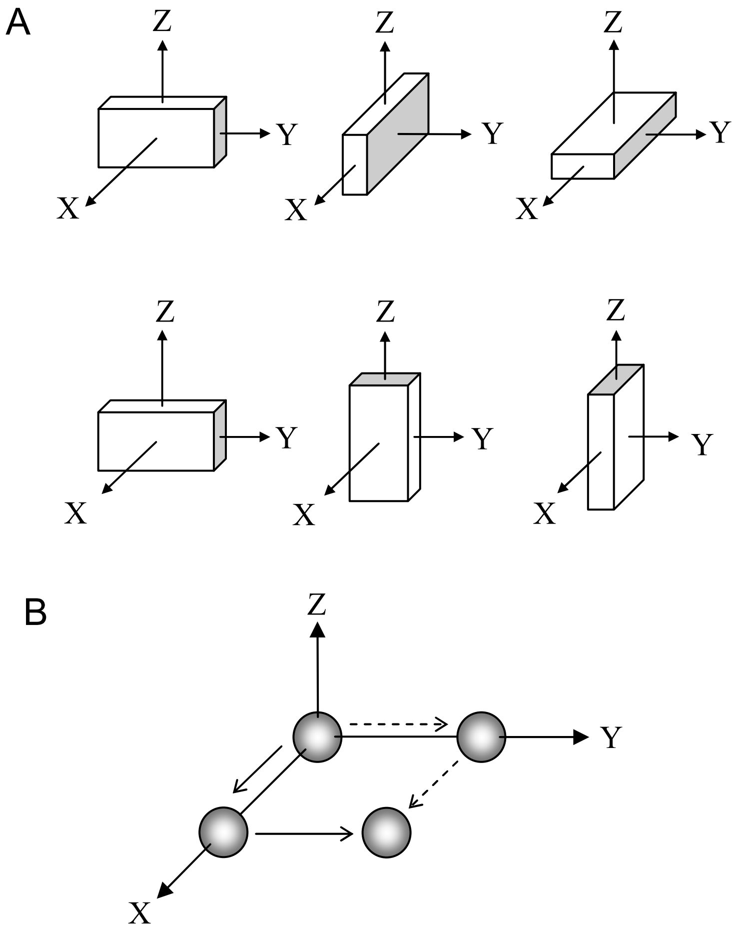

Figure 2.1: Finite rotations do not commute in addition (A), while translations do (B).

How does non-commutativity affect the wrist? Imagine a sequence of wrist rotations about body-fixed axes, as shown in Figure 2.2A. Initially, the orientation of the

---

[3] The reason for adding the word "finite" is that the phenomenon of non-commutativity vanishes for infinitesimally small rotations (which is important because it means that angular velocity *does* commute in addition, and *can* therefore be represented as a vector).

hand is represented in the space-fixed XYZ-frame by vector u (the wrist joint is at the origin). After two rotations, the hand orientation vector becomes u”:

$$\vec{u}'' = \sin\beta\cos\gamma\,\hat{i} - \cos\beta\cos\gamma\,\hat{j} - \sin\gamma\,\hat{k}$$

where $\hat{i}$, $\hat{j}$, and $\hat{k}$ are unit vectors along X, Y, and Z, respectively. If the sequence of rotations is reversed, as in Figure 2.2B, the final hand orientation vector is v”:

$$\vec{v}'' = \sin\beta\,\hat{i} - \cos\beta\cos\gamma\,\hat{j} - \cos\beta\sin\gamma\,\hat{k}$$

Because finite rotations do not commute in addition, the final orientations of u” and v” are not the same. The difference in final orientation can be quantified as ε, the arc subtended by the two vectors:

$$\cos\varepsilon = \vec{u}''\cdot\vec{v}'' = \sin^2\beta\cos\gamma + \cos^2\beta\cos^2\gamma + \cos\beta\sin^2\gamma$$

This difference can be considered as the error caused by non-commutativity because ε would be zero if rotations commuted in addition.

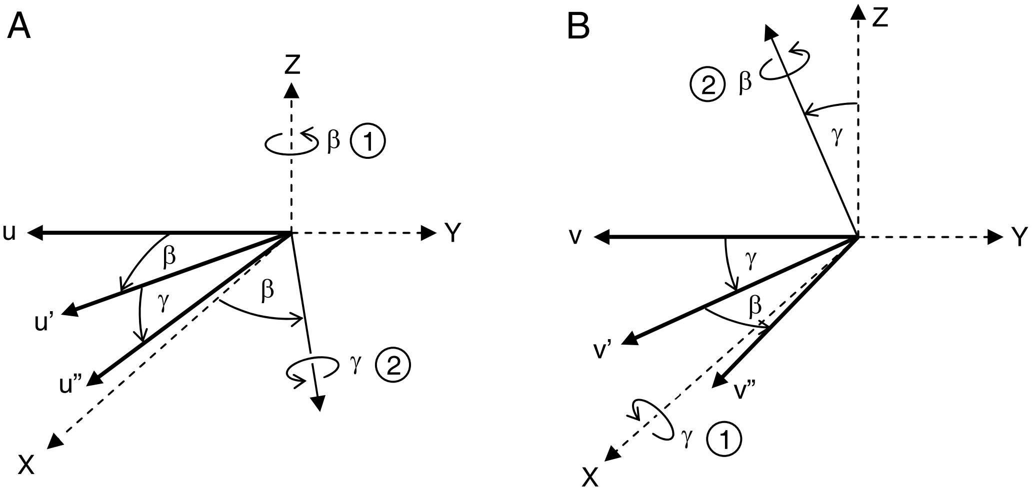

Figure 2.2: A sequence of two rotations of the wrist joint about body-fixed axes. A: The wrist joint is rotated first about Z and then about the rotated X axis. B: The order is reversed: the wrist is rotated first about X and then about the rotated Z-axis.

Reversing the order of finite rotations about non-parallel axes will always result in a non-zero commutativity error. However, this error can be quite small, as shown in

Figure 2.3. For wrist rotations limited to ±15°, ε is less than 0.5°. That said, while the difference in final orientations is almost imperceptible for 15° rotations, it grows non-linearly with increasing rotation amplitude and becomes significant well within the range of motion of the wrist. If forearm pro-sup is allowed in addition to wrist rotations, this non-commutativity error can occur for rotations which use only a small fraction of the range of motion in these three DOF. Furthermore, while the non-commutativity error associated with a single pair of 15° wrist rotations (excluding pro-sup) is small, repeated rotation sequences cause the error to accumulate unless corrected.

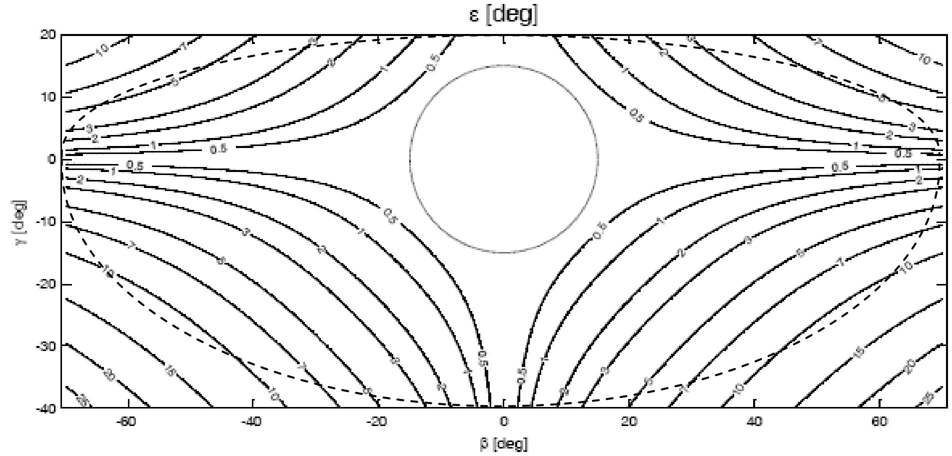

Figure 2.3: Non-commutativity error caused by reversing the rotation order.
The inner circle is at ±15°. The dashed line represents the approximate joint limits.

One might argue that this phenomenon is a consequence of mathematical representation and doesn't matter for human movement; wrist rotations are not executed as sequential rotations about specified axes, but rather as a single rotation about a single axis which, in general, does not coincide with the specified axes. This is equivalent to saying that reaching movements are not executed as sequential translations of the hand along specified axes, but rather as a single translation in a direction which is the vector sum of translations along the specified axes. *Here lies the rub: finite rotations cannot be represented as vectors.*

Finite rotations and vector spaces

As mentioned above, three variables are needed to describe the orientation of a rigid body in space. From Euler's theorem[4], it is known that a rigid body can obtain any orientation by rotation about an appropriate axis. It is tempting, therefore, "to try to associate a vector, characterized by three independent quantities, with the finite displacement of a rigid body about a fixed point. Certainly a direction suggests itself obviously—that of the axis of rotation—and any function of the rotation angle would seem suitable as the magnitude. But it soon becomes apparent that such a correspondence cannot be made successfully" [55].

By definition, vectors are elements of a vector space which allows addition satisfying certain axioms, one of which is that vector addition be commutative [56]. Translations, which commute in addition, can be represented as vectors. However, finite rotations do not commute in addition and can therefore not be accepted as vectors—*a finite rotation cannot be represented by a single vector*.

Said another way, finite rotations cannot be represented in a vector space. Outside of a vector space, there is no inner product, and therefore no norm or metric (a metric defines the notion of distance in a space). To illustrate, consider a vector specified by parameters [a, b, c]. No matter what these parameters represent (Cartesian coordinates, polar coordinates, Euler angles, etc.), one can always define a variable d as:

$$d = \sqrt{a^2 + b^2 + c^2}$$

In a vector space, d satisfies the conditions of an inner product space and can be interpreted as distance. For example, if [a, b, c] represent the endpoint coordinates of the vector in Cartesian coordinates, d is simply the distance of the vector from the origin. In contrast, outside of a vector space, d does not satisfy the conditions of an inner product space and cannot be defined as a metric or distance. For example, if [a, b, c] represent angles of rotation about body-fixed or space-fixed axes, d cannot be defined as distance (not to mention that it has no physical meaning). Not only can distance not be defined outside of a vector space, but concepts as basic as orthogonal and parallel are also not defined.

---

[4] Euler's theorem states that "the general displacement of a rigid body with one point fixed is a rotation about some axis." ([55] H. Goldstein, C. Poole, and J. Safko, *Classical Mechanics*, 3rd ed: Addison Wesley, 2002.)

Why does this matter for every-day wrist rotations? Many activities of daily living involve aligning the orientation of objects. For example, inserting a video tape into a video recorder requires careful alignment of position *and* orientation. Position alignment is commonly accomplished through feedback control involving the minimization of the distance between desired and actual positions. In contrast, control of orientation about multiple axes is challenging because distance is not defined.

Fortunately, it is possible to represent wrist orientation in a vector space and take advantage of the mathematical tools of vector analysis. A rigorous approach from physical systems theory is to define the inner product space in terms of power and energy. Following this approach, one can define a set of generalized coordinates and corresponding forces that can be represented in a vector space. If [a, b, c] represent generalized coordinates, d is a well-defined metric (though as a distance it has limited physical meaning).

2.2.3 Generalized Coordinates

Generalized coordinates are a (non-unique) set of independent variables that uniquely and completely define the configuration of a system. Crandall describes how generalized coordinates differ from normal coordinates [57]: "Point coordinates (e.g., cartesian coordinates, spherical coordinates) are used to locate a point with respect to a reference frame. *Generalized coordinates* are used to locate a dynamic system with respect to a reference frame. A set of generalized coordinates may include cartesian coordinates or spherical coordinates, but may also include convenient lengths or angles which have no association with conventional coordinate systems." See the notes at the end of this chapter for more on generalized coordinates.

While there are many possible sets of generalized coordinates that can describe wrist rotations, one type, Euler angles, is particularly well suited.

Euler angles

Euler angles are a convenient set of generalized coordinates for the purpose of describing the orientation of a body-fixed coordinate frame. Euler angles are well described by Goldstein et al. [55]. In his words, we "can carry out the transformation from a given Cartesian coordinate system to another by means of three successive rotations performed in a specific sequence. The Euler angles are then defined as the three successive angles of rotation."

It is important to remember that Euler angles are nothing but coordinates. One point of confusion arises when one assumes that the rigid body actually goes through the sequence of Euler rotations to pass from one orientation to another. Not so: Euler angles only describe the current orientation and do not pretend to say anything about the path actually taken to get there, just like a representation of the arm in Cartesian coordinates only informs about the current position and does not infer that the arm actually traveled along the axes of the coordinate frame to arrive there.

As with other coordinate systems, there are infinitely many ways to define the Euler axes. However, unlike Cartesian coordinate frames, defining the axes is not enough— because rotations do not commute in addition, one must also define the sequence of rotations. Which sequence one chooses is not important, as long as one sticks with the chosen sequence[5]. "Note that the sequence of rotations used to define the final orientation of the coordinate system is to some extent arbitrary. The initial rotation could be taken about any of the three Cartesian axes. In the subsequent two rotations, the only limitation is that no two successive rotations can be about the same axis. A total of 12 conventions is therefore possible in defining the Euler angles (in a right-handed coordinate system)" [55]. Unfortunately, different fields use different conventions, and even use different names to describe the same conventions, as shown in Table 2.1.

---

[5] A linkage physically maintains the kinematic hierarchy among its joints, effectively permitting only one rotation order. Even if distal joints are articulated before proximal ones, the rotation order is not reversed because the proximal joints carry the distal ones.

Name	Field	Sequence of Rotation Axes and *Angles*		
		First	**Second**	**Third**
x-convention	Goldstein et al.	Z	x’	z”
y-convention	quantum mechanics nuclear physics particle physics	Z	y’	z”
xyz-convention Tait-Bryan angles Cardan angles Nautical angles	flight engineering aerospace engineering	z *yaw* *heading*	y’ *pitch* *attitude*	x” *roll* *bank*
Joint Coordinate System for global wrist motion	**Wrist biomechanics**	**y (e1)** ***pro-sup angle*** α	**z’ (e2)** ***flex-ext angle*** β	**x” (e3)** ***rad-uln angle*** γ

Table 2.1: Various Euler angle definitions commonly used in science and engineering. The x-, y-, and xyz-conventions are described on pages 151 and 154 of [55]. The bottom row shows the joint coordinate system for global wrist motion recommended by the International Society of Biomechanics [8], which is followed throughout this dissertation.

Euler angles are often presented in parallel with transformation matrices. An important difference is explained by Crandall: “[A transformation] matrix has nine elements, but there are six equations interrelating these nine elements. The matrix representation lends formal simplicity to many operations with rotations, but it does not lead directly to a complete and independent set of three generalized coordinates. Such a set is, however, provided by the three [Euler] angles” [57]. In practice, both Euler angles and transformation matrices are very useful, and even more so when used together. That said, the combined use of Euler angles and transformation matrices is extremely prone to error, as discussed in the Appendix A.

2.2.4 ISB definitions of Euler angles for forearm and wrist rotations

In general, Euler angles are simply coordinates defining the state of a system and may therefore be defined in many different ways which may or may not reflect the actual kinematic behavior of the system. In contrast, Euler angles can also be used specifically to define anatomical terms of movement (such as wrist flexion), in which case the choice of Euler angles is critical and must be agree with the joint kinematics.

The International Society of Biomechanics (ISB) has recommended definitions of anatomical terms of movement [8]. While the main purpose of [8] was to define movement between two bones, the authors were careful to also define global motions involving many bones, including forearm pronation-supination (pro-sup) and wrist flexion-extension (flex-ext) and radial-ulnar deviation (rad-uln).

The ISB defines anatomical terms of movement in terms of generalized coordinates (namely Euler angles) using two joint coordinate systems (JCS), one proximal and one distal to the joint in question. The proximal JCS is fixed in the limb proximal to the joint and is considered space-fixed. The distal JCS is fixed in the limb distal to the joint and is body-fixed. The relationship between these two JCSs defines the Euler angles used in the ISB definitions.

The ISB definition of pro-sup, flex-ext, and rad-uln is illustrated in Figure 2.4. The space-fixed frame is XYZ; it is fixed in the ulna and does not rotate (the ulna does not rotate during pro-sup). The body-fixed frame is xyz; it is fixed in the third metacarpal and rotates with it. Because we're only concerned with orientation, both JCSs can be shifted to a common origin—the center of the wrist—for simplicity.

Initially, the two JCSs are aligned. As the xyz frame rotates through each Euler angle, it goes from xyz to x'y'z' to x"y"z" to x'''y'''z'''. The first rotation is by α about y and defines pro-sup (pronation is positive). The second rotation is by β about z' and defines flex-ext (flexion is positive). The third rotation is by γ about x" and defines rad-uln (ulnar deviation is positive).[6]

This definition of pro-sup, flex-ext, and rad-uln treats the forearm and wrist as a linkage in which the pro-sup axis carries the flex-ext and rad-uln axes, and the flex-ext axis carries the rad-uln axis. That the pro-sup axis should carry the flex-ext and rad-uln axes is obvious: the wrist is clearly distal to the forearm. That the flex-ext axis should

---

[6] It is important to distinguish between Euler angles (α, β, γ) and anatomical terms of movement (pronation, supination, flexion, extension, and radial and ulnar deviation). Euler angles define orientation, while the anatomical terms are terms of *movement*, not orientation. One may think of anatomical terms of movement as angular velocity vectors acting along the Euler axes.
Note also that Euler axes coincide with the axes of the body-fixed frame. This is much more practical than aligning Euler axes with space-fixed axes, in which case the inertia tensor would change with time.

carry the rad-uln axis is less obvious, but recent studies suggest that this definition is in agreement with actual wrist kinematics (see below). Therefore, we endorse this definition and use it throughout this dissertation.

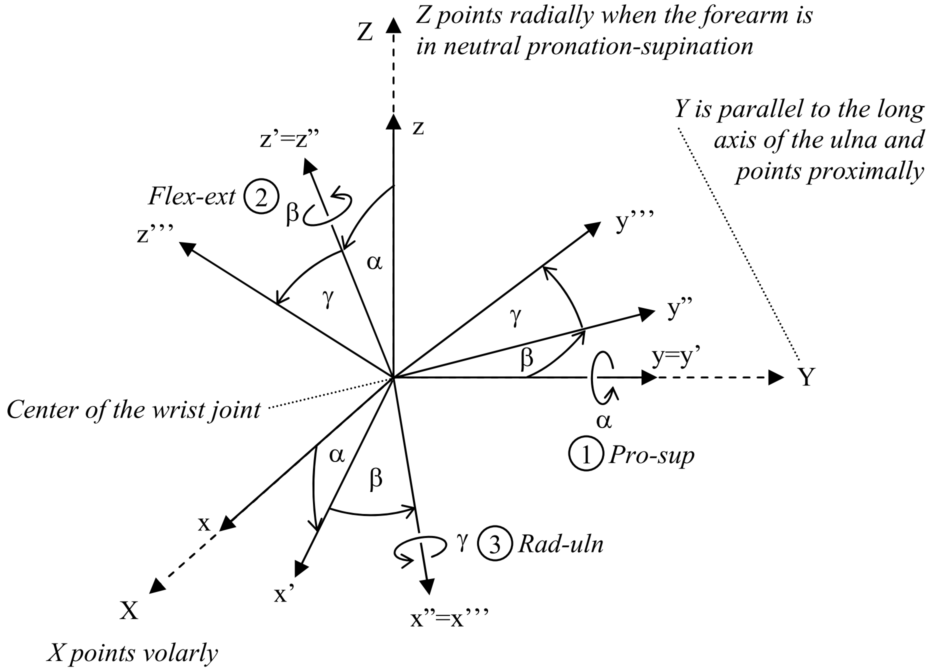

Figure 2.4: ISB definition of pro-sup, flex-ext, and rad-uln.

2.2.5 The wrist as a kinematic pair

Global wrist motion can be approximated by a simple model. The wrist has been variously modeled as a spherical, ellipsoidal, or universal joint. Spherical joint models, which have 3 DOF, group the distal radioulnar joint with the wrist joint. Ellipsoidal joints (a.k.a. condylar or condyloid joints) are like spherical joints except that the surfaces are concave and convex semi-ellipsoids instead of semi-spheres. In such a joint, an ellipsoidal articular surface is received into an ellipsoidal cavity in such a manner as to permit motion along the major and minor axes of the ellipsoid (flex-ext and rad-uln) and limited coupled motion (combined motion, including circumduction), but no axial rotation. Others model the wrist as a universal joint whose axes may be intersecting or non-intersecting (skew) and orthogonal or oblique. Importantly, universal joints, unlike spherical and ellipsoidal joints, require by nature that one axis carry the other—there exists a kinematic hierarchy. In the following paragraphs we show that a universal joint is most consistent with studies of wrist biomechanics.

The complex nature of the wrist joint has made measurements difficult, and studies over the past three decades have generated conflicting results. However, with the advent of magnetic resonance imaging and computed tomography, measurements have become less invasive and accuracy has increased.

Most recent studies of wrist biomechanics agree that flex-ext occurs more at the radiocarpal joint, and rad-uln occurs more at the midcarpal joint [58-60]. Comparing the relative amount of rotation of individual carpal bones, Kaufmann et al showed in 2005 that midcarpal motion accounts for 86% of radial deviation and 66% of ulnar deviation. In 2006, they showed that 75% and 50% of flexion occurred at the radioscaphoid and radiolunate joints, respectively, and 92% and 52% of extension occurred at the radioscaphoid and radiolunate joints, respectively. These data imply a kinematic hierarchy in which the flex-ext axis carries the rad-uln axis.

Studies which investigate global wrist motion support such a kinematic hierarchy with evidence that the wrist rotates about non-intersecting axes, with the rad-uln deviation axis distal to the flex-ext axis [12, 61]. Neu et al. quantified global wrist movement using a non-invasive, in vivo, three-dimensional technique involving computed tomography. They found that the flexion axis and the extension axis were significantly more proximal than the ulnar axis ($p<0.001$, by 3.9 ± 2.0mm and 3.9 ± 1.4mm (mean±std), respectively). The radial axis was also found to be distal to the flexion and extension axes, though not significant at the $p<0.001$ level (though they state that this may be due to a limitation in their hardware). Leonard et al. computed the axis offset from three-dimensional electromagnetic motion measurements input into a two-axis hinge computer model. They found that the flex-ext axis was, on average, 6.8 ± 9.8 mm (mean±std) proximal to the rad-uln axis. Note that while the fe-axis was proximal to the radioulnar axis on average, both of these studies (as well as [7]) reported cases where the fe-axis was estimated to be distal to the radioulnar axis. However, note also that the proximal-to-distal relationship does not necessarily imply which axis carries the other because a distal axis could conceivably carry a proximal one.

Finally, Kaufman et al. found that the capitate, scaphoid and lunate show minimal translation during wrist rotations (mean translations between carpal bones and the radius ranged from 0.1mm to 1.4mm during flex-ext and 0.1mm to 2.2mm during rad-uln [58, 59]), implying purely rotational movement.

In summary, studies of wrist biomechanics show a kinematic hierarchy in which the fe-axis carries the rud-axis. Furthermore, the rud-axis is generally found distal to the fe-axis. This kinematic description fits a universal joint with non-intersecting axes. Neither a spherical nor elliptical joint model could capture these characteristics of wrist kinematics.

2.3 Notes

2.3.1 Generalized Coordinates

Beautiful descriptions of generalized coordinates are given in [57] and [62]. From Crandall we read (p. 115-117):

“Point coordinates (e.g., cartesian coordinates, spherical coordinates) are used to locate a point with respect to a reference frame. *Generalized coordinates* are used to locate a dynamic system with respect to a reference frame. A set of generalized coordinates may include cartesian coordinates or spherical coordinates, but may also include convenient lengths or angles which have no association with conventional coordinate systems.

A set of generalized coordinates is said to be *complete* if the values of the coordinates corresponding to an arbitrary geometrically admissible configuration of the system are sufficient to fix the location of *all* parts of the system.

A set of generalized coordinates is said to be *independent* if, when all but any one of the coordinates is fixed, there still remains a continuous range of values for that one coordinate which corresponds to a range of admissible system configurations.

In addition to generalized coordinates which describe geometrically admissible configurations of a dynamic system, we can introduce generalized infinitesimal *variational variables* to describe admissible variations. In most cases the variations of the generalized coordinates are the most convenient generalized variational variables.

The concept of completeness and independence introduced for generalized coordinates can also be applied in conjunction with infinitesimal variational variables… The number of independent variational variables in a complete set of infinitesimal variational variables is called the number of *degrees of freedom* that the system has in the given configuration… For a wide class of systems the number of degrees of freedom is identical with the number of independent coordinates in a complete set of generalized coordinates, but this is *not always* the case. The relation between these numbers depends on the nature of the constraints in the system.”

3 Geometric Comparison of Wrist Rotation and Reaching

3.1 Introduction

The study of movement path shape has done much to elucidate how the nervous and biomechanical systems of the body work together to produce coordinated movements. Reaching movements have long been known to produce hand paths which are roughly straight in space [63, 64]. The straightness of the path in space is significant insofar as it suggests that reaching movements are planned primarily in terms of kinematic variables, upon which the dynamics depend. This is not to say that hand paths are perfectly straight; reaching paths do show a small degree of curvature which depends on the workspace [65]. Nevertheless, this gentle curvature has been attributed to imperfections in the control [66] or perception [67] of a path which is straight in a central representation. Evidence of kinematic control has been provided by studies in which the path is artificially curved, either mechanically [68] or visually [69]. Under such conditions, subjects adapt by straightening their paths, confirming that kinematics play a prominent role in planning reaching movements. Though dynamic considerations may play a role, the kinematic plan appears to be primary, from which the muscle activation required to produce that kinematic plan is determined. The tendency to make straight paths also indicates that the kinematic plan is represented in terms of the perceived motion of the hand in external space, as opposed to an internal representation such as the angle of rotation at the shoulder and elbow joints. In summary, planar reaching movements have been shown to be primarily under kinematic control in external space.

Planar reaching movements and wrist rotations share some important similarities. Both movements involve two degrees of freedom (DOF), allowing them a priori to produce *any* path—straight or curved—in two dimensions. To illustrate, during planar reaching movements, the hand can trace any path in the horizontal plane (within joint limits). Likewise, during wrist rotations, the hand can trace any path (within joint limits) on the roughly spherical surface surrounding the wrist joint (see Figure 3.1). While planar reaching movements and wrist rotations also have some kinematic differences, these differences are small for much of the wrist's workspace.[7]

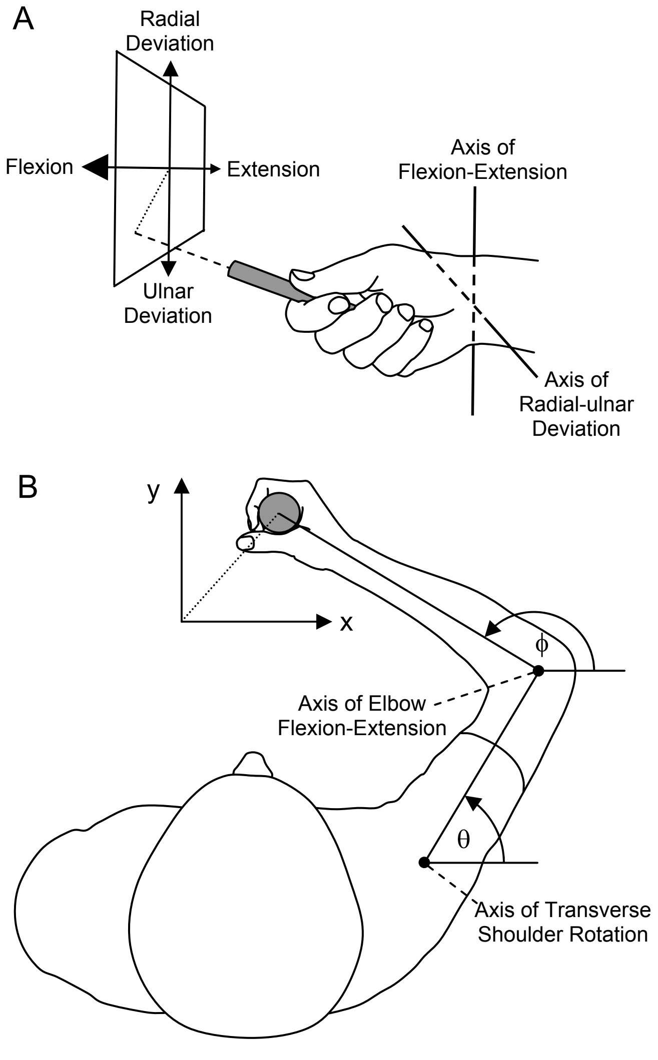

Figure 3.1: Diagrams of wrist rotation (A) and reaching movements (B) in two degrees of freedom. A: Wrist rotations, such as pointing with a laser pointer, generally involve two degrees of freedom (flexion-extension and radial-ulnar deviation). When the wrist is free to rotate in both DOF simultaneously, the tip of the laser pointer remains on a roughly spherical surface but is free to trace any path—straight or curved—on this surface (within joint limits). For simplicity, instead of analyzing the trajectory of the tip of the laser pointer on this curved surface, one can consider its

---

[7] For example, planar reaching movements commute, while finite wrist rotations do not. However, for wrist rotations within ±15°, the error in assuming that they do commute is less than 0.5°. For wrist movements within ±30° (which represents the entire range of motion in rad-uln), the error is still less than 6°.

projection onto a plane, as shown. B: Likewise, during planar reaching, the hand can trace any path—straight or curved—in the horizontal plane (within joint limits).

In apparent contrast to reaching movements, wrist rotations produce paths which can show significant curvature. Hoffman and Strick found that when monkeys rotate the wrist, their hand draws a path which is dramatically curved in certain directions [36]. In another part of that study, humans' hand paths appeared essentially straight by comparison. However, recent studies in our laboratory have shown that humans' wrist paths can also exhibit statistically significant curvature [70]. Furthermore, the pattern of curvature we observed in humans is similar to that observed by Hoffman and Strick in monkeys, though smaller in magnitude. These findings are important insofar as they suggest that wrist rotations might be represented or controlled in a way that is different from planar reaching movements. However, to our knowledge a systematic study of path shape in wrist rotations has not been reported. It is not known if the observed path curvature is indeed a result of different representation or control strategies, or if it is simply due to imperfect peripheral execution, like the gentle curvature observed in reaching movements.

Past studies of unimpaired wrist kinematics involving both DOF, flexion-extension (flex-ext) and radial-ulnar deviation (rad-uln), can be divided into two fields: A) wrist biomechanics, which focuses on individual carpal bones and muscles and how their motions combine to produce global wrist motion [7, 9, 10, 12, 13, 60, 61, 71, 72]; and B) wrist control, which examines how the nervous system encodes and controls wrist rotations [36, 42-44, 73, 74]. While many of these studies examine issues which may be related to path curvature, none report a quantitative investigation of path curvature in wrist rotations.

In this chapter, we quantitatively characterize the path shape of wrist rotations and reaching movements performed by six subjects, and we discuss the meaning of differences and similarities. While the characterization of reaching paths is a necessary part of this comparison, it is not the focus of this chapter. As discussed above, others have characterized the gentle curvature of reaching movements and attributed it to imperfect peripheral execution [66, 67]. However, knowing that humans try to make straight reaching movements but fail to make them perfectly straight, reaching path curvature provides a measure by which wrist path curvature may be interpreted. Therefore, the focus of this chapter is the characterization of wrist path shape as well as the comparison to reaching path shape.

We have found that wrist and reaching movements share many features of path shape: both types of movement exhibit non-zero curvature to the majority of targets, increasing curvature with movement speed, and differences between outbound and inbound paths. There are also important differences: wrist rotations are significantly more curved and more variable than reaching movements. However, taken together, the data presented in this chapter suggest that the curvature observed in wrist rotations is caused by imperfections in peripheral execution, as in reaching movements.

3.2 Methods

3.2.1 Subjects

Six young, healthy human subjects (mean age = 23 ± 4 years, age range = 19 to 28 years; mean BMI = 21.3 ± 1.7 kg/m^2, BMI range = 18.9 – 23.4 kg/m^2) were recruited for this test. Three of the subjects were male and three were female. None of the subjects suffered from neurological impairment or biomechanical injuries to the wrist (diagnosed fractures, tendonitis, or carpal tunnel syndrome). All subjects described themselves as right-handed, and all subjects performed the task with their right hand. Following procedures approved by MIT's Committee on the Use of Humans as Experimental Subjects, informed consent was obtained from all subjects.

3.2.2 Physical Setup

Wrist Rotations

The subjects were seated with the right forearm resting in a para-saggital plane (~25cm from the saggital plane) on a table in front of them (the arm was abducted ~40° and flexed ~35° at the shoulder, and the forearm was flexed ~60° at the elbow). The forearm was prevented from pronating and supinating by a constraint (see Pronation-supination constraint).

In their hand they held a soft-covered, light-weight handle to which a motion sensor (Flock of Birds, Ascension Technology Corporation, Burlington, VT, USA) was rigidly attached. The Flock of Birds is an electromagnetic motion sensing system that consists of a transmitter and a number of sensors. It is capable of recording position in three DOF and angular orientation in three DOF at up to 100Hz. Its range of up to four feet is more than enough for the modest range of motion of the wrist. Its positional resolution and static accuracy are 0.11mm (0.76mm @ 12”) and 2.54mm (RMS averaged over the translational range), respectively, whereas its angular resolution and static accuracy are 0.022° (0.1° RMS at 12”) and 0.5° (RMS averaged over the translational range). Combined, the handle and sensor weighed 70g, which, at 13% of the weight of an average hand, presented negligible interference to natural wrist movements.

The motion sensor tracked the position and angular orientation of the handle (6 total DOF) at a sampling frequency of 100 Hz. Displayed on a video screen in front of the subject was a circular pattern of eight targets arranged around a center target. The subject’s wrist movements were displayed on the screen as a cursor which moved as a function of the wrist’s orientation (see Representation of Wrist Rotations). A detailed derivation of wrist orientation and upper limb orientation from FOB transformation matrices is given in Appendices B and C, respectively. 15º of wrist rotation was required to move from center to periphery in any direction. The targets and cursor were approximately 2.7° and 1.35° in diameter, respectively.

Reaching Movements

The subjects were seated with the right hand placed on a table in front of them. The right forearm was oriented mid-way between pronation and supination and their hand was made into a fist. Subjects wore a wrist splint instrumented with a motion sensor (same sensor as above). Subjects slid their fist across the surface of the table to reach the targets. A shoulder belt minimized trunk movement. The video display was identical to the display used in wrist rotations, except that the cursor moved in proportion to the subject’s hand position in the plane of the table. 14 cm of hand displacement was required to move from center to periphery in any direction. The targets and cursor were 2.5cm and 1.25cm in diameter, respectively.

3.2.3 Representation of Wrist Rotations

In accordance with the recommendations of the International Society of Biomechanics (ISB) [8], global wrist orientation was defined as the orientation of the third metacarpal with respect to the radius. The orientation of the third metacarpal was detected by a sensor mounted atop a handle gripped by the subjects. Wrist orientation was displayed on a computer monitor as a cursor which moved with wrist rotation, like the projection of a laser pointer onto a screen in front of the subjects.[8] Subjects were immediately comfortable with the mapping. More details regarding the representation of wrist rotations can be found in the notes at the end of this chapter.

3.2.4 Tasks

Subjects were instructed to move from the center target to a peripheral target, or from a peripheral target to the center target, as prompted by visual cues. Each prompt was designed to elicit a discrete, separate movement by requiring that the subject come to a complete stop on the target and wait half a second before the next target was displayed. Targets were displayed in random order for a total of 240 one-way moves (i.e. 15 round-trip moves to each target).

This task was repeated for two speed instructions. First, subjects were instructed to perform the task at whatever speed they felt comfortable. Second, subjects were instructed to move “as fast as possible”. The two tasks were first completed for wrist rotations, then repeated for reaching movements after a short break (approximately 5 minutes). No instruction was given regarding end-point accuracy, type of path between targets, or correcting movements.

3.2.5 Pronation-supination constraint

Although the task only required flex-ext and rad-uln, subjects were found to make significant use of pronation-supination (pro-sup). To ensure this task was performed with only two DOF, we used a custom-built apparatus which discouraged pro-sup by fixing

---

[8] Strictly speaking, we used a parallel projection, not a point projection as produced by a laser pointer, but for the movements in this experiment (15° amplitude), the difference is negligible at 3%.

the distal forearm at three bony prominences. This apparatus placed the dorsal surface of the distal forearm in the parasaggital plane (i.e. roughly midway between pronation and supination). Subjects reported a snug squeezing sensation on the ventral and dorsal aspects of the distal forearm that largely eliminated pro-sup but did not interfere with flex-ext and rad-uln wrist rotations. More details can be found in the Notes at the end of this chapter.

3.2.6 Neutral Position

Because the angular displacement required to move from the center to the periphery was close to the maximal range of motion for radial deviation, care was taken in defining neutral position. For rad-uln, the wrist was in neutral position when the line between the distal head of the third metacarpal and the axis of rad-uln were collinear with the shaft of the forearm. The axis of rad-uln was determined as described in [4]. This method produces roughly the same neutral position as the method described in [8]. For flex-ext, the wrist was in neutral position when the handle and the mid-point of the wrist were collinear with the shaft of the forearm. This definition differs from ISB recommendations [8] to account for the fact that subjects were holding a handle.

3.2.7 Data Processing

With an angular resolution of 0.1° (RMS at 12”) and a static accuracy of 0.5° (RMS averaged over the translational range), the output of the Flock of Birds did not need filtering for analysis of the path. However, speed profiles, which did require filtering, were also used in this analysis. The data were filtered by the method of smoothing splines, where the amount of smoothing was determined by generalized cross-validation, as suggested by [75]. The specific implementation followed the technique suggested by [76]. The use of smoothing splines allowed derivatives to be obtained analytically. More details can be found in the Appendix D.

3.2.8 Analysis

As a measure of path straightness or curvature, we used the area bounded by the path and a straight line connecting the start and end points of the path, as suggested in

[77]. Deviations of the path to the right of the straight line (heading from center to target) are defined as A_R, whereas deviations of the path to the left of the straight line are defined as A_L. The net area (A_R - A_L) provides a robust metric of a path's deviation *to one side* of a straight line, and was used to compare paths to and from a given target (by Student t-test). The sign of the net area indicates the side to which the path deviates.

The total area ($A_R + A_L$) provides a measure of a path's deviation *to either or both sides* of a straight line, and was used to compare path curvature between targets, tasks and subjects by Student t-test. The variability in the total area was compared between speeds and tasks using an F-test.

Another measure of the amount by which a path deviates from a straight line is given by its maximum lateral deviation. This measure does not take the entire path into account and was not used in the statistical analysis. However, it is a more intuitive measure, so it is included (averaged over all targets and subjects, and expressed as a percentage of path length) to provide an appreciation for the magnitude of path curvature.

The low-speed "tails" at the beginning and end of a movement recording were not counted in the calculation of movement duration: the start of a move was defined as the data record immediately before movement speed first exceeded 5% of the maximum speed, and the end of a move was defined on the remaining portion as the data record immediately after movement speed first dropped below 5% of the maximum speed. To focus on the initial, high-speed portion of each move (see Results) a threshold of 20% of maximum speed was used.

3.3 Results

The paths produced during each task by subject 1 are shown in Figure 3.2. Several observations are immediately evident: 1) wrist rotations and reaching movements produce very different paths in space, 2) wrist paths are more variable than reaching paths, 3) variability increases with speed, 4) many wrist and reaching paths are visibly curved, and 5) outbound and inbound paths are different for many targets.

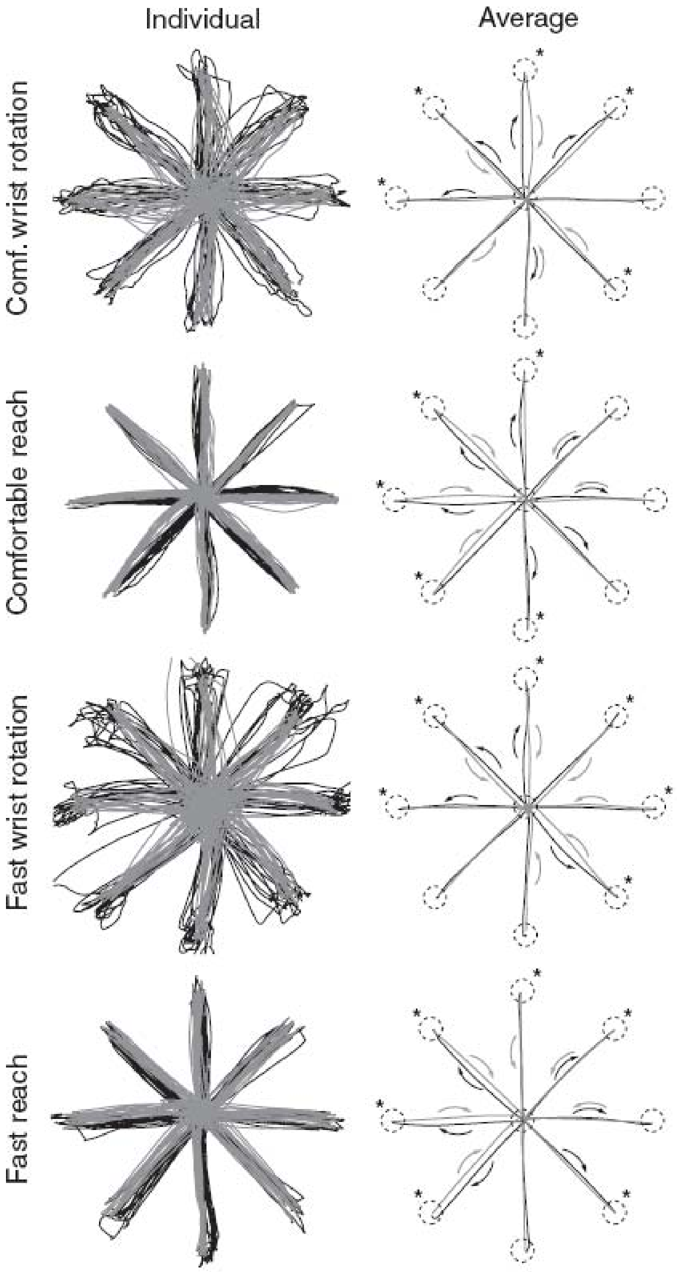

Figure 3.2: Outbound (black) and inbound (gray) paths for all four tasks.

Left column: individual paths performed by subject 1. Right column: paths averaged over all subjects and moves to a given target. Paths which differ significantly from a straight line ($p \leq 0.05$) are indicated by an arrow. The arrow also indicates the direction of curvature. Asterisks denote that outbound and inbound paths are statistically different from each other ($p \leq 0.05$).

3.3.1 Path vs. straight line

Mean paths, averaged over all subjects, are shown in Figure 3.2 for each task. Note that the mean paths appear relatively straight and belie the curvature seen in many of the individual paths—this is especially true of the wrist. In Figure 3.2, the paths which are statistically different from a straight line based on the net area, and the side to which these paths deviate, are indicated by an arrow. For the majority of targets, wrist and reaching paths both deviate significantly to one side of a straight line. This is true for outbound and inbound moves and for moves at comfortable and fast speeds. The maximum lateral deviation is 7% for comfortable and 10% for fast wrist rotations, and 4% for comfortable and 5% for fast reaching movements.

3.3.2 Outbound vs. Inbound

The net area was also used to compare outbound to inbound paths for a given target. Importantly, for wrist and reaching movements alike, outbound and inbound paths differ significantly for the majority of targets, as shown in Figure 3.2. This is true for movements at comfortable and fast speeds. More often than not, outbound and inbound movements curve in opposite directions, especially for wrist movements. Also, moves in the same direction but to opposite targets tend to curve to the same side. For example, in fast wrist rotations, inbound moves from the East target and outbound moves to the West target, both of which involve pure flexion, curve toward radial deviation. This is especially true if the measure of curvature is focused on the initial, high-speed portion of moves (see below).

3.3.3 Comfortable vs. fast

Fast wrist movements were significantly faster than comfortable ones ($p \leq 0.001$; fast: duration = 292 ± 112 msec (mean ± std), range = 90 to 890 msec; comfortable: duration = 658 ± 238 msec, range = 90 to 1780 msec). Likewise, fast arm movements were significantly faster than comfortable ones ($p \leq 0.001$; fast: duration = 409 ± 122 msec, range = 160 to 1060 msec; comfortable: duration = 936 ± 272 msec, range = 360 to 1850 msec).

The total area was used to compare path curvature between movements at fast and comfortable speeds. Moving faster accentuates path curvature: averaged over all targets, the curvature of fast moves is significantly larger than that of comfortable moves ($p \leq 0.001$). This is true for wrist and reaching movements, as shown in Figure 3.3A. Although there existed significant variation in the amount of curvature between subjects (5-9% for comfortable wrist movements and 8-12% for fast wrist movements), fast wrist rotations always showed more curvature than comfortably paced ones (see Figure 3.3B). In addition, the variability of fast movements is greater than the variability of comfortably paced movements ($p \leq 0.001$), as seen in the left column of Figure 3.2.

From the wrist data it was apparent that while moves at comfortable speed typically exhibit speed profiles composed of a number of peaks of roughly the same amplitude, fast moves are often composed of an initial, large, high speed move, followed by a series of smaller, lower-speed moves (see Figure 3.4A and B). Comparison of path and speed profiles suggests that the smaller, lower-speed moves observed in fast movements may represent mechanical oscillations or efforts to correct the initial path toward the target. Therefore, for the fast trials, path curvature was re-computed for the initial high-speed portion of the move, defined as the portion of the move continuously above 20% of the maximum speed (see Methods for details). Comparison of the re-computed mean paths, shown in Figure 3.4C, with Figure 3.2 reveals that considering only the high-speed portion of a move allows several metrics to reach statistical significance, filling out the pattern mentioned above: outbound and inbound paths deviate significantly from a straight line as well as from each other. Importantly, for fast wrist rotations, outbound and inbound paths curve in opposite directions.

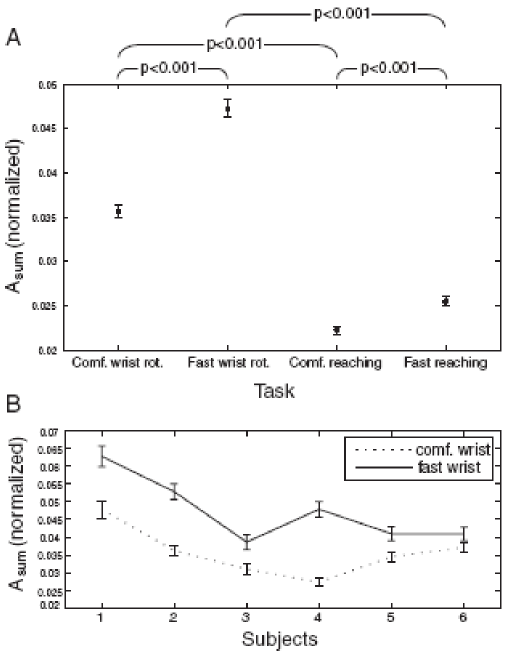

Figure 3.3: Path curvature observed in different tasks and subjects.

A: Path curvature, averaged over all targets and subjects, for each of the four tasks (mean ± standard error). B: Path curvature, averaged over all targets, for each subject (mean ± standard error).

3.3.4 Wrist vs. reaching movements

The total area was also used to compare the amount of curvature between wrist rotations and reaching movements. After normalizing by the square of path length to account for differences in path length between arm and wrist movements, the total area was found to be significantly larger for wrist rotations than for reaching movements ($p \leq 0.001$), as shown in Figure 3.3A. The variability of wrist paths was also larger than the variability of reaching paths ($p \leq 0.001$), as evident from Figure 3.2. This was true for movements at comfortable and fast speeds.

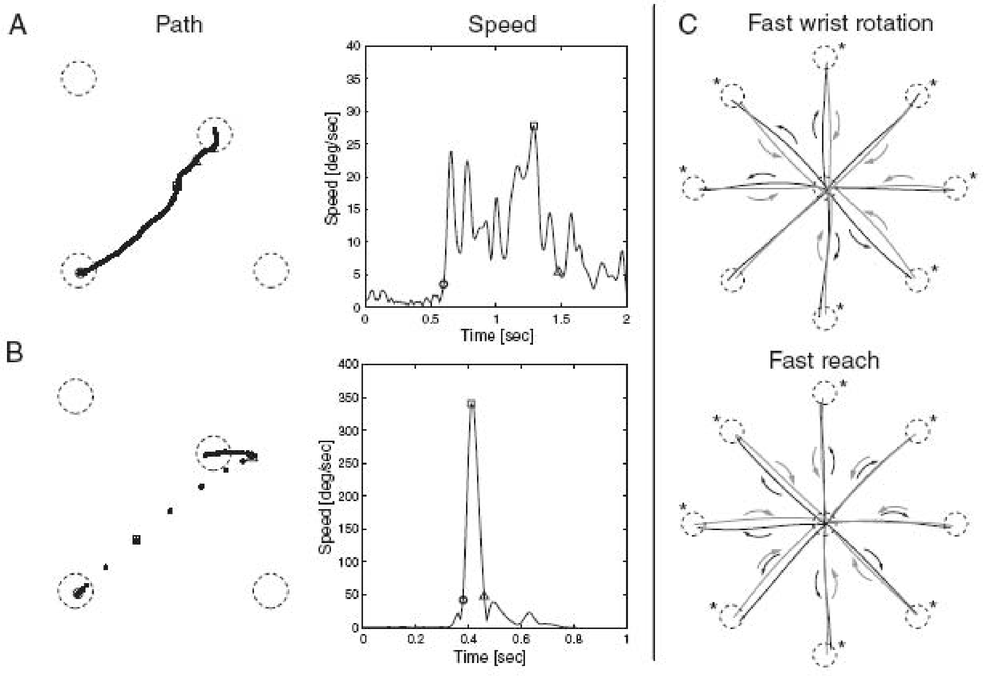

Figure 3.4: Speed and path curvature.
A-B: Path and speed for a comfortable (A) and fast wrist movement (B). The point of maximum speed (square marker) and the start and stop points of the initial, high-speed portion of the move (circle and triangle markers, respectively) are indicated. In the path plots, the points are 10 ms apart. C: Paths for wrist rotations and reaching movements at fast speeds, where only the initial, high-speed portion of the move is considered. See the caption of Figure 3.2 for the meaning of the arrows and asterisks.

3.4 Discussion

During reaching movements, the hand draws a relatively straight path through space. In experiments where a mechanical or visual perturbation increases path curvature, subjects adapt by straightening the path even though their endpoint position remains largely unchanged. This proclivity to path straightness in space indicates that reaching movements are planned primarily in terms of kinematics, rather than dynamics, and that movement kinematics are centrally represented in terms of the motion of the hand through space.

In this study, we have shown that wrist rotations exhibit significantly more curvature than reaching movements ($p \leq 0.001$). Maximum lateral deviation, averaged over all moves and subjects, is 4% for comfortable and 5% for fast reaching movements. In comparison, the maximum lateral deviation is 7% for comfortable and 10% for fast wrist rotations—roughly twice as large. Does this mean that wrist movements are not planned kinematically, or that wrist rotations have a different central representation?

3.4.1 Central representation in reaching and wrist movements

One way to infer the central representation of movement is to cast recorded data into various reference frames and compare features such as path straightness or speed profiles. The idea is that the reference frame which is closest to the central representation will have the highest degree of invariance or stereotyping. Over the past three decades, this approach has been applied with success to reaching: reaching movements are known to have straighter paths and more invariant speed profiles in hand space than joint space, supporting the hypothesis that reaching movements are centrally represented in hand space. Unfortunately, this approach is impractical for wrist rotations. We show first why this approach works for reaching movements, then why it does not work for wrist rotations.

Reaching movements

There are many possible representations of reaching movements. One obvious candidate is to visualize the position of the hand as it moves through space, as illustrated in Figure 3.1B. Thus reaching movements can be captured as (x,y)-coordinates of the hand in a reference frame called hand space. Note that the choice of hand space is not unique; for example, there are infinitely many rotated and translated versions of hand space. Another obvious way to represent reaching movements is in terms of the angular displacements at the shoulder and elbow joints. This representation allows one to capture reaching movements as (θ,ϕ)-coordinates in a reference frame called joint space. Likewise, the choice of joint space is not unique; for example, angles may be relative or absolute. The approach of comparing movement data in various reference frames works well for reaching movements because of two properties of hand and joint space: path characteristics such as straightness are preserved from one hand space to another and from one joint space to another,[9] but not between hand and joint space, as shown in Figure 3.5.

To illustrate, the choice of hand space is not unique, but it doesn't matter because path characteristics are preserved under rotation and translation. If a path is straight in one hand space, it is straight in all hand spaces. The same is true for joint space: the choice of joint space is not unique, but it doesn't matter because path characteristics are preserved between joint spaces.[9]

In contrast, path characteristics such as straightness are not preserved between hand and joint space. A path which is straight in hand space is, in general, not straight in joint space, and vice versa. This property is essential to evaluate the hypothesis that movements are straighter in one frame than another. Unfortunately, this same strategy cannot be applied to wrist rotations.

---

[9] This is only true for hand or joint spaces which are related by an affine transformation. Clearly, it is possible to imagine spaces which do not preserve straightness. However, for reaching movements, one can argue that the most obvious spaces (and therefore the most obvious central representations) are those that are related by affine transformations.

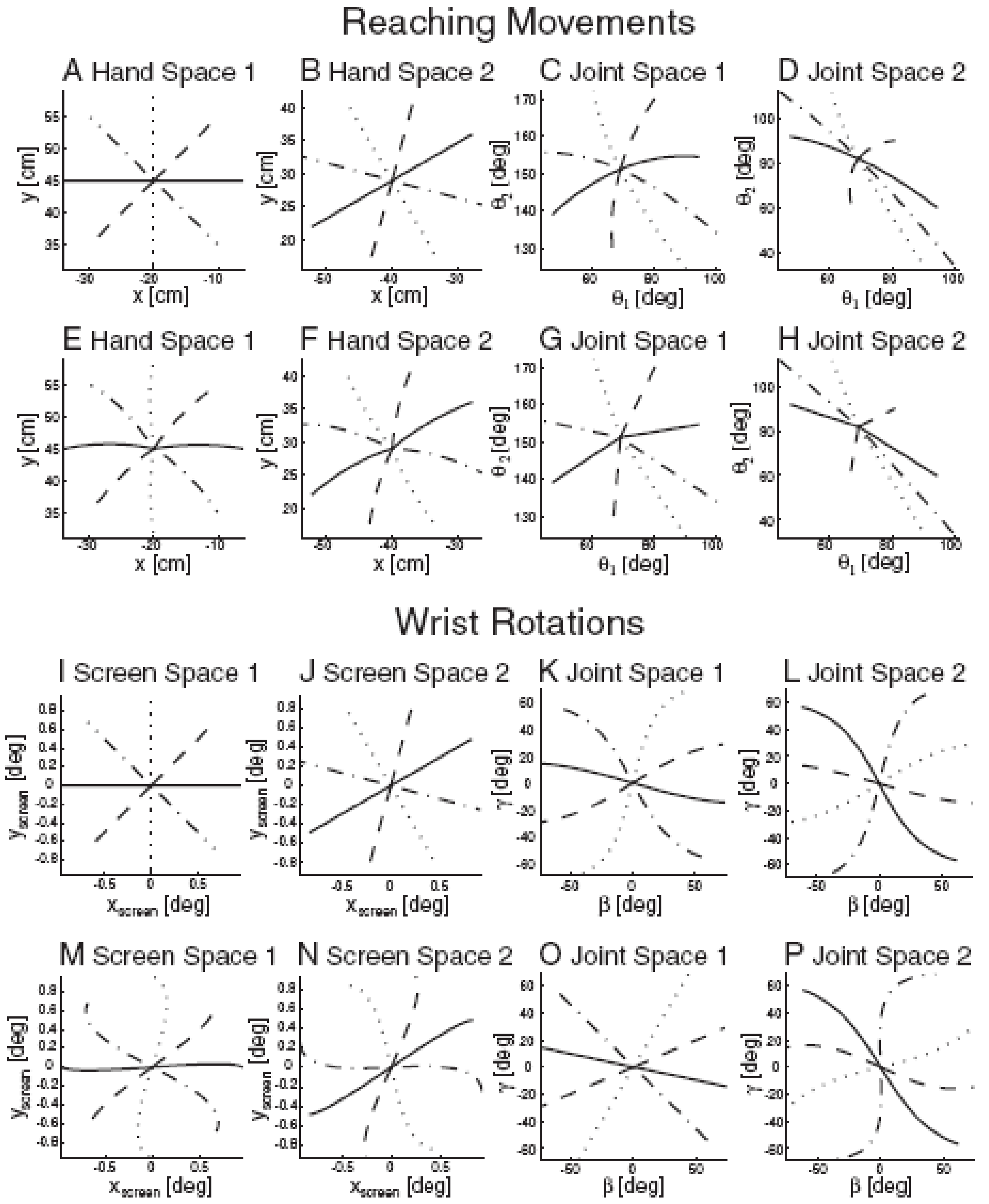

Figure 3.5: Reaching movements and wrist rotations projected in intrinsic and extrinsic spaces. ***Reaching movements (A-H):*** **Moves which are straight in one hand space (A) are straight in other hand spaces (B), and moves which are straight in one joint space (G) are straight in other joint spaces (H). However, moves which are straight in hand space (A and B) are not straight in joint space (C and D) and vice versa (G and H vs. E and F). Hand space 2 is rotated with respect to hand space 1 by**

30°. Joint space 1 uses absolute angles while joint space 2 uses relative angles. Upper arm length = 30cm; forearm length = 35cm; the center target is at (x, y) = (-20cm, 45cm).
Wrist rotations (I-P): **Moves which are straight in one screen space (I) are straight in other screen spaces (J), but moves which are straight in one joint space (O) are *not* straight in other joint spaces (P). Moves which are straight in screen space (I and J) are, in general, not straight in joint space (K and L) and vice versa (O and P vs. M and N). However, *all* moves are approximately straight close to the center target. Screen space 2 is rotated with respect to screen space 1 by 30°. Joint space 1 is rotated by 15° with respect to screen space. Joint space 2 is rotated by 45° and has a reversed rotation order with respect to joint space 1.**

Wrist rotations

As with reaching movements, there are many ways in which humans could represent their wrist rotations. One obvious representation is in terms of the angular displacement of the hand about axes fixed in the wrist joint. This representation would allow one to capture wrist rotations as (β,γ)-coordinates, as shown in Figure 3.6A. If the rotation axes are fixed in the wrist and rotate with the hand (as in the definition of Euler angles), the reference frame is called joint space. If the axes are fixed in space and do not rotate with the hand, the reference frame is called world space. Alternatively, wrist rotations could be visualized in terms of where the hand is pointing, like the laser dot produced on a screen when the wrist is rotated to move a laser pointer. By this representation, wrist rotations can be captured as (x,y)-coordinates in a reference frame called "screen space." These three representations are further explained in Figure 3.6A.

Importantly, these three spaces *do not possess the two key properties described above*: path characteristics are, in general, not preserved from one joint space to another or from one world space to another, and path characteristics are in fact often preserved between screen, joint, and world space, as shown in Figure 3.5.

To amplify, the choice of joint space is not unique (there are infinitely many rotation axes). However, unlike reaching, path characteristics such as straightness are not preserved between joint spaces. Compare, for example, joint space 1 and joint space 2 in Figure 3.6B, defined by coordinates (β_1, γ_1) and (β_2, γ_2), respectively. Joint space 2 is rotated about Y by α with respect to joint space 1, and the order of rotation is reversed. The relationship between these two joint spaces is:

$$\begin{bmatrix} \sin\beta_1 \cos\gamma_1 \\ \sin\gamma_1 \end{bmatrix} = \begin{bmatrix} \cos\alpha & -\sin\alpha \\ \sin\alpha & \cos\alpha \end{bmatrix} \begin{bmatrix} \sin\beta_2 \\ \cos\beta_2 \sin\gamma_2 \end{bmatrix}$$

This relationship is non-linear, and straight lines in joint space 1 are not, in general, straight in joint space 2, and vice versa[10]. Note, however, that the relationship is approximately linear for small displacements about the origin:

$$\begin{bmatrix} \beta_1 \\ \gamma_1 \end{bmatrix} \approx \begin{bmatrix} \cos\alpha & -\sin\alpha \\ \sin\alpha & \cos\alpha \end{bmatrix} \begin{bmatrix} \beta_2 \\ \gamma_2 \end{bmatrix}$$

To summarize, path characteristics are not preserved between joint spaces for large rotations, but they are approximately preserved for small rotations. The same is true for world space.

The second property, which describes the relation between world, joint and screen space, is even more problematic. Consider a joint space and a world space, each pronated relative to the screen space axes by α_{js} and α_{ws}, respectively (like joint space 2 in Figure 3.6B). The relationship between screen space and these joint and world spaces is:

$$\begin{bmatrix} x_{screen} \\ y_{screen} \end{bmatrix} = -\begin{bmatrix} \cos\alpha_{js} & -\sin\alpha_{js} \\ \sin\alpha_{js} & \cos\alpha_{js} \end{bmatrix} \begin{bmatrix} \sin\beta_{js} \cos\gamma_{js} \\ \sin\gamma_{js} \end{bmatrix} = -\begin{bmatrix} \cos\alpha_{ws} & -\sin\alpha_{ws} \\ \sin\alpha_{ws} & \cos\alpha_{ws} \end{bmatrix} \begin{bmatrix} \sin\beta_{ws} \\ \cos\beta_{ws} \sin\gamma_{ws} \end{bmatrix}$$

where (x_{screen}, y_{screen}), $(\beta_{js}, \gamma_{js})$ and $(\beta_{ws}, \gamma_{ws})$ are the coordinates of screen, joint, and world space, respectively. This is a non-linear relationship, so path characteristics such as straightness are, in general, not preserved between screen, joint, and world space. However, this relationship *is* approximately linear for small wrist rotations:

$$\begin{bmatrix} x_{screen} \\ y_{screen} \end{bmatrix} \approx -\begin{bmatrix} \cos\alpha_{js} & -\sin\alpha_{js} \\ \sin\alpha_{js} & \cos\alpha_{js} \end{bmatrix} \begin{bmatrix} \beta_{js} \\ \gamma_{js} \end{bmatrix} \approx -\begin{bmatrix} \cos\alpha_{ws} & -\sin\alpha_{ws} \\ \sin\alpha_{ws} & \cos\alpha_{ws} \end{bmatrix} \begin{bmatrix} \beta_{ws} \\ \gamma_{ws} \end{bmatrix}$$

Thus, path characteristics such as straightness are preserved between screen, joint, and world space for small wrist movements (see Figure 3.7). For wrist rotations less than

---

[10] In mathematical parlance, this transformation is not affine (affine transformations are transformations which preserve lines and parallelism).

15°, the three spaces are virtually indistinguishable. At 30°, the difference between screen space and joint or world space is still less than 5%. Displacements of 30° in each direction represent a significant portion of the wrist's range of motion, covering the entire range in rad-uln and almost half the range in flex-ext, and in its center. If an experiment were to distinguish between spaces, the experimental protocol would have to require subjects to make unreasonably large wrist rotations, which would have marginal relevance to most natural movements.

In summary, while comparing reaching movements projected into different spaces has provided evidence that reaching movements are centrally represented in hand space, the same approach is impractical for investigating central representation of wrist rotations because analogous spaces for the wrist are virtually indistinguishable for much of the wrist's workspace. Projecting wrist paths into different spaces cannot reveal the most likely central representation of wrist rotations, nor can it inform whether the curvature observed in wrist rotations is related to central representation.

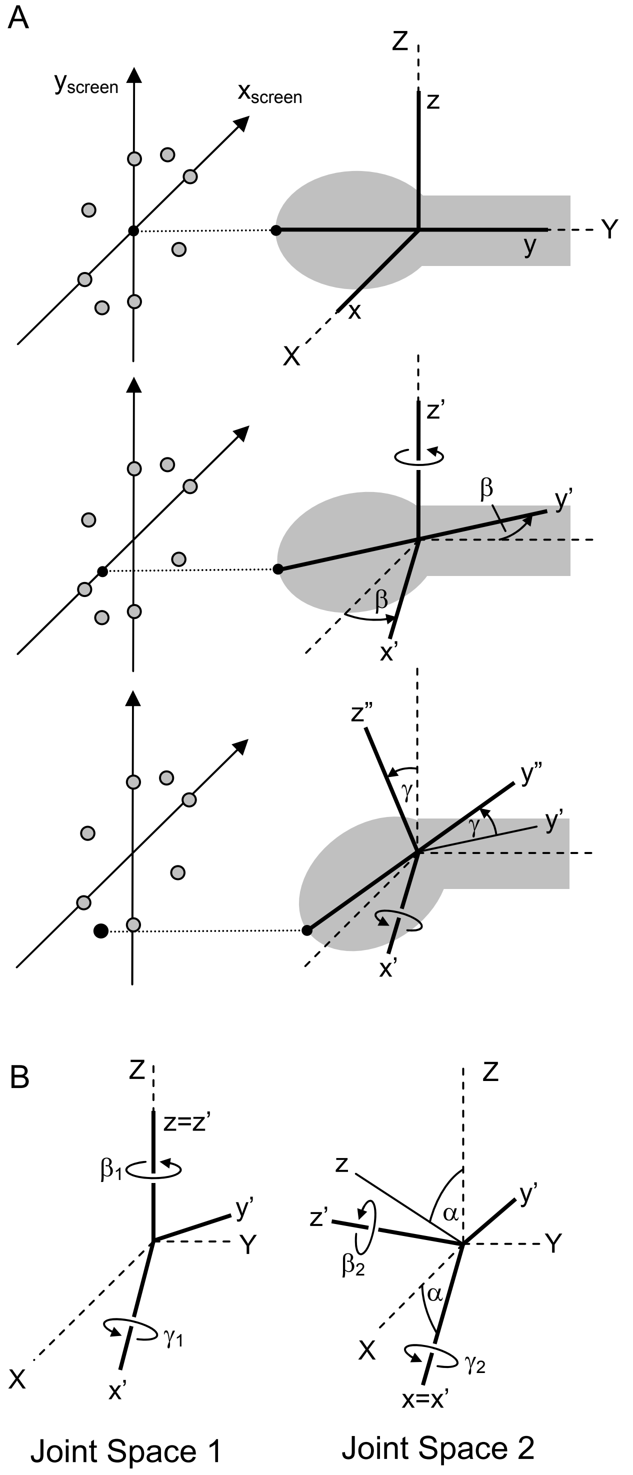

Figure 3.6: Wrist rotations can be described in terms of joint, world or screen coordinates. A: This series of schematics shows how a wrist rotation can be divided into component rotations along each degree of freedom. In this example, the actual wrist rotation is decomposed into a flexion followed by an ulnar deviation. Initially, the hand is in neutral position, and the hand-fixed

coordinate frame (xyz) is aligned with the space-fixed frame (XYZ). During the first rotation (flexion), the hand is rotated by β about the z-axis, and the resulting hand orientation is described by x'y'z'. During the second rotation (ulnar deviation), the hand is rotated by γ about the x'-axis, reaching its final orientation described by x"y"z". The angles of rotation (β,γ), commonly known as Euler angles, are the coordinates of joint space. If the two rotations had occurred about space-fixed axes instead of hand-fixed axes (e.g. Z and X instead of z and x'), the angles of rotation would be the coordinates of world space. The projection onto the XZ-plane defines the coordinates of "screen space" (x_{screen}, y_{screen}). B: Two different joint spaces. Joint space 2 is rotated by α about Y relative to joint space 1. Also, rotations in joint space 1 occur about the z and then the x' axis, whereas rotations in joint space 2 occur about the x and then the z' axis.

3.4.2 Differences between outbound and inbound paths implicate peripheral factors

Fortunately, another feature of wrist rotations provides valuable insight. The foremost observation of this chapter is that wrist path curvature depends on the direction of movement: outbound and inbound paths differ significantly for the majority of targets ($p \leq 0.05$, see Figure 3.2). This is true for moves at comfortable and fast speeds. This observation is significant because *no transformation between reference frames can make incongruent paths congruent.* In other words, the finding that path curvature differs between outbound and inbound wrist paths means that there does not exist a reference frame in which both outbound and inbound wrist movements are straight. If a high degree of path invariance implies a central representation, the curvature observed in wrist paths is likely due to peripheral causes and not attributable to central representation. Similarly, the fact that mean paths are straighter than individual paths (see Figure 3.2) supports the hypothesis that curvature is due to imperfect implementation.

3.4.3 Path curvature increases with increasing movement speed

If the curvature of wrist paths is due to imperfect peripheral execution of a central plan, the limited response time of the periphery implies that the imperfections should become more pronounced as movement speed increases. Fast wrist rotations exhibit significantly more curvature than rotations performed at a comfortable speed ($p \leq 0.001$), as shown in Figure 3.3A. The fact that curvature increases with speed further supports the hypothesis that the observed curvature is caused by peripheral and not central factors.

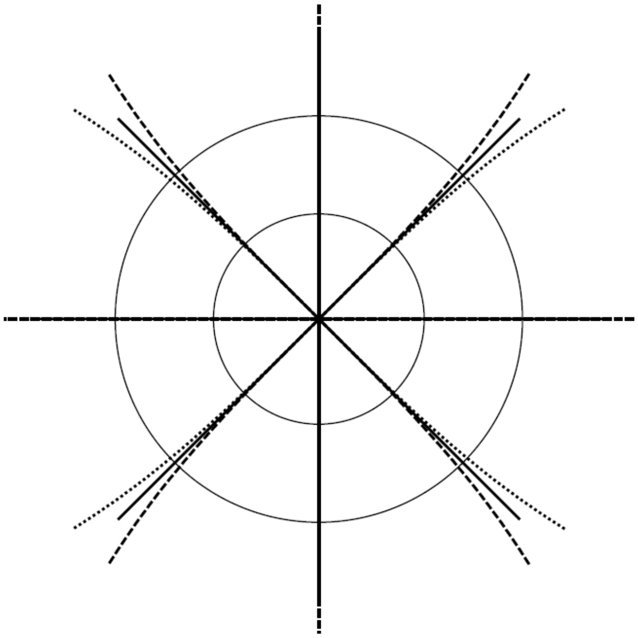

Figure 3.7: For moderately-sized wrist rotations, extrinsic and intrinsic spaces are virtually identical. Paths which are straight in screen space (solid line) are, in general, not straight in joint space (dotted line) or world space (dashed line). However, for wrist rotations less than 15° (inner circle), the difference is virtually imperceptible. For wrist rotations less than 30° (outer circle), the difference is still less than 5%.

3.4.4 Wrist rotations vs. reaching movements

Like wrist rotations, reaching paths are not ideally straight but show some degree of curvature. The gentle curvature in reaching movements has been attributed to imperfect peripheral execution [66, 67]. Although wrist rotation paths show roughly twice as much curvature as reaching paths, these two types of movements share many common features. For wrist and reaching movements to the majority of targets, paths deviate consistently to one side of a straight line; outbound and inbound paths differ; there is a systematic curvature pattern between targets (moves in the same direction but to opposite targets tend to curve to the same side); and curvature increases with movement speed (see Figure 3.2, Figure 3.3A, and Figure 3.4C). Also, despite being statistically significant, the curvature in both movements is still relatively modest: fast wrist rotations exhibit the most curvature with a maximum lateral deviation of 10% (in comparison, a semi-circular path between two targets has a maximum lateral deviation of 50%). These similarities between wrist rotations and reaching movements provide further support for the hypothesis that the curvature observed in wrist paths is also caused by peripheral factors.

The increased curvature and variability seen in wrist paths may be due to the more complex biomechanics of the wrist joint, or the fact that wrist rotations performed in this study utilized a large percentage of the wrist's range of motion—and in some directions approached the limit, where biomechanical factors are likely to be more evident. Anecdotally, subjects reported that they were much less aware of wrist orientation than hand position. In reaching movements, the hand's displacement is amplified by the arm's length, whereas in wrist rotations, the hand's displacement is only amplified by the hand's length. Thus, perhaps humans are simply less aware of the curvature of their wrist rotation paths.

3.4.5 Conclusion

In this study we quantified path curvature in wrist rotations and reaching movements. Similarities between the two types of movement include non-zero curvature in the majority of directions, a positive correlation between curvature and movement speed, and differences between outbound and inbound paths. There are also differences: wrist paths exhibit roughly twice as much curvature as reaching paths, and more variability. Taken together, our data suggest that the curvature observed in wrist paths is due to peripheral causes. The most telling evidence is the systematic difference between outbound and inbound moves. The most parsimonious explanation for these data is that wrist rotations, like reaching movements, are *planned* to be straight, but that imperfections in peripheral execution introduce curvature into the *observed* paths.

3.5 Notes

3.5.1 Representation of Wrist Rotations

The representation of finite rotations, such as the wrist rotations in this experiment, in perceptual space require care. In accordance with the recently published ISB recommendations [8], global wrist motion was considered as the motion of the third metacarpal with respect to the radius. Motion of the third metacarpal was detected as motion of the sensor atop the handle. Figure 3.8 shows the orientation of the third metacarpal (represented as the vector $\vec{p}$) as well as the orientation of the sensor, given in terms of Euler angles α, β, and γ (yaw, pitch, and roll, respectively). The orientation of the third metacarpal was computed from the Euler angles in the following manner: $\vec{p}$ points along the negative x-axis of the rotating xyz frame, i.e. $\vec{p} = -\hat{i}$, where $\hat{i}$ is the unit vector along the x-axis. The orientation of $\vec{p}$ in the stationary XYZ frame was computed by pre-multiplying $-\hat{i}$ by the transformation matrix A (see [55] for reference), where

$$A = \begin{bmatrix} \cos\alpha\cos\beta & \cos\alpha\sin\beta\sin\gamma - \sin\alpha\cos\gamma & \cos\alpha\sin\beta\cos\gamma + \sin\alpha\sin\gamma \\ \sin\alpha\cos\beta & \sin\alpha\sin\beta\sin\gamma + \cos\alpha\cos\gamma & \sin\alpha\sin\beta\cos\gamma - \cos\alpha\sin\gamma \\ -\sin\beta & \cos\beta\sin\gamma & \cos\beta\cos\gamma \end{bmatrix}$$

Therefore,

$$\vec{p} = \begin{bmatrix} -\cos\alpha\cos\beta \\ -\sin\alpha\cos\beta \\ \sin\beta \end{bmatrix}.$$

Wrist orientation was displayed on the screen as $\vec{p}'$, the parallel projection of $\vec{p}$ onto the YZ-plane (the frontal plane):

$$\vec{p}' = \begin{bmatrix} 0 \\ -\sin\alpha\cos\beta \\ \sin\beta \end{bmatrix},$$

or, written in terms of horizontal and vertical screen coordinates:

$$\begin{bmatrix} x_{screen} \\ y_{screen} \end{bmatrix} = \begin{bmatrix} \sin\alpha\cos\beta \\ -\sin\beta \end{bmatrix}$$

This representation of wrist orientation is very intuitive because the cursor moves like the projection—albeit scaled and translated to fit on the screen—of a laser pointer onto a screen in front of the subject (strictly speaking, a laser pointer produces a point projection, not a parallel projection, but at 15°, the difference is negligible at 3%). Subjects were immediately comfortable with the mapping. As with a real laser pointer, pure pronation-supination does not have any effect on the position of the cursor.

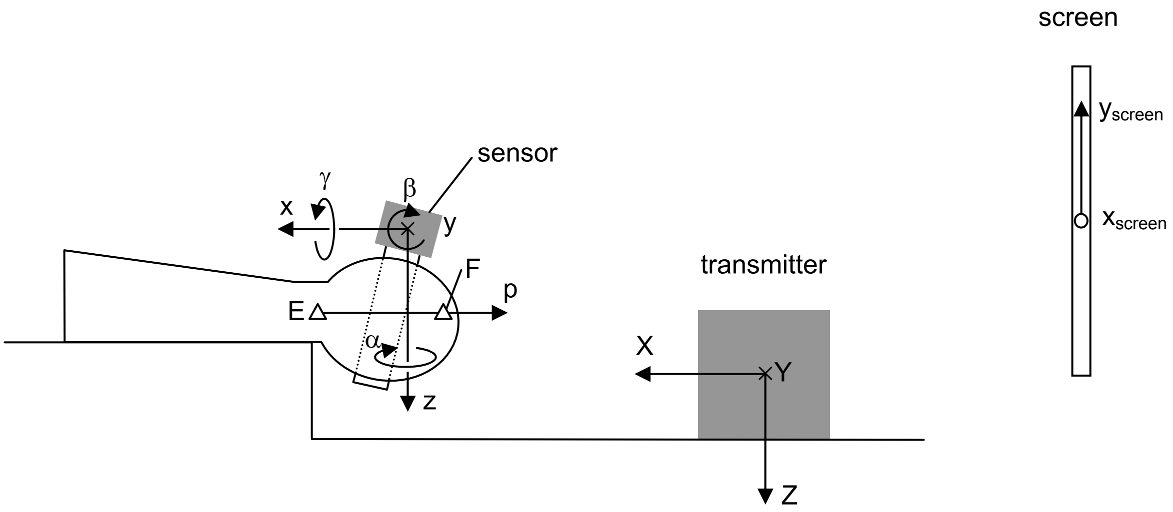

Figure 3.8: Schematic of reference frames used in computing and displaying wrist orientation.

3.5.2 Pronation-Supination

Although the task only required flexion-extension and radial-ulnar deviation, subjects were found to make significant use of pronation-supination. We wanted to control this experiment to be a 2 DOF task, so we needed to prevent the forearm from pronating and supinating without significantly affecting flexion-extension and radial-ulnar deviation. This was accomplished by use of a custom-built apparatus which prevented pronation-supination by fixing the distal forearm at three bony sites, as shown in Figure 3.9. The schematic in Figure 3.10 shows that this apparatus consists of two vertical constraints, one fixed (1) and the other constrained to move along a screw (2). The distal forearm is oriented mid-way between pronation and supination and placed between the two vertical constraints of this apparatus. By forcing constraint 2 toward constraint 1 (via the screw mechanism), the distal forearm becomes fixed in three bony locations. Dorsally, the dorsal tubercle of the radius (A) and the dorsal aspect of the ulnar head (B) rest against constraint 1. Ventrally, the ridge that runs proximodistally on the ventrolateral aspect of the radial head (C) rests against a wedge-shaped protuberance (3) on constraint 2. Additionally, the soft tissue medial to this ridge (D) rests against constraint 2. By fixing the radius and ulna at A, B, and C, the forearm is prevented from pronating and supinating without significantly affecting flexion-extension and radial-ulnar deviation. Indeed, subjects reported a snug squeezing sensation on the ventral and dorsal aspects of the distal forearm, but that this sensation did not interfere significantly with wrist rotations. However, efforts to pronate or supinate immediately caused discomfort at the three bony sites.

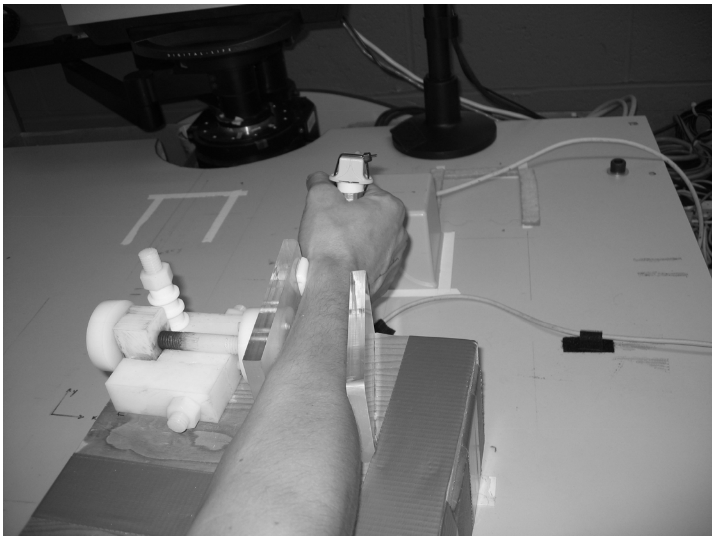

Figure 3.9: Photo of pronation-supination constraint

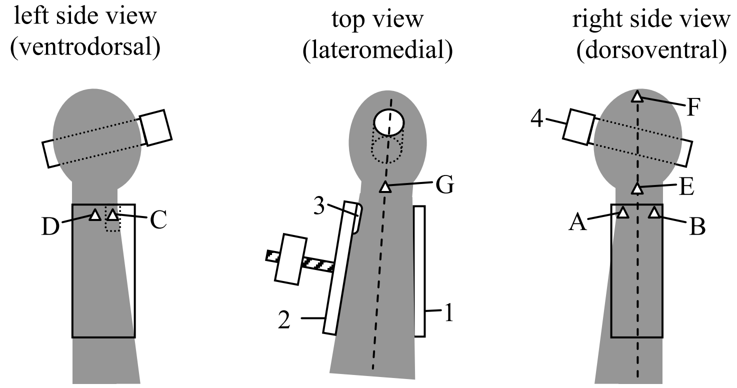

Figure 3.10: Schematic of the apparatus used to constrain pronation and supination.
Objects are labeled by number: (1) stationary constraint, (2) screw-fixed constraint, (3) protuberance attached to constraint 2, (4) handle with sensor. Locations are labeled by letter: (A) dorsal tubercle of radius, (B) dorsal aspect of ulnar head, (C) ventrolateral aspect of radial head, (D) ventral portion of distal forearm, (E) axis of radial-ulnar deviation, (F) distal head of third metacarpal, (G) axis of flexion-extension.

4 Dynamics of Wrist Rotations

4.1 Introduction

An understanding of the dynamics of the "human plant" is central to interpreting kinematic data and disambiguating which kinematic features are due to biomechanics and which are caused by neural control. It also informs one about the challenges the nervous system faces in controlling the periphery during movement. Much insight into the control of reaching movements has been gained from understanding the complex and interactive dynamics of the upper limb. Likewise, a detailed understanding of the dynamics of wrist rotations has been essential to interpreting wrist kinematics and dissecting neural from biomechanical phenomena. Understanding wrist dynamics has also illuminated the likely cause of path curvature (see Chapter 5).

This chapter presents the creation and justification of an anatomically accurate model of wrist dynamics. Experimentally measured kinematics are inserted into the model to determine the relative importance of various dynamic terms (e.g. inertial, stiffness, or gravitational). It was found that stiffness and gravitational terms dominate wrist dynamics. Inertial terms only become important for very fast movements. Even then, inertial interaction torques between the two DOF of the wrist are present but negligible. This is in stark contrast to reaching movements, where interaction torques are significant and present a challenge to the nervous system.

In order to construct a reasonable model of wrist dynamics, we begin with a discussion of the kinematic constraints of the wrist joint.

4.1.1 Wrist Kinematics

Anatomically, the wrist joint consists of eight carpal bones and their supportive tissues. Wrist rotation occurs through complex three-dimensional motions between individual carpal bones as well as between carpal bones and the neighboring bones of the forearm and hand. While it is unlikely that the motion of individual carpal bones can be reduced to a simplified model such as a two-row system [53], global wrist motion, which is the concern of this chapter, *can* be approximated by a simple model.

Global wrist motion is generally defined as flexion-extension (flex-ext) and radial-ulnar (rad-uln) deviation of the hand relative to the forearm. The second or third metacarpal is often taken to represent the orientation of the hand [8]. The distal radioulnar joint, which allows pronation-supination (pro-sup) of the forearm, is proximal to the wrist joint and is generally not considered part of the wrist. Therefore, from a mechanical point of view, the wrist can be defined as the kinematic chain which allows rotation of the hand about two different axes relative to the forearm. While a small amount of translation does occur in the wrist joint, it is minimal [58, 59], confirming that wrist motion is well approximated as purely rotational.

Several common joints allow rotation about different axes. For example, the wrist joint is often likened to a spherical, ellipsoidal, or universal joint. Spherical joint models, which have 3 DOF, group the distal radioulnar joint with the wrist joint. Ellipsoidal joints (a.k.a. condylar or condyloid joints) are like spherical joints except that the surfaces are concave and convex semi-ellipsoids instead of semi-spheres. In such a joint, an ellipsoidal articular surface is received into an ellipsoidal cavity in such a manner as to permit motion along the major and minor axes of the ellipsoid (flex-ext and rad-uln) and limited coupled motion (combined motion, including circumduction), but no axial rotation. Others model the wrist as a universal joint whose axes may be non-intersecting and/or oblique [78]. Importantly, universal joints, unlike spherical and ellipsoidal joints, require by nature that one axis carry the other—there exists a kinematic hierarchy. Which of these kinematic pairs is most consistent with wrist biomechanics?

The complex nature of the wrist joint has made measurements difficult, and studies over the past three decades have sometimes generated conflicting results. However, with the advent of magnetic resonance imaging and computed tomography, measurements have become less invasive and accuracy has increased.

Most recent studies of wrist biomechanics agree that flex-ext occurs more at the radiocarpal joint[11], and rad-uln occurs more at the midcarpal joint[12] [58-60]. Because the radiocarpal joint is proximal to the midcarpal joint, this separation suggests a kinematic hierarchy in which the flex-ext axis carries the rad-uln axis. Likewise, most studies aimed

---

[11] The radiocarpal joint is the joint between the radius and the first row of carpal bones.

[12] The midcarpal joint is the joint between the proximal and distal rows of carpal bones.

at determining the axes of rotation of global wrist motion agree that the wrist rotates about non-intersecting axes, with the flex-ext axis proximal to the rad-uln axis [78]. Such studies have estimated the average offset between axes to be on the order of 0 to 10mm—see [12] for a summary of these studies. Also, the axes of rotation need not be orthogonal. However, Sommer and Miller showed that, in modeling wrist kinematics, the axis offset is considerably more important than whether the axes are orthogonal [78].

In summary, studies of wrist biomechanics show a kinematic hierarchy in which the flex-ext axis carries the rad-uln axis. Universal joints exhibit by nature such a hierarchy, but spherical and ellipsoidal joints do not. As mentioned, there also exists a slight offset between the axes, with the flex-ext axis being proximal to the rad-uln axis. Again, (offset) universal joints can display such behavior, while spherical and ellipsoidal joints cannot. Such a universal joint with offset is shown in Figure 4.1. Its two degrees of freedom are β, the angle in flex-ext, and γ, the angle in rad-uln.

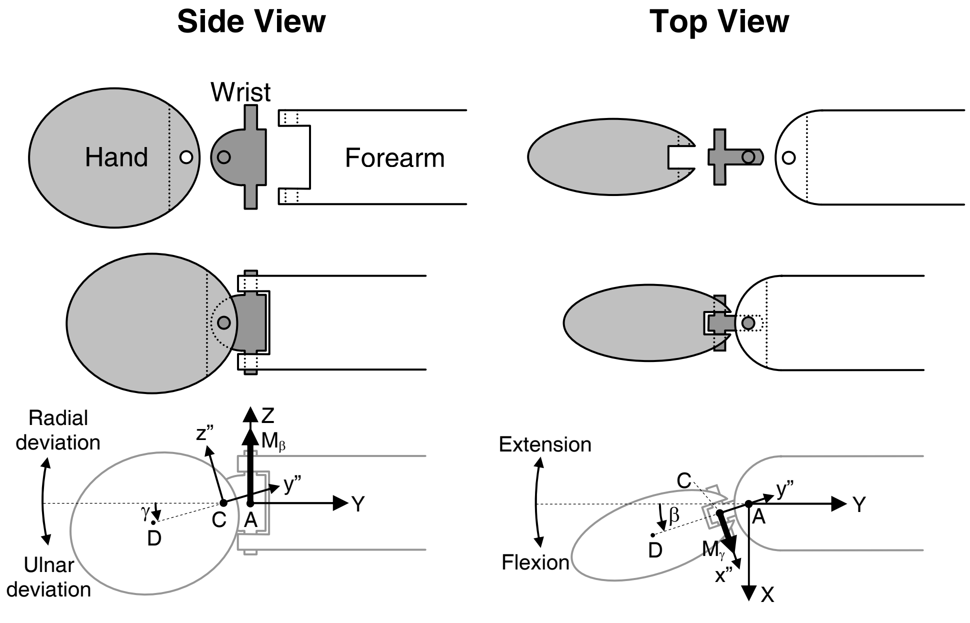

Figure 4.1: Diagram of the universal joint with non-intersecting axes used to model wrist rotations.

4.1.2 Wrist Dynamics

The equations of motion of a universal joint with non-intersecting axes, subject to stiffness and gravity, are derived in the notes at the end of this chapter as:

Equation 1

$$
\begin{aligned}
M_{\beta} = {} & \overbrace{\ddot{\beta}\left[I_{1AZ} + I_{2Cy''}\sin^{2}\gamma + I_{2Cz''}\cos^{2}\gamma + m_{2}r_{AC}\left(r_{AC} + 2r_{CD}\cos\gamma\right)\right]}^{\text{Acceleration Torque}} \\
& + \underbrace{\dot{\beta}\dot{\gamma}\left[2\left(I_{2Cy''} - I_{2Cz''}\right)\sin\gamma\cos\gamma - 2m_{2}r_{AC}r_{CD}\sin\gamma\right]}_{\text{Velocity Torque}} + \underbrace{K_{\beta\beta}\beta + K_{\beta\gamma}\gamma}_{\text{Stiffness Torque}}
\end{aligned}
$$

$$
M_{\gamma} = \underbrace{\ddot{\gamma}I_{2Cx''}}_{\text{Accel. Torque}} - \underbrace{\dot{\beta}^{2}\left[\left(I_{2Cy''} - I_{2Cz''}\right)\sin\gamma\cos\gamma - m_{2}r_{AC}r_{CD}\sin\gamma\right]}_{\text{Velocity Torque}} + \underbrace{K_{\gamma\gamma}\gamma + K_{\beta\gamma}\beta}_{\text{Stiffness Torque}} + \underbrace{m_{2}gr_{CD}\cos\gamma}_{\text{Gravity Torque}}
$$

where M_β and M_γ represent active torques generated by muscle contraction; $[\dot{\beta}, \dot{\gamma}]$ and $[\ddot{\beta}, \ddot{\gamma}]$ are the first and second time derivatives of $[\beta, \gamma]$, respectively; subscript 1 refers to the proximal link (between the axes), and subscript 2 refers to the distal link (the hand); $I_{2Cx''}$, $I_{2Cy''}$, and $I_{2Cz''}$ are the moments of inertia of the hand about the x”, y”, and z” axes at point C, respectively; I_{1AZ} is the moment of inertia about the Z axis at point A of the link between the axes; m_2 is the mass of the hand; r_{AC} is the axis offset; r_{CD} is the distance from the distal axis to the center of mass of the hand; $K_{\beta\beta}$, $K_{\beta\gamma}$, and $K_{\gamma\gamma}$ are elements of the stiffness matrix[13]; and g is the gravitational constant, as shown in Figure 4.1.

Because there are two DOF, there are two equations of motion. The left-hand side of each equation represents the torque due to active muscle contraction, while the right-hand side contains torques due to passive properties of the wrist joint and hand. These passive terms include terms due to inertia, stiffness, and gravity. The magnitude of passive damping is unknown but generally believed to be small, and was therefore neglected. The term ‘inertial torque’ can be defined in different ways[14], but we define it as the sum of torque components due to mass and inertia. According to this defition, the inertial torque in each equation is the sum of the acceleration torque, which is proportional to acceleration, and the velocity torque, which is proportional to the product

---

[13] Describing stiffness in matrix format implicitly assumes linearity, as well as symmetry between flexion and extension and between radial and ulnar deviation. As described in the Methods section, passive wrist stiffness was recently measured by Formica et al. and shown to be relatively linear for moderately-sized wrist rotations. Formica et al. did describe some asymmetry between flexion and extension and between radial and ulnar deviation, but this asymmetry was neglected for simplicity.

[14] For example, in their 1982 paper, Hollerbach and Flash define ‘inertial torques’ as torques which are proportional to acceleration (which we call acceleration torques).

of velocities. The term ‘interaction torque’ reflects inertial coupling between the DOF and refers to torques in one DOF due to motion in the other DOF. For example, the equation for the torque in flex-ext, M_β, contains a term which is proportional to the velocity in rad-uln (Coriolis term), and the equation for the torque in rad-uln, M_γ, contains a term proportional to the square of velocity in flex-ext (Centripetal term). In this model of the wrist, interaction and velocity torques are equal. More generally, however, interaction torques are characteristic of any motion involving multiple DOF and can comprise acceleration and velocity torques. Interaction torques in reaching movements have been studied extensively.

The equations of motion also contain stiffness terms. In each equation, one stiffness term is due to displacement in that DOF (e.g. $K_{\beta\beta}\beta$), while the other stiffness term is due to displacement in the other DOF (e.g. $K_{\beta\gamma}\gamma$) and reflects stiffness coupling between the DOF. Finally , the equation in rad-uln also contains a torque to counteract the effects of gravity.

If a trajectory specified by β and γ (and derivatives) is to be followed, the nervous system must command the wrist’s muscles to generate torques M_β and M_γ according to the equations of motion above. By taking a closer look at the terms in Equation 1, we can understand what challenges the nervous system faces in controlling the dynamics of wrist rotations. In this chapter, therefore, we assess the relative importance of each term. More specifically, we show which terms are negligible (and which are not) by imposing on Equation 1 a series of approximations:

1. Axis offset is negligible ($r_{AC} \approx 0$)
2. Inertial coupling is negligible (interaction torques = velocity torques ≈ 0)
3. Displacements are small (small-angle approximation)
4. Stiffness coupling is negligible ($K_{\beta\gamma} \approx K_{\gamma\beta} \approx 0$)

This allows us to sift from the control challenges placed on the nervous system those that are significant from those that are not.

4.2 Methods

In order to assess the significance of individual torque terms on the right side of Equation 1, we plugged measurements of wrist kinematics into each term and compared term magnitudes. This Methods section describes how we measured wrist kinematics and how we chose the parameters of Equation 1.

4.2.1 Measurement of Wrist Kinematics

Subjects

Six young, healthy human subjects (mean age = 23 ± 4 years, age range = 19 to 28 years; mean BMI = 21.3 ± 1.7 kg/m^2, BMI range = 18.9 – 23.4 kg/m^2) were recruited for this test. Three of the subjects were male and three were female. None of the subjects suffered from neurological impairment or biomechanical injuries to the wrist (diagnosed fractures, tendonitis, or carpal tunnel syndrome). All subjects described themselves as right-handed, and all subjects performed the task with their right hand. Following procedures approved by MIT's Committee on the Use of Humans as Experimental Subjects, informed consent was obtained from all subjects.

Physical Setup

Subjects were seated with the right forearm resting in a para-saggital plane (~25cm from the saggital plane) on a table in front of them (the arm was abducted ~40° and flexed ~35°, with the forearm flexed ~60°). The forearm was prevented from pronating and supinating by a constraint (see Pronation-supination constraint).

In their hand they held a soft-covered, light-weight handle to which a motion sensor (Flock of Birds by Ascension Technology Corporation, Burlington, VT) was rigidly attached. At a combined weight of 70g (13% of the weight of an average hand), the handle and sensor presented negligible interference to natural wrist movements. The motion sensor tracked the position and angular orientation of the handle (6 total DOF) at a sampling frequency of 100 Hz. Displayed on a video screen in front of the subject was a circular pattern of eight targets arranged around a center target. The subject's wrist movements were displayed on the screen as a cursor which moved as a function of the wrist's orientation (see Representation of Wrist Rotations). 15º of wrist rotation was required to move from center to periphery in any direction. The targets and cursor were approximately 2.7° and 1.35° in diameter, respectively.

Representation of Wrist Rotations

In accordance with the recommendations of the International Society of Biomechanics (ISB) [8], global wrist orientation was defined as the orientation of the third metacarpal with respect to the radius. The orientation of the third metacarpal was detected by a sensor mounted atop a handle gripped by the subjects. Wrist orientation was displayed on a computer monitor as a cursor which moved with wrist rotation, like the projection of a laser pointer onto a screen in front of the subjects.[15] Subjects were immediately comfortable with the mapping.

Tasks

Subjects were instructed to move from the center target to a peripheral target, or from a peripheral target to the center target, as prompted by visual cues. Each prompt was designed to elicit a discrete, separate movement by requiring that the subject come to a complete stop on the target and wait half a second before the next target was displayed. Targets were displayed in random order for a total of 240 one-way moves (i.e. 15 round-trip moves to each target).

This task was repeated for two speed instructions. First, subjects were instructed to perform the task at whatever speed they felt comfortable. Second, subjects were instructed to move “as fast as possible”. No instruction was given regarding end-point accuracy, type of path between targets, or correcting movements.

Pronation-supination Constraint

Although the task only required flex-ext and rad-uln, subjects were found to make significant use of pronation-supination (pro-sup). To ensure this task was performed with only two DOF, we used a custom-built apparatus which discouraged pro-sup by fixing the distal forearm at three bony prominences. This apparatus placed the dorsal surface of

---

[15] Strictly speaking, we used a parallel projection, not a point projection as produced by a laser pointer, but for the movements in this experiment (15° amplitude), the difference is negligible at 3%.

the distal forearm in the parasaggital plane (i.e. roughly midway between pronation and supination). Subjects reported a snug squeezing sensation on the ventral and dorsal aspects of the distal forearm that largely eliminated pro-sup but did not interfere with flex-ext and rad-uln wrist rotations.

Neutral Position

Because the angular displacement required to move from the center to the periphery was close to the maximal range of motion for radial deviation, care was taken in defining neutral position. For rad-uln, the wrist was in neutral position when the line between the distal head of the third metacarpal and the axis of rad-uln were collinear with the shaft of the forearm. The axis of rad-uln was determined as described in [4]. This method produces roughly the same neutral position as the method described in [8]. For flex-ext, the wrist was in neutral position when the handle and the mid-point of the wrist were collinear with the shaft of the forearm. This definition differs from ISB recommendations [8] to account for the fact that subjects were holding a handle.

Data Processing

The motion sensor attached to the handle held by subjects measured wrist orientation, $[\beta, \gamma]$. Velocity, $[\dot{\beta}, \dot{\gamma}]$, and acceleration, $[\ddot{\beta}, \ddot{\gamma}]$, were obtained by differentiation. Before differentiation, the data were filtered by the method of smoothing splines, where the amount of smoothing was determined by generalized cross-validation, as suggested by [75]. The specific implementation followed the technique suggested by [76]. The use of smoothing splines allowed derivatives to be obtained analytically. Details are given in Appendix D.

For each movement, the profiles of orientation, velocity and acceleration were aligned at movement onset, which was defined as the data record immediately before movement speed first exceeded 5% of the maximum speed for that movement. The aligned profiles were then averaged for each movement direction, producing mean orientation, velocity, and acceleration profiles for each direction.

The kinematic data used in this chapter is the same as the wrist data used in Chapter 3. Please refer to that chapter for more experimental details.

4.2.2 Model Variables and Parameters

Active torques M_β and M_γ

M_β and M_γ represent the active torques required to move the wrist model along the trajectory specified by $[\beta,\gamma]$, $[\dot{\beta},\dot{\gamma}]$, and $[\ddot{\beta},\ddot{\gamma}]$. The relative importance of inertial, stiffness, and gravitational terms to M_β and M_γ was evaluated as the magnitude of the corresponding terms in Equation 1. The equations of motion given in Equation 1 depend on a number of subject-specific parameters, including inertial parameters of link 1 (inertia and length), link 2 (center of mass, mass, and inertia of the hand), and the passive stiffness of the wrist.

Inertia and length of link 1

The length of link 1, r_{AC}, is the offset between the flex-ext and rad-uln axes. This offset has been estimated in a number of studies to be on the order of 0 to 10mm (see [12] for a summary of these studies). In one particularly careful study involving twenty uninjured wrists, the offset between the flexion axis and the ulnar deviation axis was 3.9±2.0mm, and the offset between the extension axis and the ulnar deviation axis was 3.9±1.4mm [61]. However, because there is some uncertainty in the exact value for each subject, we calculated the error associated with the first approximation ($r_{AC} \approx 0$) for three values of r_{AC}: 10, 4, and -2mm.[16]

The inertia of link 1, I_{1AZ}, is unknown. However, we can show that it is negligible. In the equation for M_β, I_{1AZ} is added to $I_{2Cz''}\cos^2\gamma$. Roughly speaking, I_{1AZ} depends on the square of $r_{AC}/2$, which is on the order of 2mm. $I_{2Cz''}$ depends on the square of r_{CD}, which is on the order of 5cm (see below). Because r_{AC} is more than one order of magnitude smaller than r_{CD}, I_{1AZ} is two to three orders of magnitude smaller than $I_{2Cz''}$. At 15°, $\cos^2\gamma = 0.93 \approx 1$, so $I_{2Cz''}\cos^2\gamma$ is also two to three orders of magnitude larger than I_{1AZ}, and I_{1AZ} is therefore neglected.

---

[16] Note that even though the negative sign in r_{AC} = -2mm means that the rad-uln axis is proximal to the flex-ext axis (by 2mm), the flex-ext axis still carries the rad-uln axis (as long as Equation 1 is used).

Center of mass, mass, and inertia of link 2 (the hand)

The distance between the wrist joint and the center of mass of the hand was calculated as $r_{CD} = 0.3691 \cdot L - 0.2$ cm for men and $0.3502 \cdot L - 0.2$ cm for women, where L is the distance from the stylion (the distal tip of the styloid process of the radius) to the tip of the third finger, in cm [79].

The mass of the hand was calculated as $m_2 = 0.0061 \cdot TBW$ for men and $0.0056 \cdot TBW$ for women, where TBW is the total body weight [79]. The moments of inertia of the hand about the wrist joint were calculated as

$$I_{2C} = m_2 \begin{bmatrix} (aL)^2 & 0 & 0 \\ 0 & (bL)^2 & 0 \\ 0 & 0 & (cL)^2 \end{bmatrix} + m_2 \begin{bmatrix} r_{CD}^2 & 0 & 0 \\ 0 & 0 & 0 \\ 0 & 0 & r_{CD}^2 \end{bmatrix}$$

where a, b, and c are, respectively, 0.285, 0.182, and 0.233 for men and 0.241, 0.152, and 0.206 for women, and L is the distance from the stylion (the distal tip of the styloid process of the radius) to the tip of the third finger [79].

Passive stiffness of the wrist

The passive stiffness field of the wrist has recently been measured by Formica et al. [80]. For the ten subjects from that study, the stiffness tensor was (mean ± std):

$$K = \begin{bmatrix} 1.28 & -0.178 \\ -0.178 & 1.74 \end{bmatrix} \pm \begin{bmatrix} 0.421 & 0.0829 \\ 0.0829 & 0.342 \end{bmatrix} \text{Nm/rad}$$

Three of the subjects who participated in the experiment for this chapter (subjects 1, 3, and 4) were also subjects in the study by Formica et al. Their individual stiffness measurements were obtained and used in this study. For the other three subjects, we used the mean stiffness of the male or female subjects from Formica et al., whichever applied.

For example, subject 1 (male, weight = 73kg, L = 18.5cm) had the following inertial parameters: $r_{CD} = 6.6$ cm; $m_2 = 0.45$ kg; and $I_{2Cx''} = 0.0032$, $I_{2Cy''} = 0.0005$, $I_{2Cz''} = 0.0028$ kgm^2. The passive wrist stiffness of subject 1, measured by Formica et al., was $K_{\beta\beta} = 1.83$, $K_{\beta\gamma} = K_{\gamma\beta} = -0.19$, and $K_{\gamma\gamma} = 2.13$ Nm/rad.

4.2.3 Analysis

Relative contributions

For each movement, the relative contributions of inertia and stiffness torques were compared as the ratio of the integral of the magnitude of each torque:

$$\text{Ratio of inertial to stiffness torque} = \mathrm{R}_{\text{inert/stiff}} = \frac{\int \left| \vec{M}_{\beta,\,inertia} + \vec{M}_{\gamma,\,inertia} \right| dt}{\int \left| \vec{M}_{\beta,\,stiffness} + \vec{M}_{\gamma,\,stiffness} \right| dt}$$

The relative contribution of interaction torques was similarly assessed as the ratio of velocity torques (interaction torques) to acceleration torques (non-interaction inertial torques):

$$\text{Ratio of velocity to acceleration torques} = \mathrm{R}_{\text{vel/acc}} = \frac{\int \left| \vec{M}_{\beta,\,vel} + \vec{M}_{\gamma,\,vel} \right| dt}{\int \left| \vec{M}_{\beta,\,acc} + \vec{M}_{\gamma,\,acc} \right| dt}$$

Approximation error in torque

For each movement, the torques in each DOF, M_β and M_γ, were calculated twice for each movement, once according to the full equations of motion (Equation 1), and once according to the approximated equations of motion (see Figure 4.2A). The effect of each successive approximation was calculated separately for M_β and M_γ as the mean squared error in torque between the full equations and the approximation, normalized by the mean squared torque from the full equations:

$$\text{Normalized mean squared error in } \beta = NMSE_\beta = \frac{\frac{1}{N}\sum_{n=1}^{N}\left\{\left[M_\beta(n) - M'_\beta(n)\right]^2\right\}}{\frac{1}{N}\sum_{n=1}^{N}\left\{\left[M_\beta(n)\right]^2\right\}}$$

where n is the sample number, N is the total number of samples of a movement, and M_β’ is the approximation of M_β. The equation for $NMSE_\gamma$ is similar.

Approximation error in path

For each movement, the error in path caused by successive approximations was calculated as diagrammed in

Figure 4.2B. The approximated kinematics were obtained by solving the forward dynamic model, with torques M_β and M_γ, calculated from the full equations of motion, as inputs. The error between the measured and approximated paths was specified as the area between those two paths, normalized by the square of the distance between targets (15°).

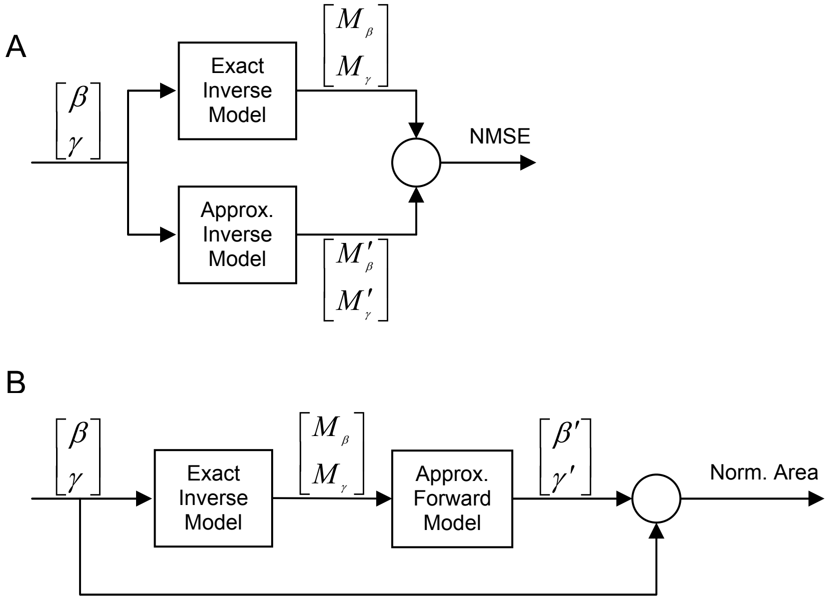

Figure 4.2: Diagram of how approximation errors in torque (A) and path (B) were calculated. Unprimed variables are either measured or calculated with the exact model, while primed variables are calculated via an approximate model. The primed variables are approximated variables, NMSE: normalized mean squared error, Norm. area: normalized area between paths. [β, γ] represents orientation and its derivatives.

4.3 Results

4.3.1 Relative contributions

Example movements from subject 1 in three directions and two speeds can be seen in Figure 4.3. Shown for each movement are plots of hand path, orientation vs. time, and torque vs. time for each DOF. The torque plots show total torque as well as the inertial, stiffness, and gravitational torque constituents that sum to give the total torque (according to Equation 1). Inertial torques are a function of acceleration and velocity and thus vary with movement duration; fast movements show greater inertial torques. In contrast, stiffness torques are proportional to hand orientation and therefore have similar magnitudes—albeit stretched in time—in comfortable and fast movements.

The gravitational torques are also shown in Figure 4.3. In flex-ext, the gravitational torque is always zero, while in rad-uln it is approximately constant because $\cos\gamma \approx 1$ for the 15°-movements in this experiment (see Equation 1). In movements involving rad-uln (vertical or diagonal directions), the gravitational torque is of the same order of magnitude as the stiffness torque.

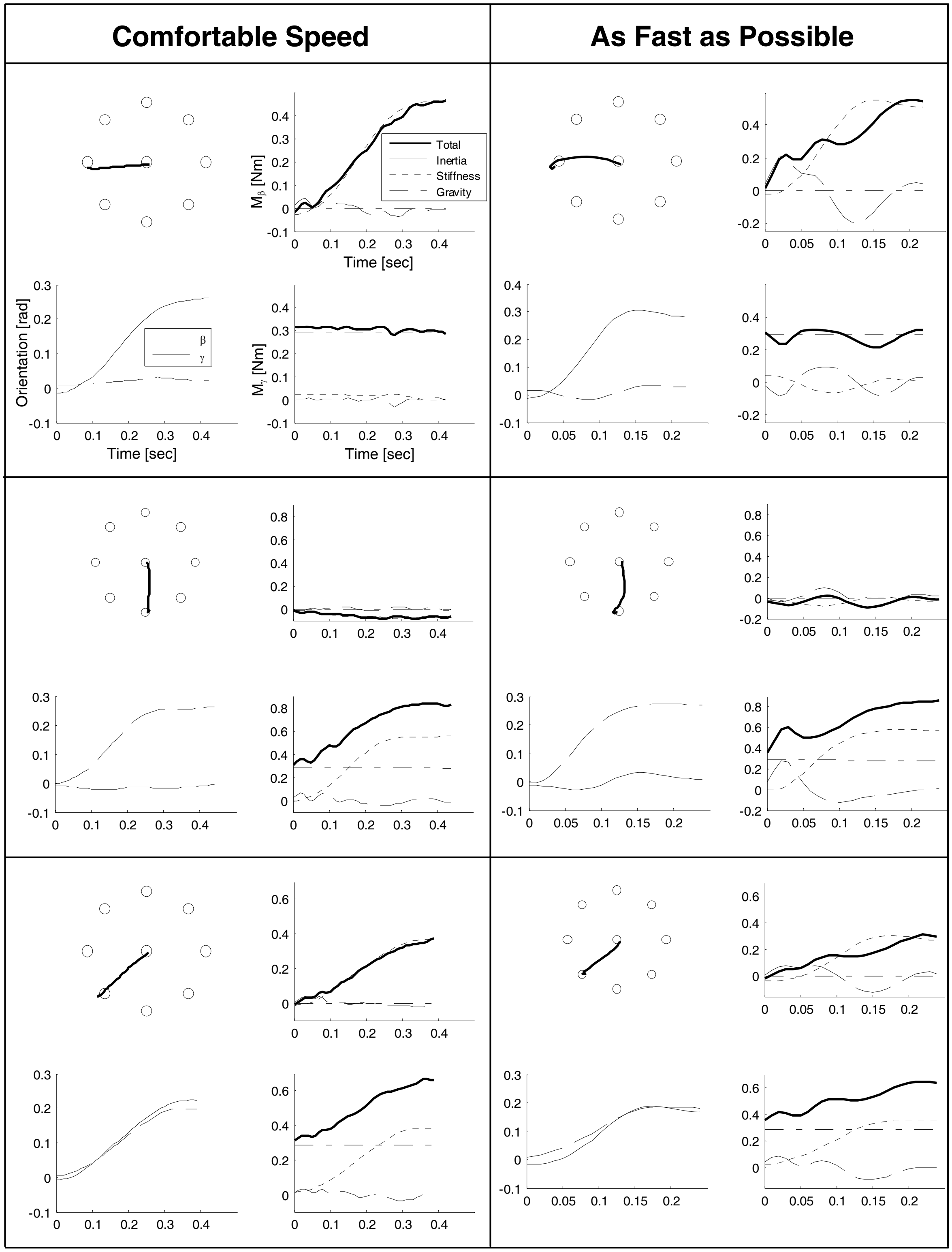

Figure 4.3: Plots of path, orientation, and torque components.

Comfortably-paced rotations are shown in the left column, while fast rotations are shown in the right column. Movements in pure flexion, pure ulnar deviation, and flexion and ulnar deviation are shown in the top, middle, and bottom row, respectively.

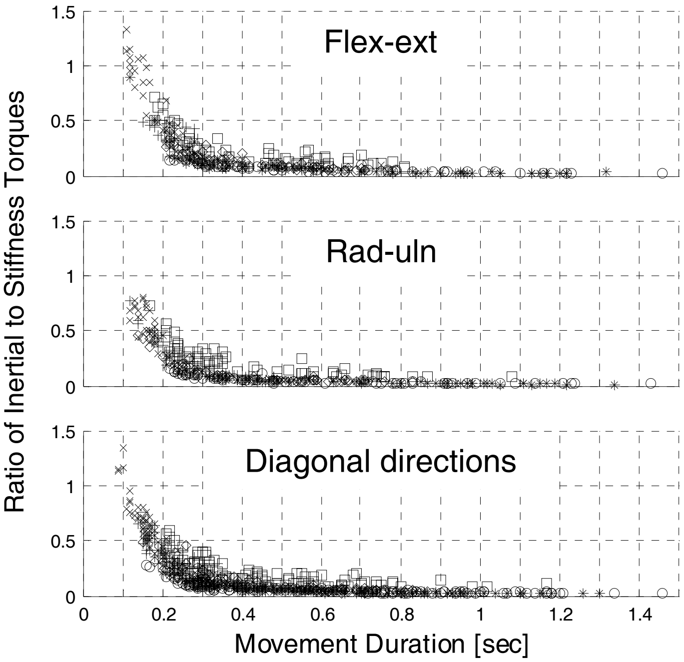

Figure 4.4: Ratio of inertial to stiffness torques vs. movement duration.

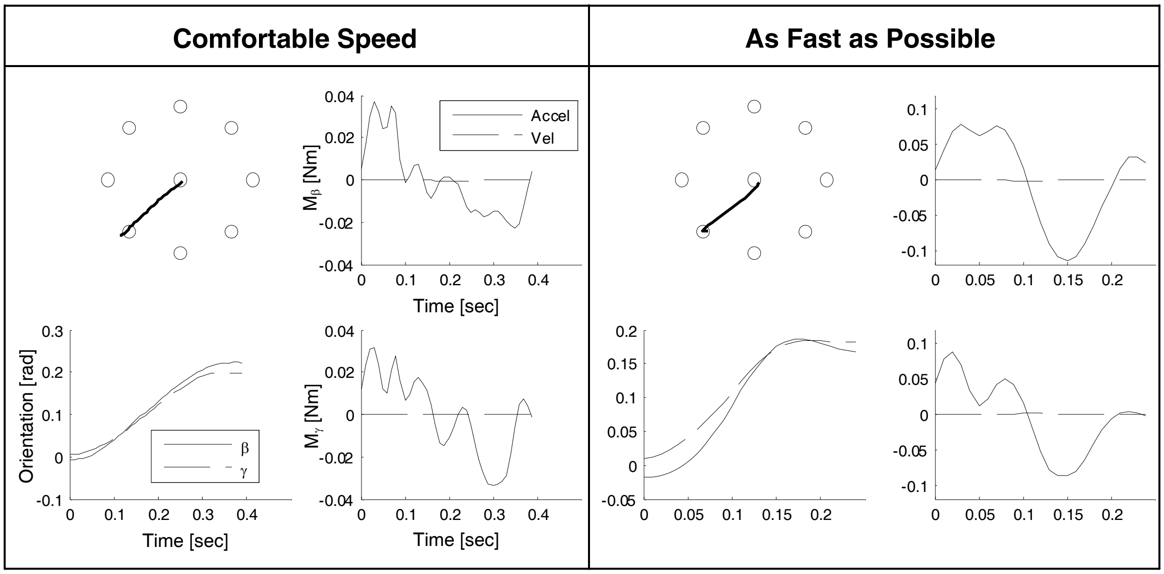

Figure 4.5: Plots of path, orientation, and torque components (velocity and acceleration torques).

The relative contributions of inertial and stiffness torques to M_β and M_γ were computed for all movements and subjects as the ratio of the integral of the magnitude of each torque, $R_{inert/stiff}$ (see Methods). $R_{inert/stiff}$ is plotted vs. movement duration in Figure 4.4. Except for the very fast moves (movement duration < 0.2 sec), stiffness torques always dominated over inertial torques. For comfortable speeds with movement durations around 0.5 sec, stiffness torques are roughly ten times larger than inertial torques. In rad-uln, inertial torques are never as large as stiffness torques because of the higher stiffness in that direction ($K_{\gamma\gamma}$).

In Figure 4.5, the inertial torques are broken out into velocity and acceleration torques for comfortable and fast movements in combined flexion and ulnar deviation. The velocity torques (interaction torques) are very small compared to acceleration torques. The relative contributions of velocity and acceleration torques were computed for all movements and subjects as the ratio of the integral of the magnitude of each torque, $R_{vel/accel}$, shown plotted vs. movement duration in Figure 4.6. The magnitude of velocity torques never exceeds 1/50 the magnitude of acceleration torques.

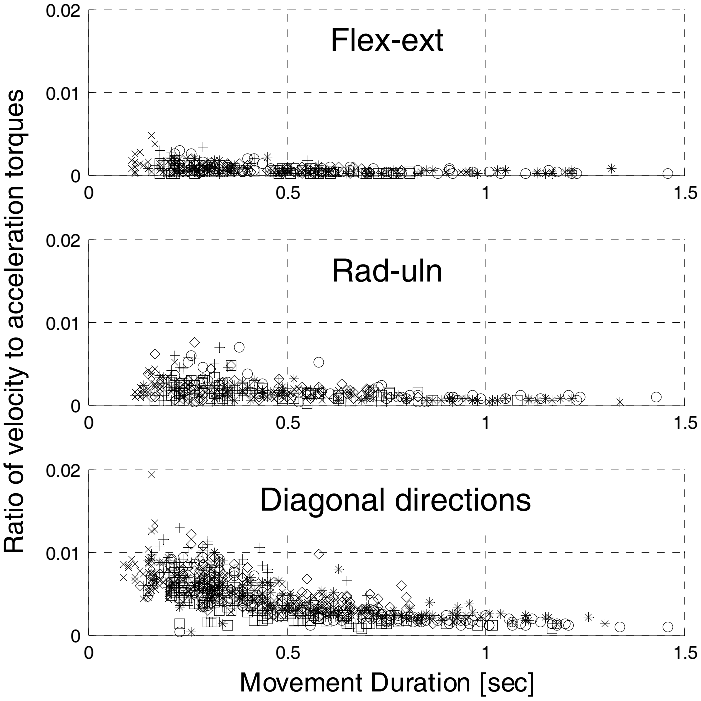

Figure 4.6: Ratio of velocity to acceleration torqus vs. movement duration.

4.3.2 Approximation Error

As described in Methods, the cumulative error associated with successive approximations was computed as 1) the difference in torques calculated from the exact and approximate inverse equations, and 2) the difference in torques measured and calculated from the approximate forward equations.

Approximation Error in Torque

The cumulative error in torque was expressed as the normalized mean squared error (NMSE) for each movement made by each subject, separately for M_β and M_γ, as shown in Figure 4.7 for rotations in flex-ext, rad-uln, and combinations. Descriptive statistics for each approximation (combining both DOF and all directions) are shown in Table 4.1.

Approx.	**r_{AC} [mm]**	**# Samples**	**Normalized Mean Squared Error**			
			Mean	**Std.**	**Min.**	**Max.**
1	10	2880	0.0036	0.0102	0.0000	0.0916
	4	2880	0.0006	0.0018	0.0000	0.0183
	-2	2880	0.0002	0.0005	0.0000	0.0059
2	4	2880	0.0006	0.0019	0.0000	0.0191
3	4	2880	0.0006	0.0012	0.0000	0.0122
4	4	2880	0.1649	0.7282	0.0000	17.9655
		2520	0.0197	0.0236	0.0000	0.2428

Table 4.1: Cumulative error in torque caused by successive approximations.
The error is expressed as normalized mean squared error. The error associated with Approximation #1 (offset ≈ 0) was calculated for three values of r_{AC}. The errors associated with the remaining approximations were calculated for r_{AC} = 4mm. The last row was computed after excluding the error in M_β for rotations in rad-uln (see *Approximation #4* in Results for an explanation).

Approximation #1: Axis offset is negligible ($r_{AC} \approx 0$)

Neglecting the offset in Equation 1 results in equations of motion for a universal joint with intersecting axes:

Equation 2

$$M_{\beta} = \ddot{\beta}\left[I_{2Cy''}\sin^{2}\gamma + I_{2Cz''}\cos^{2}\gamma\right] + \dot{\beta}\dot{\gamma}\left[2\left(I_{2Cy''} - I_{2Cz''}\right)\sin\gamma\cos\gamma\right] + K_{\beta\beta}\beta + K_{\beta\gamma}\gamma$$

$$M_{\gamma} = \ddot{\gamma}I_{2Cx''} - \dot{\beta}^{2}\left[\left(I_{2Cy''} - I_{2Cz''}\right)\sin\gamma\cos\gamma\right] + K_{\gamma\gamma}\gamma + K_{\beta\gamma}\beta + m_{2}gr_{CD}\cos\gamma$$

The exact value of the axis offset, needed to compute the approximation error, is unknown. However, it has been estimated in a number of studies to be on the order of 0 to 10mm, with one study estimating the mean to lie around 4mm (see Methods). Because the exact value is unknown for each subject, we calculated the approximation error assuming $r_{AC} \approx 0$ for three values of r_{AC} (10, 4, and -2mm). As shown in Table 4.1, the mean error (averaged over all movement directions and both DOF) associated with this first approximation was 0.0036, 0.0006 and 0.0002 for r_{AC} = 10, 4, and -2mm, respectively. The error is largest for high speed movements, as shown in Figure 4.7. The error associated with the remaining approximations was calculated assuming that r_{AC} = 4mm.

<u>Approximation #2:</u> Inertial coupling is negligible (velocity torques ≈ 0)

Removing the velocity torques from Equation 2 results in the following equations of motion:

Equation 3

$$M_{\beta} = \ddot{\beta}\left[I_{2Cy''}\sin^{2}\gamma + I_{2Cz''}\cos^{2}\gamma\right] + K_{\beta\beta}\beta + K_{\beta\gamma}\gamma$$

$$M_{\gamma} = \ddot{\gamma}I_{2Cx''} + K_{\gamma\gamma}\gamma + K_{\beta\gamma}\beta + m_{2}gr_{CD}\cos\gamma$$

The cumulative error caused by the first and second approximations remains at 0.0006 for r_{AC} = 4mm. In other words, removing the velocity torques has not changed the approximation error (to the fourth decimal point).

<u>Approximation #3:</u> Displacements are small (small-angle approximation)

The wrist range of motion is relatively small in rad-uln—approximately 20° radial deviation to 36° ulnar deviation—and the range (in rad-uln) used in most activities of daily living is even smaller [81]. For these relatively small rotations about the neutral wrist position, [β, γ] = [0, 0], the trigonometric functions in Equation 1 can be approximated by linear functions ($\sin^2\gamma \approx 0$ and $\cos\gamma \approx \cos^2\gamma \approx 1$), yielding:

Equation 4

$$M_\beta = \ddot{\beta} I_{2Cz''} + K_{\beta\beta}\beta + K_{\beta\gamma}\gamma$$
$$M_\gamma = \ddot{\gamma} I_{2Cx''} + K_{\gamma\gamma}\gamma + K_{\beta\gamma}\beta + m_2 g r_{CD}$$

The cumulative error caused by the first, second, and third approximations remains again at 0.0006 for r_{AC} = 4mm. In other words, the process of linearization has also not changed the approximation error (to the fourth decimal point).

Approximation #4: Stiffness coupling is negligible ($K_{\beta\gamma} \approx K_{\gamma\beta} \approx 0$)

For the ten subjects measured in the experiment by [80], the off-diagonal terms accounted for 15% of the stiffness in flex-ext and 10% of the stiffness in rad-uln. If these off-diagonal terms are neglected, the equations of motion become completely decoupled:

Equation 5

$$M_\beta = \ddot{\beta} I_{2Cz''} + K_{\beta\beta}\beta$$
$$M_\gamma = \ddot{\gamma} I_{2Cx''} + K_{\gamma\gamma}\gamma + m_2 g r_{CD}$$

This approximation does have a noticeable effect. The cumulative error caused by the first, second, third, and fourth approximations is 0.17. However, the error is not evenly distributed across DOF and movement directions, as shown in Figure 4.7. For movements in pure flex-ext or rad-uln, the torques in the movement direction are large and not much affected by displacements perpendicular the movement direction, which are small (see M_β for rotations in flex-ext and M_γ for rotations in rad-uln). In contrast, the torques perpendicular to the movement direction are greatly affected by displacements in the movement direction, because displacements in the movement direction are large (see M_γ for rotations in flex-ext and M_β for rotations in rad-uln). This is especially true for the error in M_β for rotations in rad-uln because M_β is small (M_γ for rotations in flex-ext always has at least the torque term due to gravity). In fact, if a radial deviation is accompanied by slight flexion or an ulnar deviation is accompanied by slight extension, the stiffness coupling term in M_β can cancel the non-coupling stiffness term in M_β (see, e.g. Equation 4), leaving M_β to be very small. If stiffness coupling is discarded, the error is divided by a very small number, allowing the normalized error to reach very large numbers (the maximum is 18.0, as seen in Table 4.1), even though the actual error (before normalizing) is relatively small. If this unrepresentative error in M_β for rotations in rad-uln is excluded, the mean cumulative error associated with the four approximations is 0.02, with a maximum at 0.2 (listed in the last row in Table 4.1). The mean effects of successive approximations are shown graphically in Figure 4.8A.

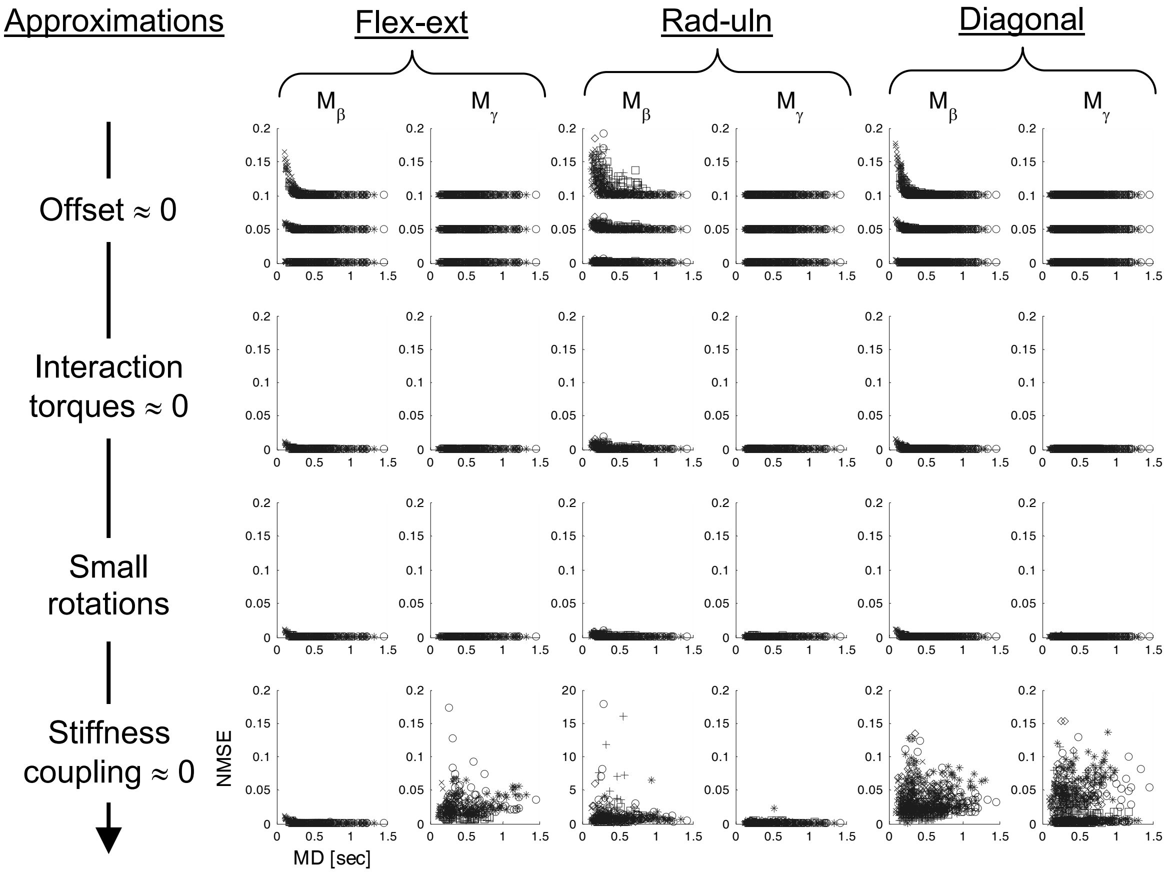

Figure 4.7: Error associated with increasing the number of approximations.

Each subplot plots the normalized mean squared error (NMSE, on the ordinate) in approximating torque caused by successive approximations vs. movement duration (MD, on the abscissa). Each row corresponds to a level of approximation, indicated on the left. The approximation errors in M_β and M_γ, shown in separate columns, were calculated for wrist rotations involving pure flex-ext, pure rad-uln, and rotations in the diagonal directions involving combinations of flex-ext and rad-uln. Because of uncertainty in the exact value of the axis offset, r_{AC}, the error associated with the first

approximation was calculated for three values of r_{AC} (10, 4, and -2mm). The errors associated with r_{AC} = 10mm and 4mm were increased by 0.1 and 0.05, respectively, to include them in the same plot. All subplots have the same scaling except for the subplot showing the error in M_β caused by the fourth approximation (zero stiffness coupling). In this subplot, the ordinate ranges from 0 to 20 (see Results).

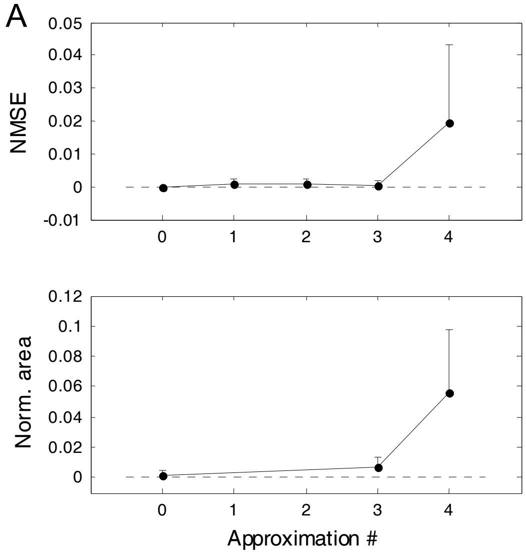

Figure 4.8: Mean error in torque (A) and path (B) caused by successive approximations. The error bars indicate 1 standard deviation. A: Normalized mean squared error (NMSE) in torque. Approximation #0 is the original. In the calculation of the error associated with the fourth approximation, the error in M_β for moves in rad-uln was not included (see Results). For all approximations, r_{AC} = 4mm. B: Normalized area between the experimentally measured path and the path computed from approximations #3 and 4 of the forward dynamic model. Approximation #0 is the normalized area between the original path and the path re-computed with the full forward dynamic equations (no approximation).

Approximation Error in Path

A small approximation error in torque does not guarantee a small approximation error in path because small perturbations in torque can have large effects on path. For example, consider the two movements shown in Figure 4.9. For both movements, the first three approximations result in almost imperceptible errors in torque and path. For the movement in the top row, the fourth approximation also produces a very small error. For the movement in the bottom row, however, the fourth approximation results in a very large error.

The cumulative effect of successive approximations on path was computed for all movements and subjects as the area between measured and approximate paths. Despite the fact that the approximation error in path is sometimes large, as shown in Figure 4.9, *on average* it is similar to the approximation in torque: the first three approximations result in almost imperceptibly small errors, whereas the fourth approximation results in a noticeable but small error. The effect of successive approximations is plotted vs. movement duration in Figure 4.10 and summarized for all movements in Table 4.2 and Figure 4.8B.

Approx.	**Normalized Area between Paths**			
	Mean	**Std.**	**Min.**	**Max.**
0	0.0011	0.0038	0.0000	0.1312
3	0.0067	0.0064	0.0000	0.1494
4	0.0557	0.0416	0.0004	0.2476

Table 4.2: Cumulative error in path caused by successive approximations.

The error is expressed as area between actual and approximated paths. r_{AC} = 4mm. The normalized area between the original path and the path re-computed with the exact forward dynamic equations (approximation #0) is shown to give an idea of the computation error.

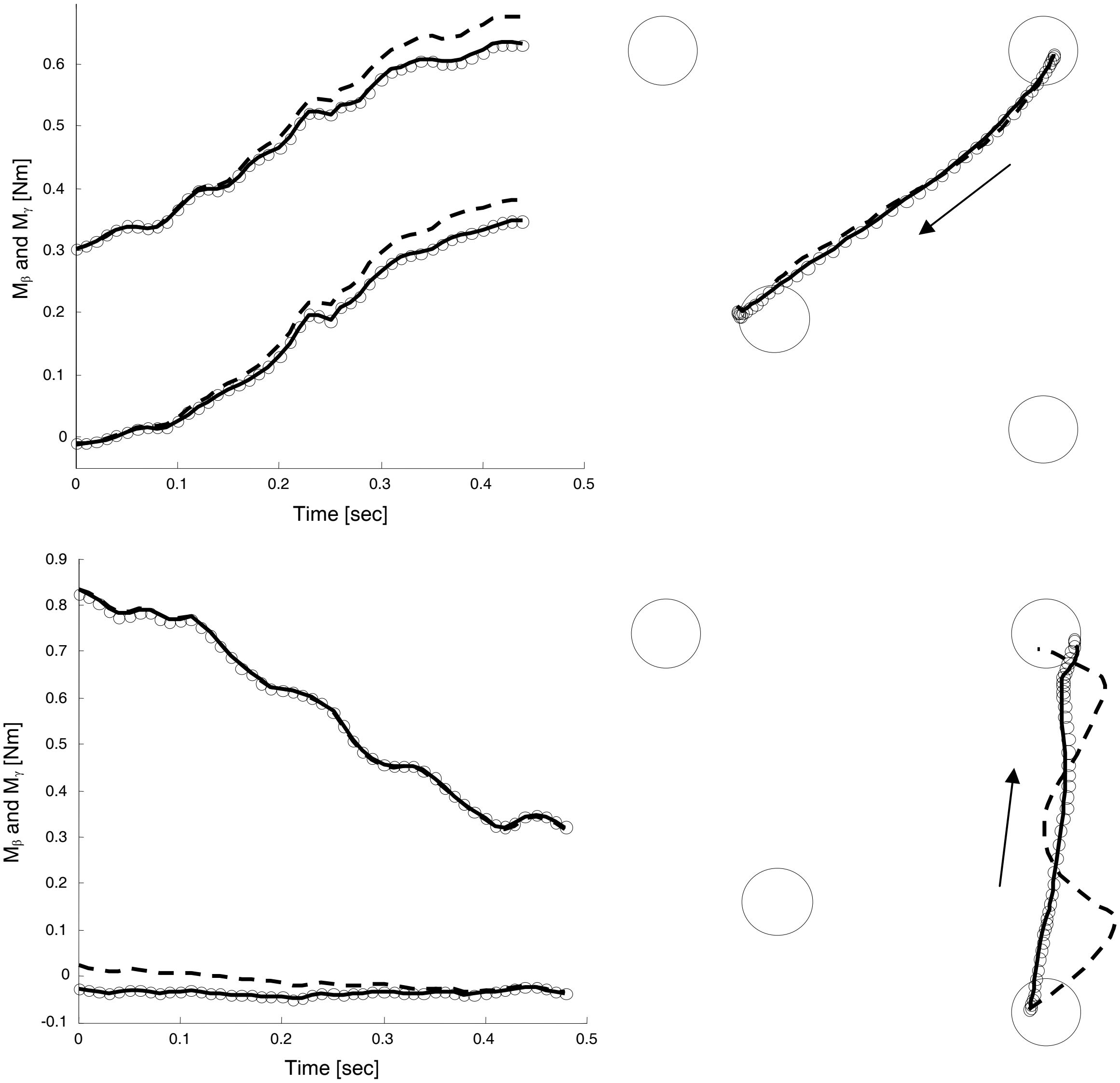

Figure 4.9: Approximation errors in torque (left column) and path (right column). Shown are an outbound movement involving flexion and ulnar deviation (top row) and an inbound movement involving radial deviation. In all plots, the exact solutions is shown as circles, while the third and fourth approximations are shown as solid and dashed lines, respectively. In the torque plots, M_γ is always greater than M_β because of the gravitational term in M_γ.

4.4 Discussion

This chapter presents a simple but anatomically accurate model of wrist rotation dynamics. Experimentally measured kinematics were inserted into the inverse dynamic model to investigate the relative importance of inertial, stiffness, and gravitational torques. Inertial torques were then broken up into acceleration and velocity (interaction) torques and compared. Finally, the effect on torque and path produced by a series of approximations demonstrated which dynamic terms are negligible and which are not.

4.4.1 Stiffness dominates over inertia

As shown in Figure 4.4, stiffness and gravity clearly dominate over inertia. For comfortably paced movements, stiffness torques are roughly one order of magnitude larger than inertial torques. Thus stiffness and gravity are the principal loads the neuromuscular system must overcome in generating wrist rotations. Only for very fast wrist rotations do inertial torques become comparable to stiffness torques. That said, many activities of daily living involve wielding an object, which could, depending on the object, substantially increase the inertia about the wrist joint.

4.4.2 Interaction Torques are Negligible

For each DOF in Equation 1, the inertial torque is the sum of a term which depends only on movement in that DOF (proportional to the acceleration in that DOF), and an interaction term which depends on movement in the other DOF (proportional to velocity in the other DOF). Two of the main results of this chapter are that 1) interaction torques (between the two DOF of the wrist) are present in wrist rotations, and 2) although present, interaction torques are two to three orders of magnitude smaller than non-interaction torques, as shown in Figure 4.6.

The significance of this result arises in part because of its stark contrast to reaching movements, where velocity torques are substantial and must be accounted for if a straight line is to be made—applying simple torques at the shoulder and elbow joints would produce markedly curved paths. The observation of straight-lined reaching movements in real life indicates that the human motor system has learned to compensate for interaction torques in reaching movements.

As a corollary, the presence of straight reaching movements despite inertial interaction also suggests that reaching movements are planned in terms of kinematics, which specify dynamics. Importantly, the presence or absence of straight *wrist rotations* cannot be used as an argument for or against kinematic control; because interaction torques are negligible in wrist rotations, even very simple torque inputs at the wrist joint will result in straight paths (in the absence of other causes of curvature).

4.4.3 Tri-phasic Burst Pattern

Because wrist rotations are dominated by stiffness, one might expect a pattern of muscle activity slightly different from the usual tri-phasic burst pattern because stiffness can (at least partially) replace the role of antagonist muscles in braking movement and maintaining posture. In [36], antagonist activity is smaller than agonist activity, as expected, despite the fact that antagonist activity may have been used to reach targets as quickly as possible after overshooting. Also as expected, agonist activity is present during the third phase of the tri-phasic pattern (to counteract stiffness), while antagonist activity is small or absent during that phase (since stiffness can fulfill that role).

4.4.4 Results are relatively insensitive to model parameters

Clearly, the results of this chapter depend on the accuracy of the model and the accuracy of the physical parameters used in the wrist model. Care was taken to minimize inaccuracies in parameters. For all subjects, inertial parameters were calculated from individual measurements of segment lengths inserted into inertial parameter equations based on in-vivo measurements of college-aged subjects (see [79]). For half the subjects, passive stiffness was measured directly by Formica et al. For the other half, the male or female average was used, whichever applied.

Perhaps more importantly, the main results presented in this chapter are relatively insensitive to inaccuracies in model parameters. For example, for comfortably paced movements, stiffness dominates over inertia by an order of magnitude. To reverse that result would require a very large error in inertia or stiffness. As another example, the interaction torques in both DOF increase with ($I_{2Cy''} - I_{2Cz''}$). Because the velocity torques are so much smaller than the acceleration torques (less than 1/50), reversing this inequality would require a very large error in ($I_{2Cy''} - I_{2Cz''}$).

In searching for a wrist model, we deliberately balanced accuracy with simplicity. While our simple model allows insight into the dynamic properties of universal joints, it clearly does not imitate the wrist in all details. Nevertheless, in Chapter 5 we show that this model can recreate many features of wrist rotations, lending credence to the model and results presented in this chapter.

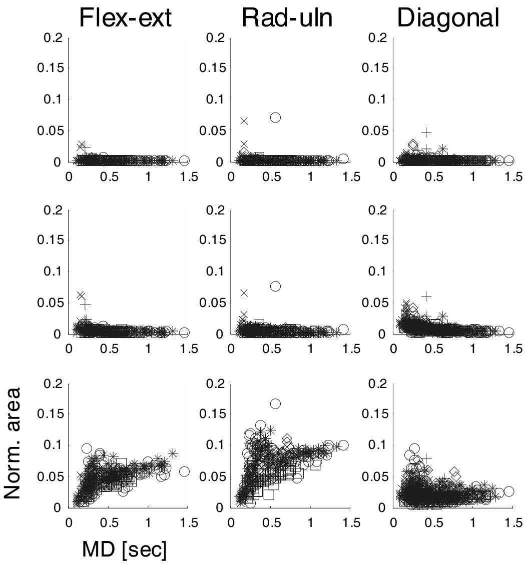

Figure 4.10: Normalized area vs. movement duration between original and approximated paths. The middle row is for approximation #3, and the bottom row for approximation #4. The normalized area between the original path and the path re-computed with the full forward dynamic equations (no approximation) is shown on the top row to give an idea of the computation error.

4.5 Notes

4.5.1 Derivation of equations of motion of 2-DOF wrist model

The equations of motion are derived via Lagrange's Equations, as outlined in [62]. Refer to Figure 4.1 for parameter definitions.

1. Generalized Coordinates: β and γ

   Admissable Variations: δβ and δγ

   ⇒ This system is holonomic.

2. Generalized Forces

   $$\delta W^{nc} = M_{\beta}\delta\beta + M_{\gamma}\delta\gamma = \Xi_{\beta}\delta\beta + \Xi_{\gamma}\delta\gamma$$

   ⇒ M_{β} and M_{γ}, which are torques acting along the Z and x" axes, respectively, are generalized forces.

3. Lagrangian

   $L = T^{*} - V$, where T^{*} is the kinetic co-energy and V is the potential energy of the system.

   The kinetic co-energy of the system, T^{*}, is equal to the sum of the kinetic co-energy of each link. The kinetic co-energy of link 1, which rotates about A, is:

   $$T_1^{*} = \frac{1}{2}\dot{\vec{\beta}}^{T} I_{1A}\dot{\vec{\beta}} = \begin{bmatrix} 0 & 0 & \beta \end{bmatrix} \begin{bmatrix} I_{1AX} & 0 & 0 \\ 0 & I_{1AY} & 0 \\ 0 & 0 & I_{1AZ} \end{bmatrix} \begin{bmatrix} 0 \\ 0 \\ \beta \end{bmatrix} = \frac{1}{2} I_{1AZ}\dot{\beta}^{2}$$

   The kinetic co-energy of link 2, which rotates about A and C, is:

$$T_2^* = \frac{1}{2} m_2 \vec{v}_D \cdot \vec{v}_D + \frac{1}{2}\left(\dot{\vec{\beta}} + \dot{\vec{\gamma}}\right)^T I_{2D} \left(\dot{\vec{\beta}} + \dot{\vec{\gamma}}\right)$$

$$T_2^* = \frac{1}{2} m_2 \begin{bmatrix} \dot{\beta} r_{AC} \cos\beta + \dot{\beta} r_{CD} \cos\beta \cos\gamma - \dot{\gamma} r_{CD} \sin\beta \sin\gamma \\ \dot{\beta} r_{AC} \sin\beta + \dot{\beta} r_{CD} \sin\beta \cos\gamma + \dot{\gamma} r_{CD} \cos\beta \sin\gamma \\ -\dot{\gamma} r_{CD} \cos\gamma \end{bmatrix} \cdot \ldots$$

$$\ldots \cdot \begin{bmatrix} \dot{\beta} r_{AC} \cos\beta + \dot{\beta} r_{CD} \cos\beta \cos\gamma - \dot{\gamma} r_{CD} \sin\beta \sin\gamma \\ \dot{\beta} r_{AC} \sin\beta + \dot{\beta} r_{CD} \sin\beta \cos\gamma + \dot{\gamma} r_{CD} \cos\beta \sin\gamma \\ -\dot{\gamma} r_{CD} \cos\gamma \end{bmatrix}$$

$$+ \frac{1}{2} \begin{bmatrix} \dot{\gamma} & \dot{\beta}\sin\gamma & \dot{\beta}\cos\gamma \end{bmatrix} \begin{bmatrix} I_{2Dx''} & 0 & 0 \\ 0 & I_{2Dy''} & 0 \\ 0 & 0 & I_{2Dz''} \end{bmatrix} \begin{bmatrix} \dot{\gamma} \\ \dot{\beta}\sin\gamma \\ \dot{\beta}\cos\gamma \end{bmatrix}$$

$$T_2^* = \frac{1}{2} m_2 \left[\dot{\beta}^2 \left(r_{AC} + r_{CD}\cos\gamma\right)^2 + \left(\dot{\gamma} r_{CD}\right)^2\right] + \frac{1}{2}\dot{\beta}^2 I_{2Dy''} \sin^2\gamma + \frac{1}{2}\dot{\beta}^2 I_{2Dz''} \cos^2\gamma + \frac{1}{2}\dot{\gamma}^2 I_{2Dx''}$$

Rewriting inertial terms of link 2 to be about C instead of D, and combining T_2^* with T_1^* yields:

$$T^* = \frac{1}{2}\left[I_{1AZ} + m_2 r_{AC}\left(r_{AC} + 2r_{CD}\cos\gamma\right) + I_{2Cy''}\sin^2\gamma + I_{2Cz''}\cos^2\gamma\right]\dot{\beta}^2 + \frac{1}{2} I_{2Cx''}\dot{\gamma}^2$$

The potential energy of the system, V, consists of potential energy due to the wrist's passive stiffness and due to gravity. If the passive stiffness of the wrist is approximated as being linear about the neutral position (β=γ=0) and conservative ($K_{\beta\gamma} = K_{\gamma\beta}$), then

$$V = \frac{1}{2}\begin{bmatrix} \beta & \gamma \end{bmatrix} \begin{bmatrix} K_{\beta\beta} & K_{\beta\gamma} \\ K_{\beta\gamma} & K_{\gamma\gamma} \end{bmatrix} \begin{bmatrix} \beta \\ \gamma \end{bmatrix} + m_2 g r_{CD} \sin\gamma$$

$$= \frac{1}{2} K_{\beta\beta}\beta^2 + K_{\beta\gamma}\beta\gamma + \frac{1}{2} K_{\gamma\gamma}\gamma^2 + m_2 g r_{CD} \sin\gamma$$

Combining T^* and -V yields the Lagrangian:

$$L = \frac{1}{2}\left[I_{1AZ} + m_2 r_{AC}\left(r_{AC} + 2r_{CD}\cos\gamma\right) + I_{2Cy''}\sin^2\gamma + I_{2Cz''}\cos^2\gamma\right]\dot{\beta}^2 + \frac{1}{2} I_{2Cx''}\dot{\gamma}^2$$

$$- \frac{1}{2} K_{\beta\beta}\beta^2 - K_{\beta\gamma}\beta\gamma - \frac{1}{2} K_{\gamma\gamma}\gamma^2 - m_2 g r_{CD} \sin\gamma$$

4. Lagrange’s Equations

The equations of motion are obtained from Lagrange’s equations:

$$M_{\beta} = \frac{d}{dt}\left(\frac{\partial L}{\partial \dot{\beta}}\right) - \frac{\partial L}{\partial \beta}$$

$$M_{\gamma} = \frac{d}{dt}\left(\frac{\partial L}{\partial \dot{\gamma}}\right) - \frac{\partial L}{\partial \gamma}$$

which yield

$$\begin{aligned} M_{\beta} &= \ddot{\beta}\left[I_{1AZ} + I_{2Cy''}\sin^2\gamma + I_{2Cz''}\cos^2\gamma + m_2 r_{AC}\left(r_{AC} + 2r_{CD}\cos\gamma\right)\right] \\ &\quad + \dot{\beta}\dot{\gamma}\left[2\left(I_{2Cy''} - I_{2Cz''}\right)\sin\gamma\cos\gamma - 2m_2 r_{AC} r_{CD}\sin\gamma\right] + K_{\beta\beta}\beta + K_{\beta\gamma}\gamma \end{aligned}$$

$$M_{\gamma} = \ddot{\gamma} I_{2Cx''} - \dot{\beta}^2\left[\left(I_{2Cy''} - I_{2Cz''}\right)\sin\gamma\cos\gamma - m_2 r_{AC} r_{CD}\sin\gamma\right] + K_{\gamma\gamma}\gamma + K_{\beta\gamma}\beta + m_2 g r_{CD}\cos\gamma$$

5 Effect of Passive Stiffness on Path Curvature

5.1 Introduction

It has long been known that humans make reaching movements in such a way that the hand draws a path which is roughly straight [63, 64]. When the hand path is artificially curved through mechanical or visual perturbations, humans adapt by learning to make straight hand paths despite the perturbation [68, 69]. This proclivity for straight hand paths is significant because it gives valuable insight into the planning and representation of reaching movements. This is not to say that hand paths are perfectly straight; reaching paths do show a small degree of curvature which depends on the workspace [65]. Nevertheless, this curvature has been attributed to imperfect control of the biomechanical and perceptual complexities inherent in movements involving multiple degrees of freedom (DOF) [66, 67].

In contrast, humans' wrist rotation paths are significantly more curved than their reaching paths. When humans rotate the wrist in combinations of flexion-extension and radial-ulnar deviation, the resulting paths (like those produced on a screen while using a laser pointer) exhibit approximately twice as much curvature as planar reaching movements (Chapter 3). This increased curvature could lead one to conclude that wrist rotations are planned or represented differently than reaching movements. However, two key properties of path curvature in wrist rotations (outbound and inbound curvature differs significantly, and curvature is highly variable—see Chapter 3) make it clear that this conclusion cannot be made from the observation of increased curvature (Chapter 3). Rather, it is likely that the curvature observed in wrist rotations is due to imperfect control of biomechanical or perceptual complexities, as in reaching movements. But what exactly causes path curvature in wrist rotations? In this chapter, we show that the stiffness of the wrist joint is the major cause of path curvature. In addition, we provide evidence against other possible causes of wrist curvature, including inertial, force, and neural causes.

The path curvature of wrist rotations has been characterized quantitatively in Chapter 3. Figure 5.1 shows individual and averaged paths of wrist movements performed “as fast as possible.” The following characteristics are notable:

1. Wrist paths are curved in the sense that paths consistently deviate to one side of a straight line for the majority of targets. This is true for outbound and inbound moves and for moves at comfortable and fast speeds.
2. Wrist path curvature depends on the direction of movement: outbound and inbound paths differ significantly for the majority of targets. This is true for moves at comfortable and fast speeds.
3. The amount and direction of curvature varies between targets, but it follows a clear pattern for fast wrist rotations: moves in the same direction but to opposite targets curve to the same side. For example, inbound moves from target 3 and outbound moves to target 7, both of which involve pure flexion, curve toward radial deviation (see Figure 5.1).
4. Wrist rotations performed “as fast as possible” show significantly more curvature than rotations performed at a comfortable speed ($p < 0.001$).

In addition, the following characteristic was gleaned from the work by Hoffman and Strick:

5. The pattern of curvature changes with the amount of pro-sup: pronating the forearm pronates the pattern of curvature, and supinating the forearm supinates the pattern. This is very nicely displayed in Figure 1 of [44]. Said another way, the pattern of curvature observed at the wrist belongs to the joint space of the forearm.

In summary, wrist rotation paths generally display the following characteristics:

1. Paths exhibit non-zero curvature.
2. Outbound and inbound paths curve in opposite directions.
3. Moves in the same direction but to opposite targets curve to the same side.
4. Fast moves show more curvature than slow moves.
5. The curvature pattern depends on pro-sup.

In this chapter, we show that wrist stiffness anisotropy is the most likely cause of path curvature in wrist rotations, and we provide evidence against alternative candidate causes.

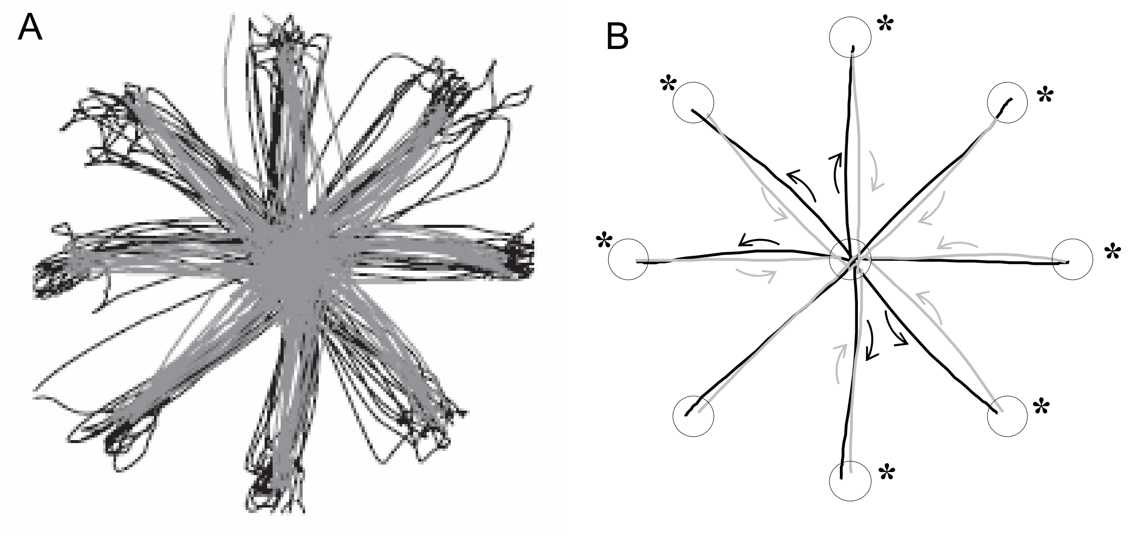

Figure 5.1: Paths produced by wrist rotations performed “as fast as possible.”
A: Individual outbound (black) and inbound (gray) paths of one subject. B: mean paths, averaged over all movements and subjects, are shown on the right. An arrow denotes that moves in that direction are statistically significantly different from a straight line ($p \leq 0.05$). An asterisk denotes that outbound and inbound movements to that target differ significantly from each other ($p \leq 0.05$).

5.2 Methods

5.2.1 Model

For relatively small wrist rotations, wrist dynamics are well-approximated by a set of two linear, coupled equations of motion (Chapter 4):

$$I_\beta \ddot{\beta} + B_\beta \dot{\beta} + K_{\beta\beta}\beta + K_{\beta\gamma}\gamma = M_\beta$$
$$I_\gamma \ddot{\gamma} + B_\gamma \dot{\gamma} + K_{\gamma\gamma}\gamma + K_{\beta\gamma}\beta = M_\gamma$$

where β represents flex-ext (flexion is positive) and γ represents rad-uln (ulnar deviation is positive). For each DOF, I, B, and K represent *passive* tissue properties: I is the inertia of the hand at the wrist in that DOF, and B and K are the passive damping and stiffness of muscles and ligaments. M represents *active* muscle contraction, which, for the moment, is assumed to be a pure force generator and is modeled as a step function of amplitude A. Note that the equations are coupled through stiffness $K_{\beta\gamma}$ (an explanation of stiffness coupling is given in the Notes at the end of this chapter).

The first part of this analysis investigates the effect of anisotropic stiffness ($K_{\gamma\gamma} \neq K_{\beta\beta}$) in the *absence* of stiffness coupling ($K_{\beta\gamma} = 0$). The equation of motion in each DOF degenerates to a second-order linear system. The response in flex-ext is:

$$\beta = \frac{A_\beta}{k_\beta}\left\{1 - e^{-t/\tau_\beta}\left[\cos(\omega_\beta t) + \frac{\zeta_\beta}{\sqrt{1-\zeta_\beta^{\,2}}}\sin(\omega_\beta t)\right]\right\}$$

where $\tau_\beta = \frac{2I_\beta}{b_\beta}$ is the time constant of the exponential decay envelope,

$\omega_\beta = \sqrt{\frac{k_\beta}{I_\beta} - \left(\frac{b_\beta}{2I_\beta}\right)^2}$ is the damped frequency of oscillation, and $\zeta_\beta = \frac{b_\beta}{2\sqrt{I_\beta k_\beta}}$ is the damping ratio. The equation for rad-uln is similar.

The second part of the analysis investigates the effect of anisotropic stiffness ($K_{\gamma\gamma} \neq K_{\beta\beta}$) in the *presence* of stiffness coupling ($K_{\beta\gamma} \neq 0$). The set of coupled equations of motion was solved for β and γ numerically using MATLAB.

5.2.2 Model Parameters

The model parameters used in this chapter are mean values of physical measurements taken from healthy subjects (see below). While it is true that physical parameters can vary greatly between subjects, the ratio of parameters in the two DOF, which is of concern in this chapter, is relatively constant across subjects.

Inertia

The moments of inertia of the hand about the wrist joint were calculated as in Chapter 4 using the method from [79]. For the six subjects from Chapter 3, the mean inertia in flex-ext, I_β, was 0.002 kgm^2 (range from 0.0010 to 0.0033 kgm^2). The inertia of the hand in rad-uln, I_γ, was always just slightly larger than the inertia in flex-ext (mean ratio = 1.12, range from 1.10 to 1.15). For the simulations in this chapter, we assumed $I_\beta = I_\gamma = 0.002$ kgm^2 (Figure 5.2 and Figure 5.3) and $I_\beta = I_\gamma = 0.0075$ kgm^2 (Figure 5.4, to account for the inertia of the wrist device), as listed in Table 5.1.

Stiffness

The passive stiffness field of the wrist has recently been measured [80]. For the ten subjects from that study, the stiffness tensor was (mean ± std):

$$K = \begin{bmatrix} 1.28 & -0.178 \\ -0.178 & 1.74 \end{bmatrix} \pm \begin{bmatrix} 0.421 & 0.0829 \\ 0.0829 & 0.342 \end{bmatrix} \text{Nm/rad}$$

Expressed alternatively along its principal axes, the mean stiffness tensor,

$$K_p = \begin{bmatrix} 1.21 & 0 \\ 0 & 1.82 \end{bmatrix} \pm \begin{bmatrix} 0.394 & 0 \\ 0 & 0.370 \end{bmatrix} \text{Nm/rad}$$

was pronated by 21.2 ± 9.20° (range from 8.81 to 37.0°) from the vertical. The ratio of eigenvalues was, on average, 1.58 ± 0.385 (range from 1.14 to 2.43). In other words, for all ten subjects, stiffness in rad-uln was larger than in flex-ext.

For the simulations in this chapter, we assumed principal stiffness ratios of 1, 1.5, and 2 (Figure 5.2), 1.25 (Figure 5.3); and 1.75 (Figure 5.4), as listed in Table 5.1. For tilt angle, we assumed 0° (Figure 5.2), 15° (Figure 5.3), and 5° (Figure 5.4), always toward pronation.

Damping

Flash summarized a few studies which investigated the relationship of stiffness and damping during reaching movements [66], and Gielen and Houk peripherally mentioned a measurement of damping in 1-DOF wrist rotations [14], but these sources were not enough to piece together a reliable estimate of damping in wrist rotations, not to mention an estimate of the relationship of damping between the two DOF of the wrist. Therefore, for the simulations in this chapter, the damping parameters were assumed to be equal in flex-ext and rad-uln ($B_\beta = B_\gamma$). In practice, we specified ζ_β, the damping ratio in flex-ext, from which we calculated B_β as

$$B_\beta = 2\zeta_\beta \sqrt{K_{\beta\beta} I_\beta}$$

and then set $B_\gamma = B_\beta$. Note that this means that $\zeta_\gamma \neq \zeta_\beta$ whenever stiffness was anisotropic (inertia was always assumed isotropic). In the simulations in this chapter, we chose ζ_β = 0.7 and 1.3 in Figure 5.2A; ζ_β = 0.7 in Figure 5.2B and Figure 5.2C and Figure 5.3; and ζ_β = 0.35 in Figure 5.4 (see Table 5.1).

The effect of simultaneously increasing or decreasing damping ratios in both DOF is to increase or decrease, respectively, the amount of overshoot in the two DOF, as expected (e.g., see Figure 5.2A). A very brief discussion of the effect of damping anisotropy on path is given in Section 5.4.3 and Figure 5.5, and a longer discussion is given in Section 6.1.1.

Figure	**$I_\beta = I_\gamma$ [kgm^2]**	**ζ_β**	**$K_{p,\beta}$ [Nm/rad]**	**$K_{p,\gamma}/K_{p,\beta}$**	**Tilt [deg]**	**$K_{p,\gamma}$ [Nm/rad]**	**ζ_γ**	**$B_\beta = B_\gamma$ [Nms/rad]**	**$K_{\beta\beta}$ [Nm/rad]**	**$K_{\gamma\gamma}$ [Nm/rad]**	**$K_{\beta\gamma} = K_{\gamma\beta}$ [Nm/rad]**
5.2A*	0.0020	0.70 1.30	1.20	1.00 1.50 2.00	0	1.20 1.80 2.40	0.70, 1.30 0.57, 1.06 0.50, 0.92	0.069, 0.127	1.200	1.200 1.800 2.400	0.000
5.2B	0.0020	0.70	1.20	1.50	0	1.80	0.57	0.069	1.200	1.800	0.000
5.2C	0.0020	0.70	1.20	1.50	0	1.80	0.57	0.069	1.200	1.800	0.000
5.3A	0.0020	0.70	1.20	1.25	15	1.50	0.64	0.069	1.220	1.480	-0.075
5.4A	0.0075	0.35	1.50	1.75	5	2.63	0.27	0.075	1.509	2.617	-0.098

Table 5.1: Model parameters used in simulations.

The parameters with no shading were specified, from which the parameters in gray shading were calculated. $K_{p,\beta\gamma}$ and $K_{p,\beta\gamma}$ are the stiffness components along the principal axes closest to the flex-ext and rad-uln axes, respectively. The tilt angle is positive in pronation.

*** Because Figure 5.2A contains paths with one of two values of ζ_β and one of three values of $K_{p,\gamma}/K_{p,\beta}$, there are multiple values of ζ_γ and $B_\beta = B_\gamma$; each row corresponds to a value of $K_{p,\gamma}/K_{p,\beta}$ and each value within a row corresponds to a value of ζ_β.**

5.3 Results

The first part of this analysis investigates the effect of anisotropic stiffness ($K_{\gamma\gamma} > K_{\beta\beta}$) in the *absence* of stiffness coupling ($K_{\beta\gamma} = 0$). The steady-state orientation of the wrist depends only on the input torques, A_β and A_γ, and the stiffness values, $K_{\beta\beta}$ and $K_{\gamma\gamma}$, in the two DOF. As shown in Figure 5.2A for a simulated move in flexion and ulnar deviation, if the stiffness in ulnar deviation is greater than in flexion ($K_{\gamma\gamma} > K_{\beta\beta}$), equal input torques ($A_\beta = A_\gamma$) will produce a path which does not reach the target on the 45°-diagonal, but deviates instead toward flexion. Because the steady-state position only depends on input torque and stiffness, this veering toward flexion will occur for any choice of time constant, damped frequency of oscillation, and damping ratio. If, however, the input torques are adjusted to reflect the unequal stiffnesses ($A_\beta/A_\gamma = K_{\beta\beta}/K_{\gamma\gamma}$), then the initial pulling direction leans toward ulnar deviation, and the path reaches the target on the diagonal, as shown in Figure 5.2B. Note that, if released from any peripheral target, the wrist will always return to its rest position in the center.

Comparing the inbound and outbound paths shown in Figure 5.2B, one can see that they curve to opposite sides. Indeed, this model is capable of reproducing the observed “petal pattern” in all diagonal directions, as shown in Figure 5.2C. Note that the direction of curvature is also the same as that observed in monkeys by Hoffman and Strick (Figure 1 in [36]).

We now consider the effect of stiffness coupling ($K_{\beta\gamma} \neq 0$). For negative values of $K_{\beta\gamma}$, the principal stiffness axes are rotated clockwise (toward pronation) relative to the movement axes. This rotation causes the curvature in the cardinal directions to wax while the curvature in the diagonal directions wanes (this is true up to 45° of rotation, at which point the pattern reverses). At 22.5° of rotation, the curvature in cardinal and diagonal directions is equal.

In Figure 5.3, mean paths from experimentally measured, fast wrist rotations (see Chapter 3 for Methods) are plotted side-by-side with simulated paths, generated for 15° pronation of stiffness. Note that, with the exception of movements to the south-west target, for which the real data shows no significant curvature, these two key features of passive wrist stiffness (anisotropy and tilt) are capable of recreating all characteristics of path curvature except #4:

1. Paths exhibit non-zero curvature.
2. Outbound and inbound paths curve in opposite directions.
3. Moves in the same direction but to opposite targets curve to the same side.
4. Fast moves show more curvature than slow moves.

5. The curvature pattern depends on pro-sup.

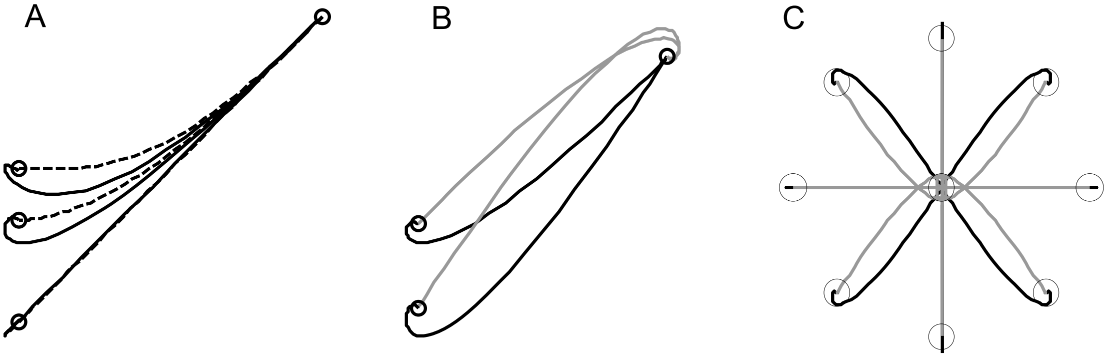

Figure 5.2: Effect of stiffness anisotropy on path (in the absence of stiffness coupling).
A: Outbound paths for three stiffness ratios (1, 1.5, 2) and equal input torques (0.15 Nm step). For each stiffness ratio, one underdamped path (solid line, $\zeta_\beta = 0.7$) and one overdamped path (dashed line, $\zeta_\beta = 1.3$) is shown. B: Outbound paths (black) and inbound paths (gray) for one stiffness ratio (1.5) but two ratios of input torque (1 and 1.5, the torque in flex-ext was 0.15 Nm in both cases). C: Using the parameters from B (stiffness ratio of 1.5, $\zeta_\beta = 0.7$), the model can recreate the petal-shaped paths in all four diagonal directions. See Table 5.1 for information about other model parameters.

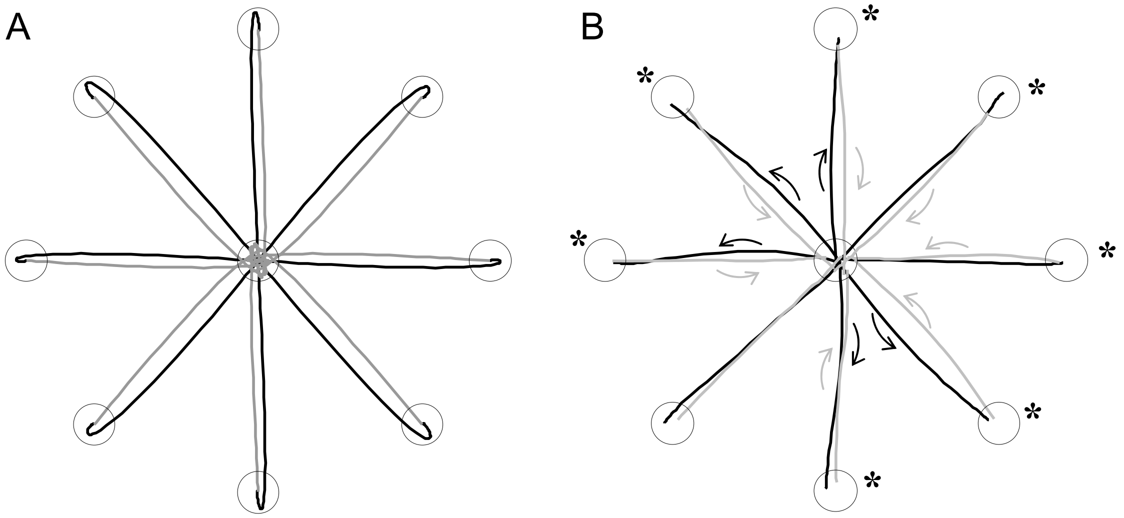

Figure 5.3: Comparison of simulated (A) and real (B) paths.
A: Simulated outbound (black) and inbound (gray) paths in a stiffness field which is anisotropic (principal stiffness ratio = 1.25) and pronated (by 15°). The damping ratio in flex-ext is 0.7. See Table 5.1 for information about other model parameters. B: Real outbound and inbound paths, averaged over all subjects. See caption of Figure 5.1 for an explanation of the arrows and asterisks.

Not only is stiffness capable of accounting for gross features of path curvature, but also for fine details. This fact is borne out especially well using data from Hoffman and Strick, whose subjects showed considerable overshoot (presumably because of the increased inertia of their wrist device). In Figure 5.4, mean paths from Hoffman and Strick's experiment are plotted next to a simulation. Note that in the simulation, stiffness is even capable of recreating the direction and shape of many of the hooks produced during overshoot.

While in these simulations the simulation parameters (principle stiffness ratio, stiffness rotation angle, damping ratio ζ) were chosen to make the simulation match the real data, the point is that a relatively simple model is capable of explaining the observed pattern. In addition, the simulation parameters are reasonable estimates of real values: the principle stiffness ratio and rotation angle are close to those measured experimentally (1.75 and 5°, respectively), and the greater inertia (0.0075 kgm^2) reflects the greater inertia present in Hoffman and Strick's setup.

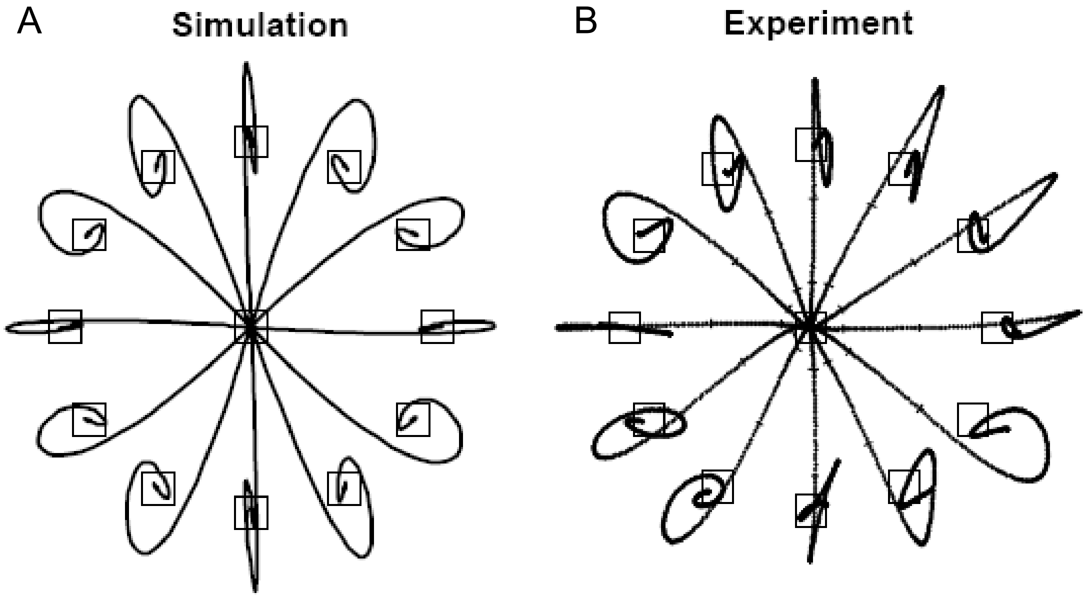

Figure 5.4: Comparison of simulated (A) and real (B) paths with significant overshoot.
A: The stiffness field has a principle stiffness ratio of 1.75 and is pronated by 5°. The damping ratio in flex-ext is 0.35. See Table 5.1 for information about other model parameters. B: Real outbound moves from an experiment by Hoffman and Strick (see [36] for details). The large amount of overshoot is supposedly due to the relatively large inertia of their wrist device.

5.4 Discussion

When humans rotate the wrist in combinations of flexion-extension and radial-ulnar deviation, the resulting paths (like those produced on a screen while using a laser pointer) exhibit a systematic pattern of curvature characterized by the five characteristics listed in the Introduction. The purpose of this chapter is to demonstrate that this pattern of curvature is likely caused by the stiffness of the wrist joint. To this end, a mathematical model of the wrist with accurate parameters was used to create simulations of wrist path which were compared to real paths.

Comparison of real and simulated data (see Figure 5.3 and Figure 5.4) reveals that this simple model is capable of explaining four of the five characteristics of path curvature. The anisotropic nature of wrist stiffness ($K_{\beta\beta} \neq K_{\gamma\gamma}$) produces paths which are curved, with outbound and inbound paths curving in opposite directions, and with moves in the same direction but to opposite targets curving to the same side (characteristics 1-3). Because stiffness is larger in rad-uln than in flex-ext ($K_{\gamma\gamma} > K_{\beta\beta}$), and because the principal stiffness axes are pronated (rotated clockwise) relative to the movement axes by less than 45°, the *direction* of the curvature (i.e. the side to which the path deviates) is the same in simulation and experiment. Wrist stiffness, which reflects the combined elastic properties of the muscles, ligaments, and carpal configuration, also rotates with changes in pro-sup[17]. Thus, wrist stiffness can explain why the pattern of curvature changes with pro-sup (characteristic 5).

5.4.1 Fast vs. slow movements

Only characteristic 4, which states that fast rotations show more curvature than slow moves, cannot be explained by wrist stiffness alone. At higher speeds, inertial and damping torques increase in relative importance. Inertia is roughly symmetric in the two DOF and would therefore not be expected to contribute much to impedance anisotropy.

---

[17] While the ligaments and carpal bones clearly rotate with the distal radio-ulnar joint (where pro-sup occurs), wrist muscles, whose proximal attachments are all at the elbow, have been shown to rotate in pro-sup by about half as much as the wrist joint (see [44] S. Kakei, D. S. Hoffman, and P. L. Strick, "Muscle and movement representations in the primary motor cortex," *Science*, vol. 285, pp. 2136-2139, 1999.).

As muscle contraction increases to achieve faster rotations, damping may increase. However, it is unclear whether (and how) the relationship of damping in the two DOF would change with increasing contraction. We have initial results suggesting that stiffness may increase with contraction more in rad-uln than in flex-ext (see Chapter 6), which would increase impedance anisotropy and therefore path curvature. Whatever the relationship in impedance between the two DOF, operating at one's speed limit tends to reveal one's biomechanical characteristics and limitations. The fact that curvature increases with speed lends credence to the idea that biomechanical factors contribute to curvature.

Alternatively, it is conceivable that a neural cause may underlie the increased curvature with movement speed. Perhaps there is limited time to straighten paths, for example through temporally shifted muscle activity (discussed next).

5.4.2 Temporally Shifted Muscle Activity

Hoffman and Strick have investigated patterns of muscle activity associated with wrist rotations in both DOF [36], for humans and monkeys. They found that humans made wrist movements by modulating muscle activity in either of two spatiotemporal patterns, termed amplitude-graded and temporally shifted.

Amplitude-graded muscle activity, which was found to be present in 80% of wrist movements, determines "movement direction [by adjusting] the amplitude, but not the timing, of agonist and antagonist bursts in multiple muscles at a single joint… The key feature of the amplitude graded pattern [is] the presence of two bursts of muscle activity: one during the agonist burst interval and one during the antagonist burst interval."

Temporally-shifted muscle activity is "characterized by a single burst of activity, the peak of which lagged that of a normal agonist burst but led that of a normal antagonist burst." Temporally-shifted muscle activity was found in ECRL, ECRB, and ECU (no consistent pattern was observed in FCR), but was only present in 20% of wrist movements, and only in directions which required some flexion. Importantly, the movement directions in which temporally shifted muscle activity was observed were approximately perpendicular to the pulling direction of the muscle. It is also important to note that while muscle activity which fit the authors' (relatively narrow) definition of "temporally shifted" occurred in directions perpendicular to the best agonist direction, there was actually a *gradual* temporal shift with movement direction, from best agonist to best antagonist direction.

Monkeys' wrist movements displayed amplitude-graded muscle activity but not temporally-shifted muscle activity. Their paths were found to be straight along the cardinal directions but dramatically curved along the diagonal directions. In contrast, humans' paths were much straighter, though they still showed a pattern of curvature which was less pronounced than, but consistent with, that of the monkeys.

Some have proposed that modification in the timing of muscle activation is the primary means by which the nervous system specifies movement direction [82-84]. In contrast, Hoffman and Strick hypothesized that "the temporally shifted pattern functions to reduce the amount of movement curvature that would occur with the contraction of particular combinations of agonist muscles." But how?

We present here a hypothesis of how temporally shifted muscle activity could act to reduce the amount of curvature, as well as evidence for and against this hypothesis. We hypothesize that temporally shifted muscle activity acts to keep the path from "slipping down" the stiffness gradient perpendicular to the movement direction. From the amplitude-graded muscle activity observed by Hoffman and Strick, agonist muscles fire during a relatively limited window in time, followed by an interim of little muscle activity (in the absence of temporally shifted muscle activity), after which antagonist muscles fire. During this interim, the hand travels a path governed by the dynamics of the wrist-hand-system (inertia, damping, stiffness) and the initial conditions (e.g. momentum) bestowed by the agonist activity.

In an anisotropic stiffness field, the path will curve, unless an appropriate force is applied perpendicular to the direction of travel and toward the higher stiffness to "keep the hand on track" toward the target. Such a force could be supplied by temporally shifted muscle activity, which Hoffman and Strick found to occur in muscles whose pulling direction was perpendicular to the movement direction.[18] The presence of this temporally shifted muscle activity would allow for much straighter paths: paths would no longer

---

[18] Close inspection of their paper shows that the best agonist direction of temporally shifted muscles may indeed pull toward the larger stiffness (see figures 2C, 3C, and 3F).

have to start out pointing off-target in order to end up on-target. Thus, the hypothesis that path curvature is caused by anisotropic stiffness also provides a reasonable mechanism by which temporally shifted muscle activity could serve to reduce path curvature, as hypothesized by Hoffman and Strick. That said, while we have shown that temporally shifted muscle activity could in theory reduce path curvature, there remain unanswered questions (see the notes at the end of this chapter), and more research is necessary to validate this hypothesis.

5.4.3 Other Candidate Causes of Path Curvature

A curved path is generated when there exists a difference (in some property or source) between movement directions, i.e. a spatial anisotropy. Possible causes of anisotropy may be grouped as geometric, mechanical, muscular, or neural.

Candidate geometric causes

The geometry of the wrist joint could cause path curvature. For example, if the wrist is modeled as a universal joint (with intersecting or non-intersecting axes), the resulting equations of motion are non-linear, as is the projection of wrist orientation onto a plane. Either of these non-linearities could potentially cause path curvature, but only for large wrist rotations; the effects of these non-linearities vanish for moderately-sized rotations. For example, the normalized error in path caused by approximating moderately-size wrist rotations by linearized equations of motion with no axis offset—as opposed to non-linear equations of motion with an offset of 4mm—is only 0.007 (see Chapter 4). In contrast, we have shown in Chapter 3 that *actual* moderately-sized wrist rotations do exhibit path curvature. In other words, the fact that *moderately-sized* rotations show curvature is significant because it immediately eliminates candidate geometric causes, which are associated with *large* rotations about multiple axes.

Candidate mechanical causes

Candidate mechanical causes include any phenomena which create an anisotropic impedance within the wrist. Wrist impedance, which quantifies the wrist's resistance to imposed motion, may be described by wrist stiffness, damping, and inertia (and possibly higher-order dynamic terms). Anisotropic impedance, therefore, could also be caused by differences in damping (of muscles and ligaments) or inertia (of the hand) between movement directions (in addition to stiffness). Thus, anisotropic damping or inertia could modify the pattern of path curvature created by the anisotropic stiffness.[19] Inertia, however, is remarkable isotropic; for the six subjects described in the Methods section, the mean ratio of the moment of inertia in rad-uln to that in flex-ext 1.12 (with a narrow range from 1.10 to 1.15). Even the largest inertial ratio (1.15) doesn't come close to changing the *pattern* of curvature, as shown in Figure 5.5A. Unfortunately, the ratio of damping between flex-ext and rad-uln is unknown. As described in the Methods section, the simulations in this chapter assumed equal damping parameters ($B_\gamma = B_\beta$). It would also be reasonable to assume that the damping parameter scales with stiffness, in which case stiffness anisotropy would be accompanied by an anisotropy in damping parameters. However, an anisotropy in damping parameter equal to the mean anisotropy in stiffness (1.5) is not enough to change the pattern of curvature along the diagonals, as shown in Figure 5.5B. Another reasonable assumption is that the damping ratios are equal in the two DOF ($\zeta_\gamma = \zeta_\beta$), as opposed to the damping parameters, but this assumption does not perturb the curvature pattern either (see Figure 5.5B).

Candidate muscular and neural causes

Candidate muscular causes include differences in the contraction force or contraction time of muscles that pull in different directions. But contraction forces, at least in steady-state, are completely constrained by the target position and the ratio of the steady-state impedance (i.e. stiffness) in the two DOF. That said, the relative timing of contraction forces could vary with direction. Such timing differences could result from differences in intrinsic muscle dynamics (muscular cause) or differences in the timing of neural impulses (neural cause). For example, if the muscles pulling in rad-uln acted more quickly than the muscles pulling in flex-ext, the resulting pattern of path curvature would roughly match that observed in experiments (see notes at the end of this chapter).

---

[19] Note that anisotropic inertia alone—in the absence of (isotropic or anisotropic) stiffness—cannot produce a curved path, at least not for small rotations. The same can be said for anisotropic damping in the absence of stiffness (unless the damping is non-linear and its rate of change is anisotropic).

There are at least three pieces of evidence against the hypothesis that differences in the timing of muscle activity are responsible for the observed pattern of path curvature. First, while Hoffman and Strick did observe temporally shifted muscle activity, it acted in the wrong direction. For example, for movements involving flexion and some radial deviation, which curve first toward radial deviation and then toward flexion, ECRL showed temporally shifted (i.e. delayed) muscle activity. Second, wrist muscles are very widely tuned and can therefore not be compartmentalized as flexors/extensors vs. radial/ulnar deviators. For example, ECRB acts as agonist for movements in pure extension as well as pure radial deviation. Likewise, ECU acts as agonist for movements in pure extension as well as pure ulnar deviation. Therefore, it is unlikely that muscles acting in rad-uln would be able to act more quickly than muscles acting in flex-ext (because for many directions they're the same muscles). Third, perhaps the strongest evidence comes from a study by Hoffman and Strick in which they recorded the path produced by individual stimulation of five wrist muscles [36]. Upon stimulating each muscle separately, the hand traced a path which was initially straight but which invariably ended up curving toward flexion or extension. In other words, while it is possible that the path curvature could be caused by differences in muscular or neural timing *between* muscles, stimulation of *individual* muscles alone produces marked path curvature which matches the experimental observation. This veering toward flexion or extension is easily explained by stiffness anisotropy: as the hand increases its deviation from neutral position, the stiffness gradient perpendicular to the movement direction will cause it to turn away from the stiffer direction (rad-uln) and toward the less stiff direction (flex-ext), which is the "path of least resistance."

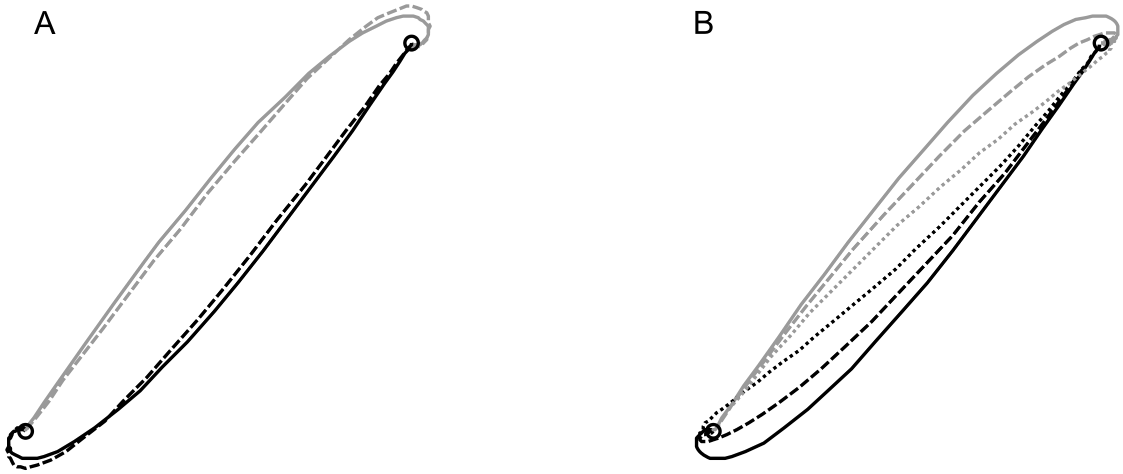

Figure 5.5: Effect of inertial anisotropy (A) and damping anisotropy (B) on path curvature. Outbound and inbound paths are drawn in black and gray, respectively. A: Paths simulated with isotropic inertia ($I_\gamma = I_\beta$, solid line) and anisotropic inertia ($I_\gamma = 1.15*I_\beta$, dashed line). B: Paths simulated with isotropic damping parameter ($B_\gamma = B_\beta$, solid line); isotropic damping ratio ($\zeta_\gamma = \zeta_\beta$, dashed line); and anisotropic damping parameter ($B_\gamma = 1.5*B_\beta$, dotted line), where the ratio of damping parameters is equal to the principal stiffness ratio. In both subplots, the stiffness field is anisotropic (principal stiffness ratio = 1.5) and tilted (15°).

5.4.4 Visual Feedback

One could argue that visual feedback may be the cause of (or a contributor to) path curvature. In our experiments, the pattern of path curvature was most prominent when movements were performed as fast as possible. Such movements were often composed of an initial, high-speed movement, which got the hand close to the target, followed by one or several lower-speed movements, which brought the hand to rest within the target boundary (Chapter 3). Importantly, the observed pattern of curvature stems from the initial, high-speed movements, not the lower-speed movements. Therefore, it is questionable if there's enough for visual feedback to play a role in path curvature; the entire movement duration (including high- and low-speed portions) was often less than 200 msec.

5.4.5 Pronation-supination

The pattern of path curvature was observed in subjects performing wrist rotations while pro-sup was constrained (Chapter 3). We felt a need to constrain pro-sup because there was clear evidence that humans involve pro-sup in pointing tasks even though the two DOF of the wrist (flex-ext and rad-uln) are perfectly sufficient. Why and how humans involve 3 DOF for a 2 DOF task is a fascinating research question. One hypothesis is that humans may modulate pro-sup to align the principle stiffness directions with the movement direction, thereby reducing curvature and the need for temporally shifted muscle activity. Alternatively, humans may modulate pro-sup in an effort to trace the "path of least resistance."

5.4.6 Limitations of this study

In searching for a wrist model, we deliberately balanced accuracy with simplicity. While our simple model allows insight into the dynamic properties of universal joints, it clearly does not imitate the wrist in all details. Nevertheless, in our judgment, the fact that a very simple, linear model can reproduce many details of the observed pattern speaks in favor of the model—and the hypothesis.

Another limitation of this study is that it treats muscles as force generators even though there is clear evidence that muscle activation is always accompanied by an increase in net stiffness. This impedance modulation can come from intrinsic muscle mechanics or local spinal reflex pathways. Because the hypothesis of this chapter rests on properties of wrist stiffness, neglecting active stiffness is potentially problematic. Unfortunately, direct measurement or estimation of stiffness during movement is notoriously difficult. However, measurements by Mussa-Ivaldi et al. of active and passive stiffness in reaching movements showed that while active contraction dramatically increases the overall amount of stiffness, the orientation and shape of the stiffness ellipse stay relatively constant [85]. Likewise, we have obtained an approximate estimate of (passive + active) wrist stiffness by measuring wrist stiffness while subjects co-contracted in an effort to maintain a constant grip force. These measurements showed that wrist stiffness is greater in rad-uln than in flex-ext, even during co-contraction (see Chapter 6).

5.4.7 Implications of this study

In Hoffman and Strick's experiment, monkeys and humans showed a similar pattern of path curvature, but the path curvature observed in humans was much less pronounced. Humans displayed temporally shifted muscle activity (delayed and roughly perpendicular to the movement direction), while monkeys did not. Hoffman and Strick hypothesized that the function of temporally shifted muscle activity was to reduce the amount of curvature produced in some directions. In this chapter, we have shown that path curvature is likely caused by stiffness anisotropy, and that temporally shifted muscle activity could indeed reduce path curvature by keeping the path from "slipping down" the stiffness gradient perpendicular to the movement direction. Because humans are not aware that their wrist paths are sometimes curved, this correction process can be assumed to be subconscious, like the process of correcting for interaction torques in the generation of straight reaching paths [86]. Importantly, this implies that movements are planned in terms of kinematics—not dynamics—and that humans care that their wrist paths be straight.

Notes

5.4.8 Linear Stiffness Field

A stiffness field can be linearized as follows (refer to Figure 5.6):

$$\vec{F} = F_x\hat{i} + F_y\hat{j}$$

$$F_x(x_0 + dx, y_0 + dy) = F_x(x_0, y_0) + \frac{\partial F_x}{\partial x}dx + \frac{\partial F_x}{\partial y}dy + H.O.T.$$

$$F_y(x_0 + dx, y_0 + dy) = F_y(x_0, y_0) + \frac{\partial F_y}{\partial x}dx + \frac{\partial F_y}{\partial y}dy + H.O.T.$$

$$\vec{F}(x_0 + dx, y_0 + dy) = F_x(x_0, y_0)\hat{i} + \frac{\partial F_x}{\partial x}dx\,\hat{i} + \frac{\partial F_x}{\partial y}dy\,\hat{i} + \ldots$$

$$\ldots + F_y(x_0, y_0)\hat{j} + \frac{\partial F_y}{\partial x}dx\,\hat{j} + \frac{\partial F_y}{\partial y}dy\,\hat{j} + H.O.T.$$

$$\vec{F}(x_0 + dx, y_0 + dy) = \begin{bmatrix} F_x(x_0, y_0) \\ F_y(x_0, y_0) \end{bmatrix} + \begin{bmatrix} \frac{\partial F_x}{\partial x} & \frac{\partial F_x}{\partial y} \\ \frac{\partial F_y}{\partial x} & \frac{\partial F_y}{\partial y} \end{bmatrix} \begin{bmatrix} dx \\ dy \end{bmatrix} + H.O.T.$$

$$\vec{F}(x_0 + dx, y_0 + dy) \approx \vec{F}(x_0, y_0) + Kd\vec{x}$$

$$\text{where } K = \begin{bmatrix} \frac{\partial F_x}{\partial x} & \frac{\partial F_x}{\partial y} \\ \frac{\partial F_y}{\partial x} & \frac{\partial F_y}{\partial y} \end{bmatrix} = \begin{bmatrix} K_{xx} & K_{xy} \\ K_{yx} & K_{yy} \end{bmatrix}$$

At point (x_0 + dx, y_0 + dy), the stiffness is given in the x-y-coordinate frame by the matrix K above.

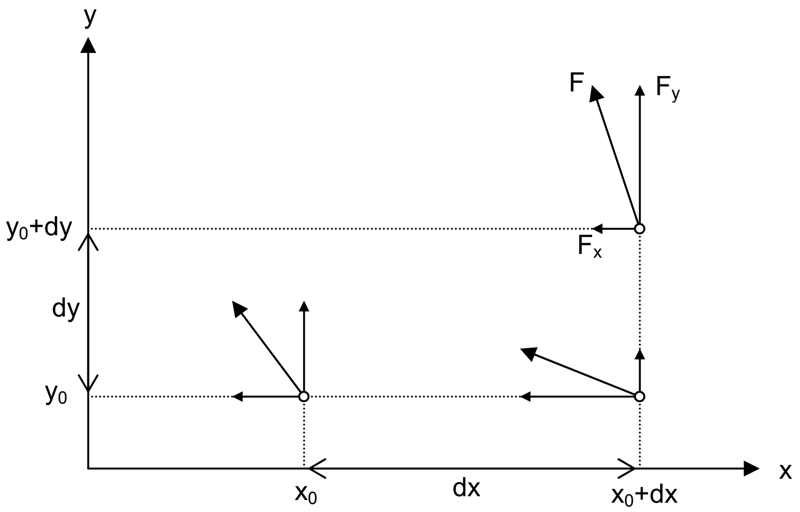

Figure 5.6: Schematic of stiffness field.

If the stiffness matrix is symmetric with real-valued eigenvectors, there exists a frame in which the stiffness matrix is diagonal, i.e. a frame in which the force on a point on an axis points along that axis. That axis is one of the eigenvectors of the stiffness matrix. The corresponding eigenvalue, λ, can be found from the relationship

$$\vec{F} = Kd\vec{x} = \lambda d\vec{x}$$
$$(K - \lambda I)d\vec{x} = 0$$

by noting that the determinant of K-λI must be zero. The eigenvectors, and hence the principle axes, can then be determined by row reduction.[20]

The angle of rotation between the axes of the coordinate frame and the principle axes is related to the stiffness matrix as follows (refer to Figure 5.7):

---

[20] An asymmetric matrix may have complex-valued eigenvectors. However, it may still be possible to identify principal directions by first decomposing into symmetric and antisymmetric matrices. The antisymmetric component is invariant under rotation. The symmetric component can be treated as described.

$$\vec{F}' = K'd\vec{x}' = K'Ad\vec{x}$$

$$\vec{F} = A^T\vec{F}' = A^T K'Ad\vec{x}$$

$$\Rightarrow K = A^T K'A$$

$$K = \begin{bmatrix} \cos\alpha & -\sin\alpha \\ \sin\alpha & \cos\alpha \end{bmatrix} \begin{bmatrix} K'_{xx} & 0 \\ 0 & K'_{yy} \end{bmatrix} \begin{bmatrix} \cos\alpha & \sin\alpha \\ -\sin\alpha & \cos\alpha \end{bmatrix}$$

$$K = \begin{bmatrix} K'_{xx}\cos^2\alpha + K'_{yy}\sin^2\alpha & \left(K'_{xx} - K'_{yy}\right)\sin\alpha\cos\alpha \\ \left(K'_{xx} - K'_{yy}\right)\sin\alpha\cos\alpha & K'_{xx}\sin^2\alpha + K'_{yy}\cos^2\alpha \end{bmatrix}$$

where K_{xx}' and K_{yy}' are the stiffness values in the principle directions.

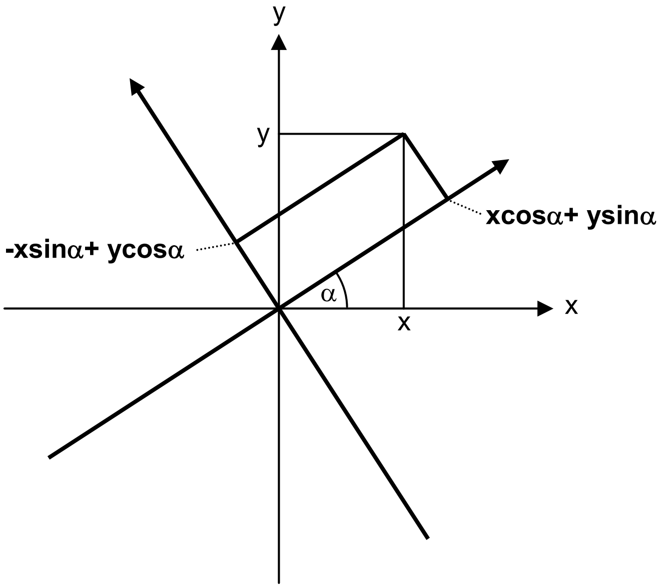

Figure 5.7: Schematic of the principle axes of the stiffness ellipse.

5.4.9 Temporally shifted muscle activity

Temporally shifted muscle activity was only seen in movements that required some flexion. If this type of muscle activity functions to straighten out paths, it stands to reason that it would be present in most or all movement directions other than along the principal stiffness axes (where the gradient is zero). In other words, movements requiring some flexion do not appear less curved than movements requiring some extension.

Why was temporally shifted muscle activity not observed in movements requiring some extension? Perhaps this is due to the uneven distribution of wrist muscles. When stimulated one at a time, ECRB and ECU pull almost totally toward radial and ulnar deviation, respectively[21], and yet they are the muscles closest to extension and are therefore the prime agonists for almost all of extension (from radial to ulnar deviation). However, over a non-negligible portion of this range, these two muscles are closer to perpendicular than to parallel. In other words, according to this hypothesis, over much of extension, ECRB and ECU would have to act both as agonist and perpendicularly (to keep the path from slipping down the stiffness gradient). In some directions, ECRB and ECU would also have to act as antagonist! For example, for a movement 15° off of pure extension (toward ulnar deviation), ECRB acts as a mild agonist and antagonist, and yet is almost perfectly perpendicular.[22] It is possible that the task of acting as agonist (or agonist and antagonist) limits a muscle's ability to also act in a temporally shifted manner. In contrast, ECRB and ECU (and ECRL) do show temporally shifted muscle activity in flexion, where FCR can provide most of the agonist activity.

Finally, if temporally shifted muscle activity does function to reduce path curvature, it is still unclear what purpose would be served by *gradually* shifting muscle activity in time (as opposed to simply placing all temporally shifted muscle activity halfway between agonists and antagonists).

---

[21] As measured by Hoffman and Strick in three monkeys, the pulling direction of ECRB is off of pure radial deviation by only 13 ± 4.5°, and ECU is off of pure ulnar deviation by only 10 ± 1.8° (both toward extension).

[22] This may be the cause of the double bursts mentioned in the paper by Hoffman and Strick.

6 Effect of Active Wrist Stiffness on Wrist Rotations

6.1 Introduction

Wrist rotations exhibit an intriguing pattern of path curvature (Chapter 3). We have previously shown that this pattern is most likely caused by wrist stiffness (Chapter 5). However, in that chapter, we used measurements of passive stiffness to estimate the effect of stiffness on path, even though there is clear evidence that stiffness increases during movement due to contraction. The purpose of this chapter is to estimate the effect of the total stiffness—passive *and* active—on path.

Paths are curved when one degree of freedom (DOF) responds more quickly than the other(s). We present a mathematical model of the relationship between stiffness and path curvature, first for passive stiffness and then for total stiffness. In particular, the model shows how active muscle contraction can modulate the system's impedance and thereby affect path curvature. Finally, we present a measurement of total (passive + active) wrist stiffness during co-contraction as an estimate of total wrist stiffness during movement, and discuss implications for path curvature.

6.1.1 Path Curvature and Passive Wrist Impedance

It is very useful to view path curvature in terms of time constant anisotropy, a situation in which one DOF has a quicker response than the other. From the equations of motion, we can determine which DOF has the quicker response. For wrist rotations within ±15°, wrist dynamics can be approximated by a set of linear, uncoupled equations of motion (see Chapter 4):

$$I_\beta \ddot{\beta} + B_\beta \dot{\beta} + K_\beta \beta = M_\beta$$
$$I_\gamma \ddot{\gamma} + B_\gamma \dot{\gamma} + K_\gamma \gamma = M_\gamma$$

where β and γ represent flex-ext and rad-uln, respectively. Parameters I_i, B_i, and K_i ($i = \beta, \gamma$) represent the inertia, damping, and stiffness of the *passive* wrist. M_i is the joint torque produced by (active) muscle contraction, which we model—for now—as pure force generation. In each DOF, the transfer function has the form

$$\frac{1/I_i}{s^2+\frac{B_i}{I_i}s+\frac{K_i}{I_i}}$$

If the system is underdamped, its poles in each DOF are complex at

$$-\sigma_i=-\frac{B_i}{2I_i}\pm j\sqrt{\frac{K_i}{I_i}-\left(\frac{B_i}{2I_i}\right)^2}=-\sigma_{d,i}\pm j\omega_{d,i}$$

where i = β, γ. Its natural response has the form $Ce^{-\sigma_d t}\cos(\omega_d t-\phi)$, where C is a constant. Although the concept of time constant is not defined for an underdamped second order system, the speed at which the system responds can be expressed as peak time, $T_p = \pi/\omega_d$. Time constant anisotropy can be expressed as the ratio of peak times:

$$\frac{T_{p,\beta}}{T_{p,\gamma}}=\frac{\omega_{d,\gamma}}{\omega_{d,\beta}}=\frac{\sqrt{\frac{K_\gamma}{I_\gamma}-\left(\frac{B_\gamma}{2I_\gamma}\right)^2}}{\sqrt{\frac{K_\beta}{I_\beta}-\left(\frac{B_\beta}{2I_\beta}\right)^2}}=\sqrt{\frac{K_\gamma I_\beta}{K_\beta I_\gamma}\cdot\left(\frac{1-\zeta_\gamma^{\,2}}{1-\zeta_\beta^{\,2}}\right)}$$

where $\zeta_i=\frac{B_i}{2\sqrt{K_iI_i}}$ (i = β, γ).

The path will curve into the DOF with the smaller response time.[23] For the path to curve into rad-uln, as observed, the ratio of peak times must be greater than unity. To evaluate the ratio of peak times, we need the ratios of stiffness, inertia, and $1-\zeta^2$ in the two DOF.

---

[23] Time constants and peak times characterize response quickness relative to the final displacement (e.g. the response reaches 63% of its final value within one time constant). While the ratio of time constants in the two DOF provides a ratio of response quickness, it does not fully determine the side to which the path veers because it does not specify *absolute* displacements. However, if the final displacements are equal, the ratio of the relative responses is equal to the ratio of the absolute responses—as long as the inputs to the two DOF are scaled versions of each other (equal final displacements in two DOF with unequal stiffnesses requires unequal inputs, but they can have the same shape). Note that so far there have been no other assumptions about the shape of the inputs.

Passive Wrist Parameters

The moments of inertia in flex-ext and rad-uln are known to be very similar. For example, for the six subjects who participated in the experiment described in Chapter 5, the inertia of the hand in rad-uln, I_γ, was always just slightly larger than the inertia in flex-ext (mean ratio = 1.12, range from 1.10 to 1.15). In this chapter, we use the approximation $I_\gamma/I_\beta = 1$.

It is known that passive wrist stiffness is anisotropic, with stiffness being greater in rad-uln than in flex-ext [80]. The ratio of stiffness along the principal axes was measured to be, on average, 1.58 ± 0.385 (range from 1.14 to 2.43). In other words, for all ten subjects, stiffness in rad-uln was larger than in flex-ext. Let λ be defined as K_γ/K_β with $\lambda > 1$.

To the best of our understanding, passive damping has not been characterized for the wrist. We have found one paper tangentially reporting a measurement of damping, but only in flex-ext [14]. We present here three specific cases of damping: isotropic damping ($B_\gamma/B_\beta = 1$), isotropic damping ratio ($\zeta_\gamma/\zeta_\beta = 1$), and anisotropic damping with the same ratio as stiffness ($B_\gamma/B_\beta = K_\gamma/K_\beta = \lambda$):

	Independent Variables			Dependent Variables	
	Stiffness	Inertia	Damping	Damping Ratio	Ratio of Peak Times
Case 1	$K_\gamma = \lambda K_\beta$	$I_\gamma = I_\beta$	$B_\gamma = B_\beta$	$\zeta_\gamma = \frac{1}{\sqrt{\lambda}}\zeta_\beta$	$\frac{T_{p,\beta}}{T_{p,\gamma}} = \frac{\sqrt{\lambda - \zeta_\beta^2}}{\sqrt{1-\zeta_\beta^2}} \geq 1$
Case 2			$B_\gamma = \sqrt{\lambda} B_\beta$	$\zeta_\gamma = \zeta_\beta$	$\frac{T_{p,\beta}}{T_{p,\gamma}} = \sqrt{\lambda} \geq 1$
Case 3			$B_\gamma = \lambda B_\beta$	$\zeta_\gamma = \sqrt{\lambda}\zeta_\beta$	$\frac{T_{p,\beta}}{T_{p,\gamma}} = \sqrt{\lambda}\frac{\sqrt{1-\lambda\zeta_\beta^2}}{\sqrt{1-\zeta_\beta^2}}$

Table 6.1: Ratio of peak times for various damping conditions.

In cases 1 and 2, the ratio of peak times is always equal to or greater than 1. In case 3, however, the ratio of time constants is multiplied by the square root of λ, but reduced by subtraction of $\lambda\zeta_1^2$ within the square root of the nominator. The net effect of λ on the ratio depends on ζ_1 (and on ζ_2 because $\zeta_2 = \sqrt{\lambda}\zeta_1$). At low values of ζ_1, the ratio is greater than 1, while at high values of ζ_1, the ratio is less than 1, as shown in Figure 6.1.

In summary, if an underdamped second order system has two DOF with equal damping or equal damping ratios, then the DOF with the larger stiffness will have the quicker response (given equal inertias and inputs). If one DOF has larger stiffness *and* damping, that DOF will have a quicker response as long as its damping ratio is relatively low (<~0.5). If its damping ratio is relatively high (>~0.5), it may have a slower response.

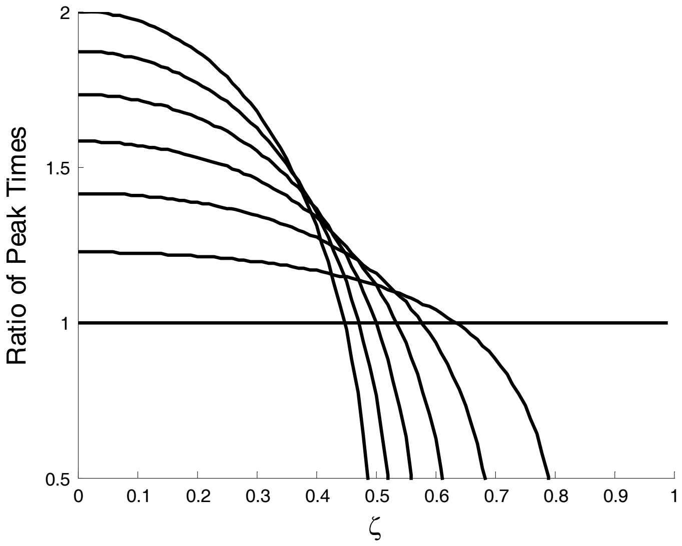

Figure 6.1: Ratio of peak times as a function of ζ and λ for case #3.
Each curve corresponds to a different value of λ. The intersection of each curve with the ordinate is equal to the square root of λ for that curve.

6.1.2 Path Curvature and Active Wrist Impedance

The effect of active muscle contraction on path curvature can be investigated in a similar manner, by investigating the relationship between physical system parameters and the speed of response in each DOF. The main difference in considering active muscle contraction is that it can alter the system's physical parameters (stiffness and damping). To assess this effect, we include in the equations of motion of the wrist a model of muscle capable of impedance modulation. The derivation of this muscle model is borrowed from [87].

Muscle Model

The torque inputs to the equations of motion result from muscle force generated by *active* muscle contraction. Such active muscle force is a function of (at least) muscle displacement, x, the rate of displacement, v, and neural activation, u. This function can be expressed as a Taylor series expansion:

$$\begin{aligned} F = F_0 &+ \frac{\partial F}{\partial x}dx + \frac{\partial F}{\partial v}dv + \frac{\partial F}{\partial u}du + \frac{1}{2}\frac{\partial^2 F}{\partial x^2}dx^2 + \frac{1}{2}\frac{\partial^2 F}{\partial v^2}dv^2 + \frac{1}{2}\frac{\partial^2 F}{\partial u^2}du^2 + \ldots \\ &\ldots + \frac{\partial^2 F}{\partial x \partial u}dxdu + \frac{\partial^2 F}{\partial v \partial u}dvdu + \frac{\partial^2 F}{\partial x \partial v}dxdv + \text{higher order terms} \end{aligned}$$

where F_0 and all partial derivatives are evaluated at (x_0, v_0, u_0). While inputs generating pure force cannot change the system's response time (which depends only on the transfer function), inputs which modify stiffness and/or damping to the system can change response time because they change the system's transfer function. It is therefore important to retain in the Taylor series (at least) those second-order components which are proportional to stiffness/damping and neural activation. Linearizing about $(x_0, v_0, u_0) = (0, 0, 0)$, and assuming that $F_0 = F(0, 0, 0) = 0$, the truncated function becomes:

$$\begin{aligned} F &\approx \frac{\partial F}{\partial x}x + \frac{\partial F}{\partial v}v + \frac{\partial F}{\partial u}u + \frac{\partial^2 F}{\partial x \partial u}ux + \frac{\partial^2 F}{\partial v \partial u}uv \\ &\approx k'x + b'v + c'u + d'ux + e'uv \\ &\approx (k' + d'u)x + (b' + e'u)v + c'u \end{aligned}$$

where k', b', c', d', and e' denote properties of *active* muscle (the *passive* properties of muscle are already accounted for on the left side of the equations of motion).[24]

Both agonist and antagonist muscle activity contribute to the net joint torque. Defining θ as a generic angle representing β or γ, the total joint torque in θ becomes (see Figure 6.2):

---

[24] All values of F are contained in planes above the x-v-plane, with slope depending on u. All planes intersect at a common line. The projection of this line onto the x-v-plane is given by $v = -(d'/e')x - c'/e'$. The value of F along this line is $F = (k' - b'd'/e')x - b'c'/e'$.

$$
\begin{aligned}
M &\approx \left(r_{ag}c'_{ag}u_{ag} - r_{an}c'_{an}u_{an}\right) - \left[r_{ag}{}^{2}\left(k'_{ag} + d'_{ag}u_{ag}\right) + r_{an}{}^{2}\left(k'_{an} + d'_{an}u_{an}\right)\right]\theta - \left[r_{ag}{}^{2}\left(b'_{ag} + e'_{ag}u_{ag}\right) + r_{ag}{}^{2}\left(b'_{ag} + e'_{ag}u_{ag}\right)\right]\dot{\theta} \\
&\approx \left(C'_{ag}u_{ag} - C'_{an}u_{an}\right) - \left(K'_{ag} + D'_{ag}u_{ag} + K'_{an} + D'_{an}u_{an}\right)\theta - \left(B'_{ag} + E'_{ag}u_{ag} + B'_{an} + E'_{an}u_{an}\right)\dot{\theta}
\end{aligned}
$$

where ‘ag’ and ‘an’ denote agonist and antagonist, respectively, r is moment arm, τ is an externally applied torque, and lower and upper case letters represent corresponding parameters in muscle and joint space, respectively.

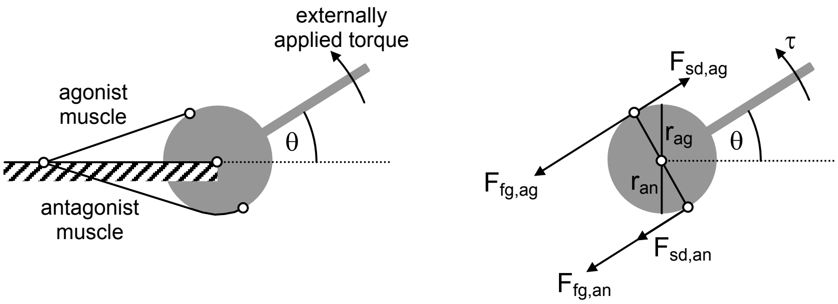

Figure 6.2: Relationship between active muscle force and torque.
ag = agonist, an = antagonist, fg = force generation, sd = stiffness and damping.

Plugging M into the equations of motion and rearranging yields:

$$I\ddot{\theta} + \left(B + B'_{ag} + B'_{an} + E'_{ag}u_{ag} + E'_{an}u_{an}\right)\dot{\theta} + \left(K + K'_{ag} + K'_{an} + D'_{ag}u_{ag} + D'_{an}u_{an}\right)\theta = C'_{ag}u_{ag} - C'_{an}u_{an}$$

What are the values of K’$_{ag}$, K’$_{an}$, B’$_{ag}$, and B’$_{an}$? In the absence of neural activity (u = 0), the system should be reduced to its passive state, forcing K’$_{ag}$, K’$_{an}$, B’$_{ag}$, and B’$_{an}$ to be zero. Therefore, the equation of motion in each DOF becomes

$$I\ddot{\theta} + \left(B + E'_{ag}u_{ag} + E'_{an}u_{an}\right)\dot{\theta} + \left(K + D'_{ag}u_{ag} + D'_{an}u_{an}\right)\theta = C'_{ag}u_{ag} - C'_{an}u_{an}$$

B and K are the damping and stiffness of passive muscle, respectively. E’ and D’ are the rates of change of muscle damping and stiffness with neural activation, respectively. By this muscle model, one can see that (active) muscle contraction adds to the passive stiffness and damping. Importantly, the total stiffness and damping of the system now depend on u, thus modeling impedance modulation. C’ is the rate of change of pure muscle torque with neural activation. Note that when C’$_{ag}$u$_{ag}$ = C’$_{an}$u$_{an}$, this model produces co-contraction with an increase in damping and stiffness, but with no displacement. Also, by this model it is possible to increase stiffness perpendicular to movement (through co-contraction in that DOF) without causing movement in that DOF.

The quickness of the natural response in each DOF is now a function of I, B+E$_{ag}$'u$_{ag}$+E$_{an}$'u$_{an}$, and K+D$_{ag}$'u$_{ag}$+D$_{an}$'u$_{an}$ instead of I, B, and K:

$$\frac{T_{p,\beta}}{T_{p,\gamma}} = \frac{\omega_{d,\gamma}}{\omega_{d,\beta}} = \frac{\sqrt{\frac{\left(K + D'_{ag}u_{ag} + D'_{an}u_{an}\right)_{\gamma}}{I_{\gamma}} - \left[\frac{\left(B + E'_{ag}u_{ag} + E'_{an}u_{an}\right)_{\gamma}}{2I_{\gamma}}\right]^2}}{\sqrt{\frac{\left(K + D'_{ag}u_{ag} + D'_{an}u_{an}\right)_{\beta}}{I_{\beta}} - \left[\frac{\left(B + E'_{ag}u_{ag} + E'_{an}u_{an}\right)_{\beta}}{2I_{\beta}}\right]^2}}$$

$$= \sqrt{\frac{\left(K + D'_{ag}u_{ag} + D'_{an}u_{an}\right)_{\gamma} I_{\beta}}{\left(K + D'_{ag}u_{ag} + D'_{an}u_{an}\right)_{\beta} I_{\gamma}}} \cdot \frac{\sqrt{1-\zeta_{\gamma}^{2}}}{\sqrt{1-\zeta_{\beta}^{2}}}$$

The path will curve into the DOF with the smaller response time. For the path to curve into rad-uln, as observed, the ratio of peak times must be greater than unity. As above, to evaluate the ratio of peak times, we need the ratios of total stiffness, inertia, and 1-ζ^2 in the two DOF. The ratio of inertia is close to unity. The rest of this chapter describes the estimation of the ratio of total wrist stiffness, λ_t, which we found to be greater in rad-uln than in flex-ext. Active damping during wrist rotations, like passive damping, is unknown. However, as above, one can show that if $\lambda_t > 1$, the ratio of peak times will be greater than unity if the ratio of total wrist damping is less than λ_t. If the ratio of total wrist damping is equal to λ_t, the ratio of peak times is still greater than unity as long as the damping ratio in rad-uln is less than approximately 0.5. The ratio of total stiffness, λ_t, was estimated as follows.

Stiffness Ratio

Because the steady-state displacements in the two DOF are equal, one can obtain a relation between the ratios of stiffness and input torque:

$$\frac{\left(K + D'_{ag}u_{ag} + D'_{an}u_{an}\right)_{\beta}}{\left(K + D'_{ag}u_{ag} + D'_{an}u_{an}\right)_{\gamma}} = \frac{\left(C'_{ag}u_{ag} - C'_{an}u_{an}\right)_{\beta}}{\left(C'_{ag}u_{ag} - C'_{an}u_{an}\right)_{\gamma}}$$

One might be tempted to use this relation to determine the stiffness ratio. Unfortunately, the ratio of inputs is also unknown.

Instead, measurements of the stiffness ratio during co-contraction can serve as an approximation, as follows. The general equation of motion in each DOF is:

$$I\ddot{\theta}+\left(B+E'_{ag}u_{ag}+E'_{an}u_{an}\right)\dot{\theta}+\left(K+D'_{ag}u_{ag}+D'_{an}u_{an}\right)\theta=C'_{ag}u_{ag}-C'_{an}u_{an}+\tau$$

where τ is a torque applied to the hand (about the wrist joint) by the robot. During co-contraction (cc), $C_{ag}'u_{ag} - C_{an}'u_{an} = 0$. Presumably this relationship remains true throughout the measurement, so that for the duration of the measurement

$$I\ddot{\theta}+\left(B+E'_{ag}u_{ag,cc}+E'_{an}u_{an,cc}\right)\dot{\theta}+\left(K+D'_{ag}u_{ag,cc}+D'_{an}u_{an,cc}\right)\theta=\tau$$

Because the stiffness measurement is slow, $\ddot{\theta}\approx\dot{\theta}\approx 0$, allowing one to compute co-contraction stiffness in each DOF as

$$\frac{\partial\tau}{\partial\theta}=K+D'_{ag}u_{ag,cc}+D'_{an}u_{an,cc}$$

As explained, this provides a measure of total (passive + active) stiffness during co-contraction, which is clearly not the same as the total stiffness during movement. However, because co-contraction and movements to diagonal targets are both symmetric activities, the ratio of stiffness values during co-contraction can serve as an estimate of the ratio of stiffness values during movement:

$$\frac{\left(K+D'_{ag}u_{ag}+D'_{an}u_{an}\right)_{\beta}}{\left(K+D'_{ag}u_{ag}+D'_{an}u_{an}\right)_{\gamma}}\approx\frac{\left(K+D'_{ag}u_{ag,cc}+D'_{an}u_{an,cc}\right)_{\beta}}{\left(K+D'_{ag}u_{ag,cc}+D'_{an}u_{an,cc}\right)_{\gamma}}$$

In summary, the contribution of active muscle contraction to path curvature can be understood in the context of impedance. Anisotropic impedance, such as the anisotropy in *passive* wrist stiffness discussed in Chapter 5, can result in path curvature. The effect of *active* muscle contraction on impedance is to add to the system's passive stiffness and damping, thereby modulating the impedance. Therefore, active muscle contraction will have the same effect on path curvature as passive wrist stiffness unless it modulates the impedance in such a way as to remove or reverse the impedance anisotropy. This chapter describes the measurement of total (passive + active) wrist stiffness and concludes that active muscle contraction (during co-contraction) contributes to the stiffness anisotropy in such a way as to enable or even enhance the pattern of path curvature observed in human wrist rotations.

6.2 Methods

6.2.1 Subjects

Seven human subjects (5 male, 2 female, age 30 ± 6 years (mean ± std)) were recruited for this experiment. Following procedures approved by MIT's Committee on the Use of Humans as Experimental Subjects, informed consent was obtained from all subjects.

6.2.2 Wrist Constraint

Subjects' metacarpals were sandwiched between two plates, connecting their hand to the end-effecter of the wrist robot (see first and second photos in Figure 6.3). A Velcro strap pressed the thenar muscle mass against the dorsal plate (see third photo in Figure 6.3), constraining the distal forearm in pro-sup. The distal forearm was also constrained against translation relative to the robot by a Velcro strap which passed under two bars constrained to the robot table (see last photo in Figure 6.3).[25]

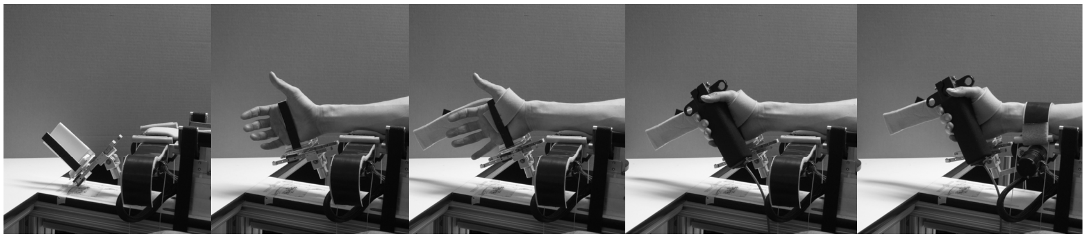

Figure 6.3: Series of photos documenting the setup procedure.

In this experiment, subjects' metacarpals were sandwiched between two plates, connecting their hand to the end effecter of the wrist robot. A Velcro strap pressed the thenar muscle mass against the dorsal plate, loading it in slight supination. The force transducer was placed in the palm and grasped

---

[25] The stiffness of this distal forearm constraint acts in series with the stiffness of the wrist. It is therefore important to design the constraint to have a much higher stiffness than the wrist joint.

by subjects' fingers. Finally, a strap placed around the forearm just proximal to the wrist constrained the forearm to the wrist robot.

6.2.3 *Wrist robot and grasp force sensor*

Subjects' fingers were free to wrap around a force transducer (see fourth photo in Figure 6.3), the output of which was magnified and filtered on a breadboard, read into the computer, and digitally filtered. During stiffness measurement (using the same protocol as in [80]), subjects were asked to maintain one of three levels of grasp force, corresponding to 0, 5.55, and 11.1 N of grasp force. To put these grasp force levels into context, the maximum contraction force of one subject was measured. These three force levels corresponded to 0, 2.8% and 5.6% of his maximum contraction force, respectively. While these percentages may seem low, they were sustainable over the 3 minutes and 36 seconds of the experiment (in contrast, maximum contraction degraded rapidly, falling to 60% of its value within 27 sec, as shown in Figure 6.4). More importantly, these force levels are of the same order of magnitude as those required to make moderately-sized wrist rotations.[26]

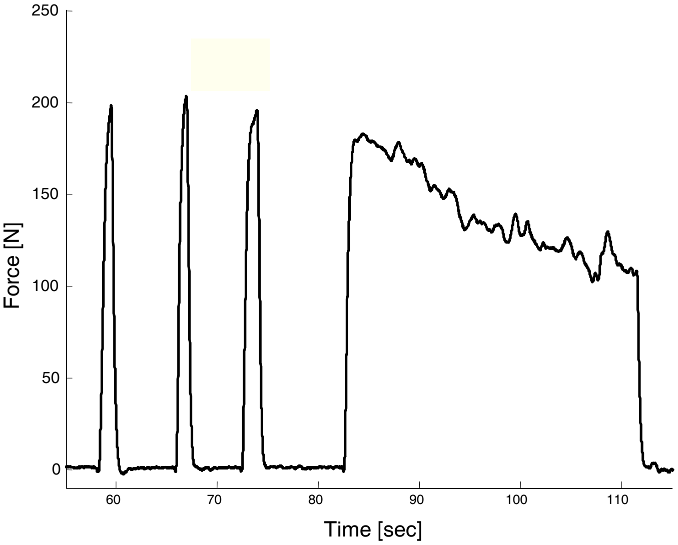

Figure 6.4: Maximum grasp force vs. time.

---

[26] To overcome the passive stiffness of the wrist (which dominates over inertial effects, as shown in Chapter 4), 0.31 and 0.47 Nm of torque are required for 15°-rotations in flex-ext and rad-uln, respectively. Assuming moment arms of 2 and 3cm, respectively, the required force is 16 N (for movements in either DOF).

Three short, maximum-contraction bursts, followed by a prolonged maximum contraction, for one subject.

6.2.4 Neutral Position

Flex-ext and Rad-uln

The neutral wrist orientation used in this experiment was different from that used in [80], as shown in Figure 6.5. In particular, care was taken to start the measurement for each subject at his or her own neutral position (where his/her forearm and third metacarpal were aligned).

Pro-sup

In this experiment, the device that holds the hand in place supinates the distal forearm by about 15° relative to the position of the distal forearm in [80]. A Velcro strap pressed the thenar muscle mass against the dorsal plate (see middle photo in Figure 6.3), loading it in slight supination.

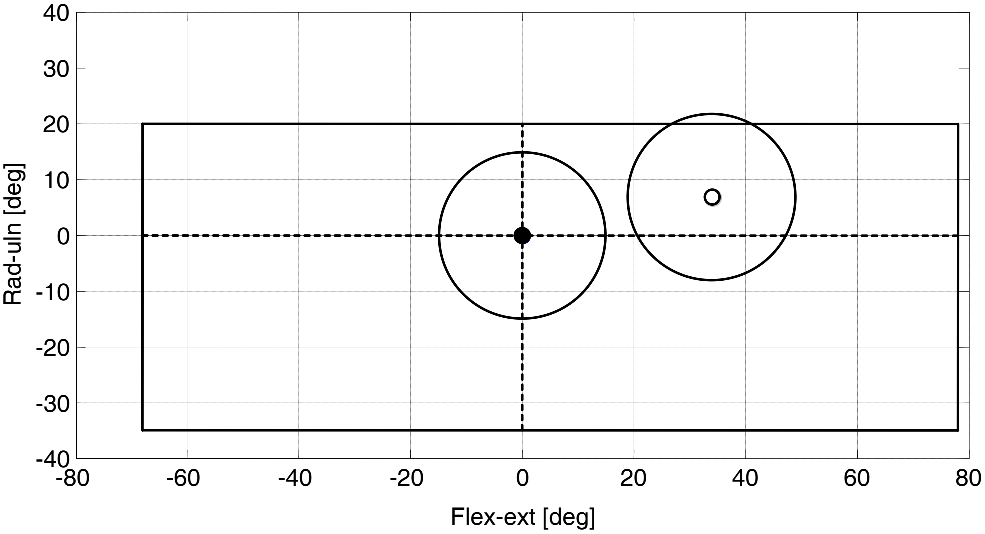

Figure 6.5: Different definitions of "neutral wrist orientation."
The definitions differed between this experiment (filled dot) and the stiffness measurements by Formica et al. (empty dot). The circles represent the approximate commanded displacement. The thick rectangle outlines the approximate biomechanical limits in flex-ext and rad-uln.

6.2.5 Protocol

The robot software used in this experiment is identical to the 2-D protocol used in [80] with one exception: a “stay” period of 3 seconds was inserted between outbound and inbound moves, forcing the wrist to remain at the final position of the outbound move for 3 seconds before initiating the inbound move. All other parameters were identical; summarizing briefly, for outbound movements (to 24 equally-spaced targets) the desired robot location increased at constant velocity over 3 seconds from 0 to 0.3 rad in each direction, sampled at 200 Hz for a total of 600 samples per movement. For inbound movements, the process was reversed. While there was a “stay” period at the periphery, there was no such waiting period at the center. The motor torque pushing against wrist stiffness was controlled by a proportional controller, $\tau = K_r(\theta_r - \theta)$, where θ_r is the reference position and K_r is the proportional gain (set at 10 Nm/rad).

6.2.6 Data Analysis

For each of the 24 movement directions, stiffness was computed as the slope of the linear regression between torque and displacement, resulting in 24 stiffness values. Appendix E gives a detailed analysis of the relationship between robot generalized coordinates/forces and wrist generalized coordinates/forces, showing that wrist stiffness is indeed equal to the slope of robot torque vs. robot displacement.

The goal of this chapter is to determine the effect of active stiffness on path. For simplicity, we focused on the effect of active stiffness (measured in 24 directions) on the path of movements *in the diagonal directions only*. For each diagonal direction, path curvature is hypothesized to result from an anisotropy in stiffness in the neighboring directions. Therefore, for each diagonal movement direction, the stiffness estimates in the three adjacent rad-uln directions were averaged and compared to the mean stiffness estimates in the three adjacent flex-ext directions, as shown in Figure 6.6.

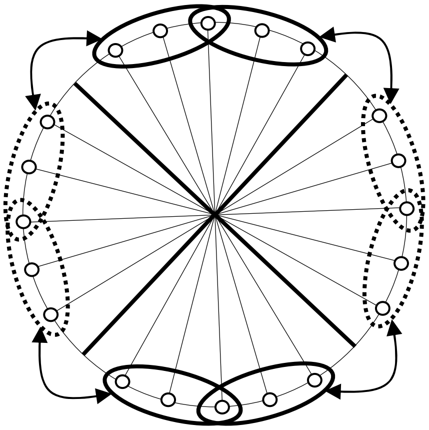

Figure 6.6: Path curvature in a given direction is influenced by stiffness in adjacent directions. For each diagonal movement direction (thick, straight lines), the stiffness estimates in the three adjacent rad-uln directions (solid ellipses) were averaged and compared to the mean stiffness estimates in the three adjacent flex-ext directions (dotted ellipses).

6.3 Results

The grasp force at each force level is shown in Figure 6.7 for all seven subjects. For subject 6, wrist stiffness was only measured at the lowest and intermediate force levels. Stiffness was then computed at each grasp force level for each subject, as shown in Figure 6.8.

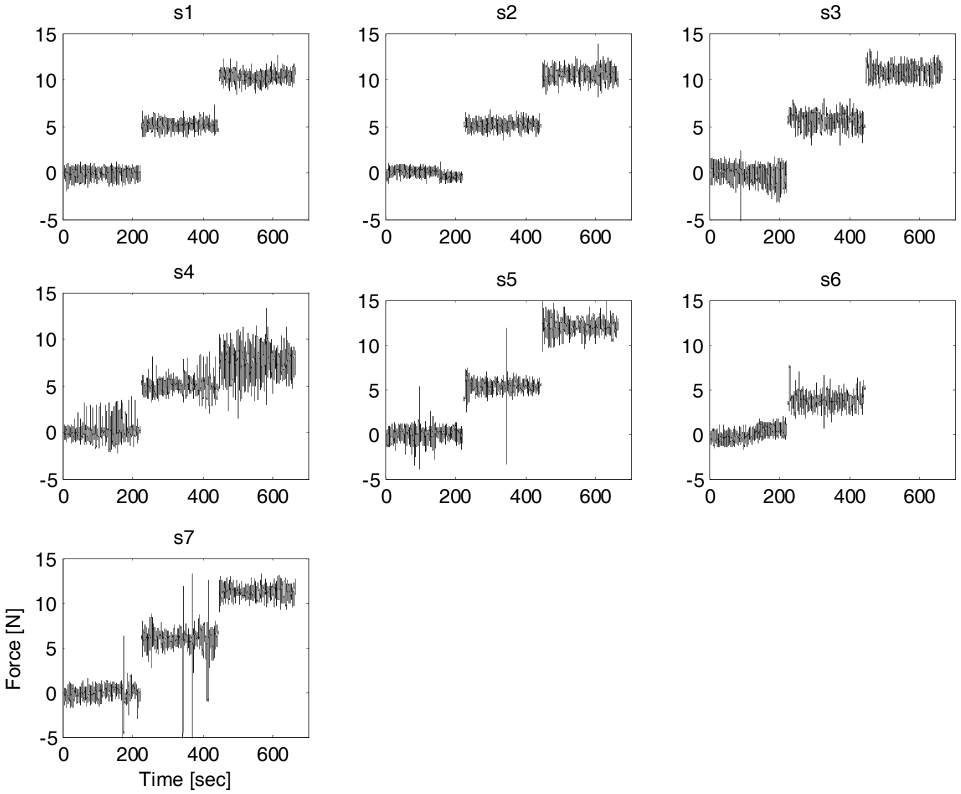

Figure 6.7: Grasp force vs. time for each of three grasp force levels.

Each subplot is for a different subject. Pauses in the experiment between force levels were removed.

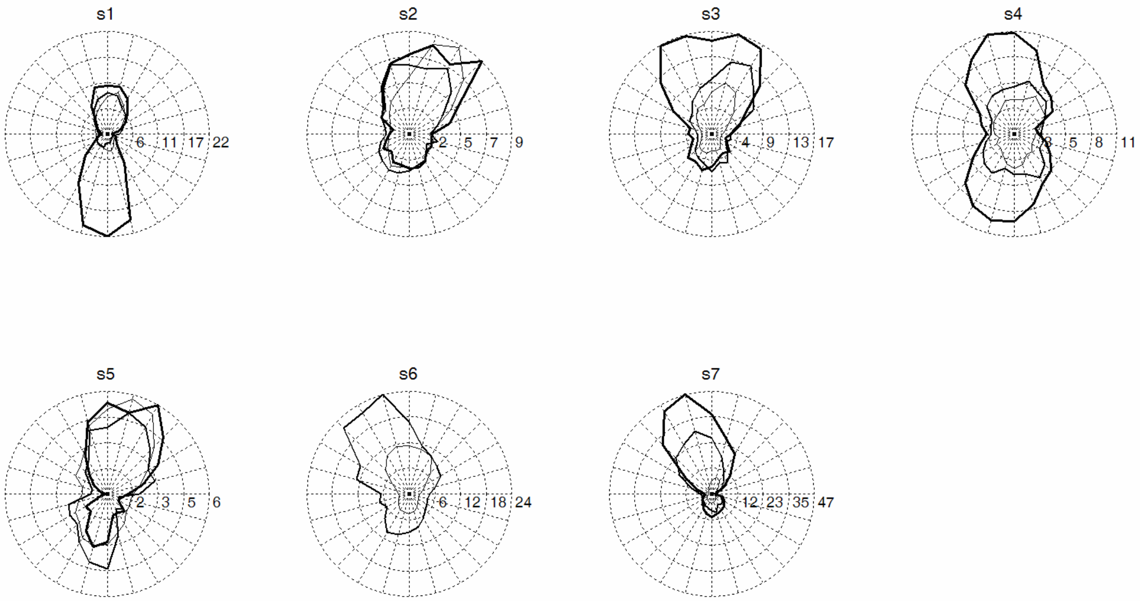

Figure 6.8: Polar plots of stiffness for various grasp force levels.

The low, intermediate, and high force levels are plotted as thin, intermediate, and thick lines, respectively. Each subplot is for a different subject. In each of 24 directions, stiffness is indicated as distance from the origin (in Nm/rad).

For each diagonal movement direction, the mean of the stiffness values in the three adjacent rad-uln directions was compared to the mean of the stiffness values in the three adjacent flex-ext directions (see Figure 6.6). This comparison is shown in Figure 6.9 for each grasp force level, each diagonal direction, and each subject. In every case (every diagonal direction, grasp force level, and subject), the mean stiffness in radial or ulnar deviation is larger than the mean stiffness in flexion or extension. This inequality is significant for all but 5 of the 80 conditions ($p \leq 0.05$)!

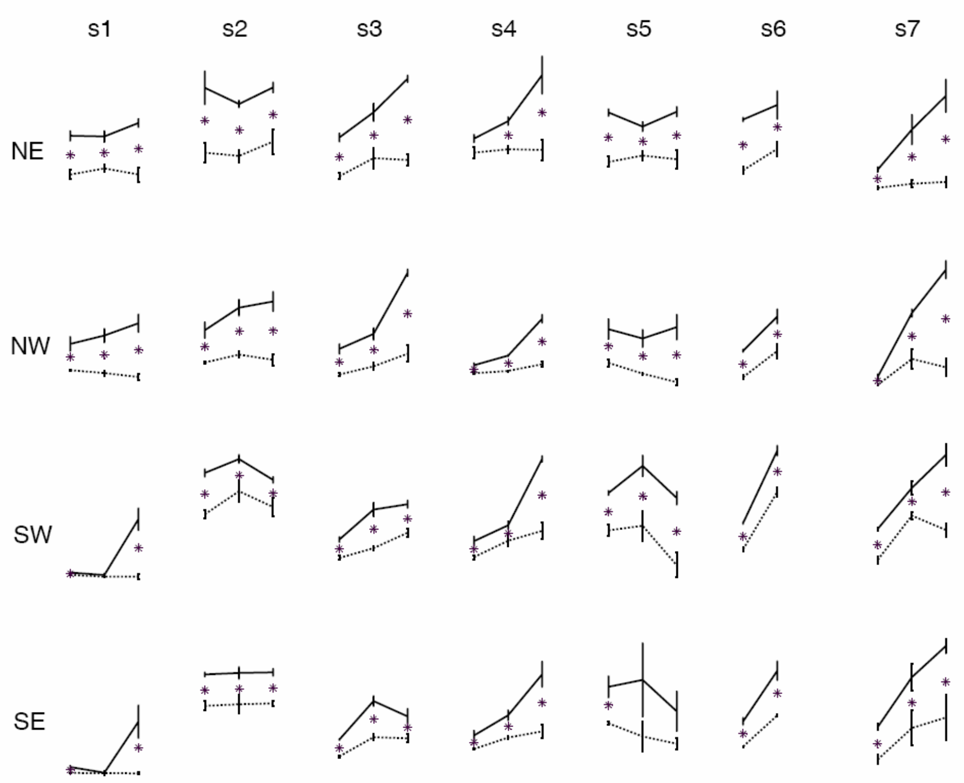

Figure 6.9: Comparison of stiffness in rad-uln vs. flex-ext.
Each row is a different diagonal direction, and each column is a different subject. Within each subplot, mean stiffness is plotted as a function of grasp force level for the three adjacent rad-uln directions (solid) and the three adjacent flex-ext directions (dotted). The error bars denote ± 1

standard error. Asterisks denote that stiffness in rad-uln is significantly greater than stiffness in flex-ext (one-tailed test, $p \leq 0.05$).

6.4 Discussion

This chapter investigates the effect of total stiffness (active + passive) on path curvature. We first showed that the problem of path curvature can be cast in terms of response time anisotropy; the path will curve toward the direction with the quicker response time. Response time is itself a function of system impedance. As an example, we reconsidered the effect of *passive* stiffness on path curvature, shown first in Chapter 5, but this time from the point of view of response time anisotropy. More specifically, we focused on the diagonal movement directions and showed that the stiffness anisotropy measured in passive stiffness creates an anisotropy in impedance, with the effect that the response time in rad-uln is quicker than in flex-ext, causing paths to curve toward rad-uln. We then showed—theoretically, through a muscle model—that active impedance (active stiffness and damping) simply adds to passive impedance (inertia and passive stiffness and damping). In other words, if total stiffness (active + passive) exhibits an anisotropy similar to passive stiffness, then the demonstration that *passive* stiffness can explain the observed pattern of path curvature (in Chapter 5) is equally valid for *total* stiffness.

It is very difficult to accurately measure total stiffness during movement. Instead, we approximated the ratio in rad-uln and flex-ext of total stiffness during movement as the ratio in rad-uln and flex-ext of total stiffness during quasi-static co-contraction. Subjects maintained a constant level of grasp force while stiffness was measured. Focusing on movements in the diagonal directions, we showed that the total stiffness in rad-uln is greater than the total stiffness in flex-ext (Figure 6.9), suggesting that *total* (active + passive) stiffness can explain the pattern of path curvature as well as *passive* stiffness.

6.4.1 Is total wrist stiffness linear?

Curves of torque vs. displacement contain linear and non-linear portions, as shown in Figure 6.10. Typically, curves start out convex (when viewed from the top) for approximately 100 samples, then become remarkably linear.[27] This linearity often persisted for the rest of the curve (see lower curves in Figure 6.10). However, curves with higher stiffness often encountered a sharp increase in slope, followed by another relatively linear portion (at a much steeper slope). This sharp increase in slope became more common with increasing levels of co-contraction.

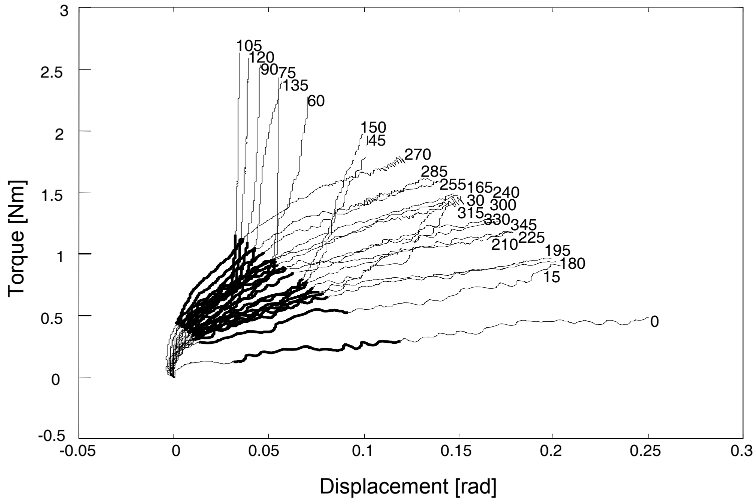

Figure 6.10: Torque vs. displacement in all 24 directions.
The initial 100 samples and final 300 samples are shown in thin lines, while the intermediate 200 samples are shown in thick lines.[27] The number next to each line indicates the direction of the measurement (in deg), measured CCW beginning in pure extension (West target).

Which portion should be used to estimate stiffness? In [80], all sample points except the first 100 were used. We experimented using all samples, all samples except the first 100, all samples except the first and last 100, and all samples except the first 100 and last 300 (which is shown in Figure 6.10). For these four scenarios, the estimates of stiffness for all three levels of co-contractions were remarkably similar: while the magnitude of stiffness decreased slightly for all directions when the first 100 and last 300 samples were discarded, the shapes of the polar stiffness plots remained almost unchanged. Therefore, it appears that it doesn't much matter which portion of the torque-displacement curve is used to obtain a linear estimate of stiffness. For simplicity, in this

---

[27] As in the study by Formica et al., the desired robot location increased at constant velocity over 3 seconds from 0 to 0.3 rad in each direction (for outbound movements), sampled at 200 Hz for a total of 600 samples per movement.

chapter we used the entire torque-displacement curve—including linear and non-linear portions—to estimate stiffness.

6.4.2 Comparison with the study by Formica et al.

The passive stiffness values obtained in the experiment described in this chapter (measured at the lowest grasp force level, which was zero) were compared to those obtained in [80]. Figure 6.11 shows passive wrist stiffness of one subject measured according to the protocol in [80] (dotted line) and the protocol described in this chapter (solid line). There are some differences between stiffness values, which arise from differences in experimental setup, including differences in neutral position and wrist constraints.

The neutral position described in this chapter (where stiffness measurements started) was based on each subject's individual, anatomically neutral position (see Methods section), whereas the neutral position used in [80] was based on neutral robot position. The effect of this difference in neutral position was assessed by repeating the experiment from [80], but with the neutral position described in this chapter (see dashed line in Figure 6.11).

The following three differences in constraints are thought to have generated differences in stiffness measurements. 1) The hand constraint described in this chapter (see first and second photos in Figure 6.3) supinates the distal forearm by about 15° relative to the position of the distal forearm in [80]. This difference arises because of differences in pro-sup between grasping a handle in the para-saggital plane (as in [80]) and sandwiching the metacarpals between two plates in para-saggital planes. The entire stiffness plot can be expected to rotate CW (toward supination) by 15° as a consequence. 2) In our experiment a Velcro strap pressed the thenar muscle mass against the dorsal plate (see middle photo in Figure 6.3), loading it in slight supination. It appears that this loading may have caused an increased stiffness in the quadrant between extension and radial deviation, accentuating the rotation of the major principal stiffness axis described in 1) above. 3) The distal forearm was constrained against *translation* relative to the robot by a Velcro strap which passed under two bars constrained to the robot table (see last photo in Figure 6.3). This distal forearm constraint was more rigid than that used in [80].

Because the stiffness of such a distal forearm constraint acts in series with the stiffness of the wrist, it is likely that the more rigid constraint used in our experiment resulted in increased stiffness measurements in radial deviation. The effect of these constraints was to increase and supinate the stiffness plot, as shown in Figure 6.11.

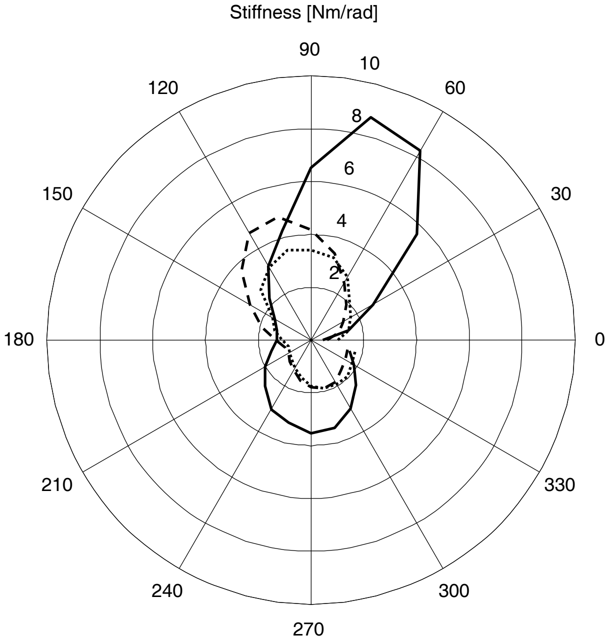

Figure 6.11: Polar plots of stiffness measured by three different protocols: the protocol described in [80] (dotted), the protocol described in [80] but with the neutral position from this study (dashed line), and the protocol described in this chapter (solid).

6.4.3 Changing the Equilibrium Position

Stiffness was calculated according to the linear relationship

$$\tau = K(\theta - \theta_0) \Rightarrow K = \frac{\tau}{(\theta - \theta_0)}$$

where τ is the torque provided by the robot to overcome wrist stiffness, K, during displacements, θ, away from the equilibrium position, θ_0. In this estimation of K, the implicit assumption is that θ_0 is constant. However, if muscle contraction is allowed (which it was in this experiment), it is possible to continuously vary θ_0 to “drag” behind θ as the robot moves. This would decrease τ, producing an artificially low value of K (if θ_0

is wrongly assumed constant). In terms of the muscle model presented in the introduction, the equation of motion in each DOF during the stiffness measurement (where velocity ≈ acceleration ≈ 0) is

$$\left(K + D'_{ag}u_{ag} + D'_{an}u_{an}\right)\theta = C'_{ag}u_{ag} - C'_{an}u_{an} + \tau$$

where u is neural activation, D' is the rate of change of stiffness with u, C' is the rate of change of muscle torque with u, and 'ag' and 'an' refer to 'agonist' and 'antagonist', respectively. This equation can be re-written as

$$\left(K + D'_{ag}u_{ag} + D'_{an}u_{an}\right)\left(\theta - \frac{C'_{ag}u_{ag} - C'_{an}u_{an}}{K + D'_{ag}u_{ag} + D'_{an}u_{an}}\right) = \tau$$

$$\left(K + D'_{ag}u_{ag} + D'_{an}u_{an}\right)\left(\theta - \theta_0\right) = \tau$$

The idea behind this experiment is that during co-contraction $C'_{ag}u_{ag}-C'_{an}u_{an} = 0$, in which case $\theta_0 = 0$ and the measured stiffness is correct. However, because this equation has two DOF (u_{ag} and u_{an}, or alternatively $D'_{ag}u_{ag}+D'_{an}u_{an}$ and $C'_{ag}u_{ag}-C'_{an}u_{an}$), it is possible to keep stiffness ($K+D'_{ag}u_{ag}+D'_{an}u_{an}$) relatively constant while varying the net muscle torque ($C'_{ag}u_{ag}-C'_{an}u_{an}$) so that θ_0 follows θ.

One piece of evidence suggesting that the equilibrium position changed during the measurement is that the inbound move in each direction did not end up in the center. This behavior is only possible if the equilibrium position changed. The motor torque pushing against wrist stiffness is controlled by a proportional controller, $\tau = K_r(\theta_r-\theta)$, where θ_r is the reference position and K_r is the proportional gain[28]. Plugging into the equation above, and replacing for clarity sake $K+D'_{ag}u_{ag}+D'_{an}u_{an}$ by K, yields

$$K\left(\theta - \theta_0\right) = K_r\left(\theta_r - \theta\right)$$

This can be re-arranged to yield the "error" between reference and actual position:

$$\theta_r - \theta = \frac{K\left(\theta_r - \theta_0\right)}{K_r + K}$$

---

[28] The value of K_r used in these experiments was 10 Nm/rad (which is greater than passive wrist stiffness but comparable to—or even smaller than—active wrist stiffness, as shown in Figure 6.8).

If the equilibrium position were always equal to zero, the error would be

$$\theta_r - \theta = \frac{\theta_r}{\frac{K_r}{K} + 1}$$

Note that the error is proportional to the reference position. If the robot stiffness K_r is sufficiently higher than the wrist stiffness (i.e. if the proportional gain is sufficiently high), the error would approach zero. At the end of the inbound movement, the reference position is zero, so θ should be zero as well. However, it was not identically zero, as shown in Figure 6.12, indicating that the equilibrium position, θ_0, was also non-zero. The value of the equilibrium position can be written as:

$$\theta_0(\theta_r = 0) = \frac{K_r + K}{K}\theta$$

Unfortunately, this is one equation with two unknowns (θ_0 and K), so it is not possible to correct for changes in the equilibrium position. Fortunately, the change in equilibrium position does not appear to be substantial. While the final positions of the inbound moves form a relatively large curve, such a curve represents the cumulative change in final position; the difference in the start of the outbound move and the end of the inbound move *for a given direction* is relatively small, suggesting that the equilibrium position did not change dramatically during measurements.

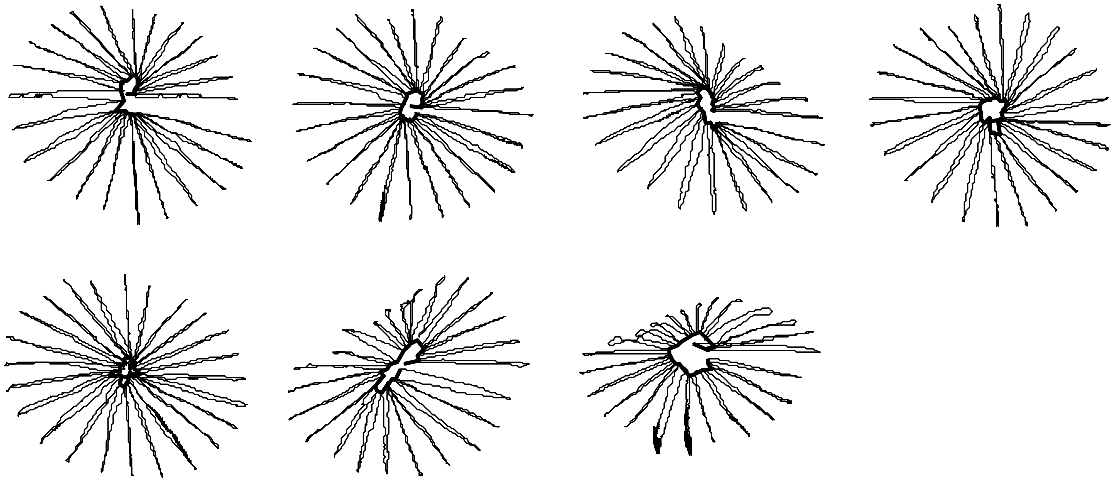

Figure 6.12: Plot of flex-ext vs. rad-uln for all seven subjects for intermediate level of co-contraction. Highlighted in thick lines are the final positions for measurements in each direction, showing that measurements did not, in general, end at the neutral position.

The magnitude of the change in equilibrium position during measurement can also be estimated by looking at the change in equilibrium position during the "stay" period between outbound and inbound movements. A change in equilibrium position during this stay period would presumably result in a drop in the robot torque required to maintain the wrist at the position of the wrist at the beginning of the stay period. However, the drop in torque during this period is very small, as shown in Figure 6.13, providing further indication that the equilibrium position did not change substantially.

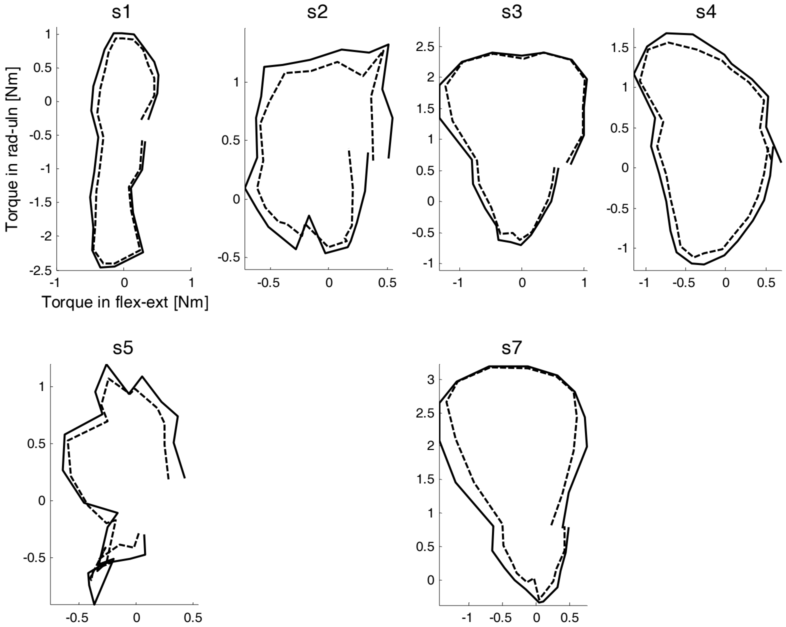

Figure 6.13: Drop in torque during the "stay" period for the highest level of grasp force. Plotted are robot torque in rad-uln vs. robot torque in flex-ext at the beginning (solid) and end (dashed) of the "stay" period.

In summary, total (active + passive) stiffness during static co-contraction exhibits—similar to passive stiffness—an anisotropy in which the stiffness in rad-uln is larger than in flex-ext, and is therefore capable of producing the observed pattern of path curvature. Assuming that the anisotropy in total stiffness *during movement* is not fundamentally different from the anisotropy during static co-contraction, then total stiffness is also capable of generating the observed pattern of curvature.

7 Are Wrist Rotations Predominantly Under Kinematic Control?

This research was performed in collaboration with Laura Dipietro, Ph.D.

7.1 Introduction

Despite a slight amount of curvature, which has been attributed to peripheral factors [66, 67], humans' reaching movements are known to be relatively straight [64]. Making straight reaching movements is not trivial; it requires either carefully compensating for the complex, non-linear dynamics of the human arm, or else implementing a stiff controller that allows little deviation from a straight path. Either way, the fact that humans' reaching paths are relatively straight suggests that reaching is kinematically controlled [86]. Further evidence for kinematic control came from studies investigating reaching movements under various perturbations. Under different inertial loads, hand kinematics (especially speed profiles) remained remarkably invariant [65]. When paths were artificially curved, either mechanically [68] or visually [69], subjects adapted by straightening their paths, confirming that, though dynamic considerations may play a role, the kinematic plan appears to be primary, from which the muscle activation required to produce that kinematic plan is determined.

When humans rotate the wrist in combinations of flex-ext and rad-uln, the hand traces a path on the roughly spherical surface surrounding the wrist joint. The paths traced on this surface[29] could be straight, like great circles on a sphere. In reality, they exhibit roughly twice as much curvature as in reaching (Chapter 3). While this path curvature is likely caused by the anisotropic nature of wrist stiffness (Chapters 5 and 6), the fact remains that wrist paths are significantly more curved than reaching paths, suggesting that wrist rotations may not be under kinematic control like reaching movements. On the other hand, Hoffman and Strick have hypothesized that humans may

---

[29] Alternatively, think of the projection of the path onto a plane, like the path produced by a laser pointer as the pointer is rotated by the wrist (for medium-sized wrist rotations, the difference between the path on the sphere and its projection on a tangential plane is negligible).

add temporally shifted muscle activity in an attempt to straighten paths (see Chapter 5), suggesting kinematic (albeit imperfect) control [36].

The purpose of this study was to provide evidence for or against kinematic control of wrist rotations by observing whether (and how) subjects adapt their wrist behavior in the face of mechanical perturbations, similar to perturbation studies in reaching (for example, see [68]). One study investigated 2-DOF wrist kinematics under different inertial loading conditions [88], but did not look at adaptation per se. The only study of adaptation to force perturbations in wrist rotations of which we are aware is by Dipietro et al. [89]. In their experiment, human subjects were exposed to a conservative, velocity-dependent perturbation (a curl field) of the form

$$\begin{bmatrix} \tau_{\text{flex-ext}} \\ \tau_{\text{rad-uln}} \end{bmatrix} = \begin{bmatrix} 0 & B \\ -B & 0 \end{bmatrix} \begin{bmatrix} \dot{\beta} \\ \dot{\gamma} \end{bmatrix}$$

where $\dot{\beta}$ and $\dot{\gamma}$ represent the angular velocity of the wrist in flexion-extension (flex-ext) and radial-ulnar deviation (rad-uln), respectively, and $\tau_{\text{flex-ext}}$ and $\tau_{\text{rad-uln}}$ are the torques applied by the robot to the hand in those directions. B represents the perturbation strength and was set at 0.15 Nms/rad. In their study, Dipietro et al. looked for adaptation in four cases: two age groups (young and elderly) and at two movement speeds. Despite a very large number of subjects (35 total), they did not observe consistent adaptation (defined in their study as a statistically significant reversion toward pre-perturbation kinematics) in any of the four groups, suggesting that wrist rotations may be controlled differently than reaching. Alternatively, it is possible that wrist rotations are under the same general control strategy, but subjects did not adapt because the perturbation strength was either too high or too low.

The purpose of this chapter is to see if adaptation occurs under conditions which are different from the study described in [89]. Specifically, we varied the perturbation strength (B = 0.05, 0.10, and 0.15 Nms/rad) and, in an effort to make sure that the perturbation was perceived—this was questionable because of the large variability normally present in wrist rotations—we amplified the error perpendicular to the movement direction (for B = 0.10 and 0.15 Nms/rad only).

7.2 Methods

7.2.1 Subjects

Twenty-two subjects (17 males, 5 females) participated in this study. All were young and healthy and denied biomechanical or neurological difficulty associated with wrist rotations. All subjects reported themselves as right-handed except for two, who were left-handed, and all subjects performed the test with their right hand. Following procedures approved by MIT's Committee on the Use of Humans as Experimental Subjects, informed consent was obtained from all subjects.

7.2.2 Setup

Subjects were seated and held in their right hand the handle of a wrist robot (see [3] for details) which allowed motion in flex-ext and rad-uln. Displayed on a monitor in front of them was a center target surrounded by a large circle on which 8 peripheral targets were equally spaced. Wrist angle was represented on the monitor as a dot that moved in proportion to wrist rotation. However, the mapping from wrist orientation to cursor position was distorted to allow subjects to use more of their range of motion in flex-ext, but still see their movements in rad-uln large enough. More specifically, reaching targets in flex-ext required 30° of rotation, while targets in rad-uln only required 15° of rotation. In other words, we included between wrist orientation and cursor position a linear transformation which stretched the flex-ext direction by a factor of 2. Consequently, reaching targets on the diagonals required 15°/sqrt(2) = 10.6° in rad-uln and 2*15°/sqrt(2) = 21.2° in flex-ext.

Because of the increased variability observed in wrist rotations, there was concern that subjects were not able to perceive the perturbation as well as in reaching studies. To make sure that subjects perceived the perturbation, we introduced an additional affine transformation that magnified the lateral deviation. For a given target direction (defined as the vector between center and peripheral target), displacements perpendicular to the target direction were stretched by a factor of 2. Because the transformation differed between directions, it was only in effect while the target was lit.

Subjects were instructed to rotate the wrist so that the cursor moved to whichever target was lit up. Movements were always made either from the center target to a peripheral target, or from a peripheral target to the center target, but the order in which peripheral targets were presented was pseudo-random. Targets remained lit for 1.6 seconds. For the first 0.8 seconds of this period, the target was one color. After 0.8 seconds, the target turned to a different color. Subjects were instructed to reach the target about when the target turned colors. After the 1.6 seconds, a new target lit up. Subjects practiced implementing these instructions while they were given (less than five minutes).

7.2.3 Blocks

Subjects performed 160 movements (80 outbound and 80 inbound) in each of 9 blocks. Blocks 1 and 2 were null fields. Blocks 3 through 6 included the force perturbation (CW for outbound, CCW for inbound moves). In blocks 7 and 8, the force field was reversed (CCW for outbound, CW for inbound moves). Block 9 was a null field. Each block was separated by a three-minute break.

7.2.4 Conditions

Each subject performed this adaptation test (consisting of 9 blocks) under one of three conditions: B = 0.05 Nms/rad without visual error amplification, B = 0.10 Nms/rad with visual error amplification, and B = 0.15 Nms/rad with visual error amplification. Table 7.1 shows how many subjects participated in each test. No subject participated in more than one test to ensure that subjects were naïve.

	Perturbation Strength, B [Nms/rad]		
	0.05	**0.10**	**0.15**
WITHOUT Visual Error Amplification	5		Dipietro et al.
WITH Visual Error Amplification		11	6

Table 7.1: Number of subjects who participated in each of the three tests.

7.2.5 Data Analysis

In traditional adaptation experiments for reaching movements, initial exposure to the curl field caused paths to curve dramatically. Typically, a metric involving the distance or area between the curved path and a straight line has been used to quantify this effect. This works well for reaching because null field paths are relatively straight. Wrist rotation paths, however, exhibit roughly twice as much curvature as reaching (Chapter 3). Also, the pattern of curvature in different directions is such that, in response to a curl field perturbation, the curvature increases in some directions and decreases in others. Consequently, averaging the metric over different movement directions tends to wash out the effect.

Therefore, we defined a slightly modified metric called the "deviation area." For a given direction, instead of comparing individual paths to a straight line, they were compared to the mean path in block 2 (null field) in that direction. By choosing the metric to be the non-negative area enclosed between these two paths, as shown in Figure 7.1, the effect is not lost when the metric is averaged between directions. Before averaging, deviation areas were scaled by the square of the distance between targets to account for the asymmetry in movement distance.

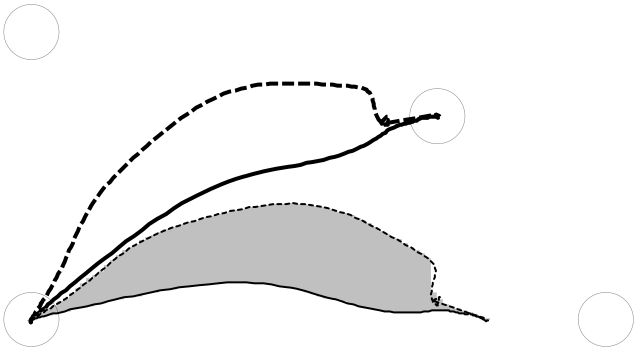

Figure 7.1: Schematic of the "deviation area."
For this move in extension and radial deviation (between the center target in the lower left corner of this figure and the NE target in the upper right corner), the mean path in this direction from block 2 and the individual path are shown in thick solid and dashed lines, respectively. The paths were rotated (thin solid and dashed lines), and the area between the two paths was computed (gray shading).

We were particularly interested in the following three questions. Did the deviation area:

- increase when the force field was introduced (from block 2 to block 3)?
- decrease while the force field was in effect (from block 3 to block 6)?
- increase when the force field was reversed (from block 6 to block 7)?

7.3 Results

Shown in Figure 7.2 are the paths and deviation area for a subject who showed an increase from block 2 to 3, a decrease from block 3 to 6, and an increase from block 6 to 7. One can immediately see that the introduction of the force field (between blocks 2 and 3) does not perturb the paths as much as in adaptation experiments involving reaching. Nevertheless, with closer inspection, one can make out that there is a difference between blocks 2 and 3, and that this difference shrinks so that blocks 6 and 2 are very similar (i.e. blocks 3 and 6 are different). Furthermore, the reversal of the field between blocks 6 and 7 has a very noticeable effect on paths in block 7.

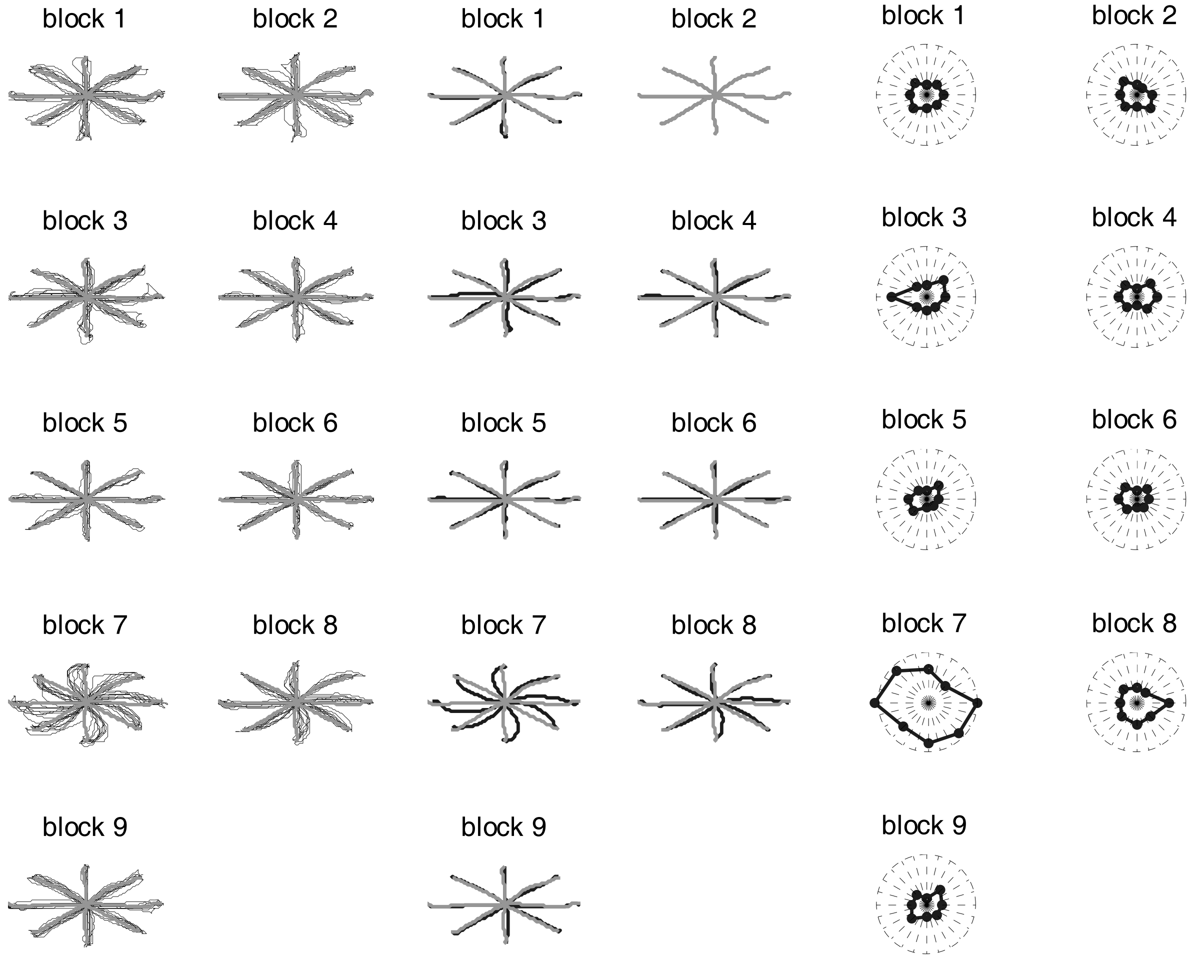

Figure 7.2: Paths and deviation area for subject exposed to 0.10 Nms/rad curl field. Columns 1 and 2 show individual paths, while columns 3 and 4 show mean paths. Overlaid on columns 1-4 in gray are the mean paths per direction for block 2. Columns 5 and 6 are polar plots of

the deviation area per direction. This subject displayed changes in deviation area between blocks 2 and 3, 3 and 6, and 6 and 7.

For comparison, Figure 7.3 shows the paths and deviation area for a subject who showed a change in deviation area from block 2 to 3 and from block 6 and 7, but not from block 3 to 6.

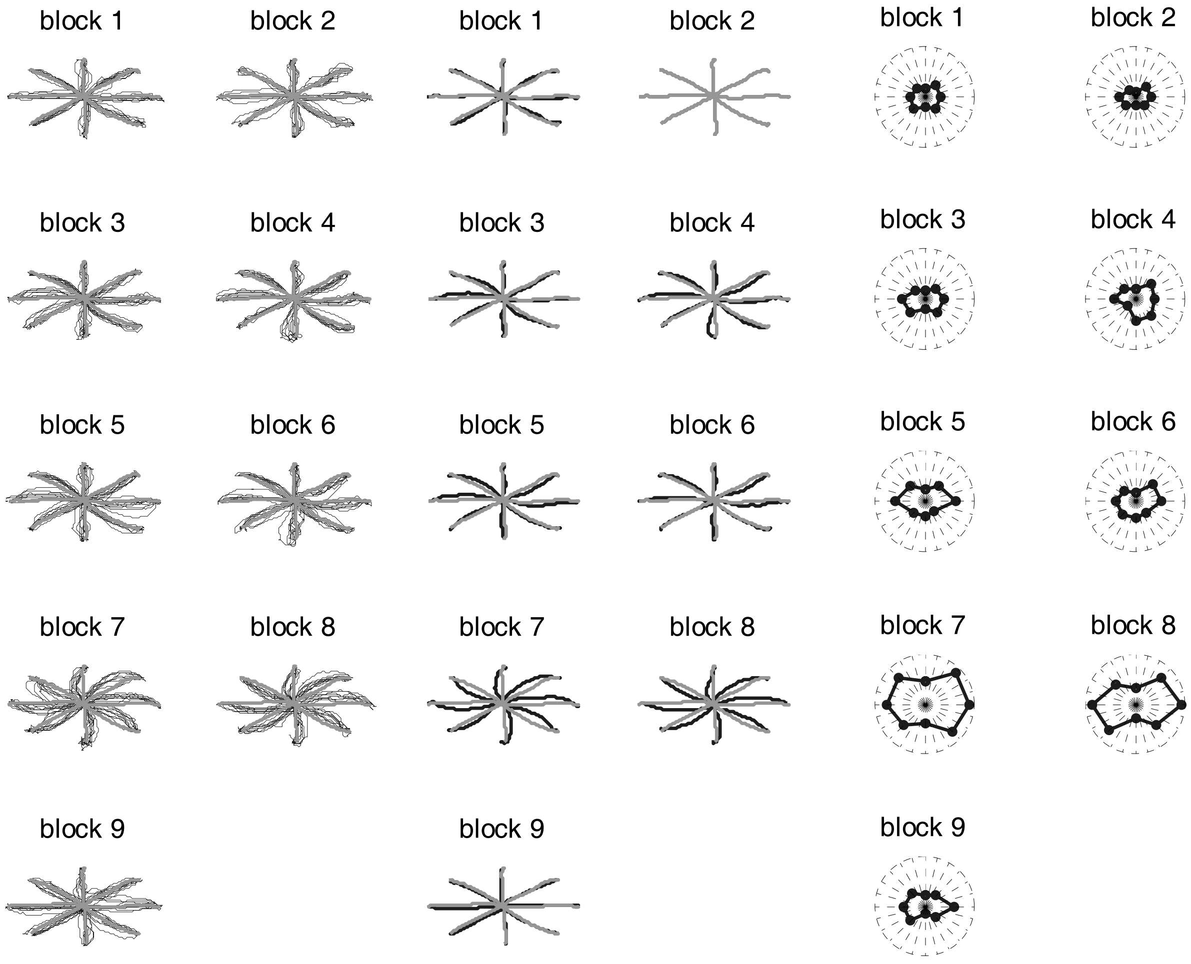

Figure 7.3: Paths and deviation area for subject exposed to 0.15 Nms/rad curl field. Shown are individual and mean outbound paths, as well as deviation area, per direction for one subject. This subject showed changes in deviation area between blocks 2 and 3 and blocks 6 and 7, but not between blocks 3 and 6. See Figure 7.2 for an explanation of the various subplots.

The mean deviation areas for each block are shown per subject in Figure 7.4 for the low force test. As indicated by the significance bars, only one of the five subjects showed an increase in deviation area when the field was introduced. None of the subjects showed a decrease from block 3 to 6, but four of the five subjects showed an increase when the field was reversed (from block 6 to 7).

Figure 7.5 shows the deviation areas for each block for the high force test. All six subjects showed an increase in deviation area when the field was introduced (from block 2 to 3). Only one subject showed a decrease from block 3 to 6, but all six showed an increase when the field was reversed (from block 6 to 7).

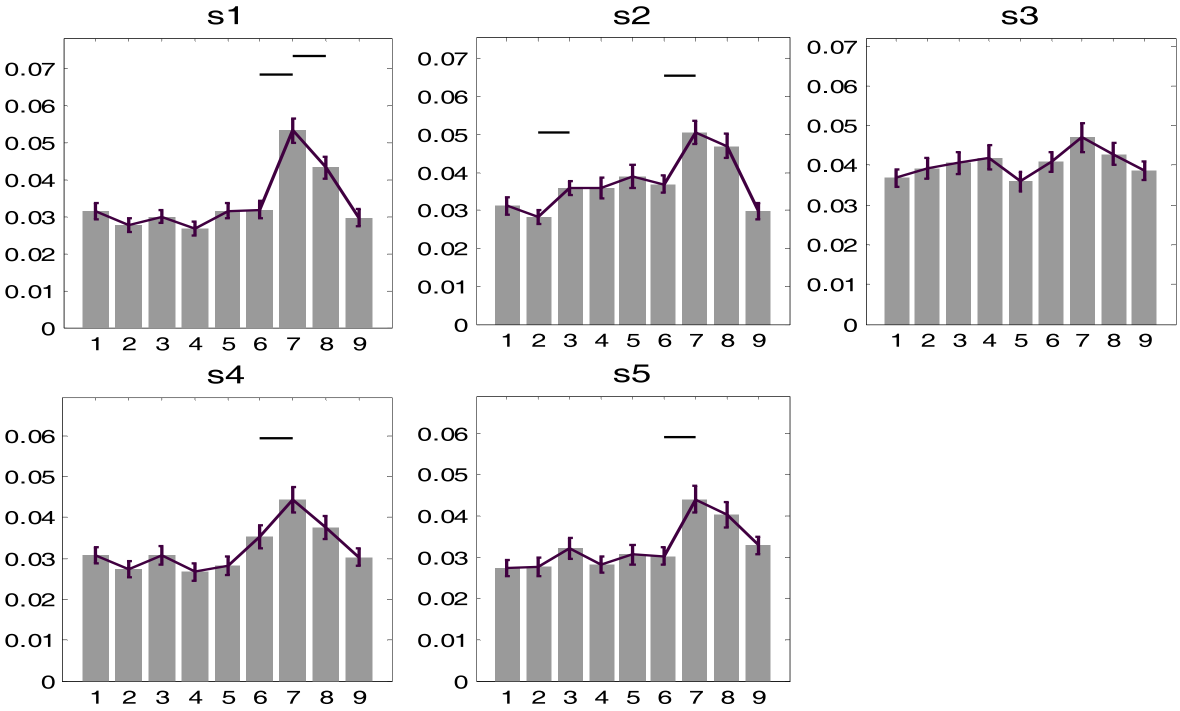

Figure 7.4: Deviation area in LOW force field.

Shown are mean deviation area ± standard error for each block for five subjects. The numbers on the abscissa indicate block number. The horizontal lines just above the bars indicate a significant difference between bars. Deviation area is dimensionless because it was normalized by the square of the target distance (see Methods).

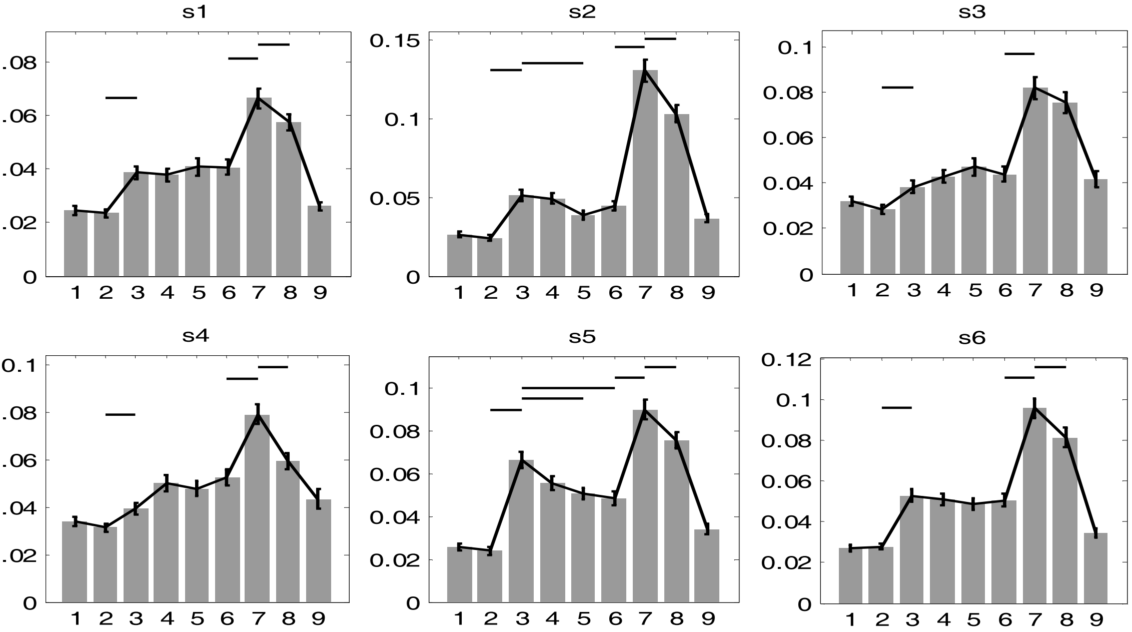

Figure 7.5: Deviation area in HIGH force field. See Figure 7.4 for plot details.

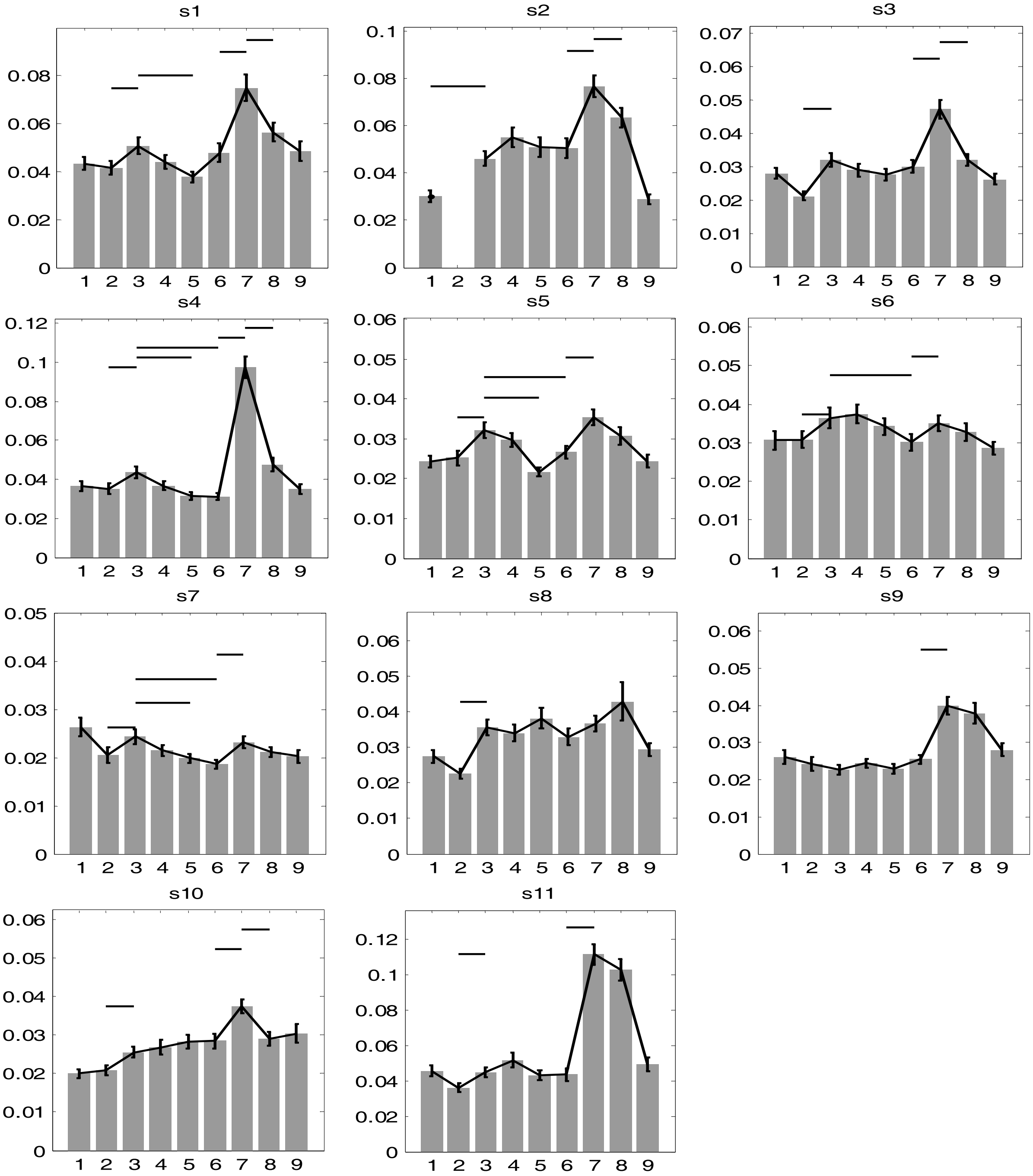

Figure 7.6: Deviation area in INTERMEDIATE force field.

Shown are mean deviation area ± standard error for each block for eleven subjects. In running the experiment with subject s2, block 2 was inadvertently skipped, so paths were instead compared to the mean paths of block 1. See Figure 7.4 for plot details.

Finally, the mean deviation areas for the intermediate force field are shown in Figure 7.6. Ten of the eleven subjects showed an increase in deviation area when the field was introduced (from block 2 to 3), four showed a decrease while the field was in effect (from block 3 to 6), and 10 of the 11 subjects showed an increase when the field was reversed (from block 6 to 7). The results of these three tests are summarized in Table 7.2.

Test	**B [Nms/rad]**	**VEA**	**# Subjects**	**Block 2 < 3 [%]**	**Block 3 > 6 [%]**	**Block 6 < 7 [%]**
Low force	**0.05**	**No**	5	20	0	80
Intermediate force	**0.10**	**Yes**	11	91	36	91
High force	**0.15**	**Yes**	6	100	17	100
Dipietro et al., 2007	**0.15**	**No**	9	56*	22*	67*

Table 7.2: Summary of results from the low, intermediate, and high force field tests.
The results from the study by Dipietro et al. ([89]) are shown for comparison. Note, however, that their results are not calculated exactly the same way as the results for the other experiments. For example, the metric they used (lateral deviation) is less sensitive than the metric described in this chapter ("deviation area"). "Block 2 < 3" indicates the percentage of subjects who showed an increase in deviation area when the field was introduced (from block 2 to 3). "Block 3 > 6" indicates the percentage of subjects who showed a decrease in deviation area while the field was in effect (from block 3 to 6). Finally, "Block 6 < 7" indicates the percentage of subjects who showed an increase in deviation area when the field was reversed (from 6 to 7). VEA stands for Visual Error Amplification.
*** Calculated based on the metric used in [89] (lateral deviation), which is less sensitive than the metric described in this chapter ("deviation area").**

Combining the results from all three tests (involving 22 subjects), 77% of subjects showed an increase in deviation area when the field was introduced (from block 2 to 3), 23% showed a decrease while the field was in effect (from 3 to 6), and 91% showed an increase when the field was reversed (from block 6 to 7).

7.4 Discussion

The purpose of this study was to provide evidence for or against kinematic control of wrist rotations by observing whether (and how) subjects adapt their wrist behavior in the face of mechanical perturbations. After 2 null-field blocks of 160 (80 round-trip) wrist rotations each, subjects were exposed to a conservative, velocity-dependent force field (curl field) of either low, intermediate, or high strength for 4 blocks, after which the force field was reversed for another 2 blocks. Subjects ended the experiment by rotating their wrist in one final, null-field block. We focused our attention on three questions: Did paths change when the field was first introduced? Over the course of the four blocks during which the force field remained unchanged? When the field was reversed?

Past experiments investigating adaptation in reaching movements (see, e.g., [68, 90]) showed a consistent pattern: upon introduction of the force field, perturbed paths were initially very curved. Over subsequent blocks, movement kinematics consistently reverted towards pre-perturbation kinematics. For example, in the study by Shadmehr and Mussa-Ivaldi, the trend toward pre-perturbation kinematics is clearly visible within 250 moves (see Figure 11 in [68]). This trend toward the original, unperturbed kinematics has been taken as a clear example of adaptation.

7.4.1 Adaptation differs between wrist rotations and reaching movements

In the experiments described in this chapter, subjects made a total of 640 wrist rotations (320 round-trip movements) in the force field in blocks 3 through 6. Yet only 23% of subjects (averaged over all three experiments) exhibited a significant trend toward pre-perturbation kinematics (measured as a significant decrease in deviation area from block 3 to 6). This lack of an obvious and consistent reversion toward pre-perturbation kinematics is in clear contrast to adaptation experiments in reaching movements. Yet adaptation did occur, as evidenced by the increase in deviation area when the field was reversed (see below).

7.4.2 Field reversal caused increase in deviation area, implying adaptation

Importantly, the deviation area increased in 91% of subjects (averaged over all three experiments) when the field was reversed (from block 6 to 7). If there were absolutely no adaptation to the force field during blocks 3 through 6, simply reversing the perturbation should have no effect; the metric we used, deviation area, is non-negative, and there is no reason to believe that one curl field direction should cause more perturbation than the other. Therefore, the consistent observation of a significant difference between blocks 6 and 7 is strong evidence that adaptation did occur.

7.4.3 Effect of Field Strength on Perturbation

Subjects were exposed to a force field with B = 0.05, 0.10, or 0.15 Nms/rad, which we termed low, intermediate, and high force fields, respectively. Comparison of the results listed in Table 7.2 indicates that the three field strengths had comparable effects: At each field strength, no or few subjects showed a decrease in deviation area from block 3 to 6, but most or all subjects showed an increase when the field was reversed. This is even true for the low force field, which, when it was first introduced (from block 2 to 3), only produced a significant change in 1 subject. In other words, adaptation was observed over a 3-fold difference in field strength, and even when the manifestation of the perturbation was weak (change from block 2 to 3 in the low force field).

7.4.4 Comparison of Torques Acting on the Wrist

At this point, it is useful to put the perturbation torques used in these experiments in reference to other torques commonly encountered during wrist rotations. The dynamics of comfortably-paced wrist rotations are known to be dominated by stiffness (and gravity), not inertia as in reaching movements (see Chapter 4). Figure 7.7 shows stiffness, gravitational, and inertial torques for simulated wrist rotations based on minimum jerk kinematics. Also shown is the perturbation torque experienced in the high force field where B = 0.15 Nms/rad (the torques for the other two field strengths are simply scaled by 2/3 and 1/3). The important thing is that the strongest perturbation torque experienced in these tests is well below the torques required to overcome stiffness and gravity, and should therefore not overwhelm the system.

Shoulder and elbow torques experienced during reaching movements are also shown for comparison (the equations of motion of the arm modeled as a two-link manipulandum are given in Appendix F). The torques due to passive stiffness are unknown for reaching movements and therefore excluded, but they are expected to be low since reaching movements are thought to be dominated by inertial effects. Also shown are perturbation torques due to a field strength (12 Ns/m) used in the literature [90]. Note that these perturbation torques are of the some order of magnitude as (and sometimes even larger than) inertial torques. This provides a point of reference, suggesting that the perturbation fields used in our wrist adaptation tests were not too strong.

Were the force fields used in our experiments too weak? While the comparison of perturbation torques between reaching and wrist rotations in Figure 7.7 suggests that the force field strength used in our experiments could have been increased (perhaps by a factor of 3), we know that the intermediate and high force fields were not too weak to produce significant changes in kinematics (from block 2 to 3), and that none of the three force fields were too weak to produce adaptation (as evidenced by the increase in deviation area from block 6 to 7).

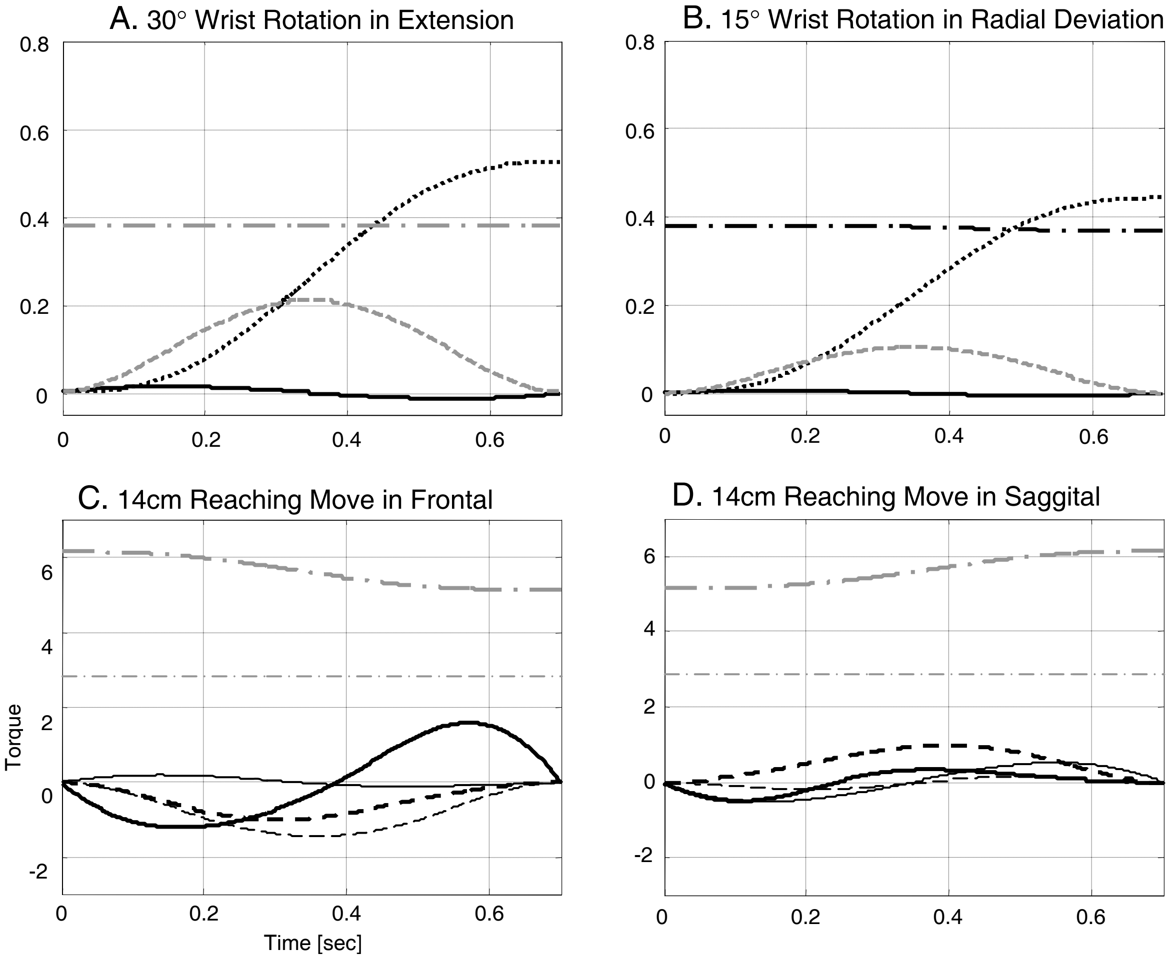

Figure 7.7: Comparison of torques during wrist rotations and reaching movements. Shown are torques acting on the wrist during wrist rotations in extension (A) and radial deviation (B), and on the shoulder and elbow during reaching movements in the frontal (C) and saggital planes (D). Inertial torques are solid, passive stiffness torques dotted, perturbation torques dashed, and gravitational torques dash-dotted. In C and D, thick and thin lines represent torques at the shoulder and elbow, respectively. Torques acting out of the plane of movement are gray. The curl field variable (B) is 0.15 Nms/rad for wrist rotations and 12 Ns/m for reaching. All torques are based on 0.7 sec movements with minimum jerk kinematics. *Wrist parameters:* The mass and moment of inertia (about the wrist joint, in both DOF) of the hand were 0.5 kg and 0.002 kgm^2, respectively, the center of mass of the hand being 7.5 cm from the wrist. Passive wrist stiffness was 1 and 1.7 Nm/rad in flex-ext and rad-uln, respectively. *Reaching parameters:* Moves in the saggital plane go from (-14, 14) cm to (-14, 28) cm, and moves in the frontal plane go from (-28, 14) cm to (-14, 14) cm (the origin is in the right shoulder joint, x points toward the left shoulder joint, and y points forward). Upper and lower arm lengths, masses, and moments of inertia were 0.30 and 0.35 m, 1.59 and 1.66 kg, and 0.0477 and 0.059 kgm^2, respectively.

7.4.5 Adaptation with imperfect control?

While adaptation in wrist rotations was clearly observed (as evidenced by the increase in deviation area from block 6 to 7), it appears that it may be more difficult to detect than in reaching movements. For example, there was no consistent decrease in deviation area from block 3 to 6 as in perturbation experiments involving reaching movements. Why not?

In chapter 3, we showed that inbound and outbound paths differ, and that mean paths are straighter than individual paths. Based on these observations, we argued that the increased path curvature and variability seen in wrist rotations is due to imperfect implementation, or control, of a centrally specified movement. The difference in adaptation between wrist rotations and reaching movements presented in this chapter may be viewed in the same light. Adaptation in wrist rotations may be more difficult to detect because wrist rotations are implemented with a less perfect, or sloppier, controller. With such an imperfect controller, it stands to reason that adaptation would occur less fully and perhaps more slowly. Given that the perturbation in path was relatively small—compared to reaching experiments—to begin with (see Figure 7.2 and Figure 7.3), and that wrist rotations are in general more variable, any adaptation of the perturbed path toward pre-perturbation conditions would be more difficult to detect. It also makes sense, then, that it wasn't until the force field was reversed (effectively unleashing *twice* the perturbation) that a significant change was perceived.[30]

7.4.6 Conclusion

Subjects consistently exhibited adaptation to force perturbations (91% of subjects, averaged over all three field strengths), as evidenced by the increase in deviation area when the force field was reversed (from block 6 to 7). Interestingly, a decrease in deviation area while the force field remained unchanged (from block 3 to 6), which is typically observed in perturbation experiments involving reaching movements, did not generally occur, signaling a difference between wrist rotations and reaching movements in the way subjects adapt. This difference in adaptation is consistent with the hypothesis that wrist rotations are implemented with an imperfect controller (see Chapter 3). Taken together, the results presented in this chapter suggest that wrist rotations are, like reaching movements, primarily under kinematic control (albeit imperfect control).

---

[30] Alternatively (or perhaps in addition), perturbations in wrist rotations may be more difficult for subjects to perceive. Because variability in wrist rotations is large even in the null field, one might speculate that it is more difficult for subjects to perceive a perturbation among the "background noise." While this is possible, we do know, from the fact that perturbation occurred in over 90% of subjects in the intermediate- and high force tests, that the field was strong enough to perturb paths beyond the normal variability of wrist rotations.

7.5 Notes

One may want to perturb wrist rotations with force fields that are not velocity-dependent. We show here two examples of force fields that are *position*-dependent (static).

7.5.1 Static anti-diagonal force field

Two key features of the curl fields traditionally used in adaptation experiments involving reaching are: 1) the perturbation force acts perpendicularly to velocity, and 2) the steady-state force is zero at the target (in fact everywhere), allowing one to reach the target without adaptation.

A static field with similar properties can be constructed for the wrist. If the perturbation torque is to act perpendicularly to the vector from the origin to the current wrist orientation, the following must be true:

$$\vec{\tau} = \begin{bmatrix} 0 & -K \\ K & 0 \end{bmatrix} \begin{bmatrix} \beta \\ \gamma \end{bmatrix}$$

Proper choice of K allows the perpendicular torque to be zero at the center and peripheral target, as shown in Figure 7.8.

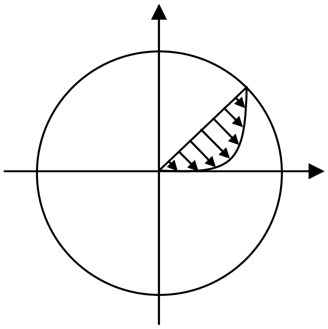

Figure 7.8: Sketch of the torque profile in the static anti-diagonal force field.

Of many possible functions, we choose to modulate the stiffness sinusoidally:

$$K = \frac{A\sin\left(\frac{\pi}{\theta_f}\sqrt{\beta^2+\gamma^2}\right)}{\sqrt{\beta^2+\gamma^2}}$$

where A is the peak perpendicular torque (experienced halfway between center and target), and θ_f is the distance from center to target. The resulting torque is plotted in Figure 7.9.

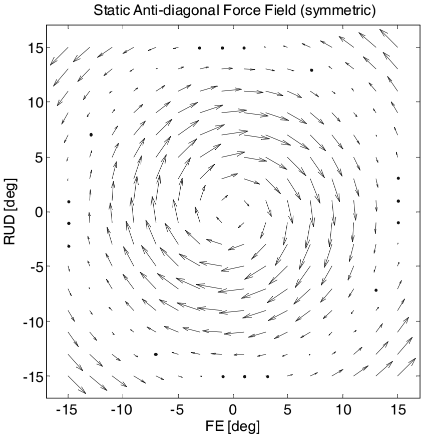

Figure 7.9: Plot of torque as a function of wrist orientation.

If the movement distance in flex-ext is twice as large as in rad-uln, the stiffness must undergo a slight modification:

$$K = \frac{A\sin\left(\frac{\pi}{\theta_f}\sqrt{\left(\frac{\beta}{2}\right)^2+\gamma^2}\right)}{\sqrt{\beta^2+\gamma^2}}$$

where θ_f is the distance from center to target in rad-uln. The resulting torque plot is shown in Figure 7.10.

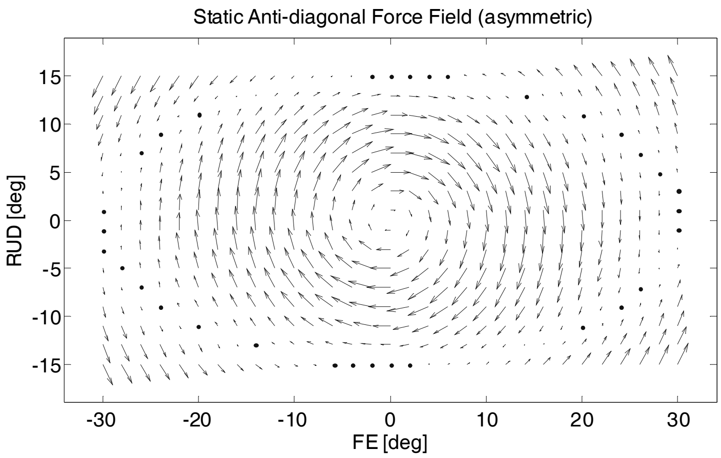

Figure 7.10: Plot of torque as a function of wrist orientation in an asymmetric field.

7.5.2 Static diagonal force field

Given that wrist rotation paths are noticeably influenced by the anisotropic nature of passive wrist stiffness, one may want to use the wrist robot to alter the stiffness encountered during wrist rotations. Here we present a simple force field which reverses the stiffness anisotropy, such that flex-ext is stiffer than rad-uln. For simplicity, assume that the principal axes of the wrist and of the wrist+robot system align with the movement axes. Then the total torque felt by the hand is:

$$\bar{\tau} = \left\{ \begin{bmatrix} K_{\beta,W} & 0 \\ 0 & K_{\gamma,W} \end{bmatrix} + \begin{bmatrix} K_{\beta,R} & 0 \\ 0 & K_{\gamma,R} \end{bmatrix} \right\} \begin{bmatrix} \beta \\ \gamma \end{bmatrix}$$

where subscripts W and R refer to wrist and robot, respectively. Under natural conditions, the stiffness in rad-uln is roughly twice as large as in flex-ext, so the torque due to stiffness is:

$$\bar{\tau} = K_{\beta,W} \begin{bmatrix} 1 & 0 \\ 0 & 2 \end{bmatrix} \begin{bmatrix} \beta \\ \gamma \end{bmatrix}$$

By choosing $K_{\beta,R}$ to be 3 times larger than $K_{\beta,W}$, and $K_{\gamma,R}$ to be zero, the final torque is

$$\bar{\tau} = K_{\beta,W} \begin{bmatrix} 4 & 0 \\ 0 & 2 \end{bmatrix} \begin{bmatrix} \beta \\ \gamma \end{bmatrix}$$

as shown schematically in Figure 7.11. The resulting torque is plotted in Figure 7.12.

$$\vec{\tau} = \left\{ \underbrace{\begin{bmatrix} K_{\beta,W} & 0 \\ 0 & K_{\gamma,W} \end{bmatrix}}_{\text{wrist}} + \underbrace{\begin{bmatrix} K_{\beta,R} & 0 \\ 0 & K_{\gamma,R} \end{bmatrix}}_{\text{robot}} \right\} \begin{bmatrix} \beta \\ \gamma \end{bmatrix}$$

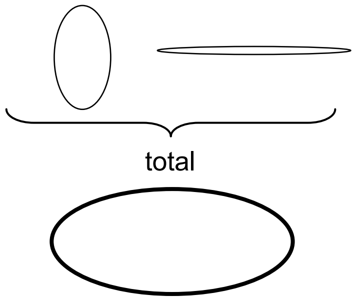

Figure 7.11: Schematic of addition of wrist and robot stiffness in static diagonal force field.

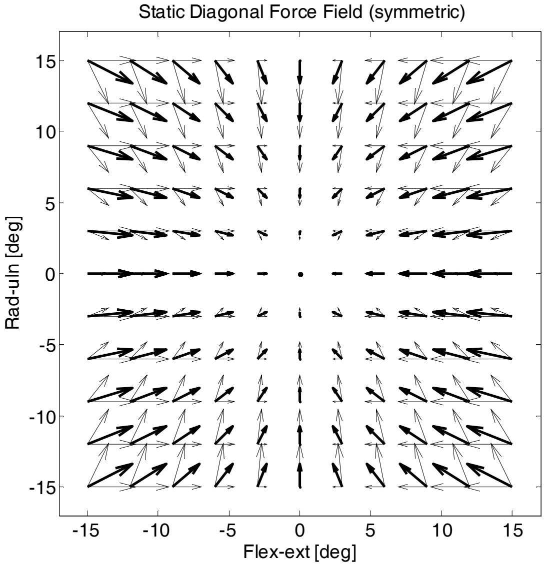

Figure 7.12: Wrist and robot force fields add to give the total force field.
Plotted are torque due to wrist stiffness (thin oblique vectors) and robot stiffness (thin horizontal vectors), and wrist+robot stiffness (thick vectors) as a function of wrist orientation.

If the movement distance in flex-ext is twice as large as in rad-uln, one can maintain the same relationship between torques felt at the target (the target at the flex-ext targets is twice as large as at the rad-uln targets) by decreasing the stiffness in flex-ext by a factor of 2:

$$\vec{\tau} = K_{\beta,W}\begin{bmatrix} 2 & 0 \\ 0 & 2 \end{bmatrix}\begin{bmatrix} \beta \\ \gamma \end{bmatrix}$$

The resulting asymmetric torque plot is shown in Figure 7.13. Both diagonal and anti-diagonal perturbation torques can be seen in reference to other torque components in Figure 7.14.

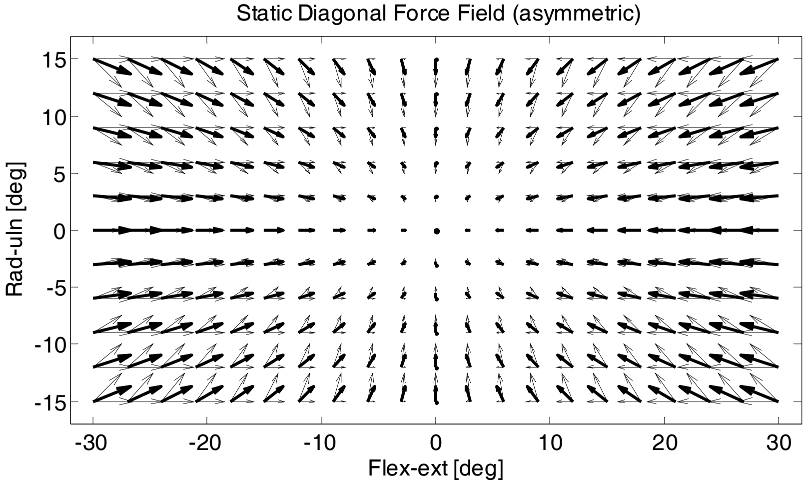

Figure 7.13: Wrist and robot force fields add to give the total force field for asymmetric field. Plotted are torque due to wrist stiffness (thin oblique vectors) and robot stiffness (thin horizontal vectors), and wrist+robot stiffness (thick vectors) as a function of wrist orientation.

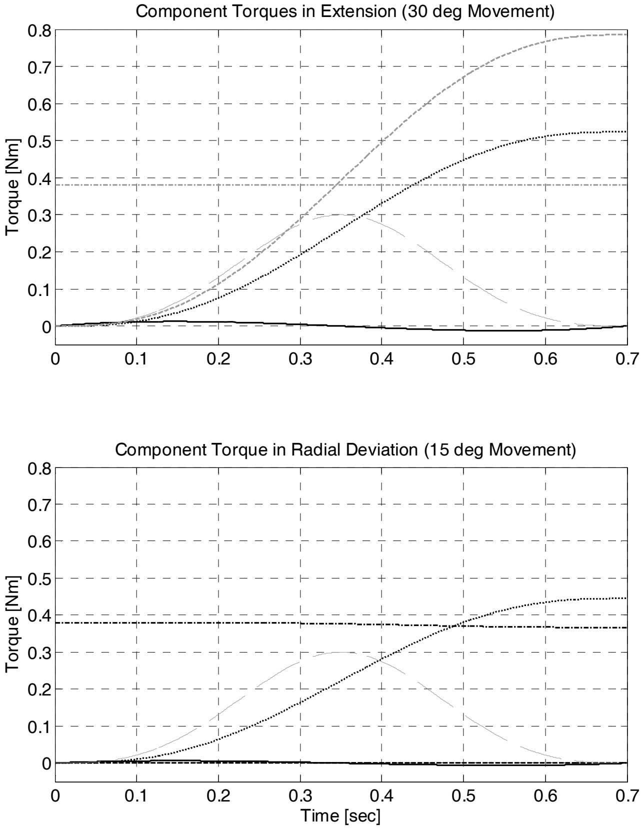

Figure 7.14: Diagonal and anti-diagonal perturbation torques.

These torques are shown in reference to other component torques in extension (30° movement) and radial deviation (15° movement) as a function of time. Inertial torques are solid, passive stiffness torques dotted, perturbation torques dashed (diagonal torques are thick dashed, while anti-diagonal torques are thin dashed), and gravitational torques dash-dotted. Torques acting out of the plane of movement are gray. Movements are derived from the minimum jerk model with a movement duration of 0.7 sec. For other parameters, see the caption of Figure 7.7.

8 Conclusion

The goal of this dissertation was to lay a quantitative foundation of unimpaired human wrist rotation behavior, on which to build and evaluate wrist rehabilitation following neurological or biomechanical injury. Such a foundation has already been laid for the rehabilitation of shoulder and elbow movements, thanks to decades of fundamental research investigating the biomechanics and neural control of *reaching* movements. By comparison, with the notable exception of Peter Strick and Donna Hoffman of the University of Pittsburgh, the coordination of wrist rotations in both its DOF has received virtually no attention. Therefore, this dissertation begins with the basics, presenting kinematic and dynamic models of wrist rotations. Though basic, the kinematics and dynamics of rigid-body rotations about multiple axes are by no means trivial, and the models presented in this dissertation provide a useful and rigorous framework in which multi-DOF wrist rotation behavior can be analyzed and interpreted. With this mathematical foundation in place, this dissertation then presents a number of experimental observations, which are best explained in comparison to reaching movements.

8.1 Comparison of wrist rotations and reaching movements

8.1.1 Reaching

The study of the kinematics and coordination of reaching movements has done much to elucidate how the nervous and biomechanical systems of the body work together to produce coordinated upper-limb movements. Decades of research have uncovered the hierarchical relationship between kinematic and dynamic control, the process of motor planning in an external representation, and challenges of (and strategies for) controlling the complex dynamics of the upper limb, among many other discoveries (see Table 8.1).

Hierarchy: The invariance of human reaching movements under different speeds and loading conditions suggested that kinematics play a prominent role in planning reaching movements. Further evidence of kinematic control was provided by adaptation studies in which human subjects straightened their reaching paths in the face of mechanical or visual perturbations. Though dynamic considerations may play a role, the kinematic plan appears to be primary.

Planning: This invariance was observed in the kinematics of the hand, but not in the kinematics of the shoulder and elbow joints, implying planning at the level of the hand, i.e. in an extrinsic reference frame.

Dynamics: Under kinematic control, the kinematic plan is established, from which the muscle activation required to produce that kinematic plan is determined. Humans' ability to make graceful movements under a large variety of conditions implies the existence of an internal model of dynamics relating muscle activation to limb kinematics. The dynamics of reaching movements are dominated by inertial effects, arising from interaction between the arm and forearm as well as from each limb separately.

Challenge: Numerous studies of reaching movements have shown that the nervous system must carefully account for inertial interaction between arm and forearm due to Coriolis and centripetal forces. Controlling reaching movements in the face of non-linear inertial coupling presents a significant control challenge to the nervous system, and has been the focus of much research.

	Reaching	**Wrist Rotation**
Hierarchy	kinematic > dynamics	kinematic > dynamics
Planning	extrinsic	intrinsic ≈ extrinsic
Dynamics	inertia	stiffness
Challenge	interaction torques	anisotropic stiffness

Table 8.1: Comparison of reaching movements and wrist rotations

8.1.2 Wrist Rotations

By comparison, the coordination of wrist rotations has received little attention. The four items in Table 8.1, in particular, have not been available for wrist rotations. The thrust of my doctoral research has been to extend the progress in understanding human movement to wrist rotations. In addition, because wrist rotations differ from translational reaching in a number of kinematically significant ways (Chapter 2), the comparison of reaching movements and wrist rotations can inform us about which control strategies are unique to each joint, and which the nervous system uses more commonly throughout the body.

Hierarchy: In apparent contrast to the invariance of reaching movements, we have shown that wrist rotations exhibit significantly more path curvature and variability than reaching movements (Chapter 3). This path curvature forms a stereotypical pattern in different directions and increases significantly with movement speed. The increased path curvature could lead one to believe that wrist rotations may not be under kinematic control of hand position. However, we have provided evidence that the observed pattern of curvature is not due to central planning or control, but rather to imperfect peripheral execution. In order to determine whether wrist rotations are under kinematic or dynamic control, we have performed perturbation experiments involving wrist rotations (Chapter 7). Subjects consistently adapted to a conservative, velocity-dependent force field. Interestingly, this adaptation was more difficult to detect than in perturbation studies involving reaching movements, consistent with the hypothesis that wrist rotations are implemented by a less perfect, or sloppier, controller. Taken together, the results in Chapter 7 suggest that wrist rotations are also primarily under kinematic control (albeit imperfect control).

Planning: Projecting the kinematics of reaching movements into extrinsic (hand) and intrinsic (joint) spaces has provided evidence that planning occurs at the level of the hand (as opposed to the should and elbow joints). The wrist is different: for much of the wrist's workspace, extrinsic and intrinsic spaces are virtually indistinguishable (Chapter 3).

Dynamics: We have created an anatomically accurate model of wrist dynamics, in which the wrist is modeled as a universal joint with an offset between the axes. Combining experimental measurements with the inverse dynamic wrist model, we have shown that wrist rotation dynamics are dominated by stiffness, not inertia as in reaching movements (Chapter 4). Only at the upper limit of movement speed do inertial effects become important in wrist rotations. Even then, inertial interactions between the degrees of freedom of the wrist are negligible.

Challenge: Using the model of wrist dynamics, we have shown that the pattern of curvature observed in wrist rotations is most likely caused by wrist stiffness (Chapters 5 and 6). In fact, two features of wrist stiffness—wrist stiffness is anisotropic and slightly pronated—can account for five of six prominent features of the observed pattern of path curvature.

8.2 Future Work

Any good study sets some things in stone while raising new questions. Following are a number of fascinating research questions which build on the research in this dissertation.

8.2.1 Adaptation

As mentioned above, subjects consistently adapted to force field perturbations, but the adaptation was more difficult to detect than in similar experiments involving reaching movements. Such differences in the way people adapt to perturbations in wrist rotations and reaching movements are fascinating, and further exploration may yield insights into central representation or control.

8.2.2 Speed

Much of this research has focused on the presence or absence of kinematic invariances in wrist rotation paths, given that reaching path shape was found to be relatively invariant. However, for reaching movements, speed profiles have been found to be even more invariant than path shape. Across different dynamic conditions, speed profiles of reaching movements are remarkably smooth with one bell-shaped peak. In contrast, preliminary investigation of speed profiles in wrist rotations (not included in this dissertation) showed speed profiles with multiple peaks. A rigorous investigation of speed profiles in wrist rotations would further clarify the role of kinematic invariances in wrist rotations, and perhaps illuminate the role of submovements in movement generation.

8.2.3 Pronation-supination

Initial wrist rotation experiments involving flex-ext and rad-uln revealed that humans made significant use of a third DOF, pro-sup, despite the fact that the tasks only required two DOF. For simplicity, the distal forearm was constrained against pro-sup in all experiments described in this dissertation. However, a fascinating research question is why humans made use of three DOF for a 2-DOF task. Does it reflect an attempt to straighten paths? Or perhaps to follow a “path of least resistance” in an effort to minimize stiffness torques?

8.2.4 Ecological wrist behavior

For ease of analysis and interpretation, all experiments in this dissertation involved discrete center-out and out-center movements. While such experiments are a necessary starting point, they are clearly not a perfect reflection of natural (ecological) wrist behavior. Experiments involving tasks of daily living (teeth brushing, writing, cooking, etc.) would provide a more reliable assessment of the kinematics, dynamics, and even adaptation of natural wrist rotations. A method for using the FOB motion sensor system to determine upper limb orientation during activities of daily living is given in Appendix C.

8.2.5 Comparison to ankle movements

The bone structure of the upper and lower limbs exhibit remarkable similarities. The joint of the lower limb that corresponds to the wrist is the ankle. Both joints consist of many, small bones, held together by an intricate network of ligaments. Though the actual motion at both joints is accomplished through complex motion of individual bones, global joint behavior at both joints can be approximated as rotation about two non-parallel, non-intersecting axes. Given that the kinematics and dynamics of rigid-body rotation about multiple axes in non-trivial, it may be useful to apply the models presented in this dissertation to the study of ankle rotation behavior. Furthermore, there may be other similarities (e.g. involving function or central control) which could prove useful in understanding the control of the ankle, with application to ankle rehabilitation.

Bibliography

[1] H. I. Krebs, B. T. Volpe, M. L. Aisen, and N. Hogan, "Increasing productivity and quality of care: Robot-aided neuro-rehabilitation," *Journal of Rehabilitation Research and Development*, vol. 37, pp. 639-652, 2000.

[2] H. I. Krebs, J. J. Palazzolo, L. Dipietro, B. T. Volpe, and N. Hogan, "Rehabilitation robotics: Performance-based progressive robot-assisted therapy," *Autonomous Robots*, vol. 15, pp. 7-20, 2003.

[3] H. Krebs, B. T. Volpe, D. Williams, J. Celestino, S. Charles, D. Lynch, and N. Hogan, "Robot-aided neurorehabilitation: a robot for the wrist rehabilitation," *IEEE Transactions on Neural Systems and Rehabilitation Engineering*, vol. 15, pp. 327-335, 2007.

[4] K.-N. An, R. A. Berger, and W. P. I. Cooney, "Biomechanics of the Wrist Joint." New York: Springer-Verlag, 1991.

[5] C. C. Norkin and D. J. White, "The Wrist and Hand," in *Measurement of Joint Motion: A Guide to Goniometry*, 2 ed. Philadelphia: F. A. Davis Company, 1985, pp. 79-93.

[6] A. Murgia, P. J. Kyberd, P. H. Chappell, and C. M. Light, "Marker placement to describe the wrist movements during activities of daily living in cyclical tasks," *Clinical Biomechanics*, vol. 19, pp. 248-254, 2004.

[7] R. B. Brumbaugh, R. D. Crowninshield, W. F. Blair, and J. G. Andrews, "An Invivo Study of Normal Wrist Kinematics," *Journal of Biomechanical Engineering-Transactions of the Asme*, vol. 104, pp. 176-181, 1982.

[8] G. Wu, F. C. T. van der Helm, H. E. J. Veeger, M. Makhsous, P. Van Roy, C. Anglin, J. Nagels, A. R. Karduna, K. McQuade, X. G. Wang, F. W. Werner, and B. Buchholz, "ISB recommendation on definitions of joint coordinate systems of various joints for the reporting of human joint motion - Part II: shoulder, elbow, wrist and hand," *Journal of Biomechanics*, vol. 38, pp. 981-992, 2005.

[9] J. G. Andrews and Y. Youm, "Biomechanical Investigation of Wrist Kinematics," *Journal of Biomechanics*, vol. 12, pp. 83-93, 1979.

[10] P. Salvia, L. Woestyn, J. H. David, V. Feipel, S. Van, S. Jan, P. Klein, and M. Rooze, "Analysis of helical axes, pivot and envelope in active wrist circumduction," *Clinical Biomechanics*, vol. 15, pp. 103-111, 2000.

[11] Y. Youm and Y. S. Yoon, "Analytical Development in Investigation of Wrist Kinematics," *Journal of Biomechanics*, vol. 12, pp. 613-621, 1979.

[12] L. Leonard, D. Sirkett, G. Mullineux, G. E. B. Giddins, and A. W. Miles, "Development of an in-vivo method of wrist joint motion analysis," *Clinical Biomechanics*, vol. 20, pp. 166-171, 2005.

[13] Z. M. Li, L. Kuxhaus, J. A. Fisk, and T. H. Christophel, "Coupling between wrist flexion-extension and radial-ulnar deviation," *Clinical Biomechanics*, vol. 20, pp. 177-183, 2005.

[14] C. Gielen and J. C. Houk, "Nonlinear Viscosity of Human Wrist," *Journal of Neurophysiology*, vol. 52, pp. 553-569, 1984.

[15] F. J. ValeroCuevas and C. F. Small, "Load dependence in carpal kinematics during wrist flexion in vivo," *Clinical Biomechanics*, vol. 12, pp. 154-159, 1997.

[16] S. Riek, "The effects of viscous loading of the human forearm flexors on the stability of coordination," *Human Movement Science*, vol. 23, pp. 431-445, 2004.

[17] M. F. Levin, Y. Lamarre, and A. G. Feldman, "Control Variables and Proprioceptive Feedback in Fast Single-Joint Movement," *Canadian Journal of Physiology and Pharmacology*, vol. 73, pp. 316-330, 1995.

[18] M. F. Levin, A. G. Feldman, T. E. Milner, and Y. Lamarre, "Reciprocal and Coactivation Commands for Fast Wrist Movements," *Experimental Brain Research*, vol. 89, pp. 669-677, 1992.

[19] C. A. Lucidi and S. L. Lehman, "Adaptation to Fatigue of Long Duration in Human Wrist Movements," *Journal of Applied Physiology*, vol. 73, pp. 2596-2603, 1992.

[20] D. C. Mackey, D. P. Meichenbaum, J. Shemmell, S. Riek, and R. G. Carson, "Neural compensation for compliant loads during rhythmic movement," *Experimental Brain Research*, vol. 142, pp. 409-417, 2002.

[21] Y. Li, O. Levin, R. G. Carson, and S. P. Swinnen, "Bimanual coordination: constraints imposed by the relative timing of homologous muscle activation," *Experimental Brain Research*, vol. 156, pp. 27-38, 2004.

[22] R. G. Carson, C. J. Smethurst, M. Forner, D. P. Meichenbaum, and D. C. Mackey, "Role of peripheral afference during acquisition of a complex coordination task," *Experimental Brain Research*, vol. 144, pp. 496-505, 2002.

[23] T. Kempf, D. M. Corcos, and D. Flament, "Time course and temporal order of changes in movement kinematics during motor learning: effect of joint and instruction," *Experimental Brain Research*, vol. 136, pp. 295-302, 2001.

[24] M. T. Turvey, C. Carello, P. Fitzpatrick, C. Pagano, and E. Kadar, "Spinors and selective dynamic touch," *Journal of Experimental Psychology-Human Perception and Performance*, vol. 22, pp. 1113-1126, 1996.

[25] S. M. P. Verschueren, P. J. Cordo, and S. P. Swinnen, "Representation of wrist joint kinematics by the ensemble of muscle spindles from synergistic muscles," *Journal of Neurophysiology*, vol. 79, pp. 2265-2276, 1998.

[26] B. E. Mustard and R. G. Lee, "Relationship between Emg Patterns and Kinematic Properties for Flexion Movements at the Human Wrist," *Experimental Brain Research*, vol. 66, pp. 247-256, 1987.

[27] R. Agostino, M. Hallett, and J. N. Sanes, "Antagonist Muscle Inhibition before Rapid Voluntary Movements of the Human Wrist," *Electroencephalography and Clinical Neurophysiology*, vol. 85, pp. 190-196, 1992.

[28] E. G. Butler, D. I. Finkelstein, M. C. Harvey, P. R. Churchward, L. M. Forlano, and M. K. Korne, "The relationship between monkey ventrolateral thalamic nucleus activity and kinematic parameters of wrist movement," *Brain Research*, vol. 736, pp. 146-159, 1996.

[29] M. Lotze, C. Braun, N. Birbaumer, S. Anders, and L. G. Cohen, "Motor learning elicited by voluntary drive," *Brain*, vol. 126, pp. 866-872, 2003.

[30] S. Slobounov, R. Simon, R. Tutwiler, and M. Rearick, "EEG correlates of wrist kinematics as revealed by averaging techniques and Morlet wavelet transforms," *Motor Control*, vol. 4, pp. 350-372, 2000.

[31] H. Topka, S. Mescheriakov, A. Boose, R. Kuntz, I. Hertrich, L. Seydel, J. Dichgans, and J. Rothwell, "A cerebellar-like terminal and postural tremor induced in normal man by transcranial magnetic stimulation," *Brain*, vol. 122, pp. 1551-1562, 1999.

[32] I. S. Chung, J. Y. Ryu, N. Ohnishi, B. Rowen, and J. Headrich, "Wrist Motion Analysis in Pianists," *Medical Problems of Performing Artists*, vol. 7, pp. 1-5, 1992.

[33] K. C. Engel, M. Flanders, and J. F. Soechting, "Anticipatory and sequential motor control in piano playing," *Experimental Brain Research*, vol. 113, pp. 189-199, 1997.

[34] A. M. Pappas, W. J. Morgan, L. A. Schulz, and R. Diana, "Wrist Kinematics During Pitching - a Preliminary-Report," *American Journal of Sports Medicine*, vol. 23, pp. 312-315, 1995.

[35] D. B. Debicki, P. L. Gribble, S. Watts, and J. Hore, "Kinematics of wrist joint flexion in overarm throws made by skilled subjects," *Experimental Brain Research*, vol. 154, pp. 382-394, 2004.

[36] D. S. Hoffman and P. L. Strick, "Step-tracking movements of the wrist. IV. Muscle activity associated with movements in different directions," *Journal of Neurophysiology*, vol. 81, pp. 319-333, 1999.

[37] K. D. Pfann, D. S. Hoffman, G. L. Gottlieb, P. L. Strick, and D. M. Corcos, "Common principles underlying the control of rapid, single degree-of-freedom movements at different joints," *Experimental Brain Research*, vol. 118, pp. 35-51, 1998.

[38] D. S. Hoffman and P. L. Strick, "Step-Tracking Movements of the Wrist in Humans. II. EMG Analysis," *Journal of Neuroscience*, vol. 10, pp. 142-152, 1990.

[39] D. S. Hoffman and P. L. Strick, "Activity of wrist muscles during step-tracking movements in different directions," *Brain Research*, vol. 367, 1986.

[40] D. S. Hoffman and P. L. Strick, "Step-Tracking Movements of the Wrist in Humans. I. Kinematic Analysis," *Journal of Neuroscience*, vol. 6, pp. 3309-3318, 1986.

[41] D. S. Hoffman and P. L. Strick, "Step-Tracking Movements of the Wrist. III. Influence of Changes in Load on Patterns of Muscle-Activity," *Journal of Neuroscience*, vol. 13, pp. 5212-5227, 1993.

[42] S. Kakei, D. S. Hoffman, and P. L. Strick, "Sensorimotor transformations in cortical motor areas," *Neuroscience Research*, vol. 46, pp. 1-10, 2003.

[43] S. Kakei, D. S. Hoffman, and P. L. Strick, "Direction of action is represented in the ventral premotor cortex," *Nature Neuroscience*, vol. 4, pp. 1020-1025, 2001.

[44] S. Kakei, D. S. Hoffman, and P. L. Strick, "Muscle and movement representations in the primary motor cortex," *Science*, vol. 285, pp. 2136-2139, 1999.

[45] J. C. Galloway and G. F. Koshland, "General coordination of shoulder, elbow and wrist dynamics during multijoint arm movements," *Experimental Brain Research*, vol. 142, pp. 163-180, 2002.

[46] F. Debaere, S. P. Swinnen, E. Beatse, S. Sunaert, P. Van Hecke, and J. Duysens, "Brain areas involved in interlimb coordination: A distributed network," *Neuroimage*, vol. 14, pp. 947-958, 2001.

[47] S. Jaric and M. L. Latash, "Learning a pointing task with a kinematically redundant limb: Emerging synergies and patterns of final position variability," *Human Movement Science*, vol. 18, pp. 819-838, 1999.

[48] N. Virjibabul and J. D. Cooke, "Influence of Joint Interactional Effects on the Coordination of Planar 2-Joint Arm Movements," *Experimental Brain Research*, vol. 103, pp. 451-459, 1995.

[49] J. Dean and M. Bruwer, "Control of Human Arm Movements in 2 Dimensions - Paths and Joint Control in Avoiding Simple Linear Obstacles," *Experimental Brain Research*, vol. 97, pp. 497-514, 1994.

[50] M. L. Latash, "The organization of quick corrections within a two-joint synergy in conditions of unexpected blocking and release of a fast movement," *Clinical Neurophysiology*, vol. 111, pp. 975-987, 2000.

[51] E. M. Robertson and R. C. Miall, "Multi-joint limbs permit a flexible response to unpredictable events," *Experimental Brain Research*, vol. 117, pp. 148-152, 1997.

[52] J. D. Cooke and N. Virjibabul, "Reprogramming of Muscle Activation Patterns at the Wrist in Compensation for Elbow Reaction Torques During Planar 2-Joint Arm Movements," *Experimental Brain Research*, vol. 106, pp. 169-176, 1995.

[53] T. M. Moojen, J. G. Snel, M. Ritt, H. W. Venema, J. M. G. Kauer, and K. E. Bos, "In vivo analysis of carpal kinematics and comparative review of the literature," *Journal of Hand Surgery-American Volume*, vol. 28A, pp. 81-87, 2003.

[54] K. Moore and A. Dalley, *Clinically Oriented Anatomy*, Fifth ed. Baltimore, MD: Lippincott Williams & Wilkins, 2006.

[55] H. Goldstein, C. Poole, and J. Safko, *Classical Mechanics*, 3rd ed: Addison Wesley, 2002.

[56] D. Zwillinger, *Standard Mathematical Tables and Formulae*, 31 ed: Chapman & Hall/CRC Press LLC, 2003.

[57] S. H. Crandall, D. C. Karnopp, E. F. J. Kurtz, and D. C. Pridmore-Brown, *Dynamics of Mechanical and Electromechanical Systems*: McGraw-Hill Inc., 1968.

[58] R. Kaufmann, J. Pfaeffle, B. Blankenhorn, K. Stabile, D. Robertson, and R. Goitz, "Kinematics of the midcarpal and radiocarpal joints in radioulnar deviation: An in vitro study," *Journal of Hand Surgery-American Volume*, vol. 30A, pp. 937-942, 2005.

[59] R. A. Kaufmann, H. J. Pfaeffle, B. D. Blankenhorn, K. Stabile, D. Robertson, and R. Goitz, "Kinematics of the midcarpal and radiocarpal joint in flexion and extension: An in vitro study," *Journal of Hand Surgery-American Volume*, vol. 31A, pp. 1142-1148, 2006.

[60] A. Goto, H. Moritomo, T. Murase, K. Oka, K. Sugamoto, T. Arimura, J. Masumoto, S. Tamura, H. Yoshikawa, and T. Ochi, "In vivo three-dimensional wrist motion analysis using magnetic resonance imaging and volume-based registration," *Journal of Orthopaedic Research*, vol. 23, pp. 750-756, 2005.

[61] C. P. Neu, J. J. Crisco, and S. W. Wolfe, "In vivo kinematic behavior of the radio-capitate joint during wrist flexion-extension and radio-ulnar deviation," *Journal of Biomechanics*, vol. 34, pp. 1429-1438, 2001.

[62] J. H. J. Williams, *Fundamentals of Applied Dynamics*: John Wiley & Sons, Inc., 1996.

[63] W. Abend, E. Bizzi, and P. Morasso, "Human Arm Trajectory Formation," *Brain*, vol. 105, pp. 331-348, 1982.

[64] P. Morasso, "Spatial Control of Arm Movements," *Experimental Brain Research*, vol. 42, pp. 223-227, 1981.

[65] C. G. Atkeson and J. M. Hollerbach, "Kinematic Features of Unrestrained Vertical Arm Movements," *Journal of Neuroscience*, vol. 5, pp. 2318-2330, 1985.

[66] T. Flash, "The Control of Hand Equilibrium Trajectories in Multijoint Arm Movements," *Biological Cybernetics*, vol. 57, pp. 257-274, 1987.

[67] D. M. Wolpert, Z. Ghahramani, and M. I. Jordan, "Perceptual-Distortion Contributes to the Curvature of Human Reaching Movements," *Experimental Brain Research*, vol. 98, pp. 153-156, 1994.

[68] R. Shadmehr and F. A. Mussaivaldi, "Adaptive Representation of Dynamics During Learning of a Motor Task," *Journal of Neuroscience*, vol. 14, pp. 3208-3224, 1994.

[69] J. R. Flanagan and A. K. Rao, "Trajectory Adaptation to a Nonlinear Visuomotor Transformation - Evidence of Motion Planning in Visually Perceived Space," *Journal of Neurophysiology*, vol. 74, pp. 2174-2178, 1995.

[70] S. Charles, S. Levy-Tzedek, L. Dipietro, H. Krebs, and N. Hogan, "Why do wrist rotations appear curved?," presented at Society for Neuroscience, Atlanta, GA, 2006.

[71] H. Moritomo, T. Murase, A. Goto, K. Oka, K. Sugamoto, and H. Yoshikawa, "In vivo three-dimensional kinematics of the midcarpal joint of the wrist," *Journal of Bone and Joint Surgery-American Volume*, vol. 88A, pp. 611-621, 2006.

[72] S. L. Delp, A. E. Grierson, and T. S. Buchanan, "Maximum isometric moments generated by the wrist muscles in flexion-extension and radial-ulnar deviation," *Journal of Biomechanics*, vol. 29, pp. 1371-1375, 1996.

[73] K. Yamamoto, D. S. Hoffman, and P. L. Strick, "Rapid and Long-Lasting Plasticity of Input-Output Mapping," *Journal of Neurophysiology*, vol. 96, pp. 2797-2801, 2006.

[74] D. S. Hoffman and P. L. Strick, "Effects of a Primary Motor Cortex Lesion on Step-Tracking Movements of the Wrist," *Journal of Neurophysiology*, vol. 73, pp. 891-895, 1995.

[75] P. Craven and G. Wahba, "Smoothing Noisy Data with Spline Functions - Estimating the Correct Degree of Smoothing by the Method of Generalized Cross-Validation," *Numerische Mathematik*, vol. 31, pp. 377-403, 1979.

[76] C. R. Dohrmann, H. R. Busby, and D. M. Trujillo, "Smoothing Noisy Data Using Dynamic-Programming and Generalized Cross-Validation," *Journal of Biomechanical Engineering-Transactions of the ASME*, vol. 110, pp. 37-41, 1988.

[77] E. Nakano, H. Imamizu, R. Osu, Y. Uno, H. Gomi, T. Yoshioka, and M. Kawato, "Quantitative examinations of internal representations for arm trajectory planning: Minimum commanded torque change model," *Journal of Neurophysiology*, vol. 81, pp. 2140-2155, 1999.

[78] H. J. Sommer and N. R. Miller, "A Technique for Kinematic Modeling of Anatomical Joints," *Journal of Biomechanical Engineering-Transactions of the Asme*, vol. 102, pp. 311-317, 1980.

[79] P. de Leva, "Adjustments to Zatsiorsky-Seluyanov's segment inertia parameters," *Journal of Biomechanics*, vol. 29, pp. 1223-1230, 1996.

[80] D. Formica, H. Krebs, S. Charles, L. Zollo, E. Guglielmelli, and N. Hogan, "Passive Wrist Joint Stiffness Estimation," *In review*, 2008.

[81] J. Ryu, A. K. Palmer, and W. P. Cooney, "Wrist Joint Motion," in *Biomechanics of the Wrist Joint*, K. N. An, R. A. Berger, and W. P. Cooney, Eds. New York: Springer Verlag, 1991, pp. 48-55.

[82] M. Flanders, J. J. Pellegrini, and S. D. Geisler, "Basic features of phasic activation for reaching in vertical planes," *Experimental Brain Research*, vol. 110, pp. 67-79, 1996.

[83] M. Flanders, J. J. Pellegrini, and J. F. Soechting, "Spatial/Temporal Characteristics of a Motor Pattern for Reaching," *Journal of Neurophysiology*, vol. 71, pp. 811-813, 1994.

[84] M. Flanders, "Temporal Patterns of Muscle Activation for Arm Movements in 3-Dimensional Space," *Journal of Neuroscience*, vol. 11, pp. 2680-2693, 1991.

[85] F. A. Mussaivaldi, N. Hogan, and E. Bizzi, "Neural, Mechanical, and Geometric Factors Subserving Arm Posture in Humans," *Journal of Neuroscience*, vol. 5, pp. 2732-2743, 1985.

[86] J. M. Hollerbach and T. Flash, "Dynamic Interactions between Limb Segments During Planar Arm Movement," *Biological Cybernetics*, vol. 44, pp. 67-77, 1982.

[87] N. Hogan, "Mechanical Impedance of Single- and Multi-Articular Systems," in *Multiple Muscle Systems: Biomechanics and Movement Organization*, J. M. Winters and S. L.-Y. Woo, Eds. New York: Springer-Verlag, 1990.

[88] L. Kai, "Effects of varying inertial load on human wrist movement," B.S. thesis, Massachusetts Institute of Technology, Cambridge, MA, 2005.

[89] L. Dipietro, S. Levy-Tzedek, M. Kaufman, S. Charles, H. I. Krebs, and N. Hogan, "Kinematic Analysis of Wrist Motor Learning," presented at Society for Neuroscience, San Diego, CA, 2007.

[90] H. I. Krebs, N. Hogan, W. Hening, S. V. Adamovich, and H. Poizner, "Procedural motor learning in Parkinson's disease," *Experimental Brain Research*, vol. 141, pp. 425-437, 2001.

[91] I. The MathWorks, "Polynomials vs. Splines," in *Splines: An Overview (Spline Toolbox)*, 7.4.0.287 (R2007a) ed, 2007.

[92] G. Strang, *Introduction to Applied Mathematics*: Wellesley Cambridge Press.

Appendix A: Euler angles and transformation matrices

Transformation matrices can be interpreted in several different ways. As a consequence, the relationship between transformation matrices and Euler angles is fraught with opportunities for error and confusion. Appendix A is meant to be helpful as an extension of a thorough introduction to Euler angles and transformation matrices (I recommend [55]).

Rotation about a single axis

For a rotation by θ about the i^{th} coordinate axis (i=x, y, or z), the transformation of coordinates of a stationary vector from xyz-coordinates to x'y'z'-coordinates is:

$$\vec{r}_{x'y'z'} = A_i(\theta)\vec{r}_{xyz}$$

$$A_x = \begin{bmatrix} 1 & 0 & 0 \\ 0 & \cos\theta & \sin\theta \\ 0 & -\sin\theta & \cos\theta \end{bmatrix}$$

$$A_y = \begin{bmatrix} \cos\theta & 0 & -\sin\theta \\ 0 & 1 & 0 \\ \sin\theta & 0 & \cos\theta \end{bmatrix}$$

$$A_z = \begin{bmatrix} \cos\theta & \sin\theta & 0 \\ -\sin\theta & \cos\theta & 0 \\ 0 & 0 & 1 \end{bmatrix}$$

Note the difference in the position of the minus sign in A_y as opposed to A_x and A_z.

Rotation about two axes

Rotate first about z, then x':

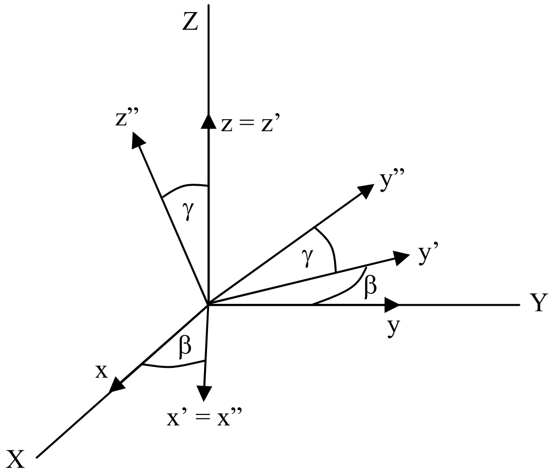

Figure A.1: Schematic of two Euler angle rotations.

First Rotation

$$\hat{i} = \cos\beta\,\hat{i}' - \sin\beta\,\hat{j}' \qquad \hat{i}' = \cos\beta\,\hat{i} + \sin\beta\,\hat{j}$$

$$\hat{j} = \sin\beta\,\hat{i}' + \cos\beta\,\hat{j}' \qquad \hat{j}' = -\sin\beta\,\hat{i} + \cos\beta\,\hat{j}$$

$$\hat{k} = \hat{k}' \qquad \Leftrightarrow \qquad \hat{k}' = \hat{k}$$

$$B = \begin{bmatrix} \cos\beta & \sin\beta & 0 \\ -\sin\beta & \cos\beta & 0 \\ 0 & 0 & 1 \end{bmatrix} \qquad B^{-1} = \begin{bmatrix} \cos\beta & -\sin\beta & 0 \\ \sin\beta & \cos\beta & 0 \\ 0 & 0 & 1 \end{bmatrix}$$

Interpretations:

Forward Transformation

a. *Passive:* $r_{x'y'z'} = Br_{xyz}$: transformation of coordinates of stationary vector r from xyz to x'y'z' frame, which is rotated by β about z relative to xyz.

b. *Active:* $r'_{xyz} = Br_{xyz}$: rotation of vector r by -β about z to r', everything expressed in xyz frame.

Inverse Transformation

c. *Passive:* $r_{xyz} = B^{-1}r_{x'y'z'}$: transformation of coordinates of stationary vector r from x'y'z' to xyz frame.

d. *Active:* $r_{xyz} = B^{-1}r'_{xyz}$: rotation of vector r' by β about z to r, everything expressed in xyz frame.

Forward Transformation in Reverse Direction

e. *Active:* $r'_{xyz} = B^{-1}r_{xyz}$: rotation of vector r by +β about z to r', everything expressed in xyz frame.

Second Rotation

$$\begin{aligned} \hat{i}' &= \hat{i}'' \\ \hat{j}' &= \cos\gamma\, \hat{j}'' - \sin\gamma\, \hat{k}'' \\ \hat{k}' &= \sin\gamma\, \hat{j}'' + \cos\gamma\, \hat{k}'' \end{aligned} \quad \Leftrightarrow \quad \begin{aligned} \hat{i}'' &= \hat{i}' \\ \hat{j}'' &= \cos\gamma\, \hat{j}' + \sin\gamma\, \hat{k}' \\ \hat{k}'' &= -\sin\gamma\, \hat{j}' + \cos\gamma\, \hat{k}' \end{aligned}$$

$$C = \begin{bmatrix} 1 & 0 & 0 \\ 0 & \cos\gamma & \sin\gamma \\ 0 & -\sin\gamma & \cos\gamma \end{bmatrix} \qquad C^{-1} = \begin{bmatrix} 1 & 0 & 0 \\ 0 & \cos\gamma & -\sin\gamma \\ 0 & \sin\gamma & \cos\gamma \end{bmatrix}$$

Interpretations:

Forward Transformation

a. *Passive:* $r_{x''y''z''} = Cr_{x'y'z'}$: transformation of coordinates of stationary vector r from x'y'z' to x"y"z" frame, which is rotated by γ about x' relative to x'y'z'.

b. *Active:* $r''_{x'y'z'} = Cr'_{x'y'z'}$: rotation of vector r' by -γ about x' to r", everything expressed in x'y'z' frame.

Inverse Transformation

c. *Passive:* $r_{x''y''z''} = C^{-1}r_{x'y'z'}$: transformation of coordinates of stationary vector r from x"y"z" to x'y'z' frame.

d. *Active:* $r'_{x'y'z'} = C^{-1}r''_{x'y'z'}$: rotation of vector r" by γ about x' to r', everything expressed in x'y'z' frame.

Forward Transformation in Reverse Direction

e. *Active:* $r''_{x'y'z'} = C^{-1}r'_{x'y'z'}$: rotation of vector r' by +γ about x' to r", everything expressed in x'y'z' frame.

Total Rotation

$$
\begin{aligned}
\hat{i} &= \cos\beta\,\hat{i}'' - \sin\beta\cos\gamma\,\hat{j}'' + \sin\beta\sin\gamma\,\hat{k}'' \\
\hat{j} &= \sin\beta\,\hat{i}'' + \cos\beta\cos\gamma\,\hat{j}'' - \cos\beta\sin\gamma\,\hat{k}'' \\
\hat{k} &= \sin\gamma\,\hat{j}'' + \cos\gamma\,\hat{k}'' \\
A &= CB \\
&= \begin{bmatrix} 1 & 0 & 0 \\ 0 & \cos\gamma & \sin\gamma \\ 0 & -\sin\gamma & \cos\gamma \end{bmatrix}\begin{bmatrix} \cos\beta & \sin\beta & 0 \\ -\sin\beta & \cos\beta & 0 \\ 0 & 0 & 1 \end{bmatrix} \\
&= \begin{bmatrix} \cos\beta & \sin\beta & 0 \\ -\sin\beta\cos\gamma & \cos\beta\cos\gamma & \sin\gamma \\ \sin\beta\sin\gamma & -\cos\beta\sin\gamma & \cos\gamma \end{bmatrix}
\end{aligned}
$$

$$\Leftrightarrow$$

$$
\begin{aligned}
\hat{i}'' &= \cos\beta\,\hat{i} + \sin\beta\,\hat{j} \\
\hat{j}'' &= -\sin\beta\cos\gamma\,\hat{i} + \cos\beta\cos\gamma\,\hat{j} + \sin\gamma\,\hat{k} \\
\hat{k}'' &= \sin\beta\sin\gamma\,\hat{i} - \cos\beta\sin\gamma\,\hat{j} + \cos\gamma\,\hat{k} \\
A^{-1} &= A^{T} = (CB)^{T} = B^{T}C^{T} = B^{-1}C^{-1} = B(-\beta)C(-\gamma) \\
&= \begin{bmatrix} \cos\beta & -\sin\beta & 0 \\ \sin\beta & \cos\beta & 0 \\ 0 & 0 & 1 \end{bmatrix}\begin{bmatrix} 1 & 0 & 0 \\ 0 & \cos\gamma & -\sin\gamma \\ 0 & \sin\gamma & \cos\gamma \end{bmatrix} \\
&= \begin{bmatrix} \cos\beta & -\sin\beta\cos\gamma & \sin\beta\sin\gamma \\ \sin\beta & \cos\beta\cos\gamma & -\cos\beta\sin\gamma \\ 0 & \sin\gamma & \cos\gamma \end{bmatrix}
\end{aligned}
$$

Interpretations:

Sequential rotations about multiple DOF differ substantially from single-DOF rotations and are extremely prone to error.

Forward Transformation

a. *Passive:* $r_{x''y''z''} = Ar_{xyz}$: transformation of coordinates of stationary vector r from xyz to x”y”z” frame, which is rotated by β about z and then by γ about x’ relative to xyz.

b. *Active:* $r''_{xyz} = Ar_{xyz}$: rotation of vector r by -γ about x and then by -β about z’ to r” (reversed order!), everything expressed in xyz frame.

c. *Active:* $r''_{xyz} = Ar_{xyz}$: rotation of vector r by -β about z and then by -γ about x (not x’!) to r”, everything expressed in xyz frame.

Inverse Transformation

d. *Passive:* $r_{xyz} = A^{-1}r_{x''y''z''}$: transformation of coordinates of stationary vector r from x”y”z” to xyz frame.

e. *Active:* $r_{xyz} = A^{-1}r''_{xyz}$: rotation of vector r” by +β about z’ and then by +γ about x to r, everything expressed in xyz frame.

f. *Active:* $r_{xyz} = A^{-1}r''_{xyz}$: rotation of vector r” by +γ about x (not x’!) and then by +β about z to r, everything expressed in xyz frame.

Forward Transformation in Reverse Order

g. $r''_{xyz} = A^{-1}r_{xyz}$: rotation of vector r by +β about z and then by +γ about x' (positive angles!), everything expressed in xyz frame.

h. $r''_{xyz} = A^{-1}r_{xyz}$: rotation of vector r by +γ about x and then by +β about z (not z'!) to r", everything expressed in xyz frame.

Forward Transformation in Reverse Direction

i. $r''_{xyz} = A(-\beta,-\gamma)r_{xyz}$: rotation of vector r by +β about z and then by +γ about x (not x'!) to r", everything expressed in xyz frame.

Summary

a. To determine the transformation matrix associated with sequential rotations of a vector—always expressed in a space-fixed frame—about body-fixed axes, express the rotated unit vectors in terms of the space-fixed unit vectors, and fill in the transformation matrix. For example, for a vector rotated first by +β about z and then by γ about x':

$$\hat{i}'' = \cos\beta\,\hat{i} + \sin\beta\,\hat{j}$$
$$\hat{j}'' = -\sin\beta\cos\gamma\,\hat{i} + \cos\beta\cos\gamma\,\hat{j} + \sin\gamma\,\hat{k}$$
$$\hat{k}'' = \sin\beta\sin\gamma\,\hat{i} - \cos\beta\sin\gamma\,\hat{j} + \cos\gamma\,\hat{k}$$
$$A = \begin{bmatrix} \cos\beta & -\sin\beta\cos\gamma & \sin\beta\sin\gamma \\ \sin\beta & \cos\beta\cos\gamma & -\cos\beta\sin\gamma \\ 0 & \sin\gamma & \cos\gamma \end{bmatrix}$$

b. Alternatively, one could compute the transformation matrix as a matrix multiplication of the individual rotations, but one must be vigilant to take the inverse of the product:

$$A = (CB)^{-1} = (CB)^{T} = B^{T}C^{T}$$

$$A = \left\{ \begin{bmatrix} 1 & 0 & 0 \\ 0 & \cos\gamma & \sin\gamma \\ 0 & -\sin\gamma & \cos\gamma \end{bmatrix} \begin{bmatrix} \cos\beta & \sin\beta & 0 \\ -\sin\beta & \cos\beta & 0 \\ 0 & 0 & 1 \end{bmatrix} \right\}^{T}$$

$$A = \begin{bmatrix} \cos\beta & -\sin\beta & 0 \\ \sin\beta & \cos\beta & 0 \\ 0 & 0 & 1 \end{bmatrix} \begin{bmatrix} 1 & 0 & 0 \\ 0 & \cos\gamma & -\sin\gamma \\ 0 & \sin\gamma & \cos\gamma \end{bmatrix}$$

$$A = \begin{bmatrix} \cos\beta & -\sin\beta\cos\gamma & \sin\beta\sin\gamma \\ \sin\beta & \cos\beta\cos\gamma & -\cos\beta\sin\gamma \\ 0 & \sin\gamma & \cos\gamma \end{bmatrix}$$

c. Rotating a vector about body-fixed axes is always the same as rotating by the same angles about space-fixed axes in reverse order. For example, rotating a vector r—always expressed in xyz—by β about z and then by γ about x’ is the same as rotating r by γ about x and then by β about z (not z’!).

Appendix B: Measuring wrist coordinates with The Flock of Birds motion sensor system

Reference frames

The reference frames of the Flock of Birds (FOB) motion sensor system is given on p. 66 of the Flock of Birds Installation and Operation Guide. Note that the equations given below only hold if the relative orientation of transmitter and sensor are as shown in Figure B.1 (front and back sides are indicated as the Flock of Birds symbol and the power cable, respectively).

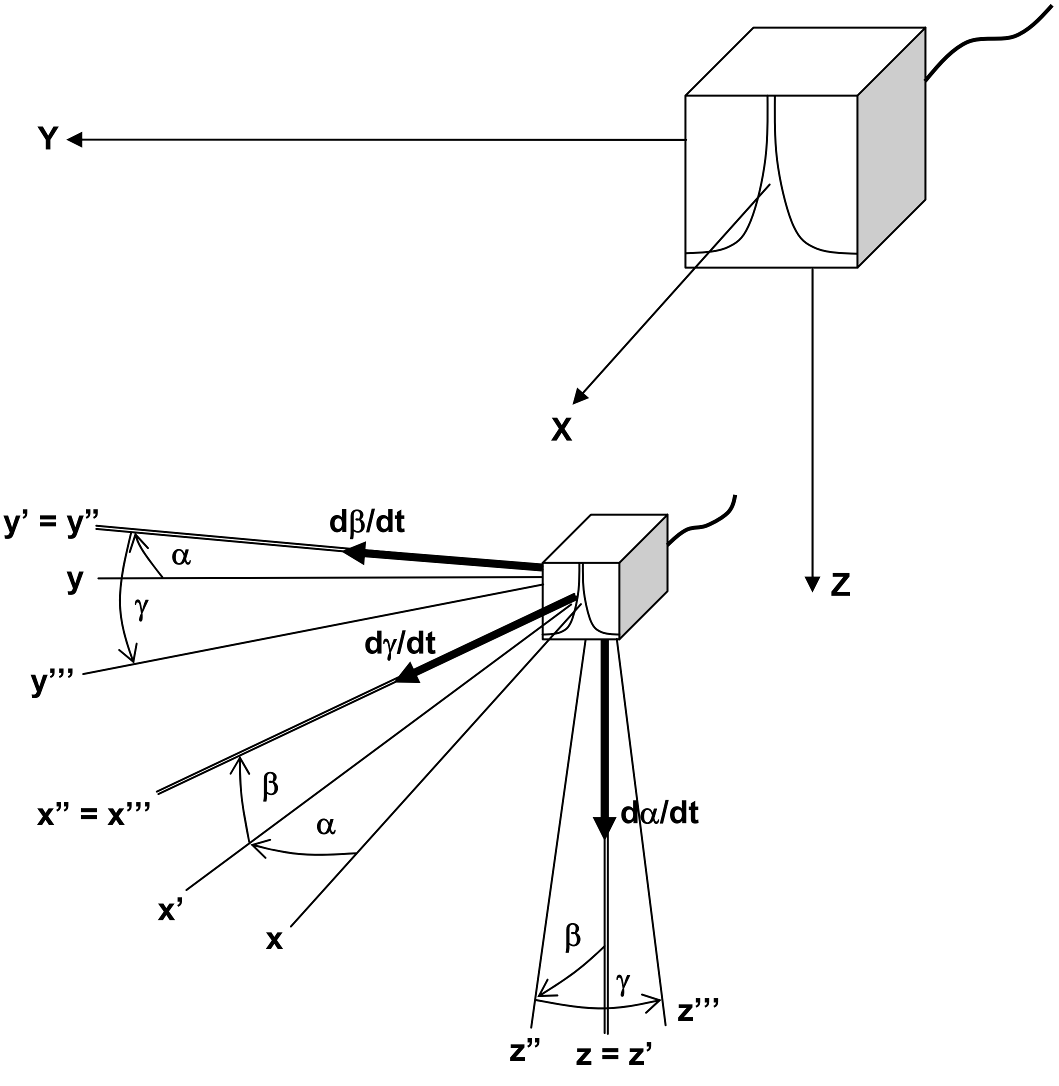

Figure B.1: Schematic of the FOB reference frames.

Consider a vector, $\vec{r}$, expressed in the xyz frame. Let this same vector be expressed in an arbitrary frame x'y'z' as $\vec{r}\,'$. First, rotate the xyz frame about the z axis by α to produce the x'y'z' frame. Then $\vec{r}\,' = D\vec{r}$, where

$$D = \begin{bmatrix} \cos\alpha & \sin\alpha & 0 \\ -\sin\alpha & \cos\alpha & 0 \\ 0 & 0 & 1 \end{bmatrix}$$

Second, rotate the x'y'z' frame about the y' axis by β to produce the x"y"z" frame. Then $\vec{r}\,'' = C\vec{r}\,' = CD\vec{r}$, where

$$C = \begin{bmatrix} \cos\beta & 0 & -\sin\beta \\ 0 & 1 & 0 \\ \sin\beta & 0 & \cos\beta \end{bmatrix}$$

Third, rotate the x"y"z" frame about the x" axis by γ to produce the x'''y'''z''' frame. Then $\vec{r}\,''' = B\vec{r}\,'' = BCD\vec{r}$, where

$$B = \begin{bmatrix} 1 & 0 & 0 \\ 0 & \cos\gamma & \sin\gamma \\ 0 & -\sin\gamma & \cos\gamma \end{bmatrix}$$

The vector $\vec{r}$ is expressed in the x'''y'''z''' frame as $\vec{r}\,''' = BCD\vec{r} = A\vec{r}$, where

$$A = \begin{bmatrix} \cos\alpha\cos\beta & \sin\alpha\cos\beta & -\sin\beta \\ \cos\alpha\sin\beta\sin\gamma - \sin\alpha\cos\gamma & \sin\alpha\sin\beta\sin\gamma + \cos\alpha\cos\gamma & \cos\beta\sin\gamma \\ \cos\alpha\sin\beta\cos\gamma + \sin\alpha\sin\gamma & \sin\alpha\sin\beta\cos\gamma - \cos\alpha\sin\gamma & \cos\beta\cos\gamma \end{bmatrix}$$

In the *Flock of Birds* Installation and Operation Guide, the angles are named for the rotated axis about which the rotation occurs: Z = α, Y = β, and X = γ. The matrix A is given on p. 97 of this guide as

$$A = \begin{bmatrix} \cos Z \cos Y & \sin Z \cos Y & -\sin Y \\ \cos Z \sin Y \sin X - \sin Z \cos X & \sin Z \sin Y \sin X + \cos Z \cos X & \cos Y \sin X \\ \cos Z \sin Y \cos X + \sin Z \sin X & \sin Z \sin Y \cos X - \cos Z \sin X & \cos Y \cos X \end{bmatrix}$$

If the vector is given in terms of the x'''y'''z''' frame (i.e. if $\vec{r}'''$ is given), then this vector can be expressed in terms of the xyz frame as $\vec{r} = A^{-1}\vec{r}''' = A^{T}\vec{r}'''$, where

$$A^{-1} = A^{T} = \begin{bmatrix} \cos\alpha\cos\beta & \cos\alpha\sin\beta\sin\gamma - \sin\alpha\cos\gamma & \cos\alpha\sin\beta\cos\gamma + \sin\alpha\sin\gamma \\ \sin\alpha\cos\beta & \sin\alpha\sin\beta\sin\gamma + \cos\alpha\cos\gamma & \sin\alpha\sin\beta\cos\gamma - \cos\alpha\sin\gamma \\ -\sin\beta & \cos\beta\sin\gamma & \cos\beta\cos\gamma \end{bmatrix}$$

Wrist orientation

The third metacarpal bone points in the direction of $-\hat{i}'''$. If $\vec{r}''' = -\hat{i}'''$, then this same vector is expressed in the xyz frame as $\vec{r} = A^{T}\vec{r}''' = -A^{T}\hat{i}'''$. Because the XYZ and xyz frames are rotationally identical, $\vec{r} = -A^{T}\hat{i}'''$ is also the expression of $\vec{r}$ in the XYZ frame. Note that $\vec{r} = -A^{T}\hat{i}'''$ is independent of γ because rotating about the pointing direction cannot influence the pointing direction. The projection of $\vec{r}$ onto the YZ frame can be computed as

$$\vec{r}_{YZ} = \begin{bmatrix} 0 & 0 & 0 \\ 0 & 1 & 0 \\ 0 & 0 & 1 \end{bmatrix} \vec{r} = -\begin{bmatrix} 0 & 0 & 0 \\ 0 & 1 & 0 \\ 0 & 0 & 1 \end{bmatrix} A^{T}\hat{i}''' = -\begin{bmatrix} 0 & 0 & 0 \\ 0 & 1 & 0 \\ 0 & 0 & 1 \end{bmatrix} \begin{bmatrix} \cos\alpha\cos\beta \\ \sin\alpha\cos\beta \\ -\sin\beta \end{bmatrix} = \begin{bmatrix} 0 \\ -\sin\alpha\cos\beta \\ \sin\beta \end{bmatrix}$$

Speed

The angular velocity vector $\vec{\omega}$ can be written as:

$$\vec{\omega} = \dot{\alpha}\hat{k} + \dot{\beta}\hat{j}' + \dot{\gamma}\hat{i}'' \cdot$$

In order to express $\vec{\omega}$ in terms of the space-fixed reference frame XYZ, $\hat{j}'$ and $\hat{i}''$ must be written in terms of xyz unit vectors. The vector $\hat{j}'$ can be written as $-\sin\alpha\hat{i} + \cos\alpha\hat{j}$, while the vector $\hat{i}''$ can be written as $A^{-1}\hat{i}'' = \cos\alpha\cos\beta\hat{i} + \sin\alpha\cos\beta\hat{j} - \sin\beta\hat{k}$. Therefore,

$$\vec{\omega} = \left(-\dot{\beta}\sin\alpha + \dot{\gamma}\cos\alpha\cos\beta\right)\hat{i} + \left(\dot{\beta}\cos\alpha + \dot{\gamma}\sin\alpha\cos\beta\right)\hat{j} + \left(\dot{\alpha} - \dot{\gamma}\sin\beta\right)\hat{k}$$

The magnitude of $\vec{\omega}$ can then be computed as:

$$|\vec{\omega}| = \sqrt{\left(-\dot{\beta}\sin\alpha + \dot{\gamma}\cos\alpha\cos\beta\right)^2 + \left(\dot{\beta}\cos\alpha + \dot{\gamma}\sin\alpha\cos\beta\right)^2 + \left(\dot{\alpha} - \dot{\gamma}\sin\beta\right)^2}$$

Terms combine or cancel to give

$$\boxed{|\vec{\omega}| = \sqrt{\dot{\alpha}^2 + \dot{\beta}^2 + \dot{\gamma}^2 - 2\dot{\alpha}\dot{\gamma}\sin\beta}}$$

The correction term in $|\vec{\omega}|$ accounts for the fact that while $\hat{k}$ and $\hat{j}'$ are always perpendicular (and their magnitudes can therefore be added as sum of the squares), $\hat{k}$ and $\hat{i}''$ are only perpendicular if β is equal to zero or 180°. If β is not equal to zero or 180°, then $\hat{k}$ and $\hat{i}''$ will have parallel components, and their magnitudes cannot simply be added as a sum of the squares. For example, if $\beta = -90°$, then $\hat{k}$ and $\hat{i}''$ point in the same direction, and

$$|\vec{\omega}| = \sqrt{\dot{\alpha}^2 + \dot{\beta}^2 + \dot{\gamma}^2 + 2\dot{\alpha}\dot{\gamma}} = \sqrt{\left(\dot{\alpha} + \dot{\gamma}\right)^2 + \dot{\beta}^2}$$

Note that for small β, $\sin\beta \approx \beta \approx 0$, and

$$|\vec{\omega}| \approx \sqrt{\dot{\alpha}^2 + \dot{\beta}^2 + \dot{\gamma}^2}$$

Appendix C: Derivation of upper-limb coordinates from transformation matrices

This section illustrates how to derive elbow flex-ext, forearm pro-sup, and wrist flex-ext and rad-uln from Flock of Birds (FOB) sensors on the arm, forearm and hand. A specific example is used. For simplicity, Figure C.1 shows movement in the parasaggital plane, but the derivation is valid for general 3-D movements. The coordinates of the arm, forearm and hand are defined according to ISB definition and denoted by $[u_i,v_i,w_i]$, where i = 1 (arm), 2 (forearm), and 3 (hand). The coordinates of the corresponding sensors are denoted $[x_i,y_i,z_i]$. The coordinates of the space-fixed FOB transmitter are [X,Y,Z].

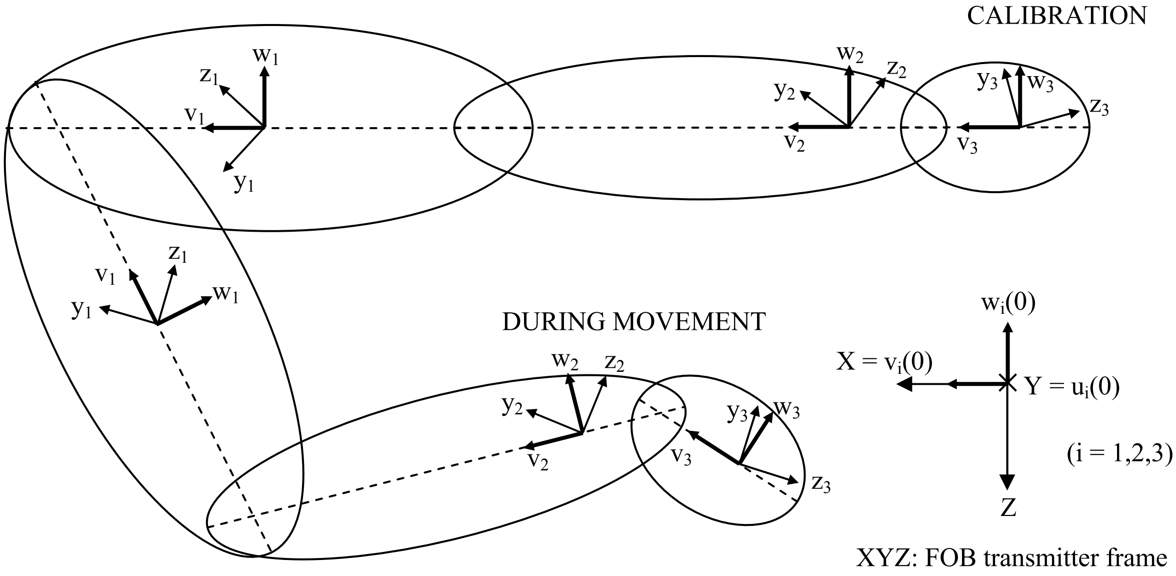

Figure C.1: Schematic of the sensor placement

The FOB software outputs for every point in time the transformation from XYZ to $x_iy_iz_i$. In order to determine elbow flex-ext, forearm pro-sup, and wrist flex-ext and rad-uln, the transformations from $u_1v_1w_1$ to $u_2v_2w_2$ and from $u_2v_2w_2$ to $u_3v_3w_3$ must be known.

	Transformation	Matrix	Time

Given	from XYZ to $x_1y_1z_1(0)$	A	Initial
	from XYZ to $x_1y_1z_1$	B	Time-varying
	from XYZ to $x_2y_2z_2(0)$	C	Initial
	from XYZ to $x_2y_2z_2$	D	Time-varying
	from XYZ to $x_3y_3z_3(0)$	E	Initial
	from XYZ to $x_3y_3z_3$	F	Time-varying
Find	from $u_1v_1w_1$ to $u_2v_2w_2$	G	Time-varying
	from $u_2v_2w_2$ to $u_3v_3w_3$	H	Time-varying

Initially (at time t=0), the arm, forearm and wrist are calibrated by aligning $u_i(0)$ with Y, $v_i(0)$ with X, and $w_i(0)$ with –Z, as shown in Figure C.1. Therefore, the transformation from XYZ to $u_iv_iw_i(0)$ is given by O:

$$O = \begin{bmatrix} 0 & 1 & 0 \\ 1 & 0 & 0 \\ 0 & 0 & -1 \end{bmatrix}$$

During calibration the FOB software outputs the transformation from XYZ to $x_iy_iz_i(0)$. The transformation from $u_iv_iw_i(0)$ to $x_iy_iz_i(0)$ can be determined as follows for each sensor:

$$\text{Sensor 1}: XYZ \xrightarrow{O} u_1v_1w_1(0) \xrightarrow{R} x_1y_1z_1(0) \xrightarrow{A^{-1}} XYZ$$

$$A^{-1}RO = I$$

$$R = AO^{-1}$$

$$\text{Sensor 2}: XYZ \xrightarrow{O} u_2v_2w_2(0) \xrightarrow{S} x_2y_2z_2(0) \xrightarrow{C^{-1}} XYZ$$

$$C^{-1}SO = I$$

$$S = CO^{-1}$$

$$\text{Sensor 3}: XYZ \xrightarrow{O} u_3v_3w_3(0) \xrightarrow{T} x_3y_3z_3(0) \xrightarrow{E^{-1}} XYZ$$

$$E^{-1}TO = I$$

$$T = EO^{-1}$$

The key to finding G and H is to realize that at any point in time the transformation from $u_iv_iw_i$ to $x_iy_iz_i$ is the same as the transformation from $u_iv_iw_i(0)$ to $x_iy_iz_i(0)$, which is given by R, S, and T. With this in mind, one can determine G from the following series of transformations:

$$XYZ \xrightarrow{B} x_1y_1z_1 \xrightarrow{R^{-1}} u_1v_1w_1 \xrightarrow{G} u_2v_2w_2 \xrightarrow{S} x_2y_2z_2 \xrightarrow{D^{-1}} XYZ$$
$$D^{-1}SGR^{-1}B = D^{-1}CO^{-1}GOA^{-1}B = I$$
$$G = OC^{-1}DB^{-1}AO^{-1}$$

Similarly, H can be found from the following series of transformations:

$$XYZ \xrightarrow{D} x_2y_2z_2 \xrightarrow{S^{-1}} u_2v_2w_2 \xrightarrow{H} u_3v_3w_3 \xrightarrow{T} x_3y_3z_3 \xrightarrow{F^{-1}} XYZ$$
$$F^{-1}THS^{-1}D = F^{-1}EO^{-1}HOC^{-1}D = I$$
$$H = OE^{-1}FD^{-1}CO^{-1}$$

To derive elbow flex-ext and forearm pro-sup from G, one must represent G in terms of Euler angles that match the anatomy. To transform from $u_1v_1w_1$ to $u_2v_2w_2$, rotate first about u_1 by δ (elbow flex-ext, extension is positive), then about the once-rotated v_1 axis by α (pro-sup, pronation is positive), and finally about the twice-rotated w_1 axis by ε (negligible). This transformation is of type x-y-z:

$$G = \begin{bmatrix} \cos\varepsilon & \sin\varepsilon & 0 \\ -\sin\varepsilon & \cos\varepsilon & 0 \\ 0 & 0 & 1 \end{bmatrix} \begin{bmatrix} \cos\alpha & 0 & -\sin\alpha \\ 0 & 1 & 0 \\ \sin\alpha & 0 & \cos\alpha \end{bmatrix} \begin{bmatrix} 1 & 0 & 0 \\ 0 & \cos\delta & \sin\delta \\ 0 & -\sin\delta & \cos\delta \end{bmatrix}$$
$$= \begin{bmatrix} \cos\alpha\cos\varepsilon & \sin\delta\sin\alpha\cos\varepsilon + \cos\delta\sin\varepsilon & -\cos\delta\sin\alpha\cos\varepsilon + \sin\delta\sin\varepsilon \\ -\cos\alpha\sin\varepsilon & -\sin\delta\sin\alpha\sin\varepsilon + \cos\delta\cos\varepsilon & \cos\delta\sin\alpha\sin\varepsilon + \sin\delta\cos\varepsilon \\ \sin\alpha & -\sin\delta\cos\alpha & \cos\delta\cos\alpha \end{bmatrix}$$

The angle α equals pro-sup, with α = asin[G(3,1)], where pronation is positive. The angle δ equals elbow elbow flex-ext, with δ = asin[-G(3,2)/cosα], where extension is positive. Note that pro-sup may reach ±90° at the joint limits, causing a division by zero in the equation for δ, so it may be necessary to worry about gimble lock.

Likewise, wrist flex-ext and rad-uln can be derived from H by writing H in terms of Euler angles. To transform from $u_2v_2w_2$ to $u_3v_3w_3$, rotate first about w_2 by β (wrist flex-ext, flexion is positive), then about the once-rotated u_2 axis by γ (wrist rad-uln, ulnar deviation is positive), and finally about the twice-rotated v_1 axis by ϕ (pro-sup at the wrist, pronation is positive, but it's negligible—this is not the same as pro-sup at the distal radioulnar joint). This transformation is of type z-x-y:

$$H=\begin{bmatrix}\cos\phi & 0 & -\sin\phi\\ 0 & 1 & 0\\ \sin\phi & 0 & \cos\phi\end{bmatrix}\begin{bmatrix}1 & 0 & 0\\ 0 & \cos\gamma & \sin\gamma\\ 0 & -\sin\gamma & \cos\gamma\end{bmatrix}\begin{bmatrix}\cos\beta & \sin\beta & 0\\ -\sin\beta & \cos\beta & 0\\ 0 & 0 & 1\end{bmatrix}$$

$$=\begin{bmatrix}-\sin\beta\sin\gamma\sin\phi+\cos\beta\cos\phi & \cos\beta\sin\gamma\sin\phi+\sin\beta\cos\phi & -\cos\gamma\sin\phi\\ -\sin\beta\cos\gamma & \cos\beta\cos\gamma & \sin\gamma\\ \sin\beta\sin\gamma\cos\phi+\cos\beta\sin\phi & -\cos\beta\sin\gamma\cos\phi+\sin\beta\sin\phi & \cos\gamma\cos\phi\end{bmatrix}$$

The angle γ equals rad-uln, with γ = asin[H(2,3)], where ulnar deviation is positive. Note that rad-uln is constrained by joint limits to lie well within ±90°, so no algorithm is necessary. The angle β equals wrist flex-ext, with β = asin[-H(2,1)/cosγ], where flexion is positive. Because γ never comes close to ±90°, cosγ never comes close to zero, so there is no danger of dividing by zero and running into gimble lock.

In summary,

$$\text{Elbow flex - ext angle} = \delta = \arcsin\left[-\frac{G(3,2)}{\cos\alpha}\right]\text{(extension is positive)}$$

$$\text{Forearm pro - sup angle} = \alpha = \arcsin[G(3,1)]\text{(pronation is positive)}$$

$$\text{Wrist flex - ext angle} = \beta = \arcsin\left[-\frac{H(2,1)}{\cos\gamma}\right]\text{(flexion is positive)}$$

$$\text{Wrist rad - uln angle} = \gamma = \arcsin[H(2,3)]\text{(ulnar deviation is positive)}$$

where

$$G = OC^{-1}DB^{-1}AO^{-1}$$

$$H = OE^{-1}FD^{-1}CO^{-1}$$

How does one represent the limbs in 3-D Cartesian space?

From the equation for G, the transformation from XYZ to $u_1v_1w_1$ is $R^{-1}B = OA^{-1}B$. So the transformation from $u_1v_1w_1$ to XYZ is $B^{-1}AO^{-1}$. During calibration, B = A, so the transformation from $u_1v_1w_1(0)$ to XYZ is O^{-1}, as it should be. Likewise, the transformation from $u_2v_2w_2$ to XYZ is $D^{-1}CO^{-1}$, and the transformation from $u_3v_3w_3$ to

XYZ is $F^{-1}EO^{-1}$. Each axis of $u_iv_iw_i$ can be expressed in XYZ as one of the columns of the transformation matrix.

Appendix D: Spline filtering

Introduction

For applications where several derivatives of the measured variables are needed (most biomechanics applications), it makes sense to filter with smoothing splines. Splines are polynomials (e.g. of degree 5) fitted through several points of a data set. By stringing together a many such splines, and making sure they (and some of their derivatives) match where they join, one can fit an entire data set with a series of splines. The fit can be exact, as in "interpolating splines" (in which case the series of splines goes through each point), or one can achieve a balance between fit and smoothness, as in "smoothing splines" (in which case the splines miss the points in favor of being smooth).

The advantage of using splines is that, once the splines are found for the measured variable, all derivatives can be obtained analytically (simply by analytically differentiating the spline's formula) instead of amplifying noise through some approximate differentiation.

Smoothing with splines is similar to smoothing with any other method in that one must specify by how much to smooth. In frequency domain filters, one must choose a cut-off frequency. In smoothing splines, one specifies a "smoothing parameter." How is this parameter chosen? One option is to use generalized cross-validation. This is a method suggested by Grace Wahba and Peter Craven [75]. Later, Dohrmann, Busby, and Trujillo came up with an elegant way to numerically implement Wahba and Craven's method [76]. Roughly speaking, this method compares certain parts of a data set to other parts of the same set to estimate the noise in the signal, and from that to determine the smoothing parameter.

The following subsections introduce the concept of spline interpolation and spline smoothing; identify a problem with, and present a solution to, one of Matlab’s spline smoothing functions; and present an implementation of a spline smoothing method which allows identification of the optimal smoothing parameter.

Interpolating with Splines

A good description of spline interpolation is given in the documentation to Matlab's Spline Toolbox: "Polynomials are the approximating functions of choice when a smooth function is to be approximated locally… But if a function is to be approximated on a larger interval, the degree… of the approximating polynomial may have to be chosen unacceptably large. The alternative is to subdivide the interval… of approximation into sufficiently small intervals…, so that on each such interval, a polynomial… of relatively low degree can provide a good approximation… This can even be done in such a way that the polynomial pieces blend smoothly, i.e., so that the resulting patched or composite function… has several continuous derivatives. Any such smooth piecewise polynomial function is called a *spline*. I.J. Schoenberg coined this term since a twice continuously differentiable cubic spline with sufficiently small first derivative approximates the shape of a draftsman's spline." [91]

The order N of a spline is equal to the number of coefficients needed to specify each piecewise polynomial. The highest exponent in the polynomial equation, i.e. the degree of the polynomial, is therefore $N-1$. A cubic spline seems to be a misnomer; it is 4th order. Each polynomial (of any order) bridges two data points. In other words, fitting n points requires $n-1$ polynomials. For example, if 2834 data points are fit with a 6th order spline, one needs 2833 6th-order polynomials.

Consider the following example:

Given: n = 4 points: (x_0,y_0), (x_1,y_1), (x_2,y_2), and (x_3,y_3)

Find: Cubic spline that interpolates between these points

Definition: "A cubic spline is a piecewise cubic [polynomial] in which not only the function y and the slope dy/dx but also the second derivative d^2y/dx^2 is continuous." [92][31]

---

[31] Also given in this reference is an intuitive comparison of spline interpolation to bending a beam through data points.

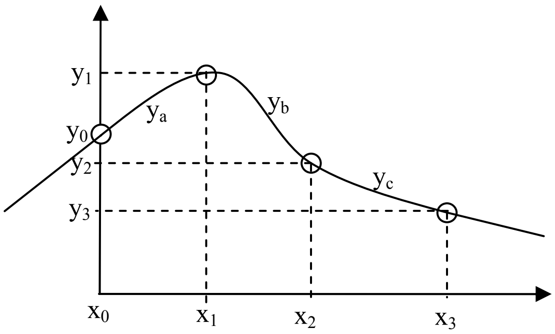

Figure D.1: Schematic of 3 splines fit through 4 data points.

Spline Equations

Interpolating 4 points by a piecewise cubic spline requires 3 spline pieces:

$y_a(x) = a_0 + a_1x + a_2x^2 + a_3x^3 \rightarrow \quad y_a'(x) = a_1 + 2a_2x + 3a_3x^2 \quad y_a''(x) = 2a_2 + 6a_3x$

$y_b(x) = b_0 + b_1x + b_2x^2 + b_3x^3 \rightarrow \quad y_b'(x) = b_1 + 2b_2x + 3b_3x^2 \quad y_b''(x) = 2b_2 + 6b_3x$

$y_c(x) = c_0 + c_1x + c_2x^2 + c_3x^3 \rightarrow \quad y_c'(x) = c_1 + 2c_2x + 3c_3x^2 \quad y_c''(x) = 2c_2 + 6c_3x$

Each cubic polynomial has 4 parameters, for a total of *m=4*(n-1)* system parameters (12 in this case). Finding *m* parameters requires *m* boundary conditions.

Boundary Conditions

Boundary conditions 1-6 follow from the goal, which is to interpolate between points. Boundary conditions 7-8 and 10-11 follow from the definition of a cubic spline above. Boundary conditions 9 and 12 indicate that no points outside of the data set influence the spline.

y: $y_a(x_0) = y_0 \rightarrow a_0 + a_1x_0 + a_2x_0^2 + a_3x_0^3 = y_0$ 1
$y_a(x_1) = y_1 \rightarrow a_0 + a_1x_1 + a_2x_1^2 + a_3x_1^3 = y_1$ 2
$y_b(x_1) = y_1 \rightarrow b_0 + b_1x_1 + b_2x_1^2 + b_3x_1^3 = y_1$ 3
$y_b(x_2) = y_2 \rightarrow b_0 + b_1x_2 + b_2x_2^2 + b_3x_2^3 = y_2$ 4
$y_c(x_2) = y_2 \rightarrow c_0 + c_1x_2 + c_2x_2^2 + c_3x_2^3 = y_2$ 5
$y_c(x_3) = y_3 \rightarrow c_0 + c_1x_3 + c_2x_3^2 + c_3x_3^3 = y_3$ 6

y': $y_a'(x_0) = ?$
$y_a'(x_1) = y_b'(x_1) \rightarrow a_1 + 2a_2x_1 + 3a_3x_1^2 = b_1 + 2b_2x_1 + 3b_3x_1^2$ 7

$y_b'(x_2) = y_c'(x_2)$ → $b_1 + 2b_2x_2 + 3b_3x_2^2 = c_2 + 2c_2x_2 + 3c_3x_2^2$ 8
$y_c'(x_3) = ?$

y”: $y_a''(x_0) = 0$ → $2a_2 + 6a_3x_0 = 0$ 9
$y_a''(x_1) = y_b''(x_1)$ → $2a_2 + 6a_3x_1 = 2b_2 + 6b_3x_1$ 10
$y_b''(x_2) = y_c''(x_2)$ → $2b_2 + 6b_3x_2 = 2c_2 + 6c_3x_2$ 11
$y_c''(x_3) = 0$ → $2c_2 + 6c_3x_3 = 0$ 12

Solution

The boundary conditions represent a set of *m* equations which must be solved simultaneously for the *m* spline parameters. This set of equations can be written in matrix form as X*C = Y, where X is an *m* by *m* matrix of elements made up of non-linear combinations of x_0 through x_3, C is an *m* by 1 vector of parameters, and Y is an *m* by 1 vector of elements made up of linear combinations of y_0 through y_3. Assuming that X has an inverse, this matrix equation can be solved for C: $C = X^{-1} * Y$.

Smoothing with Splines

Splines can be used not only to interpolate between data points but also to provide a smooth approximation to data points. The fundamental concept is that there are two competing interests. The goal is to create a function that

1. passes, as closely as possible, through all data points
2. is as smooth as possible

Mathematically, condition 1 can be expressed as minimizing the sum of the vertical distances between n data points, y(j) (j = 1, …, n), and the approximation to the data points, f(x(j)).

$$E(f) = \sum_{j=1}^{n} \left(y(j) - f(x(j))\right)^2$$

Condition 2 can be expressed as minimizing the m’th derivative of the approximating function f:

$$F\left(\frac{\partial^m f}{\partial x^m}\right) = \left|\frac{\partial^m f(x)}{\partial x^m}\right|^2$$

A compromise is reached when a weighted sum of *E* and *F* is minimized. For example, the Matlab function *csaps* minimizes the sum *pE+(1-p)F*:

$$p\sum\left(y(j) - f(x(j))\right)^2 + (1-p)\left|\frac{\partial^m f(x)}{\partial x^m}\right|^2$$

Alternatively, the Matlab function *spaps* minimizes the sum *ρE+F*, where *ρ* = *p/(p-1):*

$$\rho\sum\left(y(j) - f(x(j))\right)^2 + \left|\frac{\partial^m f(x)}{\partial x^m}\right|^2$$

Matlab's spaps function

Matlab's *spaps* function computes interpolating and smoothing splines of various orders. This function fails if one attempts to smooth too much. Below is a description of *spaps*, its failure problem, and a statement of how to enhance the *spaps* code in order to completely remove its failure problem. Read the Summary for a quick repair job or the Details for more depth.

Summary

Description: The matlab function

```
[sp, values, rho] = spaps(x, y, tol, m, ...)
```

takes the data set *y=y(x)* and creates the smoothed, interpolating spline *f(x)* of order[32] 2**m* described by *sp* with values *f* contained in *values.*

f(x) is computed as the function that minimizes

---

[32] Note that the order of a polynomial, as defined in Matlab, is the number of coefficients needed to describe it, i.e. one higher than the highest power.

$$O = \rho \sum_i \left[y_i - f(x_i)\right]^2 + \int \left[\frac{\partial^m f}{\partial x^m}\right]^2 dx = \rho E(f) + F\left(\frac{\partial^m f}{\partial x^m}\right)$$

where m can be chosen up to m=3 (in Marcos' code, m=3), and ρ is computed as the parameter that minimizes O with the constraint

$\sum_i \left[y_i - f(x_i)\right]^2 = E(f) \leq tol.$

Problem: Matlab uses a root-finding technique to find ρ. Occasionally, this root-finding technique fails. The failure does not occur because the root is somehow more difficult than other roots for which the technique does not fail, but rather because the starting position of the root finding algorithm is not optimal.

Solution: The above-mentioned failure can be completely avoided by giving the root-finding algorithm a more suitable starting position. This can be done by enhancing the Matlab code for *spaps* (usually found in C:\MATLAB7\toolbox\splines\spaps). The original code for finding ρ is found on lines 369-375:

```
while ~isnan(rho)&&delrho>0
      u = (ctwic + rho*A)\cty; ymf = wic*u; E = trace(u'*Ct*ymf);
      if 100*abs(E-tol)<tol, break, end
      grho = 1/sqrt(E) - oost;
      delrho = delrho/(g0/grho-1);
      g0 = grho; rho = rho+delrho;
end
```

These lines must be modified as following (the highlighted portions must be added):

```
while ~isnan(rho)&&delrho>0
      u = (ctwic + rho*A)\cty; ymf = wic*u; E_new =
      trace(u'*Ct*ymf);
      if E_new == E
          rho = 2*rho;
          continue
      end
      E = E_new;
```

```
        if 100*abs(E-tol)<tol, break, end
        grho = 1/sqrt(E) - oost;
        delrho = delrho/(g0/grho-1);
        g0 = grho; rho = rho+delrho;
    end
```

Details

Description: Matlab finds the parameter ρ that makes $E(f) \leq tol$ by finding the unique root of the monotonically increasing function $g(\rho)$:

$$g(\rho) = \frac{1}{\sqrt{E(\rho)}} - \frac{1}{\sqrt{tol}}$$

Even though $E(\rho)$—and therefore $g(\rho)$—are not known a priori, the root can be found by an iterative root finding algorithm. Matlab's approach is to start with ρ=0 and use the Newton-Raphson Method for the first iteration. Subsequent iterations are then performed with the Secant Method. Here is a step-by-step description of the process (see Figure 1):

1. Choose ρ_0=0. Compute $E(\rho_0)$ and $g(\rho_0)$.
2. Compute ρ_1 by Newton-Raphson method:

   $$\rho_1 = \rho_0 - \frac{g(\rho_0)}{g'(\rho_0)} = \rho_0 + \frac{2g(\rho_0)[E(\rho_0)]^{\frac{3}{2}}}{\left.\frac{dE}{d\rho}\right|_{\rho=0}} = \frac{-g(\rho_0)[E(\rho_0)]^{\frac{3}{2}}}{u^T Au}$$

   since ρ_0=0 and $dE/d\rho=u^T Au$ at $\rho=0$.
3. Compute $E(\rho_1)$ from ρ_1
4. If $E(\rho_1)$ is within 1% of *tol*, quit. If not, continue.
5. Compute ρ_2 by the Secant Method:

   $$\rho_2 - \rho_1 = \frac{\rho_1 - \rho_0}{\frac{g(\rho_0)}{g(\rho_1)} - 1}$$

   Repeat steps 4 and 5.

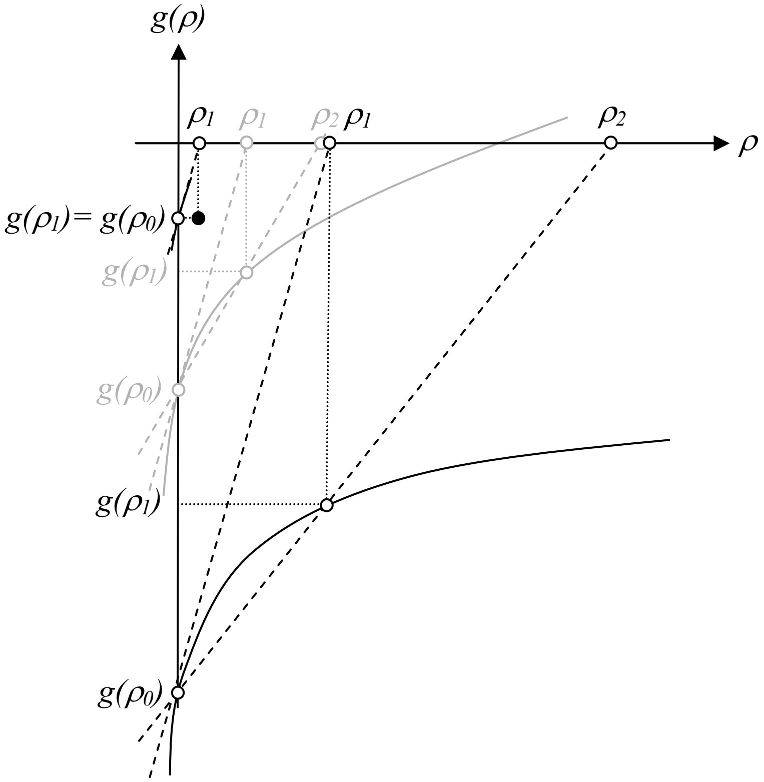

Figure D.2: g(ρ) vs. ρ for three different values of tol: smallest (black, farther from origin), intermediate (gray), and largest (black, close to origin). Also shown for each g(ρ) is the method of finding ρ for which E(ρ)=tol, namely by finding the root of g(ρ), as follows: $\rho_0=0$; $g(\rho_0)$ is evaluated, and ρ_1 is estimated by the Newton-Raphson Method; $g(\rho_1)$ is evaluated, and ρ_2 is found by the Secant Method; $g(\rho_2)$ is evaluated, and ρ_3 is estimated by the Secant Method, and so on. Note that for sufficiently large values of tol (black, close to origin), $\rho_1 \approx \rho_0$, and $g(\rho_1)= g(\rho_0)$. Subsequently, the Secant Method fails to find the root of the line passing through $g(\rho_1)$ and $g(\rho_0)$ despite the fact that there is a perfectly well behaved root of g(ρ) at some larger value of ρ. The solution is to check if $g(\rho_1)= g(\rho_0)$; if so, try again with a slightly larger value of ρ_1.

Problem: As *tol* is increased, $g(\rho_0)$ moves closer to zero, which in turn moves ρ_1 closer to zero (the slope of $g(\rho)$ at ρ_0 is always the same). As ρ_1 decreases, there comes a point when $E(\rho_0)= E(\rho_1)$ so $g(\rho_0)= g(\rho_1)$. This may be caused by numerical error. The important thing to note is that the root of $g(\rho)$ still exists, but the Secant method can't find it because the first two points, ρ_0 and ρ_1 (obtained by the Newton-Raphson method), are too close.

<u>Solution:</u> A simple programming solution is to insert in Step 3 (see above) a loop to check if $E(\rho_n)= E(\rho_{n-1})$; if so, try again with a slightly larger value of ρ_n, and repeat this until $E(\rho_n)$ is no longer equal to $E(\rho_{n-1})$. Then continue with the Secant Method as normal.

Smoothing Noisy Data Using Dynamic Programming and Generalized Cross-Validation

In 1988, Dohrmann, Busby and Trujillo suggested a method of spline smoothing which was computationally efficient and allowed determination of the optimal smoothing parameter via generalized cross-validation [76]. The following Matlab function *dohrmann* implements the spline smoothing method suggested in [76]. Note that the smoothing parameter, B, is unknown but must be specified as an input to *dohrmann*. According to Craven and Wahba, the optimal value of the smoothing parameter is the one which minimizes the function V(B) calculated at the end of *dohrmann* [75]. In order to find this optimal value, one must run *dohrmann* with many different smoothing parameter values and home in on the one which minimizes V(B). The idea is that once this optimal value is found, one can trust the filtered output.

```
function [x,v,a,j,V] = dohrmann(data, f, B)

% BRIEF DESCRIPTION
% This function filters data using smoothing splines. The smoothing
% spline fit is then differentiated analytically, so that the outputs
% include the filtered data with its first, second and third
% derivatives.
% The amount of smoothing and the particular implementation is taken
% from the following paper:
% Dohrmann CR, Busby HR, Trujillo DM (1988) Smoothing Noisy Data Using
% Dynamic Programming and Generalized Cross-Validation. J Biomech Eng
% 110:37-41.
%
% Steven Charles, February 2006

% INPUTS
% data: an N-by-1 vector
% f:    frequency at which data was sampled (in Hz)
% B:    smoothing parameter (the optimal value is the one which
%       minimizes the function V, calculated at the end of this
%       function)
```

```
% OUTPUTS
% x:    filtered data
% v:    first derivative of x
% a:    second derivative of x
% j:    third derivative of x
% V:    parameter involved in estimation of optimal smoothing parameter

% OVERVIEW
% 1. Initialize parameters
% 2. Do backward sweep
% 3. Do forward sweep
% 4. Isolate filtered data and its derivatives
% 5. Compute V(B)


% 1. INITIALIZATION
% kinematics
N = length(data);
h = 1/f;
M = [1 h (h^2)/2; 0 1 h; 0 0 1];
Theta = zeros(3,1,N);
P = [(h^3)/6; (h^2)/2; h];
% general
e = zeros(3,1,N);
e(1,1,:) = data;
U = [1 0 0; 0 0 0; 0 0 0];
I = eye(3);
% Backward sweep
D = zeros(N,1);
H = zeros(1,3,N);
R = zeros(3,3,N);
s = zeros(3,1,N);
% Forward sweep
g = zeros(N,1);
% Computing V(B)
M_hat = zeros(3,3,N);
E = zeros(3,3,N);
Q = zeros(3,3,N);   % I'm only looking at Qkj, where k=j


% 2. BACKWARD SWEEP
% Final condition
R(:,:,N) = U;
s(:,:,N) = -2*U*e(:,:,N);

% Loop from N-1 to 1
for k = N-1:-1:1
    D(k) = 1/(2*B + 2*P'*R(:,:,k+1)*P);
    H(:,:,k) = (2*R(:,:,k+1)*P)';
    R(:,:,k) = U + M'*(R(:,:,k+1) - 0.5*H(:,:,k)'*D(k)*H(:,:,k))*M;
    s(:,:,k) = -2*U*e(:,:,k) + M'*(I - H(:,:,k)'*D(k)*P')*s(:,:,k+1);
end


% 3. FORWARD SWEEP
% Initial Condition
Theta(:,:,1) = -0.5 * inv(R(:,:,1)) * s(:,:,1);
```

```
Q(:,:,1) = inv(R(:,:,1));

% Loop from 2 to N-1
for k = 1:N-1
    g(k) = -inv(2*B + 2*P'*R(:,:,k+1)*P)*P'*(s(:,:,k+1) +
2*R(:,:,k+1)*M*Theta(:,:,k));
    Theta(:,:,k+1) = M*Theta(:,:,k) + P*g(k);
    M_hat(:,:,k+1) = (M' * (I - H(:,:,k)'  * D(k) * P'))';
    E(:,:,k+1) = -P * D(k) * P';
    Q(:,:,k+1) = M_hat(:,:,k+1) * Q(:,:,k) * (M_hat(:,:,k+1)') -
2*E(:,:,k+1);
end


% 4. ISOLATE FILTERED DATA AND ITS DERIVATIVES
x = Theta(1,1,:);
x = x(:);
v = Theta(2,1,:);
v = v(:);
a = Theta(3,1,:);
a = a(:);
j = g;       % the g(k) computed above is jerk

% For comparison: unfiltered data and its derivatives
data_prime = 100*diff(data);
data_prime(end+1) = data_prime(end);
data_double_prime = 100*diff(data_prime);
data_double_prime(end+1) = data_double_prime(end);


% 5. COMPUTE MINIMIZING FUNCTION V(B)
Tr_A = sum(Q(1,1,:));
% If the variance of the noise is known, an optimal value of B can be
% chosen as the value of B which minimizes R_sigma:
%sigma = sqrt(1/12);
%R_sigma = (1/N) * dot((x-data),(x-data)) - (2*(sigma^2)/N)*(N - Tr_A)
+ sigma^2;
V = (1/N) * dot((x-data),(x-data)) / ((1/N) * (N - Tr_A))^2;
```

Appendix E: Relationship between the wrist robot and the wrist joint

Orientation of the robot handle

In order to determine an analytical expression for the orientation of the robot handle, one must understand the robot's kinematic chain shown in Figure E.1.

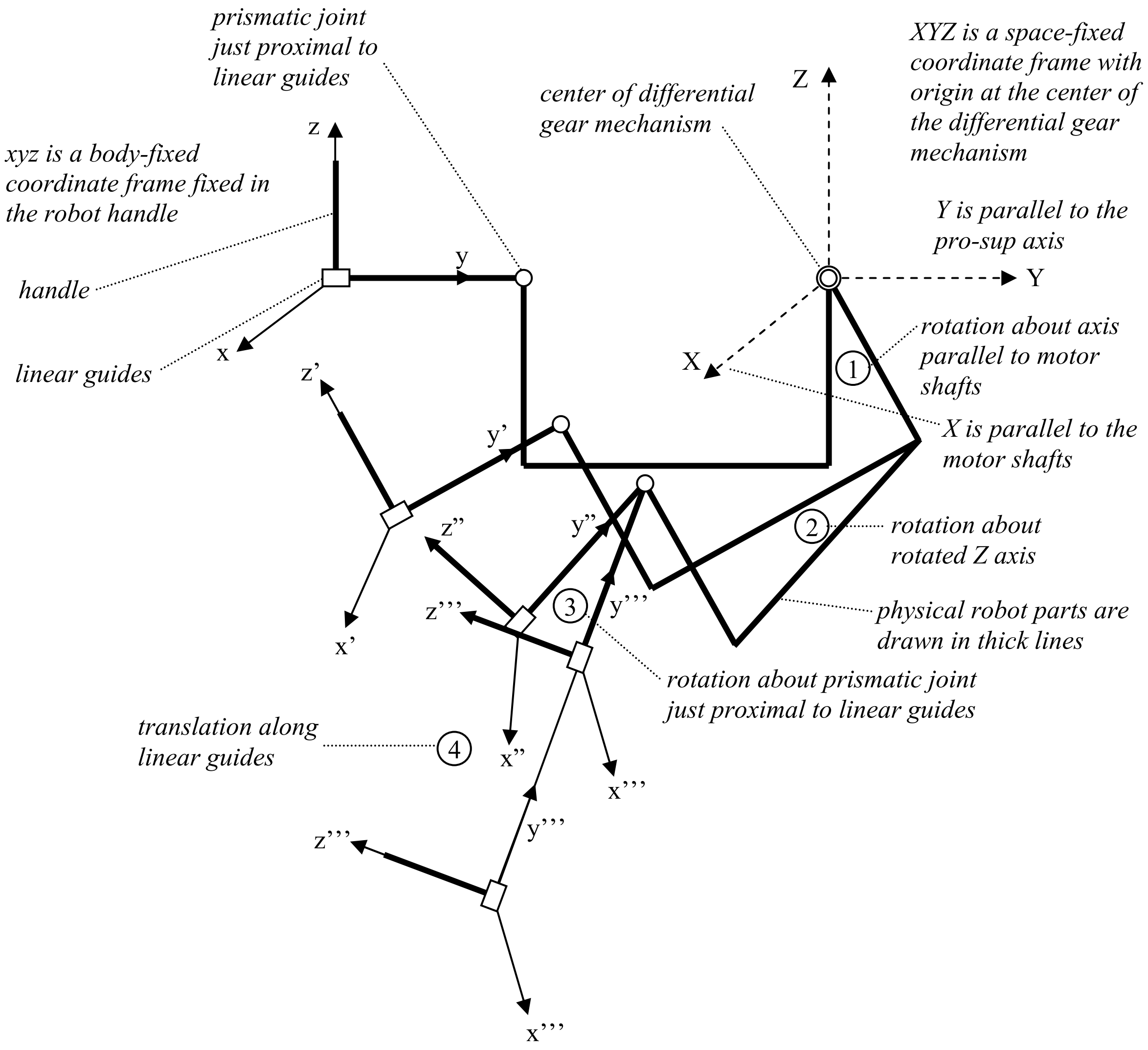

Figure E.1: Schematic of the wrist robot's kinematic chain.

The orientation of each link in this kinematic chain can be expressed in terms of Euler angles, as shown in Figure E.2.

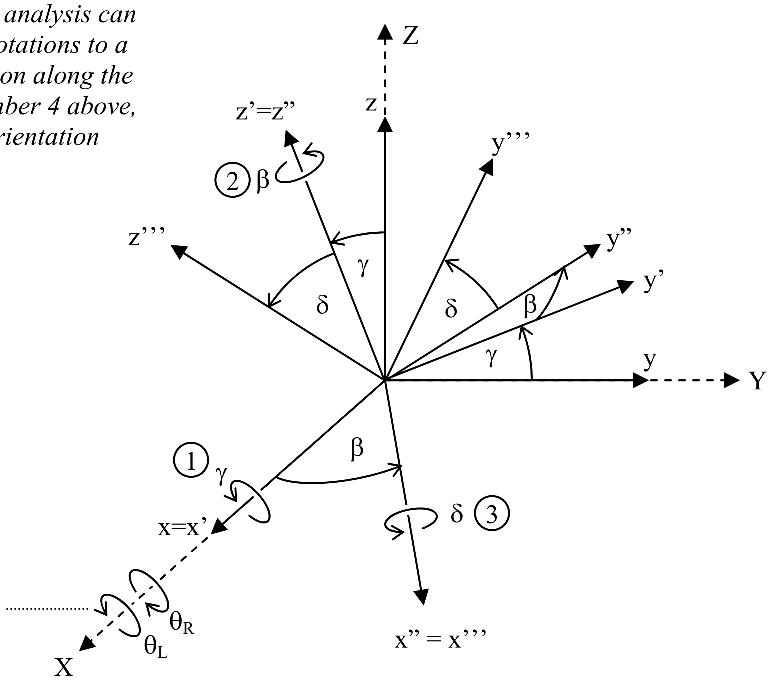

Since the object of this analysis is the orientation of the handle, the analysis can be simplified by shifting all rotations to a common origin. The translation along the linear guides, marked by number 4 above, has no influence on handle orientation and is therefore neglected.

θ_L and θ_R are the angles encoded by the left and right encoders, respectively.

Figure E.2: Definition of Euler angles used to describe robot kinematics.

The total transformation matrix is the product of the rotation matrices of the individual rotations. Consider the vector r which is stationary—it does not rotate with respect to the space-fixed XYZ frame (which is the same as the xyz frame). If the coordinates of r are given in the xyz frame as r_{xyz}, then the coordinates of r in the x’y’z’ frame are $r_{x'y'z'} = Ar_{xyz}$, where A is the transformation matrix of the first rotation. Likewise, the coordinates of r in the x”y”z” frame are $r_{x''y''z''} = Br_{x'y'z'}$, and the coordinates of r in the x’’’y’’’z’’’ frame are $r_{x'''y'''z'''} = Cr_{x''y''z''}$. The transformation from the xyz frame to the x’’’y’’’z’’’ frame is then $r_{x'''y'''z'''} = CBAr_{xyz}$, where

$$CBA = \begin{bmatrix} 1 & 0 & 0 \\ 0 & \cos\delta & \sin\delta \\ 0 & -\sin\delta & \cos\delta \end{bmatrix} \begin{bmatrix} \cos\beta & \sin\beta & 0 \\ -\sin\beta & \cos\beta & 0 \\ 0 & 0 & 1 \end{bmatrix} \begin{bmatrix} 1 & 0 & 0 \\ 0 & \cos\gamma & \sin\gamma \\ 0 & -\sin\gamma & \cos\gamma \end{bmatrix}$$

$$= \begin{bmatrix} \cos\beta & \sin\beta\cos\gamma & \sin\beta\sin\gamma \\ -\sin\beta\cos\delta & \cos\beta\cos\gamma\cos\delta - \sin\gamma\sin\delta & \cos\beta\sin\gamma\cos\delta + \cos\gamma\sin\delta \\ \sin\beta\sin\delta & -\cos\beta\cos\gamma\sin\delta - \sin\gamma\cos\delta & -\cos\beta\sin\gamma\sin\delta + \cos\gamma\cos\delta \end{bmatrix}$$

The transformation from the x'''y'''z''' frame to the xyz frame is then $r_{xyz} = (CBA)^{-1}$ $r_{x'''y'''z'''}$, where $(CBA)^{-1}$ is:

$$(CBA)^{-1} = (CBA)^{T}$$

$$= \begin{bmatrix} \cos\beta & -\sin\beta\cos\delta & \sin\beta\sin\delta \\ \sin\beta\cos\gamma & \cos\beta\cos\gamma\cos\delta - \sin\gamma\sin\delta & -\cos\beta\cos\gamma\sin\delta - \sin\gamma\cos\delta \\ \sin\beta\sin\gamma & \cos\beta\sin\gamma\cos\delta + \cos\gamma\sin\delta & -\cos\beta\sin\gamma\sin\delta + \cos\gamma\cos\delta \end{bmatrix}$$

Because the wrist robot is often used to record the direction in which the hand is pointing, the orientation of the robot handle is perhaps best represented by –j''', the unit vector pointing in the –y''' direction. The orientation of the robot handle in the space-fixed XYZ frame, r_{xyz}, is then:

$$\vec{r}_{xyz} = -\hat{j}'''_{xyz} = (CBA)^{-1}\left(-\hat{j}'''_{x'''y'''z'''}\right)$$

$$= \begin{bmatrix} \cos\beta & -\sin\beta\cos\delta & \sin\beta\sin\delta \\ \sin\beta\cos\gamma & \cos\beta\cos\gamma\cos\delta - \sin\gamma\sin\delta & -\cos\beta\cos\gamma\sin\delta - \sin\gamma\cos\delta \\ \sin\beta\sin\gamma & \cos\beta\sin\gamma\cos\delta + \cos\gamma\sin\delta & -\cos\beta\sin\gamma\sin\delta + \cos\gamma\cos\delta \end{bmatrix} \begin{bmatrix} 0 \\ -1 \\ 0 \end{bmatrix}$$

$$= \begin{bmatrix} \sin\beta\cos\delta \\ -\cos\beta\cos\gamma\cos\delta + \sin\gamma\sin\delta \\ -\cos\beta\sin\gamma\cos\delta - \cos\gamma\sin\delta \end{bmatrix}$$

The video monitor displays the projection of the r onto a screen in the frontal plane. This projection can be given in terms of "screen coordinates":

$$\begin{bmatrix} x_{screen} \\ y_{screen} \end{bmatrix} = \begin{bmatrix} -\sin\beta\cos\delta \\ -\cos\beta\sin\gamma\cos\delta - \cos\gamma\sin\delta \end{bmatrix}$$

where x_{screen} points parallel to –X and y_{screen} points parallel to Z. The angle δ is not read, but is known from observation to be close to zero and surprisingly constant during wrist movement. The angles γ and β can be obtained through an additional transformation from the encoder angles θ_L and θ_R:

$$\begin{bmatrix} \gamma \\ \beta \end{bmatrix} = \frac{1}{2G} \begin{bmatrix} 1 & -1 \\ 1 & 1 \end{bmatrix} \begin{bmatrix} \theta_L \\ \theta_R \end{bmatrix},$$

where G is the gear ratio.

Orientation of the hand in terms of robot coordinates

The orientation of the hand is slightly different from the orientation of the robot handle and is normally defined as the orientation of the long shaft of the third metacarpal. Neutral position in flexion-extension (flex-ext) and radial-ulnar deviation (rad-uln) can then be defined as the hand configuration in which the third metacarpal is parallel with the long shaft of the forearm. This works well when the hand is extended, but when the hand is flexed—like when gripping the handle of the wrist robot—it makes more sense to define neutral flex-ext when the robot handle lies in the parasaggital plane[33], i.e. when the robot is in neutral "robot flex-ext." However, neutral rad-uln differs from neutral "robot rad-uln" because it is best defined as the hand configuration in which the third metacarpal lies in the horizontal plane[34]. Taken together, this means that in neutral flex-ext and rad-uln, the *handle* will lie in the saggital plane[33] but be tilted downward by angle ε with respect to the horizontal plane[34]. The angle ε varies between approximately 15° and 30° for different subjects.

In summary, the orientation of the hand, h, can be computed from the orientation of the robot handle, r, by performing another rotation (this time by -ε) about the x''' axis. Because this is the same axis as in the last rotation (rotation by δ), one can simply replace

---

[33] More rigorously, it is the plane spanned by the flex-ext axis of rotation and the long shaft of the forearm, which differs from the parasaggital plane when the forearm is in pronation or supination.

[34] More rigorously, it is the plane spanned by the rad-uln axis of rotation and the long shaft of the forearm.

δ by δ-ε in the equations above. The transformation matrix of the hand from body-fixed to space-fixed coordinates is then:

$$\begin{bmatrix} \cos\beta & -\sin\beta\cos(\delta-\varepsilon) & \sin\beta\sin(\delta-\varepsilon) \\ \sin\beta\cos\gamma & \cos\beta\cos\gamma\cos(\delta-\varepsilon)-\sin\gamma\sin(\delta-\varepsilon) & -\cos\beta\cos\gamma\sin(\delta-\varepsilon)-\sin\gamma\cos(\delta-\varepsilon) \\ \sin\beta\sin\gamma & \cos\beta\sin\gamma\cos(\delta-\varepsilon)+\cos\gamma\sin(\delta-\varepsilon) & -\cos\beta\sin\gamma\sin(\delta-\varepsilon)+\cos\gamma\cos(\delta-\varepsilon) \end{bmatrix}$$

The orientation of the hand is given in the space-fixed XYZ frame as:

$$\vec{h}_{xyz} = \begin{bmatrix} \sin\beta\cos(\delta-\varepsilon) \\ -\cos\beta\cos\gamma\cos(\delta-\varepsilon)+\sin\gamma\sin(\delta-\varepsilon) \\ -\cos\beta\sin\gamma\cos(\delta-\varepsilon)-\cos\gamma\sin(\delta-\varepsilon) \end{bmatrix}$$

Relationship between robot and wrist coordinates, and implications for the measurement of stiffness

During stiffness measurements combining flex-ext and rad-uln, we measure the torque output of the motors required to maintain the robot end-effecter in equilibrium against externally applied forces and moments. Therefore, of all the externally applied forces and moments, the robot is capable of measuring only components that act along the degrees of freedom of its motors. The vector sum of these components is the sum of forces and moments measured by the robot. This vector sum is transmitted from the end-effecter to the motor shafts through the differential gear mechanism. Therefore, the sentence above could be rephrased to read: of all the externally applied forces and moments, the robot is capable of measuring only components that act along the degrees of freedom of its *end-effecter*.

With the pro-sup-axis locked, the robot has two degrees of freedom corresponding to generalized coordinates γ (defined as angular displacement about Z=z=z') and β (defined as angular displacement about x'=x'')[35]. By definition, the sum of torque components acting along the Z-axis is the generalized force (torque), M_γ, corresponding to γ, and the sum of torque components acting along x'-axis is the generalized force (torque), M_β, corresponding to β.

However, what is measured by the robot is not γ, β, M_γ, and M_β, but rather the angular displacements of the encoders, θ_L and θ_R, and the torque outputs of the motors, M_L and M_R. θ_L and θ_R also qualify as generalized coordinates, and M_L and M_R are the corresponding generalized forces (torques). The relationship between the two pairs of generalized coordinates is:

---

[35] Only rotational DOF are of importance here, so the linear guides are ignored. Also, the prismatic joint just proximal to the linear guides (δ) does not have an encoder but is known to vary little during wrist rotations.

$$\begin{bmatrix}\gamma\\ \beta\end{bmatrix}=\frac{1}{2G}\begin{bmatrix}1 & -1\\ 1 & 1\end{bmatrix}\begin{bmatrix}\theta_L\\ \theta_R\end{bmatrix}$$

$$\begin{bmatrix}\dot{\gamma}\\ \dot{\beta}\end{bmatrix}=\underbrace{\frac{1}{2G}\begin{bmatrix}1 & -1\\ 1 & 1\end{bmatrix}}_{J}\begin{bmatrix}\dot{\theta}_L\\ \dot{\theta}_R\end{bmatrix}$$

where J is the Jacobian and G is the gear ratio of the differential transmission. The relationship between the two pairs of generalized forces can be determined from conservation of power:

$$P=\begin{bmatrix}M_\gamma\\ M_\beta\end{bmatrix}^T\begin{bmatrix}\dot{\gamma}\\ \dot{\beta}\end{bmatrix}=\begin{bmatrix}M_\gamma\\ M_\beta\end{bmatrix}^T J\begin{bmatrix}\dot{\theta}_L\\ \dot{\theta}_R\end{bmatrix}=\begin{bmatrix}M_L\\ M_R\end{bmatrix}^T\begin{bmatrix}\dot{\theta}_L\\ \dot{\theta}_R\end{bmatrix}$$

$$\Rightarrow\begin{bmatrix}M_L\\ M_R\end{bmatrix}=J^T\begin{bmatrix}M_\gamma\\ M_\beta\end{bmatrix}$$

In summary, either [θ_L, θ_R] and [M_L, M_R] or [γ, β] and [M_γ, M_β] can be used as generalized coordinates and forces. If [γ, β] and [M_γ, M_β] are used, they must be computed from the measured variables [θ_L, θ_R] and [M_L, M_R] following the equations above.

Note that so far there have been no assumptions regarding the wrist. Nevertheless, if wrist stiffness is to be determined from robot measurements, the generalized coordinates of the wrist must be defined, from which the transformation between robot coordinates and forces and wrist coordinates and forces can be determined. However, defining generalized coordinates for the wrist is equivalent to modeling its kinematics.

If the wrist is modeled to mirror the wrist robot, namely as a universal joint in which the rad-uln axis carries the flex-ext axis, then the transformation is trivial:

$$\begin{bmatrix}RUD\\ FE\end{bmatrix}=\begin{bmatrix}\gamma\\ \beta\end{bmatrix}$$

$$\frac{d}{dt}\begin{bmatrix}RUD\\ FE\end{bmatrix}=\begin{bmatrix}\dot{\gamma}\\ \dot{\beta}\end{bmatrix}\Rightarrow J=\begin{bmatrix}1 & 0\\ 0 & 1\end{bmatrix}$$

$$\Rightarrow\begin{bmatrix}M_{RUD}\\ M_{FE}\end{bmatrix}=\begin{bmatrix}M_\gamma\\ M_\beta\end{bmatrix}$$

where RUD is the angle in rad-uln and FE is the angle in flex-ext. In other words, making statements about [RUD, FE] and [M_{RUD}, M_{FE}] is equivalent to making statements about [γ, β] and [M_γ, M_β], and vice versa. The stiffness matrix of the wrist can then be determined from robot variables as

$$K = \frac{\partial \begin{bmatrix} M_\gamma \\ M_\beta \end{bmatrix}}{\partial \begin{bmatrix} \gamma \\ \beta \end{bmatrix}}$$

Unfortunately, to the best of our knowledge, the wrist is better modeled as a universal joint in which the flex-ext axis carries the rad-uln axis. This is how the International Society of Biomechanics has defined wrist flex-ext and rad-uln. Fortunately, for the range of motion covered during wrist stiffness experiments, the difference between the two universal joint models is negligible, so FE $\approx \beta$ and RUD $\approx \gamma$, as shown below.

If the wrist is modeled as a universal joint in which the flex-ext axis carries the rad-uln axis, then the transformation from the space-fixed to the body-fixed frame of the wrist is the same product as for the wrist robot, but in reverse order:

$$\begin{aligned} ED &= \begin{bmatrix} 1 & 0 & 0 \\ 0 & \cos RUD & \sin RUD \\ 0 & -\sin RUD & \cos RUD \end{bmatrix} \begin{bmatrix} \cos FE & \sin FE & 0 \\ -\sin FE & \cos FE & 0 \\ 0 & 0 & 1 \end{bmatrix} \\ &= \begin{bmatrix} \cos FE & \sin FE & 0 \\ -\sin FE \cos RUD & \cos FE \cos RUD & \sin RUD \\ \sin FE \sin RUD & -\cos FE \sin RUD & \cos RUD \end{bmatrix} \end{aligned}$$

The transformation from body-fixed to space-fixed frames is the inverse:

$$(DE)^{-1} = (DE)^T = \begin{bmatrix} \cos FE & -\sin FE \cos RUD & \sin FE \sin RUD \\ \sin FE & \cos FE \cos RUD & -\cos FE \sin RUD \\ 0 & \sin RUD & \cos RUD \end{bmatrix}$$

Assuming that the hand and the wrist robot handle have the identical orientation, then $(DE)^{-1}$ should be identical $(CBA)^{-1}$, allowing one to determine the relationship between the generalized coordinates of the wrist, [FE, RUD], and those of the wrist robot, [γ, β]. Comparing the (3,1) entry in both transformation matrices, one sees that $\sin\beta\sin\gamma$ would have to always be zero, which doesn't make sense. This phenomenon arises because it is not actually possible to achieve the exact same orientation with two universal joints in which the role of "carrying axis" and "carried axis" is reversed. In other words, it is not possible to match the x, y, and z axes of the frames fixed in the output shafts of two universal joints with reversed axes. However, it is possible to match the direction in which the output shafts are pointing, although the rotation about that direction (the roll) will differ (only slightly for small displacements). More specifically, it is possible to match the direction in which the robot is pointing to the direction in which the third metacarpal is pointing, which is of biggest concern in studying wrist orientation. This is equivalent to matching the middle columns of $(DE)^{-1}$ and $(CBA)^{-1}$, from which follows:

$$RUD = \sin^{-1}\left[\cos\beta\sin\gamma\cos(\delta-\varepsilon)+\cos\gamma\sin(\delta-\varepsilon)\right]$$

$$FE = \sin^{-1}\left[\frac{\sin\beta\cos(\delta-\varepsilon)}{\cos RUD}\right]$$

The error that results from assuming the identity transformation between robot and wrist coordinates is negligible for moderately sized wrist rotations; a simple linearization around [β, γ] = [0, 0] with $\delta-\varepsilon = 0$ reveals that $FE \approx \beta$ and $RUD \approx \gamma$. For larger rotations, however, the error can become significant, as shown in Figure E.3. Fortunately, such large wrist rotations are very uncommon, if not impossible.

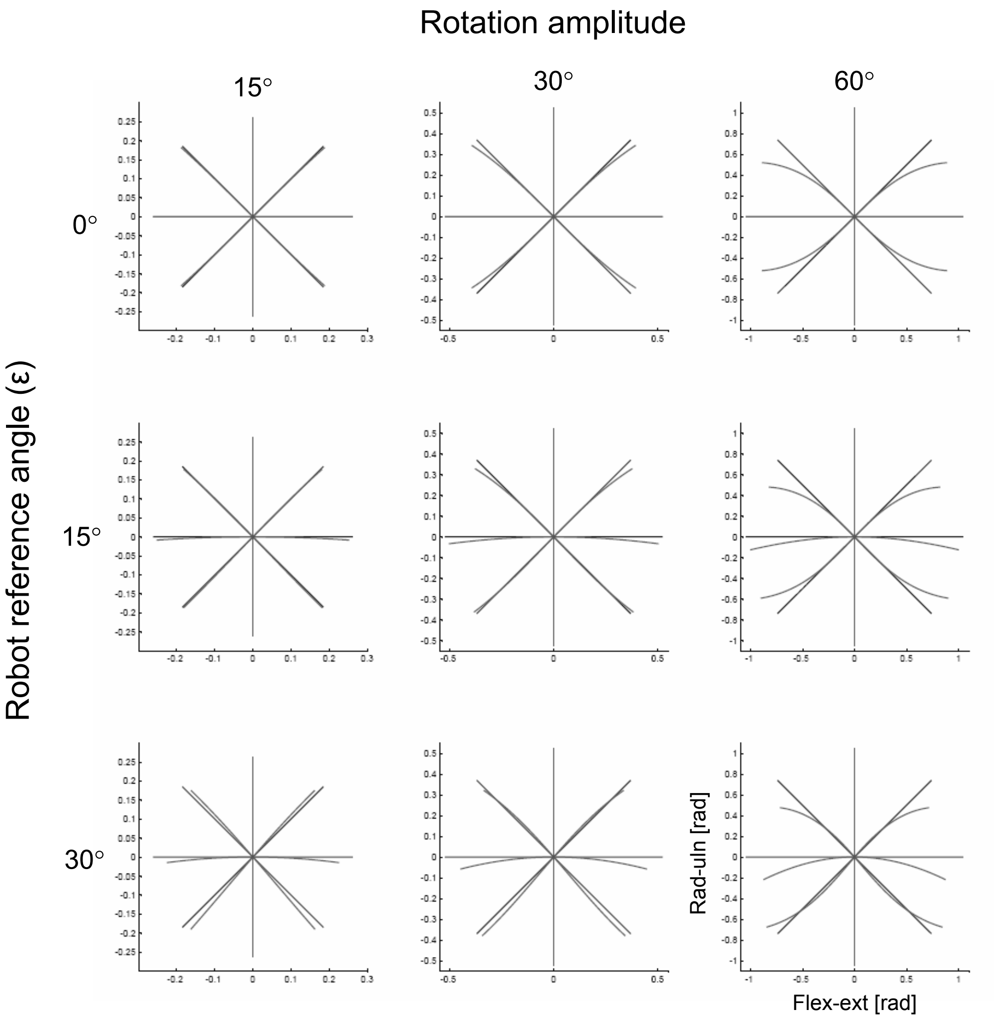

Figure E.3: Relationship between robot and wrist coordinates.

This figure illustrates the error associated with assuming the identity transformation between wrist and robot coordinates. Each subplot shows the robot coordinates (curved lines) that correspond to straight wrist rotations (straight lines). ε is the same angle as in the equations above. For these plots, δ = 0.

The effect of this error on the Jacobian was evaluated numerically as

$$J = \begin{bmatrix} \dfrac{\partial FE}{\partial \beta} & \dfrac{\partial FE}{\partial \gamma} \\ \dfrac{\partial RUD}{\partial \beta} & \dfrac{\partial RUD}{\partial \gamma} \end{bmatrix}$$

as shown in Figure E.4. The two subfigures in the left-most column show FE and RUD as functions of β and γ. The other four subfigures represent the four elements of the Jacobian matrix. Note that, over the range of -0.3 rad ≤ β, γ ≤ 0.3 rad, the Jacobian is

$$J \approx \begin{bmatrix} 1 & 0 \\ 0 & 1 \end{bmatrix}$$

The range of motion covered in the wrist stiffness experiments is not -0.3 rad ≤ β, γ ≤ 0.3 rad, but rather $\sqrt{(\beta-\beta_0)^2+(\gamma-\gamma_0)^2} \le 0.3\,rad$, as shown in Figure E.5 for $[\beta_0, \gamma_0] = [0, 0]$. The deviation of the actual Jacobian from the identity matrix can be expressed in terms of the maximum, mean, and minimum Jacobian elements over this range, which are:

$$J_{\max} = \begin{bmatrix} 1.0464 & 0.0452 \\ 0.0452 & 1.0000 \end{bmatrix} \qquad J_{mean} = \begin{bmatrix} 1.0111 & 0.0000 \\ 0.0000 & 0.9886 \end{bmatrix} \qquad J_{\min} = \begin{bmatrix} 1.0000 & -0.0452 \\ -0.0452 & 0.9556 \end{bmatrix}$$

In actuality, the origin of the wrist stiffness experiment is at $[\beta_0, \gamma_0] = [0, -13°]$, and δ-ε ≈ -15°. However, the Jacobian for these conditions is still very close to the identity matrix (see Figure E.6):

$$J_{\max} = \begin{bmatrix} 1.0224 & 0.0529 \\ 0.0919 & 1.0000 \end{bmatrix} \qquad J_{mean} = \begin{bmatrix} 0.9769 & 0.0000 \\ 0.0000 & 0.9894 \end{bmatrix} \qquad J_{\min} = \begin{bmatrix} 0.9628 & -0.0529 \\ -0.0919 & 0.9585 \end{bmatrix}$$

In summary, if the wrist is modeled as a universal joint in which the flex-ext axis carries the rad-uln axis, then the angular displacements about the "carrying axis" and the "carried axes", FE and RUD, respectively, are generalized coordinates. The corresponding generalized forces (torques), M_β and M_γ, act along the same axes. The relationship between these generalized coordinates and forces and those of the robot is:

$$\begin{bmatrix} FE \\ RUD \end{bmatrix} \approx \begin{bmatrix} \beta \\ \gamma \end{bmatrix}$$

$$\begin{bmatrix} M_{FE} \\ M_{RUD} \end{bmatrix} \approx \begin{bmatrix} M_\beta \\ M_\gamma \end{bmatrix}$$

The stiffness of the wrist can then be determined as

$$K = \frac{\partial \begin{bmatrix} M_{FE} \\ M_{RUD} \end{bmatrix}}{\partial \begin{bmatrix} FE \\ RUD \end{bmatrix}} = \frac{\partial \begin{bmatrix} M_{\beta} \\ M_{\gamma} \end{bmatrix}}{\partial \begin{bmatrix} \beta \\ \gamma \end{bmatrix}}$$

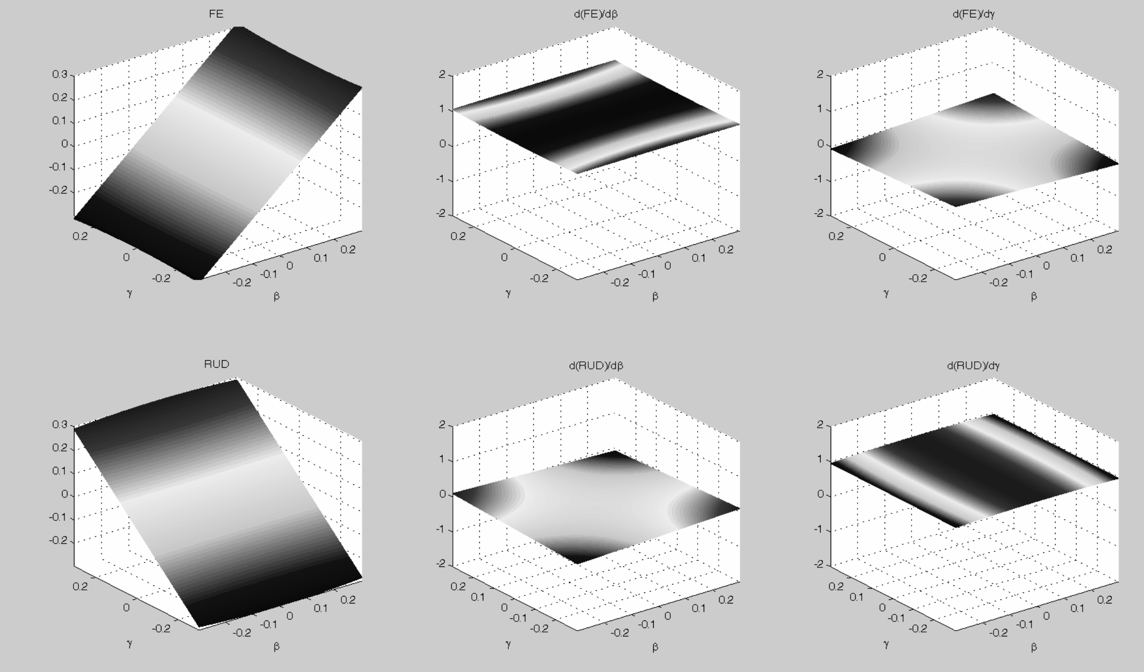

Figure E.4: Relationship between robot and wrist coordinates.

The two subplots in the first column show FE and RUD as functions of β and γ. The remaining four subplots represent the four elements of the Jacobian matrix.

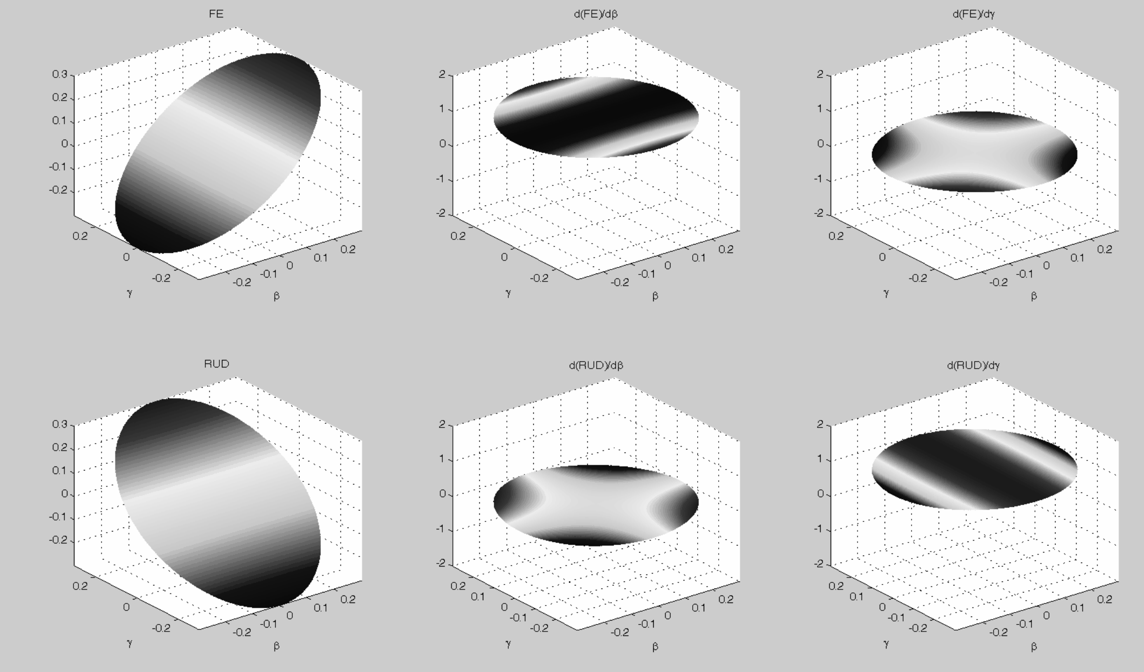

Figure E.5: Relationship between robot and wrist coordinates.

Same as Figure E.4, but limited to the range of motion of the stiffness measurement experiment, which was 0.3 rad in all directions.

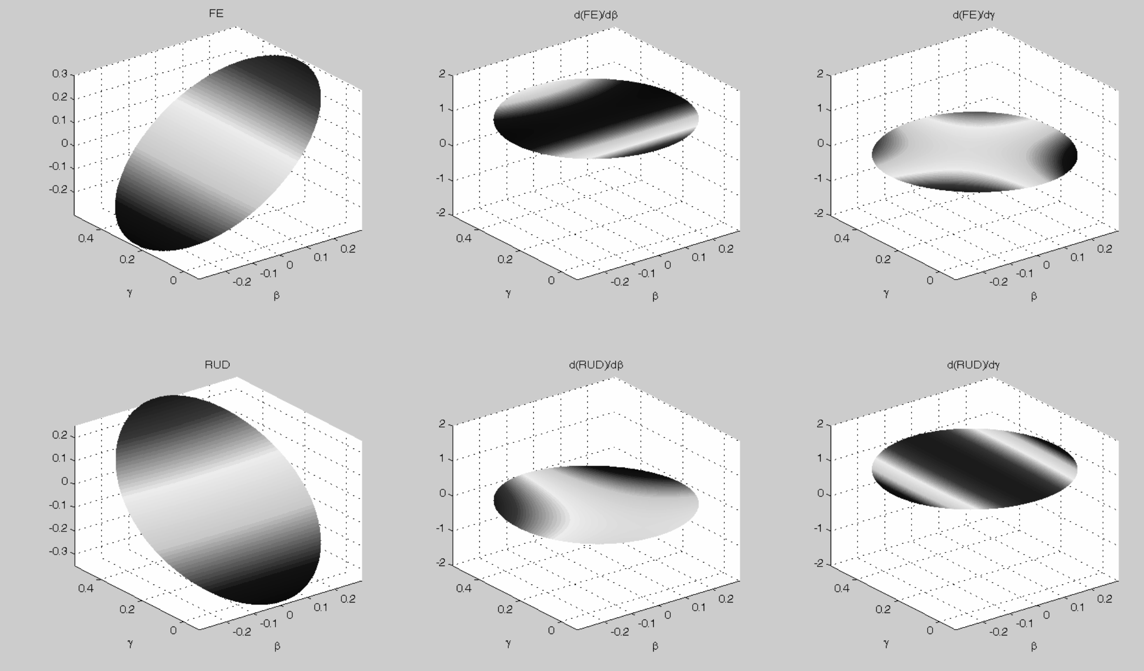

Figure E.6: Relationship between robot and wrist coordinates.

Same as Figure E.5, except that $[\beta_0, \gamma_0] = [0, -13°]$, and δ-$\varepsilon = -15°$.

Appendix F: Kinematics and Dynamics of a 2-Link Manipulandum

Forward and Inverse Kinematics

The state of a two-link manipulandum can be described in terms of generalized coordinates (θ_1,θ_2) or in terms of (x_1,x_2).

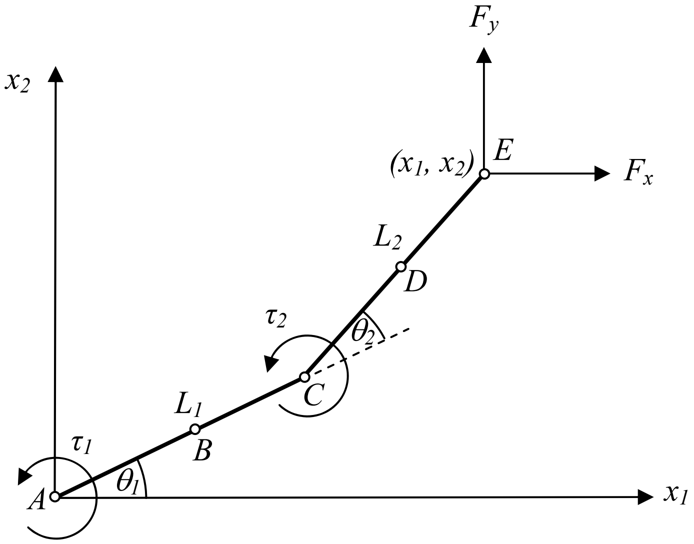

Figure F.1: Schematic of two-link manipulandum.

$$\vec{r}_{C/A} = L_1 \begin{bmatrix} \cos\theta_1 \\ \sin\theta_1 \end{bmatrix}$$

$$\vec{r}_{E/C} = L_2 \begin{bmatrix} \cos(\theta_1+\theta_2) \\ \sin(\theta_1+\theta_2) \end{bmatrix}$$

$$\vec{r}_{E/A} = \vec{r}_{C/A} + \vec{r}_{E/C} = \begin{bmatrix} L_1\cos\theta_1 + L_2\cos(\theta_1+\theta_2) \\ L_1\sin\theta_1 + L_2\sin(\theta_1+\theta_2) \end{bmatrix}$$

The forward kinematics express (x_1,x_2) in terms of generalized coordinates (θ_1,θ_2). This relationship is always well-defined:

$$\vec{x} = \begin{bmatrix} x_1 \\ x_2 \end{bmatrix} = \vec{r}_{E/A} = \begin{bmatrix} L_1 \cos\theta_1 + L_2 \cos(\theta_1 + \theta_2) \\ L_1 \sin\theta_1 + L_2 \sin(\theta_1 + \theta_2) \end{bmatrix} = L(\vec{\theta})$$

The inverse relationship, which expresses (θ_1,θ_2) in terms of (x_1,x_2), can be found using Figure F.2:

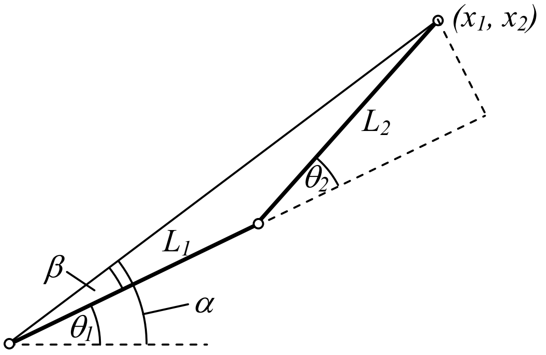

Figure F.2: Definitions of various angles used in the calculation of inverse kinematics.

First, find θ_2 using the Law of Cosines. Then, find θ_1 in terms of θ_2.

$$x_1^2 + x_2^2 = L_1^2 + L_2^2 - 2L_1L_2 \cos(180° - \theta_2)$$

$$\theta_2 = \arccos\left(\frac{x_1^2 + x_2^2 - L_1^2 - L_2^2}{2L_1L_2}\right)$$

$$\theta_1 = \alpha - \beta = \arctan\left(\frac{x_2}{x_1}\right) - \arctan\left(\frac{L_2 \sin\theta_2}{L_1 + L_2 \cos\theta_2}\right)$$

Jacobian

The Jacobian can be determined from the forward kinematics:

$$\vec{x} = \begin{bmatrix} x_1 \\ x_2 \end{bmatrix} = \vec{r}_{E/A} = \begin{bmatrix} L_1 \cos\theta_1 + L_2 \cos(\theta_1 + \theta_2) \\ L_1 \sin\theta_1 + L_2 \sin(\theta_1 + \theta_2) \end{bmatrix} = L(\vec{\theta})$$

$$\dot{\vec{x}} = \begin{bmatrix} \dot{x}_1 \\ \dot{x}_2 \end{bmatrix} = \begin{bmatrix} -L_1 \sin\theta_1\dot{\theta}_1 - L_2 \sin(\theta_1 + \theta_2)(\dot{\theta}_1 + \dot{\theta}_2) \\ L_1 \cos\theta_1\dot{\theta}_1 + L_2 \cos(\theta_1 + \theta_2)(\dot{\theta}_1 + \dot{\theta}_2) \end{bmatrix}$$

$$\dot{\vec{x}} = \begin{bmatrix} -L_1 \sin\theta_1 - L_2 \sin(\theta_1 + \theta_2) & -L_2 \sin(\theta_1 + \theta_2) \\ L_1 \cos\theta_1 + L_2 \cos(\theta_1 + \theta_2) & L_2 \cos(\theta_1 + \theta_2) \end{bmatrix} \begin{bmatrix} \dot{\theta}_1 \\ \dot{\theta}_2 \end{bmatrix} = J(\vec{\theta})\dot{\vec{\theta}}$$

where the J is termed the Jacobian and is a function of $\vec{\theta}$:

$$J(\vec{\theta}) = \begin{bmatrix} -L_1 \sin\theta_1 - L_2 \sin(\theta_1 + \theta_2) & -L_2 \sin(\theta_1 + \theta_2) \\ L_1 \cos\theta_1 + L_2 \cos(\theta_1 + \theta_2) & L_2 \cos(\theta_1 + \theta_2) \end{bmatrix}$$

In general, the Jacobian can be written as :

$$J(\vec{\theta}) = \frac{\partial \vec{x}}{\partial \vec{\theta}} = \frac{\partial L(\vec{\theta})}{\partial \vec{\theta}} \text{ because } \dot{\vec{x}} = \frac{d\vec{x}}{dt} = \frac{\partial \vec{x}}{\partial \vec{\theta}}\frac{d\vec{\theta}}{dt} = \frac{\partial L(\vec{\theta})}{\partial \vec{\theta}}\frac{d\vec{\theta}}{dt} = J(\vec{\theta})\dot{\vec{\theta}}$$

Velocity and Acceleration in a Rotating Frame of Reference

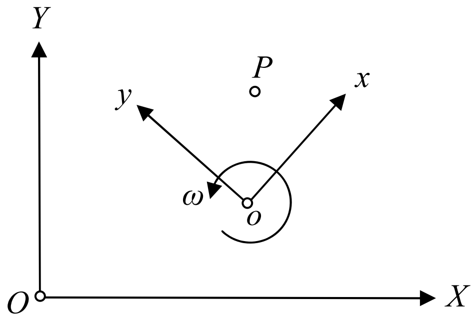

Figure F.3: Schematic of rotating and static reference frames.

$$\vec{r}_{P/O} = \vec{r}_{P/o} + \vec{r}_{o/O} = x_P\hat{i} + y_P\hat{j} + X_o\hat{I} + Y_o\hat{J}$$

$$\vec{v}_P = \frac{d}{dt}\left(\vec{r}_{P/O}\right) = \dot{x}_P\hat{i} + x_P\dot{\hat{i}} + \dot{y}_P\hat{j} + y_P\dot{\hat{j}} + \dot{X}_o\hat{I} + \dot{Y}_o\hat{J} = \left(\dot{x}_P\hat{i} + \dot{y}_P\hat{j}\right) + x_P\left(\vec{\omega}\times\hat{i}\right) + y_P\left(\vec{\omega}\times\hat{j}\right) + \left(\dot{X}_o\hat{I} + \dot{Y}_o\hat{J}\right)$$
$$\vec{v}_P = \left(\dot{X}_o\hat{I} + \dot{Y}_o\hat{J}\right) + \left(\dot{x}_P\hat{i} + \dot{y}_P\hat{j}\right) + \vec{\omega}\times\left(x_P\hat{i} + y_P\hat{j}\right) = \vec{v}_o + \vec{v}_{rel} + \vec{\omega}\times\vec{r}_{P/o}$$

$$\vec{a}_P = \frac{d}{dt}\left(\vec{v}_P\right) = \left(\ddot{x}_P\hat{i} + \dot{x}_P\dot{\hat{i}} + \ddot{y}_P\hat{j} + \dot{y}_P\dot{\hat{j}}\right) + \dot{\vec{\omega}}\times\left(x_P\hat{i} + y_P\hat{j}\right) + \vec{\omega}\times\left(\dot{x}_P\hat{i} + x_P\dot{\hat{i}} + \dot{y}_P\hat{j} + y_P\dot{\hat{j}}\right) + \left(\ddot{X}_o\hat{I} + \ddot{Y}_o\hat{J}\right)$$
$$\vec{a}_P = \left(\ddot{x}_P\hat{i} + \ddot{y}_P\hat{j}\right) + \left[\dot{x}_P\left(\vec{\omega}\times\hat{i}\right) + \dot{y}_P\left(\vec{\omega}\times\hat{j}\right)\right] + \dot{\vec{\omega}}\times\left(x_P\hat{i} + y_P\hat{j}\right) + \vec{\omega}\times\left(\dot{x}_P\hat{i} + \dot{y}_P\hat{j}\right) + \ldots$$
$$\ldots + \vec{\omega}\times\left[x_P\left(\vec{\omega}\times\hat{i}\right) + y_P\left(\vec{\omega}\times\hat{j}\right)\right] + \left(\ddot{X}_o\hat{I} + \ddot{Y}_o\hat{J}\right)$$
$$\vec{a}_P = \left(\ddot{x}_P\hat{i} + \ddot{y}_P\hat{j}\right) + \vec{\omega}\times\left(\dot{x}_P\hat{i} + \dot{y}_P\hat{j}\right) + \dot{\vec{\omega}}\times\left(x_P\hat{i} + y_P\hat{j}\right) + \vec{\omega}\times\left(\dot{x}_P\hat{i} + \dot{y}_P\hat{j}\right) + \ldots$$
$$\ldots + \vec{\omega}\times\left[\vec{\omega}\times\left(x_P\hat{i} + y_P\hat{j}\right)\right] + \left(\ddot{X}_o\hat{I} + \ddot{Y}_o\hat{J}\right)$$
$$\vec{a}_P = \left(\ddot{X}_o\hat{I} + \ddot{Y}_o\hat{J}\right) + \left(\ddot{x}_P\hat{i} + \ddot{y}_P\hat{j}\right) + 2\vec{\omega}\times\left(\dot{x}_P\hat{i} + \dot{y}_P\hat{j}\right) + \dot{\vec{\omega}}\times\left(x_P\hat{i} + y_P\hat{j}\right) + \vec{\omega}\times\left[\vec{\omega}\times\left(x_P\hat{i} + y_P\hat{j}\right)\right]$$
$$\vec{a}_P = \vec{a}_o + \vec{a}_{rel} + 2\vec{\omega}\times\vec{v}_{rel} + \dot{\vec{\omega}}\times\vec{r}_{P/o} + \vec{\omega}\times\left(\vec{\omega}\times\vec{r}_{P/o}\right)$$

where

$\vec{a}_o$ = acceleration of o with respect to OXY

$\vec{a}_{rel}$ = relative acceleration of P with respect to oxy

$2\vec{\omega}\times\vec{v}_{rel}$ = Coriolis acceleration

$\dot{\vec{\omega}}\times\vec{r}_{P/o}$ = Euler acceleration

$\vec{\omega}\times\left(\vec{\omega}\times\vec{r}_{P/o}\right)$ = Centripetal acceleration $= -\omega^2\vec{r}_{P/o}$

Dynamics via Newton-Euler equations

Link 1

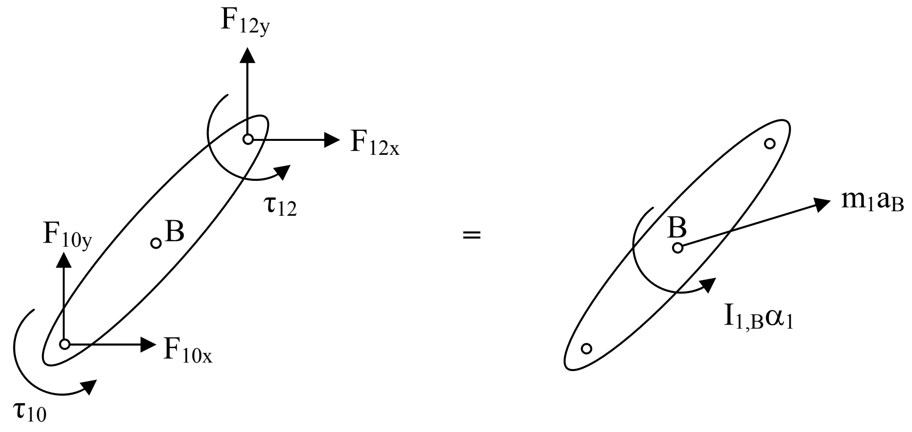

Figure F.4: Free-body diagram of link 1.

The linear acceleration of *B* and the angular acceleration of link 1 can be written using an intermediate frame centered at *A* and rotating at $\vec{\omega} = \dot{\theta}_1\hat{K}$. According to the equation for acceleration above:

$$\vec{a}_B = \left(\ddot{X}_A\hat{I} + \ddot{Y}_A\hat{J}\right) + \left(\ddot{x}_B\hat{i} + \ddot{y}_B\hat{j}\right) + 2\vec{\omega}\times\left(\dot{x}_B\hat{i} + \dot{y}_B\hat{j}\right) + \dot{\vec{\omega}}\times\left(x_B\hat{i} + y_B\hat{j}\right) + \vec{\omega}\times\left[\vec{\omega}\times\left(x_B\hat{i} + y_B\hat{j}\right)\right]$$

$$\vec{a}_B = 0 + 0 + 0 + \ddot{\theta}_1\hat{K}\times\left(\frac{1}{2}L_1\cos\theta_1\hat{I} + \frac{1}{2}L_1\sin\theta_1\hat{J}\right) - \dot{\theta}_1^2\left(\frac{1}{2}L_1\cos\theta_1\hat{I} + \frac{1}{2}L_1\sin\theta_1\hat{J}\right)$$

$$\vec{a}_B = -\left(\frac{1}{2}L_1\sin\theta_1\ddot{\theta}_1 + \frac{1}{2}L_1\cos\theta_1\dot{\theta}_1^2\right)\hat{I} + \left(\frac{1}{2}L_1\cos\theta_1\ddot{\theta}_1 - \frac{1}{2}L_1\sin\theta_1\dot{\theta}_1^2\right)\hat{J}$$

$$\alpha_1 = \ddot{\theta}_1$$

Newton's Equations of Motion can be written for the X-, Y-, and Z-directions:

X - direction

$$F_{10x} + F_{12x} = -\frac{1}{2} m_1 L_1 \sin\theta_1 \ddot{\theta}_1 - \frac{1}{2} m_1 L_1 \cos\theta_1 \dot{\theta}_1^2$$

Y - direction

$$F_{10y} + F_{12y} = \frac{1}{2} m_1 L_1 \cos\theta_1 \ddot{\theta}_1 - \frac{1}{2} m_1 L_1 \sin\theta_1 \dot{\theta}_1^2$$

Z - direction at B

$$\tau_{10} + \tau_{12} + \frac{1}{2} F_{10x} L_1 \sin\theta_1 - \frac{1}{2} F_{10y} L_1 \cos\theta_1 - \frac{1}{2} F_{12x} L_1 \sin\theta_1 + \frac{1}{2} F_{12y} L_1 \cos\theta_1 = I_{1,B} \ddot{\theta}_1$$

The equation for the Z-direction has 6 unknowns: τ_{10}, τ_{12}, F_{10x}, F_{10y}, F_{12x}, and F_{12y}, but can be solved for τ_{10} in the following way. Equations for F_{10x}, F_{10y} can be obtained from the equations for the X- and Y-directions for link 1. Equations for F_{12x} and F_{12y} can be obtained from the equations for the X- and Y-directions for link 2 since $F_{12x} = -F_{21x}$ and $F_{12y} = -F_{21y}$. An equation for τ_{12} can be obtained from the final solution for link 2 since $\tau_{12} = -\tau_{21}$. All 5 equations can then be plugged into the equation for the Z-direction of link 1, resulting in:

$$\tau_{10} - F_x\left[L_1 \sin\theta_1 + L_2 \sin(\theta_1 + \theta_2)\right] + F_y\left[L_1 \cos\theta_1 + L_2 \cos(\theta_1 + \theta_2)\right] =$$

$$\ddot{\theta}_1\left(I_{1,B} + I_{2,D} + m_2 L_1 L_2 \cos\theta_2 + \frac{1}{4} m_1 L_1^2 + m_2 L_1^2 + \frac{1}{4} m_2 L_2^2 \right) + \ddot{\theta}_2\left(I_{2,D} + \frac{1}{4} m_2 L_2^2 + \frac{1}{2} m_2 L_1 L_2 \cos\theta_2 \right) + \ldots$$

$$\ldots - \dot{\theta}_2^2\left(\frac{1}{2} m_2 L_1 L_2 \sin\theta_2\right) - \dot{\theta}_1 \dot{\theta}_2 \left(m_2 L_1 L_2 \sin\theta_2\right)$$

Link 2

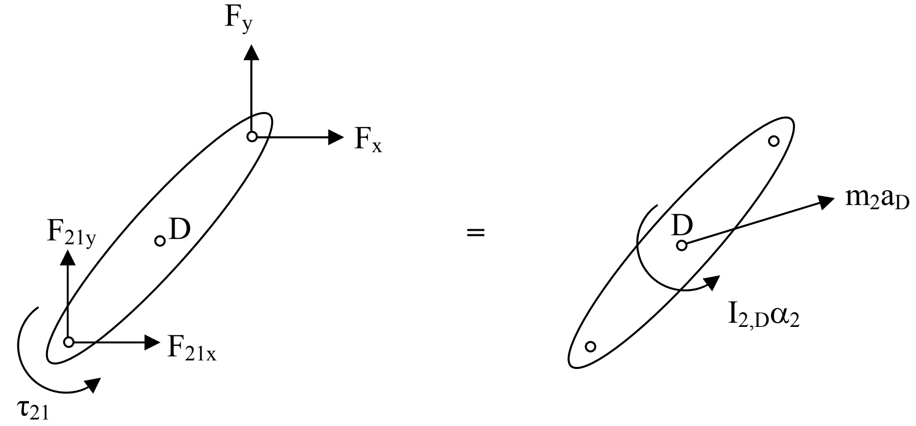

Figure F.5: Free-body diagram of link 2.

The linear acceleration of *D* and the angular acceleration of link 2 can be written using an intermediate frame centered at C and rotating at $\vec{\omega} = \left(\dot{\theta}_1 + \dot{\theta}_2\right)\hat{K}$. According to the equation for acceleration above:

$$\vec{a}_D = \left(\ddot{X}_C\hat{I} + \ddot{Y}_C\hat{J}\right) + \left(\ddot{x}_D\hat{i} + \ddot{y}_D\hat{j}\right) + 2\vec{\omega}\times\left(\dot{x}_D\hat{i} + \dot{y}_D\hat{j}\right) + \dot{\vec{\omega}}\times\left(x_D\hat{i} + y_D\hat{j}\right) + \vec{\omega}\times\left[\vec{\omega}\times\left(x_D\hat{i} + y_D\hat{j}\right)\right]$$

$$\vec{a}_D = \frac{d^2}{dt^2}\vec{r}_{C/A} + 0 + 0 + \left(\ddot{\theta}_1 + \ddot{\theta}_2\right)\hat{K}\times\vec{r}_{D/C} - \left(\dot{\theta}_1 + \dot{\theta}_2\right)^2\vec{r}_{D/C}$$

$$\vec{a}_D = -L_1\sin\theta_1\ddot{\theta}\hat{I}_1 + L_1\cos\theta_1\ddot{\theta}_1\hat{J} - L_1\cos\theta_1\dot{\theta}_1^2\hat{I} - L_1\sin\theta_1\dot{\theta}_1^2\hat{J} + \ldots$$

$$\ldots - \frac{1}{2}L_2\sin(\theta_1 + \theta_2)\left(\ddot{\theta}_1 + \ddot{\theta}_2\right)\hat{I} + \frac{1}{2}L_2\cos(\theta_1 + \theta_2)\left(\ddot{\theta}_1 + \ddot{\theta}_2\right)\hat{J} + \ldots$$

$$\ldots - \frac{1}{2}L_2\cos(\theta_1 + \theta_2)\left(\dot{\theta}_1 + \dot{\theta}_2\right)^2\hat{I} - \frac{1}{2}L_2\sin(\theta_1 + \theta_2)\left(\dot{\theta}_1 + \dot{\theta}_2\right)^2\hat{J}$$

$$\alpha_2 = \ddot{\theta}_1 + \ddot{\theta}_2$$

Note that the acceleration of *D* does not contain a Coriolis term. This is because the various acceleration terms depend on the intermediate frame of reference. For example, the linear acceleration of *D* can alternatively be written using an intermediate frame centered at A and rotating at $\vec{\omega} = \dot{\theta}_1\hat{K}$. According to the equation for acceleration above:

$$\vec{a}_D = \left(\ddot{X}_A\hat{I} + \ddot{Y}_A\hat{J}\right) + \left(\ddot{x}_D\hat{i} + \ddot{y}_D\hat{j}\right) + 2\vec{\omega}\times\left(\dot{x}_D\hat{i} + \dot{y}_D\hat{j}\right) + \dot{\vec{\omega}}\times\left(x_D\hat{i} + y_D\hat{j}\right) + \vec{\omega}\times\left[\vec{\omega}\times\left(x_D\hat{i} + y_D\hat{j}\right)\right]$$

$$\vec{r}_{D/A} = \left(L_1 + \frac{1}{2}L_2\cos\theta_2\right)\hat{i} + \frac{1}{2}L_2\sin\theta_2\hat{j}$$

$$\vec{v}_D = -\frac{1}{2}L_2\sin\theta_2\dot{\theta}_2\hat{i} + \frac{1}{2}L_2\cos\theta_2\dot{\theta}_2\hat{j} + \left(L_1 + \frac{1}{2}L_2\cos\theta_2\right)\dot{\hat{i}} + \frac{1}{2}L_2\sin\theta_2\dot{\hat{j}}$$

$$\vec{a}_D = \left(-\frac{1}{2}L_2\cos\theta_2\dot{\theta}_2^2 - \frac{1}{2}L_2\sin\theta_2\ddot{\theta}_2\right)\hat{i} + \left(-\frac{1}{2}L_2\sin\theta_2\dot{\theta}_2^2 + \frac{1}{2}L_2\cos\theta_2\ddot{\theta}_2\right)\hat{j} + \text{other terms}$$

$$\vec{a}_D = 0 + \left(-\frac{1}{2}L_2\cos\theta_2\dot{\theta}_2^2 - \frac{1}{2}L_2\sin\theta_2\ddot{\theta}_2\right)\hat{i} + \left(-\frac{1}{2}L_2\sin\theta_2\dot{\theta}_2^2 + \frac{1}{2}L_2\cos\theta_2\ddot{\theta}_2\right)\hat{j} + \ldots$$

$$\ldots + 2\dot{\theta}_1\hat{K}\times\left(-\frac{1}{2}L_2\sin\theta_2\dot{\theta}_2\hat{i} + \frac{1}{2}L_2\cos\theta_2\dot{\theta}_2\hat{j}\right) + \ddot{\theta}_1\hat{K}\times\left[\left(L_1 + \frac{1}{2}L_2\cos\theta_2\right)\hat{i} + \frac{1}{2}L_2\sin\theta_2\hat{j}\right] + \ldots$$

$$\ldots - \dot{\theta}_1^2\left[\left(L_1 + \frac{1}{2}L_2\cos\theta_2\right)\hat{i} + \frac{1}{2}L_2\sin\theta_2\hat{j}\right]$$

$$\vec{a}_D = \ddot{\theta}_2\left(-\frac{1}{2}L_2\sin\theta_2\hat{i} + \frac{1}{2}L_2\cos\theta_2\hat{j}\right) + \dot{\theta}_2^2\left(-\frac{1}{2}L_2\cos\theta_2\hat{i} - \frac{1}{2}L_2\sin\theta_2\hat{j}\right) + \ldots$$

$$\ldots - \dot{\theta}_1\dot{\theta}_2\left(-L_2\cos\theta_2\hat{i} + L_2\sin\theta_2\hat{j}\right) + \ddot{\theta}_1\left[-\frac{1}{2}L_2\sin\theta_2\hat{i} + \left(L_1 + \frac{1}{2}L_2\cos\theta_2\right)\hat{j}\right] + \ldots$$

$$\ldots - \dot{\theta}_1^2\left[\left(L_1 + \frac{1}{2}L_2\cos\theta_2\right)\hat{i} + \frac{1}{2}L_2\sin\theta_2\hat{j}\right]$$

The acceleration of *D*, $\vec{a}_D$, is the same as that derived above using an alternate intermediate reference frame (although $\vec{a}_D$ still needs to be written in terms of the XY frame). Note that now $\vec{a}_D$ does contain a Coriolis acceleration. According to the terminology defined below, acceleration (and torque) terms which are proportional to the product of angular velocities at different joints are called Coriolis terms, while acceleration (and torque) terms which are proportional to the square of angular velocity are called centripetal terms—no matter the intermediate frame.

Newton's Equations of Motion can be written for the X-, Y-, and Z-directions:

X - direction

$$F_{21x} + F_x = -m_2 L_1 \sin\theta_1 \ddot{\theta}_1 - m_2 L_1 \cos\theta_1 \dot{\theta}_1^2 - \frac{1}{2} m_2 L_2 \sin(\theta_1 + \theta_2)(\ddot{\theta}_1 + \ddot{\theta}_2) - \frac{1}{2} m_2 L_2 \cos(\theta_1 + \theta_2)(\dot{\theta}_1 + \dot{\theta}_2)^2$$

Y - direction

$$F_{21y} + F_y = m_2 L_1 \cos\theta_1 \ddot{\theta}_1 - m_2 L_1 \sin\theta_1 \dot{\theta}_1^2 + \frac{1}{2} m_2 L_2 \cos(\theta_1 + \theta_2)(\ddot{\theta}_1 + \ddot{\theta}_2) - \frac{1}{2} m_2 L_2 \sin(\theta_1 + \theta_2)(\dot{\theta}_1 + \dot{\theta}_2)^2$$

Z - direction at B

$$\tau_{21} - \frac{1}{2} F_x L_2 \sin(\theta_1 + \theta_2) + \frac{1}{2} F_y L_2 \cos(\theta_1 + \theta_2) + \frac{1}{2} F_{21x} L_2 \sin(\theta_1 + \theta_2) - \frac{1}{2} F_{21y} L_2 \cos(\theta_1 + \theta_2) = I_{2,D}(\ddot{\theta}_1 + \ddot{\theta}_2)$$

The equations for the X- and Y-directions can be solved for *F21x* and *F21y*, respectively, and plugged into the equation for the Z-direction:

$$\begin{aligned} &\tau_{21} - F_x L_2 \sin(\theta_1 + \theta_2) + F_y L_2 \cos(\theta_1 + \theta_2) \\ &= \ddot{\theta}_1 \left(I_{2,D} + \frac{1}{2} m_2 L_1 L_2 \cos\theta_2 + \frac{1}{4} m_2 L_2^2 \right) + \ddot{\theta}_2 \left(I_{2,D} + \frac{1}{4} m_2 L_2^2 \right) + \dot{\theta}_1^2 \left(\frac{1}{2} m_2 L_1 L_2 \sin\theta_2 \right) \end{aligned}$$

The generalized force is comprised of inertial torques and a velocity torque. The inertial torques represent the normal inertial term due to single joint movement (the torque proportional to $\ddot{\theta}_2$; the equation of motion of a single joint movement (with no forces at the free end) is $\tau = \left(I + \frac{1}{4} m L^2 \right) \ddot{\theta}$) and an interaction term due to movement at the other joint (the torque proportional to $\ddot{\theta}_1$). The velocity torque is centripetal.

Interaction Forces

The equations for the X- and Y-directions for link 2 can be solved for the interaction forces between the two links, *F12x = -F21x* and *F12y = -F21y*. The X- and Y-direction for link 1 can then be solved for the forces acting on link 1 from ground (i.e. the shoulder), *F10x* and *F10y*.

In summary,

$$\ddot{\theta}_1\left(I_{1,B}+I_{2,D}+m_2L_1L_2\cos\theta_2+\frac{1}{4}m_1L_1^2+m_2L_1^2+\frac{1}{4}m_2L_2^2\right)+\ddot{\theta}_2\left(I_{2,D}+\frac{1}{4}m_2L_2^2+\frac{1}{2}m_2L_1L_2\cos\theta_2\right)+\ldots$$
$$\ldots-\dot{\theta}_2^2\left(\frac{1}{2}m_2L_1L_2\sin\theta_2\right)-\dot{\theta}_1\dot{\theta}_2\left(m_2L_1L_2\sin\theta_2\right)$$
$$=\tau_{10}-F_x\left[L_1\sin\theta_1+L_2\sin(\theta_1+\theta_2)\right]+F_y\left[L_1\cos\theta_1+L_2\cos(\theta_1+\theta_2)\right]$$

$$\ddot{\theta}_1\left(I_{2,D}+\frac{1}{2}m_2L_1L_2\cos\theta_2+\frac{1}{4}m_2L_2^2\right)+\ddot{\theta}_2\left(I_{2,D}+\frac{1}{4}m_2L_2^2\right)+\dot{\theta}_1^2\left(\frac{1}{2}m_2L_1L_2\sin\theta_2\right)$$
$$=\tau_{21}-F_xL_2\sin(\theta_1+\theta_2)+F_yL_2\cos(\theta_1+\theta_2)$$

Dynamics via Lagrange's Equation

Generalized Coordinates and Admissible Variations

Generalized coordinates: θ_1, θ_2

Admissible variations: $\delta\theta_1$, $\delta\theta_2 \Rightarrow$ 2 DOF

2 DOF and 2 generalized coordinates $\Rightarrow$ holonomic

Generalized Forces

$$\delta W^{nc} = \tau_1\delta\theta_1 + \tau_2\delta\theta_2 + \vec{r}_{E/A} \times \left(\vec{F}_x + \vec{F}_y\right)\delta\theta_1 + \vec{r}_{E/C} \times \left(\vec{F}_x + \vec{F}_y\right)\delta\theta_2 = \Xi_1\delta\theta_1 + \Xi_2\delta\theta_2$$

$$\vec{r}_{E/A} \times \left(\vec{F}_x + \vec{F}_y\right) = \left\{\left[L_1\cos\theta_1 + L_2\cos(\theta_1 + \theta_2)\right]\hat{i} + \left[L_1\sin\theta_1 + L_2\sin(\theta_1 + \theta_2)\right]\hat{j}\right\} \times \left\{F_x\hat{i} + F_y\hat{j}\right\}$$
$$\vec{r}_{E/A} \times \left(\vec{F}_x + \vec{F}_y\right) = \left\{-F_x\left[L_1\sin\theta_1 + L_2\sin(\theta_1 + \theta_2)\right] + F_y\left[L_1\cos\theta_1 + L_2\cos(\theta_1 + \theta_2)\right]\right\}\hat{k}$$

$$\vec{r}_{E/C} \times \left(\vec{F}_x + \vec{F}_y\right) = \left[L_2\cos(\theta_1 + \theta_2)\hat{i} + L_2\sin(\theta_1 + \theta_2)\hat{j}\right] \times \left[F_x\hat{i} + F_y\hat{j}\right]$$
$$\vec{r}_{E/C} \times \left(\vec{F}_x + \vec{F}_y\right) = \left[-F_xL_2\sin(\theta_1 + \theta_2)\hat{i} + F_yL_2\cos(\theta_1 + \theta_2)\hat{j}\right]\hat{k}$$

$$\delta W^{nc} = \tau_1\delta\theta_1 + \tau_2\delta\theta_2 + \left\{-F_x\left[L_1\sin\theta_1 + L_2\sin(\theta_1 + \theta_2)\right] + F_y\left[L_1\cos\theta_1 + L_2\cos(\theta_1 + \theta_2)\right]\right\}\delta\theta_1$$
$$+\left[-F_xL_2\sin(\theta_1 + \theta_2) + F_yL_2\cos(\theta_1 + \theta_2)\right]\delta\theta_2 = \Xi_1\delta\theta_1 + \Xi_2\delta\theta_2$$

$$\Rightarrow \Xi_1 = \tau_1 - F_x\left[L_1\sin\theta_1 + L_2\sin(\theta_1 + \theta_2)\right] + F_y\left[L_1\cos\theta_1 + L_2\cos(\theta_1 + \theta_2)\right]$$
$$\Rightarrow \Xi_2 = \tau_2 - F_xL_2\sin(\theta_1 + \theta_2) + F_yL_2\cos(\theta_1 + \theta_2)$$

Lagrangian

$$L = T^* - V$$

$$T^* = T_1^* + T_2^*$$

$$T_1^* = \frac{1}{2} m_1 v_B^{\,2} + \frac{1}{2} I_{1/B}\,\omega_1^{\,2}$$

$$\omega_1 = \dot{\theta}_1$$

$$T_1^* = \frac{1}{2} m_1 \left(\dot{\theta}_1 \frac{L_1}{2} \right)^2 + \frac{1}{2} I_{1/B}\,\dot{\theta}_1^{\,2}$$

$$T_1^* = \frac{1}{2}\left[I_{1/B} + m_1 \left(\frac{L_1}{2} \right)^2 \right] \dot{\theta}_1^{\,2} = \frac{1}{2} I_{1/A}\,\dot{\theta}_1^{\,2}$$

$$T_1^* = \frac{1}{8} m_1 \dot{\theta}_1^{\,2} L_1^{\,2} + \frac{1}{2} I_{1/B}\,\dot{\theta}_1^{\,2}$$

$$T_2^* = \frac{1}{2} m_2 v_D^{\,2} + \frac{1}{2} I_{2/D}\,\omega_2^{\,2}$$

$$\vec{v}_D = \frac{d}{dt}\left(\vec{r}_{D/A} \right)$$

$$\vec{r}_{D/A} = \vec{r}_{D/C} + \vec{r}_{C/A} = \begin{bmatrix} \frac{L_2}{2}\cos(\theta_1 + \theta_2) \\ \frac{L_2}{2}\sin(\theta_1 + \theta_2) \end{bmatrix} + \begin{bmatrix} L_1 \cos\theta_1 \\ L_1 \sin\theta_1 \end{bmatrix} = \begin{bmatrix} L_1 \cos\theta_1 + \frac{L_2}{2}\cos(\theta_1 + \theta_2) \\ L_1 \sin\theta_1 + \frac{L_2}{2}\sin(\theta_1 + \theta_2) \end{bmatrix}$$

$$\vec{v}_D = \frac{d}{dt}\left(\vec{r}_{D/A} \right) = \begin{bmatrix} -L_1\dot{\theta}_1 \sin\theta_1 - \frac{L_2}{2}\sin(\theta_1 + \theta_2)\left(\dot{\theta}_1 + \dot{\theta}_2\right) \\ L_1\dot{\theta}_1 \cos\theta_1 + \frac{L_2}{2}\cos(\theta_1 + \theta_2)\left(\dot{\theta}_1 + \dot{\theta}_2\right) \end{bmatrix}$$

Note that $\vec{v}_D$ could have been obtained more quickly using the Jacobian for D : $\vec{v}_D = J_D \begin{bmatrix} \dot{\theta}_1 \\ \dot{\theta}_2 \end{bmatrix}$.

$$v_D^{\,2} = -\left[L_1\dot{\theta}_1 \sin\theta_1 + \frac{L_2}{2}\sin(\theta_1 + \theta_2)\left(\dot{\theta}_1 + \dot{\theta}_2\right) \right]^2 + \left[L_1\dot{\theta}_1 \cos\theta_1 + \frac{L_2}{2}\cos(\theta_1 + \theta_2)\left(\dot{\theta}_1 + \dot{\theta}_2\right) \right]^2$$

$$v_D^{\,2} = L_1^{\,2}\dot{\theta}_1^{\,2} + \frac{L_2^{\,2}}{4}\dot{\theta}_1^{\,2} + L_1 L_2 \dot{\theta}_1^{\,2}\cos\theta_2 + \frac{L_2^{\,2}}{4}\dot{\theta}_2^{\,2} + \frac{L_2^{\,2}}{2}\dot{\theta}_1\dot{\theta}_2 + L_1 L_2 \dot{\theta}_1\dot{\theta}_2 \cos\theta_2$$

$$\omega_2 = \dot{\theta}_1 + \dot{\theta}_2$$

$$T_2^* = \frac{1}{2} m_2 L_1^{\,2}\dot{\theta}_1^{\,2} + \frac{1}{8} m_2 L_2^{\,2}\dot{\theta}_1^{\,2} + \frac{1}{2} I_{2/D}\dot{\theta}_1^{\,2} + \frac{1}{2} m_2 L_1 L_2 \dot{\theta}_1^{\,2}\cos\theta_2 + \frac{1}{8} m_2 L_2^{\,2}\dot{\theta}_2^{\,2} + \frac{1}{2} I_{2/D}\dot{\theta}_2^{\,2} + \ldots$$

$$\ldots + \frac{1}{4} m_2 L_2^{\,2}\dot{\theta}_1\dot{\theta}_2 + I_{2/D}\dot{\theta}_1\dot{\theta}_2 + \frac{1}{2} m_2 L_1 L_2 \dot{\theta}_1\dot{\theta}_2 \cos\theta_2$$

$$V = 0$$

$$L = T_1 * + T_2 *$$

$$L = \dot{\theta}_1^2 \left(\frac{1}{8} m_1 L_1^2 + \frac{1}{2} m_2 L_1^2 + \frac{1}{8} m_2 L_2^2 + \frac{1}{2} I_{1/B} + \frac{1}{2} I_{2/D} + \frac{1}{2} m_2 L_1 L_2 \cos\theta_2 \right) + \dot{\theta}_2^2 \left(\frac{1}{8} m_2 L_2^2 + \frac{1}{2} I_{2/D} \right) + \ldots$$

$$\ldots + \dot{\theta}_1 \dot{\theta}_2 \left(\frac{1}{4} m_2 L_2^2 + I_{2/D} + \frac{1}{2} m_2 L_1 L_2 \cos\theta_2 \right)$$

Lagrange's Equations of Motion

θ_1 :

$$\frac{d}{dt}\left(\frac{\partial L}{\partial \dot{\theta}_1} \right) - \frac{\partial L}{\partial \theta_1} = \Xi_1$$

$$\ddot{\theta}_1 \left(\frac{1}{4} m_1 L_1^2 + m_2 L_1^2 + \frac{1}{4} m_2 L_2^2 + m_2 L_1 L_2 \cos\theta_2 + I_{1/B} + I_{2/D} \right) + \ddot{\theta}_2 \left(\frac{1}{4} m_2 L_2^2 + \frac{1}{2} m_2 L_1 L_2 \cos\theta_2 + I_{2/D} \right) + \ldots$$

$$\ldots - \dot{\theta}_2^2 \left(\frac{1}{2} m_2 L_1 L_2 \sin\theta_2 \right) - \dot{\theta}_1 \dot{\theta}_2 \left(m_2 L_1 L_2 \sin\theta_2 \right)$$

$$= \tau_1 - F_x \left[L_1 \sin\theta_1 + L_2 \sin(\theta_1 + \theta_2) \right] + F_y \left[L_1 \cos\theta_1 + L_2 \cos(\theta_1 + \theta_2) \right]$$

θ_2 :

$$\frac{d}{dt}\left(\frac{\partial L}{\partial \dot{\theta}_2} \right) - \frac{\partial L}{\partial \theta_2} = \Xi_2$$

$$\ddot{\theta}_1 \left(\frac{1}{4} m_2 L_2^2 + \frac{1}{2} m_2 L_1 L_2 \cos\theta_2 + I_{2/D} \right) + \ddot{\theta}_2 \left(\frac{1}{4} m_2 L_2^2 + I_{2/D} \right) + \dot{\theta}_1^2 \left(\frac{1}{2} m_2 L_1 L_2 \sin\theta_2 \right)$$

$$= \tau_2 - F_x L_2 \sin(\theta_1 + \theta_2) + F_y L_2 \cos(\theta_1 + \theta_2)$$

In summary,

$$\ddot{\theta}_1\left(I_{1/B}+I_{2/D}+m_2L_1L_2\cos\theta_2+\frac{1}{4}m_1L_1^2+m_2L_1^2+\frac{1}{4}m_2L_2^2\right)+\ddot{\theta}_2\left(I_{2/D}+\frac{1}{4}m_2L_2^2+\frac{1}{2}m_2L_1L_2\cos\theta_2\right)+\ldots$$

$$\ldots-\dot{\theta}_2^2\left(\frac{1}{2}m_2L_1L_2\sin\theta_2\right)-\dot{\theta}_1\dot{\theta}_2\left(m_2L_1L_2\sin\theta_2\right)$$

$$=\tau_1-F_x\left[L_1\sin\theta_1+L_2\sin\left(\theta_1+\theta_2\right)\right]+F_y\left[L_1\cos\theta_1+L_2\cos\left(\theta_1+\theta_2\right)\right]$$

$$\ddot{\theta}_1\left(I_{2/D}+\frac{1}{2}m_2L_1L_2\cos\theta_2+\frac{1}{4}m_2L_2^2\right)+\ddot{\theta}_2\left(I_{2/D}+\frac{1}{4}m_2L_2^2\right)+\dot{\theta}_1^2\left(\frac{1}{2}m_2L_1L_2\sin\theta_2\right)$$

$$=\tau_2-F_xL_2\sin\left(\theta_1+\theta_2\right)+F_yL_2\cos\left(\theta_1+\theta_2\right)$$